
**Characterisation of the effects of intrinsically disordered
protein (IDP)–solvent and IDP–lipid interactions
in aqueous solution and lipid monolayers**

DISSERTATION
ZUR ERLANGUNG DES DOKTORGRADES DER NATURWISSENSCHAFTEN
(DR. RER. NAT.)

der
Naturwissenschaftlichen Fakultät II
Chemie, Physik und Mathematik

der
Martin-Luther-Universität
Halle-Wittenberg

vorgelegt von
Frau KATHARINA WIDDER
geboren am 30.12.1989 in Bad Frankenhausen

Erstgutachter: Prof. Dr. Dariush Hinderberger
Zweitgutachter: Prof. Dr. Heinz-Jürgen Steinhoff

Tag der öffentlichen Verteidigung: 22.05.2019

A straight line may be the
shortest distance between two
points, but it is by no means
the most interesting.

(Robert Holmes)

Contents

1	Introduction	1
2	Theory	5
2.1	Electron paramagnetic resonance	5
2.1.1	Basic principles	5
2.1.2	Spin Hamilton operator	6
2.1.3	Nitroxides	9
2.1.4	Simulation of CW EPR spectra	12
2.2	Monolayer measurements	13
2.2.1	Model lipid monolayers	13
2.2.2	Film balance methods	15
2.2.3	Line tension	17
2.2.4	Monolayer electrostatics	18
3	Thermoresponsive peptide polymers	21
3.1	Introduction	21
3.2	Hydration and nanophase separation of elastin-like polypeptide diblock copolymers	23
3.2.1	Diblock ELP	23
3.2.2	Results and discussion	24
3.2.2.1	EPR spectroscopic changes during the loss of hydration	24
3.2.2.2	Microscopic phase transition	25
3.2.2.3	Type of inhomogeneities	27
3.2.2.4	Influence of the hydrophobic block	29
3.2.2.5	Influence of the hydrophilic block	30
3.2.3	Conclusions	31
3.3	Dehydration and rehydration of hysteretic temperature-responsive peptide polymers	32
3.3.1	Hysteretic peptide polymers	32
3.3.2	Results and discussion	32
3.3.2.1	EPR spectroscopic changes during the loss of hydration	32
3.3.2.2	Hysteretic behaviour of (VAPVG) and (TPVAVG)	36
3.3.2.3	Stabilisation of aggregates by a hydrophilic amino acid	39
3.3.2.4	Chain length dependence	42
3.3.3	Conclusions	43
3.4	Outlook	44

4	Myelin basic protein	47
4.1	Introduction	47
4.2	Interaction of bovine myelin basic protein with lipid monolayers	50
4.2.1	MBP–lipid interactions	50
4.2.2	Results and discussion	51
4.2.2.1	Monolayers of the normal myelin composition	51
4.2.2.2	Various combinations of brain lipids of the myelin-like monolayers	53
4.2.2.3	Electrostatic interaction	58
4.2.3	Conclusions	66
4.3	Interaction of myelin basic protein charge variants with lipid monolayers	67
4.3.1	MBP C1 and MBP C8	67
4.3.2	Results and discussion	68
4.3.2.1	Monolayers of the normal myelin composition	68
4.3.2.2	Various combinations of brain lipids of the myelin-like monolayers	70
4.3.2.3	Line tension vs. electrostatic attraction	75
4.3.3	Conclusions	77
4.4	Outlook	78
5	Experimental	83
5.1	Thermoresponsive peptide polymers	83
5.1.1	Materials	83
5.1.2	Methods	84
5.2	Myelin basic protein	85
5.2.1	Materials	85
5.2.2	Methods	86
6	Summary	91
	Zusammenfassung	95
	Bibliography	99
	Appendix	115
A	Thermoresponsive peptide polymers	115
A.1	Diblock ELP	115
A.2	Hysteretic polymers	134
B	Myelin basic protein	151
B.1	Bovine myelin basic protein	151
B.2	Recombinant murine myelin basic protein C1 and C8 charge variants . .	164
B.3	Outlook	175
	Publications	181
	Curriculum Vitae	183

CHAPTER 1

Introduction

The central paradigm in structural biology—a well-defined tertiary protein structure specified by an amino acids sequence is essential for its biological function¹⁻³—seemed indisputable over a long time. Several biological functions (e.g. immunological recognition,⁴ enzymatic catalysis⁵ or molecular discrimination by receptors⁶) accomplish the structure–function paradigm as a stable globular structure is absolutely necessary. As opposed to this, physiological functions such as signal transduction,^{7,8} cell-signalling^{8,9} or chaperone activity¹⁰ are related to proteins that possess disordered regions in solution.^{1,3,11} These so-called intrinsically disordered proteins (IDP) challenge the structure–function paradigm. Intrinsically disordered proteins are not completely unstructured.¹² However, IDPs contain function-related elements of local structural organisation¹³ undergoing disorder-to-order transitions as a response to biological signals such as binding to other biomolecules¹⁴ or environmental changes (e.g. temperature or pH).¹⁵ The fact that the conformation of IDPs depends on their environment or on association with binding partners provides several advantages. The protein may respond rapidly to environmental changes. Furthermore, a fast interaction or association with, and control of, multiple binding partners at once is possible.¹ Being shaped by the environment endows disordered proteins with an inherent flexibility that enables them to recognise a broad variety of biomolecular targets for purposeful specific interactions.^{1,16} The interactions leading to the disorder-to-order transition of IDPs are determined by hydrogen bonding, hydrophobic interactions, electrostatic interactions as well as entropic contributions arising from conformational changes.

Whether a protein folds into a stable, globular state or remains either unfolded in solution or adopts non-globular structures is encoded in its specific amino acid sequence.^{1,17} Compared to proteins obeying the lock-and-key mechanism of function, the primary structure of IDPs features a higher proportion of charged and a lower proportion of hydrophobic amino acids.¹⁸⁻²⁰ Furthermore, IDPs are enriched in disorder-promoting amino acids (A, R, G, Q, S, P, E and K) and depleted in order-promoting amino acids (W, C, F, I, Y, V, L and N).²

Due to their involvement in physiological and pathological processes,^{21,22} the transition behaviour of IDPs is of high scientific interest. To derive medical or pharmaceutical benefit from IDPs, more insights into the origins of disorder and the adoption of multiple aggregation states as a response to specific environmental conditions are required. Therefore, this thesis approaches the aggregation behaviour of two types of IDPs providing different perspectives from a variety of characterisation techniques.

The first chosen type of IDPs are stimuli-responsive peptide polymers. Polymer-like repetitive amino acid sequences with intrinsical disorder serve as model systems to examine the relation of amino acid sequence and biophysical behaviour of IDPs.^{15,23,24} Promising candidates for prototypes of IDPs are polypeptides that are rich in amino acids contributing to disorder, especially glycine and proline.^{15,24} Glycine possesses a high chain mobility since it has no side chain that facilitates to adopt a diversity in conformations.²⁵ The conformational restriction of proline's main chain hampers the formation of stable secondary structure elements.²⁵ The stimuli-responsive behaviour of intrinsically disordered peptide polymers such as elastin- or resilin-like polypeptides has attracted a broad attention over the last decades due to their potential for applications as drug delivery systems in cancer therapy,^{26,27} or in tissue engineering.^{28,29} Advantages of the pharmaceutical use of amino acid-derived polymers arise from their non-toxicity,³⁰ biodegradability³¹ and their precisely controllable primary structure by gene encoding.³² For a purposeful application, the disorder-to-order transition of these polypeptides has to be understood to enable a precise tuning of the desired response to external stimuli. Focussing on hydration processes during the disorder-to-order transition, Chapter 3 of this thesis addresses the temperature-dependent behaviour of two types of thermoresponsive peptide polymers studied by continuous wave (CW) electron paramagnetic resonance (EPR) spectroscopy. (A brief introduction of the theoretical aspects of the quantum-mechanical principles and the spin Hamilton operator of an EPR experiment in general, theoretical aspects of the EPR measurement on nitroxide spin probes and the theory applied for the simulation of CW EPR spectra is given in Section 2.1.) First, diblock elastin-like polypeptides (ELPs) composed of a hydrophobic and a hydrophilic block are investigated with respect to their temperature-driven phase-separating behaviour (Section 3.2). The influence of polarity and hydrophobic mass fraction on the transition temperature and the molecular structure of the polymer aggregates is analysed in this section. Second, thermoresponsive peptide polymers with differing dehydration and rehydration processes during heating and cooling, respectively, of the polymers are investigated in Section 3.3. Analysing the influence of primary amino acid sequence and chain length of the polymer on its phase transition reveals information about the reversibility of the dehydration process of the polymer chains. Experiments verifying the conclusions are suggested in an outlook (Section 3.4).

The second type of IDPs, investigated in this thesis, is myelin basic protein (MBP). This protein is a major component of the central nervous system and related to neurodegenerative diseases like multiple sclerosis (MS). It adheres to the cytoplasmic leaflets of the oligodendrocyte membrane to ensure a high compaction of the myelin sheath, which serves as an insulator of neuronal axons to facilitate nerve impulse transmission. The different isoforms of MBP are invariably intrinsically disordered.²⁰ The amino acid sequence of MBP corresponds to specific characteristics of IDPs. In particular, MBP has a higher proportion of charged amino acids, a lower proportion of hydrophobic amino acids and exhibits an enrichment in prolines compared to proteins that fulfil the classic structure–function paradigm.^{20,33} MBP's lack of tertiary structure facilitates a rapid association with various biomolecules. Representing a random coil in aqueous solution,³⁴ MBP undergoes a disorder-to-order transition during the interaction with its environment or binding partners.³⁵ The interaction with lipid layers plays an important role in the formation of α -helical structures of MBP.^{36,37}

This thesis focusses on the interaction of MBP with myelin-like membranes. Upon application of monolayer adsorption techniques, the interaction of MBP and monolayers composed of different lipid compositions that resemble the myelin sheath at the air-water interface is studied in Chapter 4. (Lipid monolayers and different techniques for investigations concerning their phase behaviour and the general interaction of proteins with lipid monolayers are introduced in Section 2.2. Furthermore, this section contains a short summary about the line tension of different monolayer domains and about electrostatic interactions between charged monolayers interacting with charged proteins.) In a first step, different lipid compositions are tested to reveal the role of every single major lipid of the myelin sheath for the incorporation of MBP. For this purpose, bovine MBP is used to leave possible influences of different charge variants aside (Section 4.2). Based on these results, in the next step the influence of the charge of MBP is involved by using recombinant murine MBP variants of different charge (Section 4.3), relevant for the pathogenesis of neurodegenerative diseases like multiple sclerosis. An outlook containing preliminary experiments for further investigations is given in Section 4.4.

CHAPTER 2

Theory

2.1 Electron paramagnetic resonance

2.1.1 Basic principles

EPR spectroscopic methods are based on the detection of the resonance behaviour of unpaired electrons in an external magnetic field \mathbf{B} . The intrinsic angular momentum \mathbf{S} of a spinning electron is related to a magnetic moment $\boldsymbol{\mu}_S$ by the relation

$$\boldsymbol{\mu}_S = -\frac{g_e\mu_B}{\hbar}\mathbf{S} \quad (2.1)$$

with the Bohr magneton μ_B and the g value of the free electron $g_e \approx 2.00232$.

The degenerated energy level of a single electron in an external magnetic field splits into two energy levels, depending on its magnetic quantum number $m_S = \pm 1/2$ and on the strength of the magnetic field B_0 . Therefore, the magnetic moment of the electron can adopt two orientations relative to the magnetic field: $|\alpha\rangle$ antiparallel ($m_S = +1/2$) or $|\beta\rangle$ parallel ($m_S = -1/2$). Boltzmann's distribution gives the relative populations n of the two respective energy states:

$$\frac{n_\alpha}{n_\beta} = \exp\left(-\frac{\Delta E}{k_B T}\right). \quad (2.2)$$

The difference in energy between these two energy levels defines the resonance condition

$$\Delta E = \hbar\omega = g_e\mu_B B_0. \quad (2.3)$$

Thus, irradiation of an electromagnetic wave with a frequency ω results in a change of the spin quantum state of the electron from $|\beta\rangle$ to $|\alpha\rangle$. The detection of the energy difference ΔE absorbed by the electron is the fundamental principle of EPR spectroscopy. Practically, the paramagnetic system is brought into resonance by keeping the irradiated frequency constant and varying the energy level separation by sweeping the magnetic field. To increase the signal-to-noise ratio of the spectrum, the magnetic field is additionally modulated by a sinusoidal field with amplitude dB and a frequency of $\omega = 100$ kHz. This modulation leads to the detection of the first derivative of the absorption signal.

2.1.2 Spin Hamilton operator

In the case of a paramagnetic system with a bound unpaired electron, the energetic state of the electron spin is influenced by the external magnetic field, other electronic spins as well as nuclear spins in direct vicinity of the electron. The energetic eigenvalues of the paramagnetic system can be described by solving the Schrödinger equation $i\hbar \frac{\partial}{\partial t} \psi(\mathbf{r}, t) = \hat{\mathbf{H}} \psi(\mathbf{r}, t)$. The static spin Hamiltonian $\hat{\mathbf{H}}$ contains all magnetic interactions of the electron spin:

$$\hat{\mathbf{H}}(S) = \hat{\mathbf{H}}_{\text{ez}} + \hat{\mathbf{H}}_{\text{zfs}} + \hat{\mathbf{H}}_{\text{hf}} + \hat{\mathbf{H}}_{\text{nz}} + \hat{\mathbf{H}}_{\text{nq}} + \hat{\mathbf{H}}_{\text{nn}}, \quad (2.4)$$

arranged in descending order of their typical contribution to the overall energy state (in angular frequency units). The single contributions to $\hat{\mathbf{H}}$ are explained in the following.

The interaction of the electron spin with the external magnetic field is described by the electron Zeeman term

$$\hat{\mathbf{H}}_{\text{ez}} = \frac{\mu_B}{\hbar} \mathbf{B}_0^T \mathbf{g} \mathbf{S}. \quad (2.5)$$

Due to the orientation-dependence of the applied magnetic field \mathbf{B}_0 and the electron spin operator \mathbf{S} , \mathbf{g} has the form of a tensor with 3×3 elements. Euler angle transformation* yields a diagonalised form of the \mathbf{g} tensor:

$$\mathbf{g} = \begin{pmatrix} g_{xx} & 0 & 0 \\ 0 & g_{yy} & 0 \\ 0 & 0 & g_{zz} \end{pmatrix}. \quad (2.6)$$

In an atom, the deviation of the principal values of \mathbf{g} of the spin system from the g value of a free electron depends on the spin-orbit interaction term:³⁸

$$\mathbf{g} = g_e \mathbf{1} + 2\lambda \mathbf{\Lambda} \\ \Lambda_{ij} = \sum_{k \neq 0} \frac{\langle \psi_0 | L_i | \psi_k \rangle \langle \psi_k | L_j | \psi_0 \rangle}{E_0 - E_k} \quad (2.7)$$

with the spin-orbit coupling constant λ . The orbital angular momentum L is zero in the case of a non-degenerated ground state. The elements Λ_{ij} describe the interaction of the ground state $\langle \psi_0 |$ with energy E_0 and the excited state $|\psi_k\rangle$ with energy E_k . The indices of summation in Equation 2.7 run over the coordinate axes x, y and z .

Fast molecular motion of the paramagnetic system in solution leads to an isotropic value $g_{\text{iso}} = (g_{xx} + g_{yy} + g_{zz})/3$, which is an average of the orientation dependence of the \mathbf{g} tensor.

*The successive rotation of the lab coordinate system around the so-called Euler angles α, β and γ transforms it into the molecular coordinate system of the radical corresponding to the relation³⁸

$$R = R_{z''}(\gamma) \cdot R_{y'}(\beta) \cdot R_z(\alpha) = \begin{pmatrix} \cos \gamma & \sin \gamma & 0 \\ -\sin \gamma & \cos \gamma & 0 \\ 0 & 0 & 1 \end{pmatrix} \cdot \begin{pmatrix} \cos \beta & 0 & -\sin \beta \\ 0 & 1 & 0 \\ \sin \beta & 0 & \cos \beta \end{pmatrix} \cdot \begin{pmatrix} \cos \alpha & \sin \alpha & 0 \\ -\sin \alpha & \cos \alpha & 0 \\ 0 & 0 & 1 \end{pmatrix}.$$

Contributions of the zero-field splitting term

$$\hat{\mathbf{H}}_{\text{zfs}} = \mathbf{S}^T \mathbf{D}_0 \mathbf{S} \quad (2.8)$$

with zero-field interaction tensor \mathbf{D}_0 to the overall spin Hamiltonian emerge for spin systems of strongly coupled spins with a group spin $S > 1/2$. The energetic degeneracy of the ground state is removed, even in the absence of an external magnetic field. However, in this thesis, the zero-field splitting can be neglected due to $S = 1/2$.

The Hamiltonian of the hyperfine interaction

$$\begin{aligned} \hat{\mathbf{H}}_{\text{hf}} &= \sum_k \mathbf{S}^T \mathbf{A}_k \mathbf{I}_k = \hat{\mathbf{H}}_{\text{fc}} + \hat{\mathbf{H}}_{\text{dd}} \\ \hat{\mathbf{H}}_{\text{fc}} &= \sum_k a_{\text{iso},k} \mathbf{S}^T \mathbf{I}_k \\ \hat{\mathbf{H}}_{\text{dd}} &= \sum_k \mathbf{S}^T \mathbf{T}_k \mathbf{I}_k \end{aligned} \quad (2.9)$$

with hyperfine coupling tensor \mathbf{A}_k and nuclear spin operator \mathbf{I}_k of the k th nucleus coupled to the electron spin contains information about the magnetic environment of the electron spin. It describes the interaction between the magnetic moment of an electron spin $\boldsymbol{\mu}_e$ and the magnetic moments of surrounding nuclear spins $\boldsymbol{\mu}_n$. The hyperfine interaction is composed of a Fermi contact term $\hat{\mathbf{H}}_{\text{fc}}$ (isotropic) and a dipolar term $\hat{\mathbf{H}}_{\text{dd}}$ (anisotropic) that is described by the hyperfine coupling tensor:³⁸

$$\mathbf{A} = a_{\text{iso}} \mathbf{1} + \frac{g\mathbf{T}}{g_e}. \quad (2.10)$$

The isotropic part arises from the non-vanishing spatial probability density $|\psi_0(0)|^2$ of an s-orbital electron at the location of the nucleus:

$$a_{\text{iso}} = \frac{2\mu_0}{3\hbar} g_e \mu_B g_n \mu_n |\psi_0(0)|^2. \quad (2.11)$$

In the case of entire motional freedom a_{iso} is given as the trace of the hyperfine coupling tensor $a_{\text{iso}} = \text{Tr}(\mathbf{A}) = (A_{xx} + A_{yy} + A_{zz})/3$.

The anisotropic part $\hat{\mathbf{H}}_{\text{dd}}$ of the hyperfine interaction arises from dipole–dipole interaction between the magnetic moments of the electron spin $\boldsymbol{\mu}_e$ and of the nuclear spin $\boldsymbol{\mu}_n$ with distance r_{en} , which is generally given by:

$$E_{\text{en}} = \frac{\mu_0}{4\pi r_{\text{en}}^3} \left[\boldsymbol{\mu}_e^T \boldsymbol{\mu}_n - \frac{3(\boldsymbol{\mu}_e^T \mathbf{r}_{\text{en}})(\boldsymbol{\mu}_n^T \mathbf{r}_{\text{en}})}{r_{\text{en}}^2} \right]. \quad (2.12)$$

The dipolar term $\hat{\mathbf{H}}_{\text{dd}}$ of $\hat{\mathbf{H}}_{\text{hf}}$ contains the dipolar coupling tensor \mathbf{T} :

$$\mathbf{T}_k = \frac{\mu_0}{4\pi\hbar r_{\text{en}}^3} g_e \mu_B g_n \mu_n \begin{pmatrix} -1 & 0 & 0 \\ 0 & -1 & 0 \\ 0 & 0 & -2 \end{pmatrix}. \quad (2.13)$$

The dipolar coupling tensor \mathbf{T} neglects spin–orbit coupling and g anisotropy and is deter-

mined by the dipole–dipole interaction of the magnetic moments $\boldsymbol{\mu}_e$ and $\boldsymbol{\mu}_n$ with distance r_{en} .

Analogous to the already addressed electron Zeeman interaction, atomic nuclei also couple to an external magnetic field, which is called nuclear Zeeman interaction:

$$\hat{H}_{nz} = -\frac{\mu_n}{\hbar} \sum_k g_{n,k} \mathbf{B}_0^T \mathbf{I}_k \quad (2.14)$$

considering the intrinsic properties of atomic nuclei as $g_{n,k}$, $\boldsymbol{\mu}_n$ and \mathbf{I}_k . The nuclear Zeeman interaction has the opposite sign to the electron Zeeman interaction due to the opposite charge of electron and nucleus. The number of energy levels n_H of k interacting spins in an external magnetic field is described by a Hilbert space with dimension^{†39}

$$n_H = \prod_k (2J_k + 1). \quad (2.15)$$

Atomic nuclei with a spin angular momentum of $I \geq 1$ exhibit a non-spherical charge distribution giving rise to a nuclear electrical quadrupole momentum Q . This quadrupole momentum interacts with the electrical field gradient at the location of the nucleus, which is induced by the charge distribution of the electron and surrounding nuclei. The nuclear quadrupole interaction is described by the Hamiltonian:

$$\hat{H}_{nq} = \sum_k \mathbf{I}_k^T \mathbf{P}_k \mathbf{I}_k \quad (2.16)$$

with the nuclear quadrupole tensor \mathbf{P} and results in second order effects such as a shift of resonance lines and appearance of forbidden transitions, which are difficult to observe in CW EPR spectroscopy but detectable with HYSORE (hyperfine sub-level correlation) measurements.³⁹

In solid-state NMR, the dipolar coupling tensor $\mathbf{d}^{(k,l)}$ yields structural information on inter-spin distances in macromolecules.⁴⁰ In EPR spectroscopy, the dipolar coupling between the k th and l th nuclear spin

$$\hat{H}_{nn} = \sum_{k,l} \mathbf{I}_k^T \mathbf{d}^{(k,l)} \mathbf{I}_l \quad (2.17)$$

is too weak to be detected directly.

Weakly coupled electrons are conveniently described by the addition of the Hamiltonians of the single electrons and of terms arising from their coupling:³⁹

$$\begin{aligned} \hat{H}(S_1, S_2) &= \hat{H}(S_1) + \hat{H}(S_2) + \hat{H}_{ex} + \hat{H}_{ee} \\ \hat{H}_{ex} &= \mathbf{S}_1^T \mathbf{J}_{ex} \mathbf{S}_2 \\ \hat{H}_{ee} &= \mathbf{S}_1^T \mathbf{T}_{ee} \mathbf{S}_2. \end{aligned} \quad (2.18)$$

[†]The total angular momentum $\mathbf{J} = \mathbf{S} + \mathbf{L}$ of a gyrating spin arises from the coupling of the spin angular momentum \mathbf{S} and the orbital angular momentum \mathbf{L} leading to the total magnetic momentum $\boldsymbol{\mu}_J = \boldsymbol{\mu}_S + \boldsymbol{\mu}_L$.

The so-called Heisenberg exchange term $\hat{\mathbf{H}}_{\text{ex}}$ with an exchange coupling tensor \mathbf{J}_{ex} contains the contribution of the overlapping wave functions of two electron spins in spatial proximity ($r < 1.5$ nm).⁴¹ The exchange term arises from a spin state exchange reaction or the exchange of the unpaired electrons. In liquid solutions, the orbitals overlap for short times due to collisions of paramagnetic species depending on molecular diffusion and spin concentration.⁴² The spin exchange is characterised by the exchange integral J_{12} of the colliding spins, which determines the exchange frequency⁴³

$$\omega_{\text{ex}} = \frac{J_{12}^2 \tau_1^2}{\tau_2(1 + J_{12}^2 \tau_1^2)} \quad (2.19)$$

with the lifetime τ_1 of the colliding pair and the mean time between spin exchanges τ_2 . The overlap of the wave functions, and thus J_{12} and ω_{ex} , depends on the distance r_{ee} between the interacting electron spins.⁴² Consequently, the exchange component of the EPR spectrum is characterised by a distribution of exchange frequencies $\omega_{\text{ex}}(r)$.

The interaction energy of the dipolar term $\hat{\mathbf{H}}_{\text{ee}}$ containing the dipolar coupling tensor \mathbf{T}_{ee} can be described in analogy to the dipolar part of the hyperfine interaction (Equation 2.12). The dipole–dipole coupling frequency of electrons depends on the distance between the electrons with r_{ee}^{-3} . The extraction of this coupling frequency and corresponding inter-electron spin distances is addressed by pulsed EPR methods as DEER (double electron-electron resonance).^{44,45}

2.1.3 Nitroxides

Since covalent chemical bonds are based on the pairing of electrons, due to their diamagnetic properties only few macromolecular systems are suitable for investigation with EPR spectroscopy. This situation can be circumvented by the use of EPR-active, paramagnetic tracer molecules that interact with the system of interest via non-covalent interactions. This phenomenon of self-assembly depends on the systems environment and is called the ‘spin probing’ approach. In this thesis, nitroxide radicals with the structural unit $\text{R}^1\text{R}^2\text{N}\dot{\text{O}}$ are used as spin probes. In such nitroxides, the unpaired electron is delocalised along the N–O bond. Energetically relevant terms of the spin Hamiltonian are the electron Zeeman interaction $\hat{\mathbf{H}}_{\text{ez}}$, nuclear Zeeman interaction $\hat{\mathbf{H}}_{\text{nz}}$ and the hyperfine interaction $\hat{\mathbf{H}}_{\text{hf}}$ between electron and the nitrogen nucleus with $I = 1$:

$$\hat{\mathbf{H}}_{\text{NO}} = \frac{\mu_{\text{B}}}{\hbar} \mathbf{B}_0^{\text{T}} \mathbf{g} \mathbf{S} - \frac{\mu_{\text{N}} g_{\text{N}}}{\hbar} \mathbf{B}_0^{\text{T}} \mathbf{I} + \mathbf{S}^{\text{T}} \mathbf{A} \mathbf{I} + \hat{\mathbf{H}}_1(t) \quad (2.20)$$

leading to the energy diagram of nitroxides as depicted in Figure 2.1. The contribution of nuclear quadrupole interaction $\hat{\mathbf{H}}_{\text{nq}}$ can be neglected.⁴⁶ The time-dependent term $\hat{\mathbf{H}}_1(t)$ arises from the interaction between the electron spin and the oscillating magnetic field $\mathbf{B}(t)$ of the incident microwave. The solution of the Schrödinger equation for isotropic rotation has six eigenstates with energies:

$$E_{\text{NO}} = g_{\text{e}} \mu_{\text{B}} B_0 m_{\text{S}} - g_{\text{N}} \mu_{\text{N}} B_0 m_{\text{I}} + a_{\text{iso}} m_{\text{S}} m_{\text{I}}. \quad (2.21)$$

The rules for magnetic dipole transitions ($\Delta m_{\text{S}} = 1$ and $\Delta m_{\text{I}} = 0$) allow for three transitions with energy difference:

$$\Delta E_{\text{NO}} = \hbar \omega_{\text{I}} = g_{\text{e}} \mu_{\text{B}} B_0 + a_{\text{iso}} m_{\text{I}}. \quad (2.22)$$

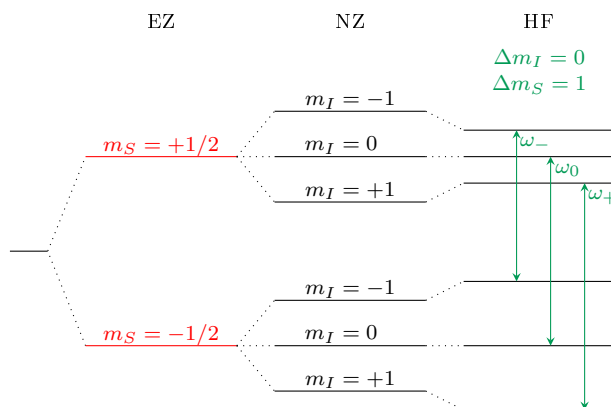


Figure 2.1: Energy diagram for a spin system with $S = 1/2$ and $I = 1$, e.g. a nitroxide radical, considering electron Zeeman (EZ), nuclear Zeeman (NZ) and hyperfine interactions (HF). Following the transition rules for magnetic dipole transitions $\Delta m_S = 1$ and $\Delta m_I = 0$, three transition frequencies ω_- , ω_0 and ω_+ are detected for this spin system (green arrows) resulting in a three peak spectrum (see Figure 2.2 a).

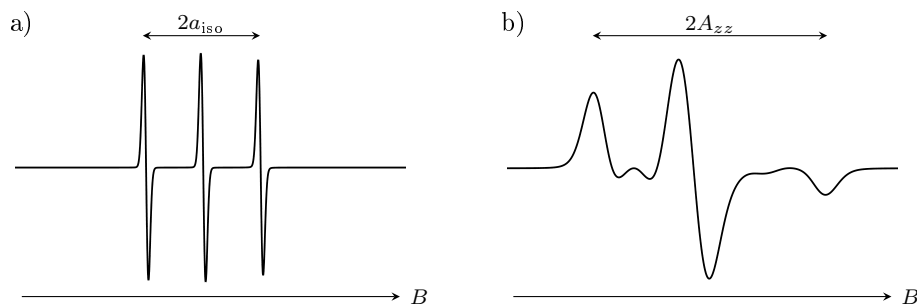


Figure 2.2: CW EPR spectra of nitroxides with different rotational correlation times τ : a) fast rotational motion with $\tau = 10$ ps, b) slow rotational motion with $\tau = 100$ ns. The spectra were generated with the EasySpin software package (see Section 2.1.4).

As a consequence, the B -dependent EPR spectrum of nitroxides shows three peaks. The zero crossing of the central peak coincides with the g value of the spectrum according to the resonance condition shown in Equation 2.3.

The anisotropy of the g value of nitroxides cannot be detected with X-band frequencies ($\nu \approx 9.4$ GHz) as used in this work but rather with higher frequencies (W-band, $\nu \approx 94$ GHz). However, the anisotropy of the hyperfine coupling a can be investigated with X-band frequencies, since the hyperfine interaction is strongly orientation dependent.

The EPR spectrum of nitroxides is sensitive to environmental parameters and thus reports indirectly about the system of interest. The values of g and a , especially g_{xx} and A_{zz} , strongly depend on the polarity of the environment of the spin probe and can therefore be utilised to distinguish between regions of high and low polarity.^{47,48} In polar regions hyperfine coupling is stronger than in apolar regions, since in a polar environment the zwitterionic structure is favoured compared to the neutral form and the electron spin

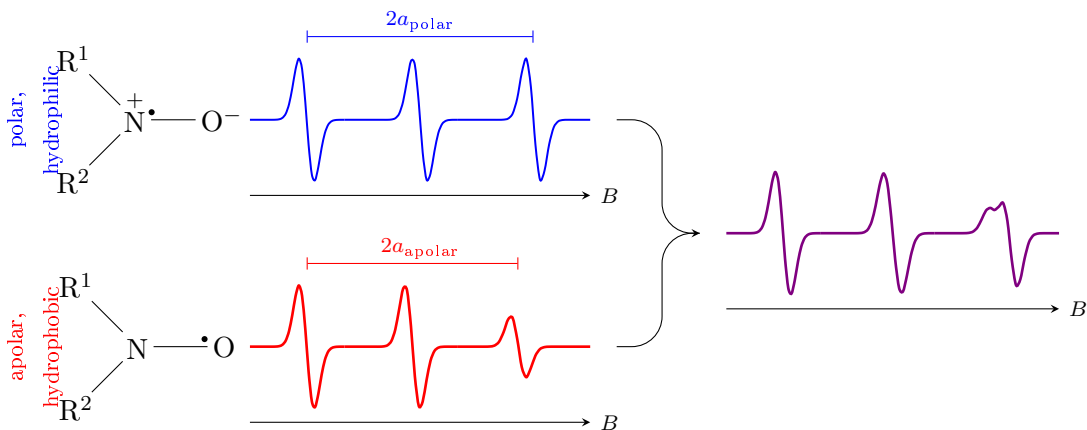


Figure 2.3: Schematic depiction of nitroxide radicals in polar, hydrophilic (blue) and apolar, hydrophobic (red) environments with $g_{\text{polar}} < g_{\text{apolar}}$, $a_{\text{polar}} > a_{\text{apolar}}$ and corresponding CW EPR spectra. In a polar environment, the unpaired electron is predominantly localised near the nitrogen nucleus and in an apolar environment near the oxygen nucleus affecting the g value and the hyperfine coupling constant a . In systems with regions of different polarities, a superposition of both spectral types is obtained (violet).

density is therefore increased at the nitrogen nucleus (blue spectrum in Figure 2.3). With increasing hydrophobicity of the nitroxide environment, the g value shifts to slightly lower field positions and hyperfine coupling decreases. The effects of polarity on g and a are added up in the EPR spectrum, leading to a detectable shift at the high-field peak (red spectrum in Figure 2.3). If spin probe molecules are present in both environments, a splitting of the high-field peak is visible due to superposition of the two described spectra (violet spectrum in Figure 2.3).

Furthermore, the nitroxide spectrum is sensitive towards solution viscosity that affects the rotational dynamics of the spin probe. The translational diffusion of the nitroxide cannot be resolved in an EPR spectrum, since only the angular motion in an external magnetic field affects the magnetic interactions and the line shape. Rotational diffusion as a random process is characterised by the rotational correlation time τ , which is generally defined by the integration over the rotational autocorrelation functions $\rho(t)$:

$$\tau = \int_{t_0}^{\infty} \rho(t) dt = \int_{t_0}^{\infty} \langle D_{m,n}^l(\Omega(t)) \mid D_{m,n}^l(\Omega(t_0)) \rangle dt \quad (2.23)$$

with Wigner rotation matrices $\mathbf{D}(\Omega(t))$ that describe the time-dependence of the nitroxide orientation $\Omega(t)$. Solving Equation 2.23 and applying the Stokes-Einstein equation results for spherical molecules[‡] in

$$\tau = \frac{1}{6D_r} = \frac{4\pi\eta R_h}{3k_B T} \quad (2.24)$$

with solvent viscosity η and rotational hydrodynamic radius R_h . For an asymmetrically tumbling molecule ($D_{xx} \neq D_{yy} \neq D_{zz}$), the rotational diffusion coefficient results from

[‡]A model for ellipsoidal molecules has been proposed by Perrin.⁴⁹

the geometric average $D_r = \sqrt[3]{D_{xx}D_{yy}D_{zz}}$. By means of the rotational correlation time, the mobility of the spin probe can be subdivided into different dynamic regimes. In the case of fast rotation, anisotropic properties are averaged out. The spectrum is characterised by g_{iso} , a_{iso} and spectral lines of similar heights (Figure 2.2 a). With decreasing mobility of the spin probe, τ increases and anisotropic effects become more visible. The hyperfine coupling constant differs increasingly from a_{iso} . Restricted rotational motion results in an anisotropic spectrum with broad and inhomogeneous line shapes. The hyperfine coupling constant of an anisotropic spectrum amounts to A_{zz} (Figure 2.2 b).

2.1.4 Simulation of CW EPR spectra

Rotational correlation times of (virtually) isotropic EPR spectra can be calculated with the relative heights of the spectral peaks.^{50,51} However, this method cannot be applied if the system of interest involves regions of different environmental properties and thus, different spectroscopic species contribute to the spectrum. The experimental EPR spectrum

$$S_{\text{exp}} = \sum_p f_p S_p \quad \text{with} \quad \sum_p f_p = 1 \quad (2.25)$$

consists of the summation of sub-spectra S_p of each spectral species that contributes with the fraction f_p (violet spectrum in Figure 2.3). Spectral simulation facilitates the separation of the EPR spectra into individual spectral contributions and concomitantly the extraction of the parameters needed to further analyse the investigated system. In this thesis, home-written MATLAB (The MathWorks, Inc., Natick, MA, USA) routines that are based on the simulation toolbox EasySpin⁵² have been used to calculate CW EPR spectra of up to four spectral components.

The spectral simulation reproduces EPR spectra by quantum-mechanical numerical calculations, incorporating the Hamiltonian of the spin probe (Equation 2.20). The spectrum is calculated for a certain set of the parameters governing the shape of the resonance peaks: \mathbf{g} tensor, hyperfine coupling tensor \mathbf{A} , line width ΔB_{pp} and the rotational diffusion tensor \mathbf{D}_r . The rotational motion of the spin system gives rise to fluctuating local magnetic fields influencing the resonance frequencies and the line shape of the spectral lines. The characterisation of the rotational diffusion by the rotational correlation time τ (Equation 2.23) allows for a classification of the mobility of the spin probe molecule into four dynamic regimes with different EPR spectroscopic characteristics: isotropic limit, fast motion, slow motion and rigid limit (anisotropic powder spectrum). The dynamic regime determines the mathematical algorithm that should be applied for the spectral simulation. In this thesis, only the slow-motion regime is of interest.

For the simulation of the EPR spectrum of slow tumbling molecules, the stochastic Liouville equation:

$$\frac{\partial}{\partial t} \rho(\mathbf{\Omega}, t) = -i[\hat{\mathbf{H}}_2(t), \rho] = -i[\hat{\mathbf{H}}_2(\mathbf{\Omega}(t)), \rho(\mathbf{\Omega}, t)] - \Gamma_{\Omega}[\rho(\mathbf{\Omega}, t) - \rho_0(\mathbf{\Omega})] \quad (2.26)$$

has to be solved.^{53,54} It describes the time-dependent density matrix ρ with regard to the spin Hamiltonian $\hat{\mathbf{H}}_2(t)$, the rotational diffusion super operator Γ_{Ω} and the density matrix at thermal equilibrium ρ_0 . Rotational motion results in the time-dependence of $\hat{\mathbf{H}}_2(t)$, which is expressed by the time-dependent random variable $\mathbf{\Omega}$. The random angles

are described in terms of the Euler angles: $\Omega \in \{\alpha, \beta, \gamma\}$.

To calculate line positions, intensities and widths of the EPR spectra of a spin system in the slow-motion regime, EasySpin uses Equation 2.26 in the modified form⁵⁵

$$\frac{\partial}{\partial t}\chi(\Omega, t) = -[i\hat{H}_2^*(\Omega(t)) + \Lambda_\Omega]\chi(\Omega, t) = -L(\Omega, t)\chi(\Omega, t) \quad (2.27)$$

with out-of-equilibrium spin density $\chi = \rho - \rho_0$, Hamilton commutation superoperator \hat{H}_2^* and stochastic Liouville superoperator L . The diffusion matrix Γ_Ω is determined by the model describing the rotational motion. These models involve jump diffusion, free diffusion and Brownian rotational motion. The latter is the most common. The intensity $I(\omega_0 - \omega)$ at a point ω relative to the centre of the EPR spectrum ω_0 is described by^{55, 56}

$$I(\omega_0 - \omega) \propto \text{Re}(\mathbf{v}^T \mathbf{u}) \quad \text{with } (L + i(\omega_0 - \omega))\mathbf{u} = \mathbf{v} \quad (2.28)$$

with the superoperator \mathbf{v} that describes the magnetisation in x -direction and auxiliary vector \mathbf{u} . The simulation of EPR spectra using EasySpin algorithms proceeds in three steps. First, orientation-dependent $\hat{H}_2^*(\Omega)$, Γ_Ω and \mathbf{v} are computed with the help of Wigner rotation functions $D_{m,n}^l(\Omega)$. Second, the matrix L is transformed into a tridiagonal form, applying \mathbf{v} as starting vector. Third, every point of the spectrum is calculated.

2.2 Monolayer measurements

2.2.1 Model lipid monolayers

Phospholipids constitute the main component of biological membranes. These lipids are composed of glycerol, esterified with a hydrophilic phosphoric headgroup at the *sn*-3 position and two hydrophobic fatty acid chains at *sn*-1 and *sn*-2 position (Figure 2.4). Phospholipids are classified by the structure of the headgroup (e.g. choline, ethanolamine).

Due to their amphiphilic character, phospholipids, when dispersed in water, build aggregates (e.g. micelles) to minimise the interface between hydrophobic parts and surrounding water molecules. The structure of these aggregates is determined by water content (lyotropic mesomorphism), temperature (thermotropic mesomorphism), pH, salt concentration and the structure of the respective lipid, including the structure and charge of the headgroup, its length and the corresponding saturation of the acyl chains.

Lipids dissolved in a water-insoluble solvent can be spread onto a water surface building a monolayer at the air–water interface. In this monolayer the hydrophilic headgroup points towards the aqueous subphase and the hydrophobic chains point towards the air.⁵⁷

Using film balance methods, the phase behaviour of lipid monolayers can be investigated by reducing the available area A at the air–water interface while the surface pressure π is recorded simultaneously. The surface pressure–area isotherm of saturated lipids like DPPC (1,2-dipalmitoyl-*sn*-glycero-3-phosphocholine) shows a typical phase behaviour during compression of the monolayer (black curve in Figure 2.5). At large areas per molecule, the lipid molecules at the air–water interface show no interaction with each other, resulting in very low surface pressures. In this gas-analogue phase (G), the lipids

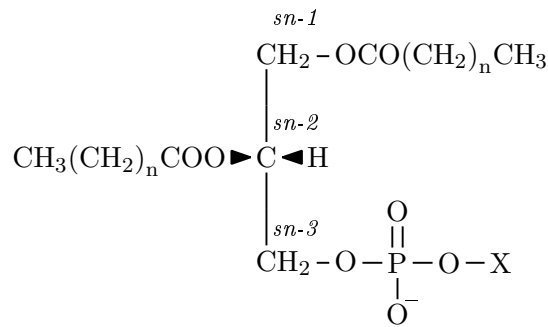


Figure 2.4: Basic structure of phospholipids. The X-group determines structure and properties of the phospholipid headgroup.

behave like a two-dimensional gas, which can be described by the ideal gas law:⁵⁸

$$\pi A = k_B T. \quad (2.29)$$

Reducing the available area per molecule by compression of the film with moveable barriers, the monolayer reaches the liquid-expanded phase (LE), in which attractive van der Waals interactions occur between the molecules. In contrast, the polar headgroups of the lipids are strongly hydrated resulting in repulsive forces. In this isotherm region, the acyl chains still have a high content of *gauche* conformation as in the gas-analogue state. Further compression increases the interaction of the molecules. A plateau in the $\pi(A)$ isotherm indicates the transition from the LE to the liquid-condensed phase (LC). In this phase the lipid chains are arranged in *all-trans* conformation and tilted against the surface. The lipids are in a higher ordered state with a lower compressibility. The ideal gas law is no longer sufficient to describe the lipids in the LE and LC phase. In this case, the van der Waals interactions have to be taken into account:⁵⁸

$$\left(\pi + \frac{a}{A^2} \right) \cdot (A - A_0) = k_B T \quad (2.30)$$

where a and A_0 include the attractive interaction of the lipid molecules and the minimum required area of these molecules. In the subsequent solid-condensed phase (S), the molecules are closer packed. Further compression leads to the collapse of the film.

The physiologically relevant lipids used in this study are mixtures of different structures of the respective lipids containing saturated, as well as unsaturated fatty acids. These lipids do not show the typical phase behaviour in the surface pressure–area isotherm as described above. Due to double bonds that lead to a higher disorder in the hydrophobic part of the lipid, the film shows no transition from LE to LC state (at 20 °C). Instead, the collapse occurs directly after the LE phase (blue curve in Figure 2.5).

In addition to phospholipids, cholesterol is a major component of eukaryotic membranes. Cholesterol is only slightly amphiphilic due to its hydrophilic hydroxyl group bound terminally at the hydrophobic part of the molecule. Since cholesterol has no acyl chains it does not adopt an LE phase. The $\pi(A)$ isotherm shows a direct transition from gas-analogue to LC phase (green curve in Figure 2.5).

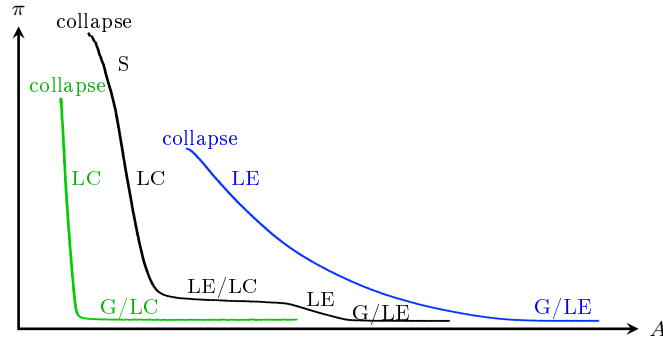


Figure 2.5: Schematic depiction of a $\pi(A)$ isotherm of cholesterol (green curve), brain phosphatidylcholine (blue curve) and 1,2-dipalmitoyl-*sn*-glycero-3-phosphocholine (black curve) with different monolayer phases: gas-analogue region (G), liquid-expanded state (LE), liquid-condensed state (LC), LE/LC phase transition, solid-condensed state (S).

2.2.2 Film balance methods

The surface pressure π of a lipid monolayer at the air–water interface is measured as the difference between the surface tension of pure water γ_0 and the surface tension of the monolayer γ_m .⁵⁸

$$\pi = \gamma_0 - \gamma_m. \quad (2.31)$$

Applying the Wilhelmy plate method,^{59,60} a thin plate of high surface roughness (e.g. filter paper) is immersed into the subphase. The exerted force on this plate is measured, which results from the surface tension of the subphase. The total force F results from downward directed forces that emerge due to gravity and surface tension, as well as upward directed buoyancy as a result of the displaced water by the plate, resulting in:

$$F = m_p g + 2\gamma_m(w_p + t_p) \cos \theta - \rho_w g w_p t_p h \quad (2.32)$$

with mass m_p , gravitational acceleration g , width w_p and thickness t_p of the plate, contact angle θ of the liquid on the plate, density of water ρ_w and penetration depth of the filter paper h . The gravitational part $m_p g$ in Equation 2.32 is constant and can be determined during the calibration of the Wilhelmy system. Due to the high roughness of the plate, the filter can be assumed to be completely wet and the contact angle is then $\theta = 0^\circ$. The buoyancy part can be neglected since the width of the plate is much higher than the thickness ($w_p \gg t_p$). These simplifications in combination with equation 2.31 allow for the determination of the surface pressure. This is facilitated by measuring the difference between the force of a clean surface and of a lipid monolayer on the filter paper:

$$\pi = \frac{\Delta F}{2w_p}. \quad (2.33)$$

To minimise the influence of the width of the plate, the pressure sensor is calibrated using the surface pressure of ultrapure water (72.8 mN/m)^{61,62} and that of air (0 mN/m) as reference points.

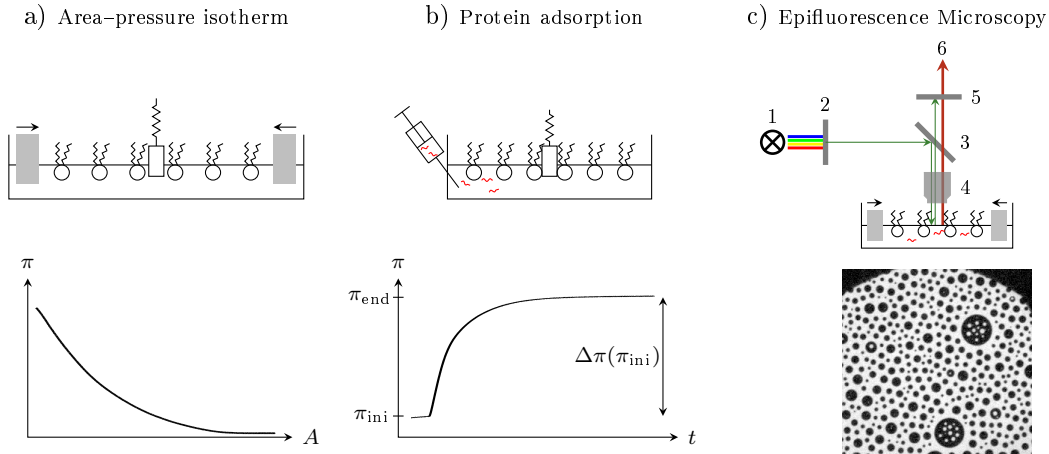


Figure 2.6: Schematic depiction of the monolayer techniques used in this work (top) and corresponding data assessment (bottom). a) Trough with moveable barriers to study the compression behaviour of lipid monolayers. The recorded area-dependent surface pressure (diagram below) is measured with the Wilhelmy plate method. b) Protein (\sim) injected below a monolayer at the initial surface pressure π_{ini} in a trough of constant area. The recorded time-dependent surface pressure (diagram below) is also measured with the Wilhelmy plate method. The difference in surface pressure $\Delta\pi = \pi_{\text{end}} - \pi_{\text{ini}}$ is determined for different π_{ini} . c) Epifluorescence microscope setup with 1) light source, 2) excitation filter, 3) dichroic mirror, 4) microscope with aperture, objective, and lenses, 5) emission filter and 6) camera. Upon addition of a fluorescent dye to the lipid mixture, dark and bright domains become visible, depending on the phase behaviour of the lipids in the monolayer (image below).

In the present work, the surface pressure is measured in dependence of molecular area A , of time t and in combination with epifluorescence microscopy.

In the case of the area-dependent measurement, the surface pressure is recorded during constant reduction of the available area per lipid molecule with two symmetric moving barriers for analysing the compression behaviour of the monolayer⁶³ (Figure 2.6 a). The velocity of the barriers has to be slow enough to ensure thermodynamic equilibrium conditions ($v = 2 \text{ \AA}^2/(\text{molecule}\cdot\text{min})$).

Time-dependent surface pressure measurements with a constant available area is a suitable tool to follow the adsorption process of e.g. proteins at the lipid monolayer film (Figure 2.6 b). With different amounts of lipids spread onto the subphase surface, the initial surface π_{ini} is adjusted. If the protein injected below adsorbs to the monolayer, a change in surface pressure $\Delta\pi$ can be detected since the area of the surface is kept constant. The adsorption leads to a gain in Gibbs free energy resulting from enthalpic (hydrogen bonding, van der Waals and Coulomb forces) and entropic contributions (rearrangement of the protein, release of water molecules and counter ions). If $\Delta\pi$, the difference of the surface pressure at the end of the adsorption experiment π_{end} and the initial surface pressure π_{ini} , is a linear function of π_{ini} , it reveals the maximum insertion pressure (MIP) of the protein adsorbed to the lipid monolayer, which is defined as the

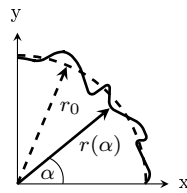


Figure 2.7: Schematic depiction of the first quadrant of a lipid domain with an averaged radius r_0 . Considering fluctuations of the domain contour, the radius $r(\alpha)$ is angle dependent.

initial surface pressure, above which no adsorption of the protein to the monolayer occurs:

$$\begin{aligned}\Delta\pi &= \pi_{\text{end}} - \pi_{\text{ini}} = a + b \cdot \pi_{\text{ini}} \\ \text{MIP} &= \pi_{\text{ini}}(\Delta\pi = 0 \text{ mN/m}) = -a/b.\end{aligned}\tag{2.34}$$

Parameters a and b can be received from linear regression.

The combination of film balance methods with epifluorescence microscopy allows for a visual detection of the phase behaviour of lipid monolayers (Figure 2.6 c). A fluorescent amphiphilic molecule is added to the lipid composition in a low concentration to prevent an influence on the microstructure of the monolayer. Different solubilities of the lipid dye in i.e. LE and LC phases allow for the microscopic observation of coexisting domains. The shape of the domains (circular, starlike, propeller, bean, fractal...) is determined by e.g. the chemical composition of the lipid layer and the surface pressure. The excitation wavelength matching the fluorophore in the sample is selected by an excitation filter after the polychromatic light is generated by a mercury vapour lamp. The light of the specific wavelength is directed onto the sample. Light absorption excites the electrons of the aromatic system of the fluorescent lipid from the energetic ground state S_0 into different vibrational states ν' of the excited state S_1 or higher excited states S_i . The excited electrons decay into the lowest vibrational state ($\nu' = 0$) of S_1 (internal conversion) releasing thermal energy. The relaxation into the ground state leads to emission of light of a higher wavelength than initially applied. The emitted light passes a dichroic mirror, which separates the excitation light and the emitted fluorescence light. The coexisting phases and domains of the lipid monolayer become observable by just combining the fluorescence system with a microscope.

2.2.3 Line tension

The fluorescent dye used in this work (1,2-dihexadecanoyl-*sn*-glycero-3-phosphoethanolamine-N-(lissamine rhodamine B sulfonyl), Rh-DHPE, for chemical structure, see Figure 5.3) is preferentially located in LE or fluid phases of the lipid monolayer. Hence, these phases appear as bright domains and LC phases as dark domains in epifluorescence microscopy images of phase separated lipid monolayers. The domains observed in this thesis are of a circular shape. After a deformation due to an external disturbance, the circular shape is reconstituted rapidly. The driving force results from the line tension γ at the domain boundary.⁶⁴ This energy per unit length is a measure for the energy difference of lipids located in the interface between LE and LC phase domains and lipids

inside the phases. The free energy of the domain boundary arising from line tension:

$$E_{\text{line}} = \gamma \int dC \quad (2.35)$$

depends on the contour C of the respective domain interface, where

$$C = \int_0^{2\pi} r d\alpha + \frac{1}{2r} \int_0^{2\pi} \left(\frac{\partial r}{\partial \alpha} \right)^2 d\alpha. \quad (2.36)$$

Equation 2.36 considers small fluctuations and thus radii $r(\alpha)$ that deviate from the average radius r_0 of a circular shaped domain (Figure 2.7).⁶⁵ If spherical domains are assumed, the contour simplifies to $C = 2\pi r_0$.

2.2.4 Monolayer electrostatics

Electrostatic interactions between negatively charged lipids in the monolayer and positively charged adsorbing molecules like proteins often play an important role for the overall protein–lipid interaction. The Coulomb interaction between protein and lipid is screened if their interaction is investigated in a buffer solution. Following the Debye–Hückel theory,⁶⁶ the electrostatic potential of a charged molecule in an electrolyte solution is decreasing exponentially with distance x from the charge surface of the potential φ_0 :

$$\varphi(x) = \varphi_0 \exp(-\kappa x) \quad \text{with } \kappa = \sqrt{\frac{2c_b z^2 e^2}{\varepsilon_r \varepsilon_0 k_B T}} \quad (2.37)$$

with Debye length κ^{-1} , bulk ion concentration c_b and charge number z of the ion in bulk solution and the dielectric constant of water ε_r and of vacuum ε_0 .

The monolayer at the air–water interface is characterised as a charged surface. The theory of Gouy and Chapman^{67,68} describes the electrostatic surface potential of a lipid layer assuming that the thermal motion of counterions in the electrolyte results in a diffuse layer of ions.^{69–73} The Poisson equation

$$\rho(x) = -\varepsilon_r \varepsilon_0 \frac{d^2 \varphi}{dx^2} \quad (2.38)$$

with charge density $\rho(x)$ and electrostatic surface potential φ can be used to describe the electrostatic attraction between the charged surface and the respective counterions. The charge density at point x in the aqueous subphase can be calculated by summarising the charge densities of all ion species in the aqueous solution:

$$\rho(x) = \sum_i N_A z_i e c_i(x) \quad (2.39)$$

with charge z_i and concentration c_i of the respective ions. The statistical distribution of the ions in the solution follows a Boltzmann law:

$$c_i(x) = c_{b,i} \exp\left(-\frac{z_i e \varphi}{k_B T}\right). \quad (2.40)$$

Combining equations 2.38–2.40 reveals the Poisson–Boltzmann equation:

$$\frac{d^2\varphi}{dx^2} = -\frac{N_A e}{\varepsilon_r \varepsilon_0} \sum_i z_i c_{b,i} \exp\left(-\frac{z_i e \varphi}{k_B T}\right). \quad (2.41)$$

Taking $N_A \cdot k = R$ and the boundary conditions i) $\varphi(x \rightarrow \infty) = 0$ and ii) $d\varphi(x=0)/dx = \varphi_0$ into account, integration of equation 2.41 results in

$$\frac{1}{2} \left(\frac{d\varphi}{dx}\right)^2 = \frac{RT}{\varepsilon_r \varepsilon_0} \sum_i c_{b,i} \left[\exp\left(-\frac{z_i e \varphi}{k_B T}\right) - 1 \right]. \quad (2.42)$$

Assuming that the model system contains only symmetrical electrolytes leads to the expression

$$\frac{d\varphi}{dx} = \sqrt{\frac{8RTc_b}{\varepsilon_r \varepsilon_0}} \sinh\left(\frac{ze\varphi}{2k_B T}\right). \quad (2.43)$$

As a consequence, the charge density σ at the surface amounts to

$$\sigma = \varepsilon_r \varepsilon_0 \left(\frac{d\varphi}{dx}\right)_0 = \sqrt{8RT\varepsilon_r \varepsilon_0 c_b} \sinh\left(\frac{ze\varphi_0}{2k_B T}\right). \quad (2.44)$$

This equation allows to draw conclusions about the charge distribution of ions in an electrolyte, which depends on the distance from the charged surface or the monolayer containing charged lipids, respectively (Gouy–Chapman theory).

With the general definition of the surface charge density, σ can directly be obtained from the averaged area per charged molecule A_c :

$$\sigma_{gc} = \frac{z_h e}{A_c} \quad (2.45)$$

with the charge of the lipid headgroup z_h .

Stern combined the theory of a diffuse layer of ions with a hypothetical layer of counterions adsorbed to the headgroups of charged lipids.⁷⁴ This relatively rigid layer was already anticipated by Helmholtz.⁷⁵ The surface charge density of this layer depends on the number of ions bound to the surface n_s and the number of lipid binding sites n_l :

$$\sigma_s = \frac{z e n_s}{n_l A_c}. \quad (2.46)$$

The addition of σ_{gc} and σ_s results in the total surface charge density $\sigma = \sigma_{gc} + \sigma_s$, which can be used in equation 2.44 to obtain the electrostatic surface potential φ_0 and $\varphi(x)$ with equation 2.37.

The consideration of the electrostatic potential of a positively charged protein in the buffer solution has to be performed in a similar manner.

The electrostatic interaction energy E_{elec} that affects the positively charged protein can be described with:

$$E_{elec} = \int \rho_p(r-x)\varphi_{ext}(x)dx \quad (2.47)$$

where the distance between protein and monolayer is r , the charge density of the protein ρ_p and the external electrostatic potential φ_{ext} , which is the superposition of the electrostatic potential of the protein and the potential of the monolayer.

It has been shown that the surface potential and concomitantly the surface charge density depends on the concentration of ions in the bulk solution c_b , temperature and the dielectric constant of the subphase ϵ_r . Amongst others, the Gouy–Chapman theory, as well as Stern theory includes the simplification that ions only interact electrostatically in the diffuse layer. Furthermore, the dielectric constant has to be assumed as constant. In fact, the latter depends on the degree of hydration and the orientation of bound water molecules.^{71,76} Thus, in the interfacial region of lipid layer and bulk subphase, ϵ_r amounts to values between the value for water ($\epsilon_{r,\text{water}}(20\text{ }^\circ\text{C}) = 80.20$)⁷⁷ and the lipid acyl chains ($\epsilon_{r,\text{lipid}} \approx 2$).⁷⁸

CHAPTER 3

Thermoresponsive peptide polymers

3.1 Introduction

Peptide polymers showing a temperature-dependent conformational or solvation transition in aqueous solution are of particular interest e.g. for use in regenerative medicine^{28,29} and protein purification.^{79,80} Moreover, these polymers can host small molecules to serve as drug delivery systems,^{26,27} due to their temperature-triggered encapsulation or release properties.⁸¹ Thermoresponsive polymers that show a lower critical solution temperature (LCST) behaviour exhibit a phase transition when the solution is heated above the LCST. This inverse phase transition of LCST polymers is a complex process, which is neither completely understood for synthetic polymers (like PNiPAAm,⁸² PPns⁸³) nor for biological peptide polymers, which have been studied intensely in the last decades.^{15,84,85} Biological examples include polymers with amino acid sequences similar to those of elastin, collagen fibres or resilin.²⁴ They all have in common that they are rich in proline (P) and glycine (G)^{86,87} containing regions, which have structure-breaking abilities.²⁵ These polypeptides can be summarised as having a P-X_n-G motif ($n \in \mathbb{N}, 0 \leq n \leq 4$).²⁴ Amino acid-derived polymers gain an advantage over synthetic LCST polymers through their precisely controllable sequence and chain length by use of recombinant DNA- and protein-engineering techniques.^{88,89} Molecular parameters like the amino acid sequence of the peptide monomer or the number of repeats of the monomer control the LCST behaviour of peptide polymers.⁹⁰

The phase transition behaviour of thermoresponsive polymers at the transition temperature is entropically-driven as a disruption of the water network hydrating the polymer chains leading to molecular conformational changes and a phase separation into polymer-rich and water-rich phases.⁹¹⁻⁹³ This phase transition is accompanied by a decreasing radius of gyration of the α -carbons and a state in which intra- and intermolecular hydrogen bonding between the polymer chains (e.g. secondary structures like β -turns) are favoured over solvation, i.e. over hydrogen bonding to water molecules hydrating the polymer chains.⁹³⁻⁹⁶

The hydration of a polymer chain can furthermore be differentiated between the hydration layer of the backbone and the hydration layer of the side chains of the amino acid chain. It was shown by Kurzbach et al.⁹² for elastin-like polypeptides (ELP) that both hydration layers can exist in a coupled or in a decoupled state. Depending on the primary sequence of the peptide polymer the backbone and side chains can be dehydrated in a cooperative way at the transition temperature or independently from each other. In the

latter case two different transition temperatures were observed.

Continuous wave (CW) electron paramagnetic resonance (EPR) spectroscopy on reporter molecules (spin probes) as a non-invasive, intrinsically local technique can help to understand the temperature-dependent phase transition. The sensitive time scale of EPR ranges from 10 ps to 1 μ s.⁹⁷ This makes EPR a powerful tool to investigate the inverse phase transition since the exchange processes of amphiphilic spin probes between polar and apolar regions of the LCST polymers coincide with the time scale of EPR.⁹² The spin probes are incorporated by non-covalent interactions and molecular self-assembly. They act as reporter molecules and provide local information about their different nanoscopically sized environments (e.g. polarity, local concentration in spin probes) and concomitantly of the water-rich and the aggregated hydrophobic regions of the polymer and the exchange dynamics between them. The CW EPR spectrum of a nitroxide radical in the fast and in the slow tumbling regime shows three peaks. The hydrophobic collapse at the transition temperature is indicated by a change in the hyperfine coupling a , which is reflected in a splitting of the high-field line. The change in a stems from spin probes that reside in the dehydrated, polymer-rich regions, which sense less polar environments.

During the temperature-induced aggregation of thermoresponsive polymers, nanoscale inhomogeneities occur,⁹⁷ which can be detected using CW EPR spectroscopy. Kurzbach described them as nanoscopic clusters of collapsed polymer segments, which represent an apolar, hydrophobic environment compared to a fully solvated polymer.⁹⁷ Nanoscale inhomogeneities cannot be separated from the inverse phase transition of thermoresponsive polymers, since a few local dynamic inhomogeneities on a nanometre scale already lead to a transition that is macroscopically observable by turbidity measurements.⁹⁸ Depending on the observed spectral developments of the reporter molecules, the prevalent processes and aggregated regions reflect nanoscopic behaviour that was characterised as either of three types of nanoscale inhomogeneities:⁹⁷

1. *static inhomogeneities*: The spin probe is incorporated inside the inhomogeneity and a dynamic exchange is impossible at any temperature. This type is characterised in the EPR spectra by a splitting of the high-field line of the nitroxide radical (spin probe), which is partitioned between two environments of different hydrophilicity. The line splitting remains constant during a change in temperature. Only the relative weight of the two spectral components changes.
2. *dynamic inhomogeneities (I)*: In this case, a spin-probe exchange between polymer-rich and water-rich nanophases is featured at intermediate temperatures slightly above the initial formation of hydrophobic aggregates. The high-field peak of the EPR spectra is split characteristically and the two peaks diverge continually with temperature, due to a decreasing guest-exchange with increasing temperature.
3. *dynamic inhomogeneities (II)*: The spin-probe exchange is featured at high temperatures. The EPR spectra show two lines merging with increasing temperature, due to an increasing spin-probe exchange with increasing temperatures.

Depending on the timescales, the different types of inhomogeneities lead to a multimodal or an averaged total EPR spectrum of the probe in the polymer-rich and in the water-rich phase. For many systems it was found that the amphiphilic nitroxide spin probes TEMPO (2,2,6,6-Tetramethylpiperidine 1-oxyl)^{82,83,99} and 16-DSA (16-DOXYL stearic acid)^{92,100} with rather large partition coefficients between hydrophobic and aqueous

phases (TEMPO: $\log P_{\text{octanol/water}} = 1.77$, 16-DSA: $\log P_{\text{octanol/water}} = 4.49$)¹⁰¹ was best suited for the measurement of the temperature-dependent behaviour of responsive polymers.

In this chapter the temperature-dependent behaviour of two types of peptide polymers is investigated with CW EPR spectroscopy with regard to the aggregation and hydration behaviour of the polymer chains.

3.2 Hydration and nanophase separation of elastin-like polypeptide diblock copolymers

This section is already published in:

Widder et al. Characterisation of hydration and nanophase separation during the temperature response in hydrophobic/hydrophilic elastin-like polypeptide (ELP) diblock copolymers. *Soft Matter*, 13:1816–1822, 2017.

3.2.1 Diblock ELP

Elastin-like polypeptides (ELP) are high-precision peptide polymers based on the hydrophobic domain of tropoelastin.¹⁰² They are composed of the amino acid sequence $(\text{VPGXG})_n$ ($\forall X \setminus \text{P}$)⁹⁴ and correspond to the P- X_n -G amino acid motif for $n = 0$. The temperature-triggered self-assembly of a multitude of ELP-derived polymers has already been studied by various methods like light and neutron scattering techniques,¹⁰³ molecular dynamics simulation,⁹³ NMR^{104,105} and EPR spectroscopy.⁹²

A study by Garanger and co-workers¹⁰³ investigated diblock ELPs composed of a hydrophobic block and a hydrophilic block with different hydrophobic block size by light and neutron scattering techniques (absorbance spectroscopy, DLS, SLS and SANS). Their study yielded that once above the first transition temperature the hydrophobic block has been desolvated independently from the hydrophilic block, the ELP block copolymers form aggregates with a core of hydrophobic blocks and a corona of hydrophilic blocks. The aggregates are first strongly hydrated and then continue to evolve thermally. A further increase in temperature leads to a temperature-driven desolvation and compaction of the core. As a consequence the aggregates expel water. At a second transition temperature macroscopic aggregates are built through aggregation of the globular aggregates through their hydrophilic coronas.

Since these diblock ELPs are possibly applicable as a drug delivery system, it is important to investigate what small molecules sense in their environment and how they are expelled or taken up during the phase transition. Hence, spin probing EPR is used here to investigate the temperature-triggered self-assembly of the diblock ELPs of Garanger and co-workers on the molecular scale at a constant molar concentration. Diblock ELPs with different lengths x_1 of the hydrophobic block $(\text{VPGVG})_{x_1}$ and x_2 of the hydrophilic block $(\text{VPGXG})_{x_2}$ ($X = \text{A, G}$ (1:1)) were examined and compared with regard to the influence of the length of the hydrophobic block on the one hand and of the length of the hydrophilic block on the other hand. Moreover, the effect of the guest residue in the hydrophilic block without significantly changing its hydrophilicity is considered. For complete amino acid sequences of the investigated diblock ELPs and experimental details see Section 5.1. In the following, it will be referred to the diblock ELPs as ‘ELP x_1 - x_2 ’.

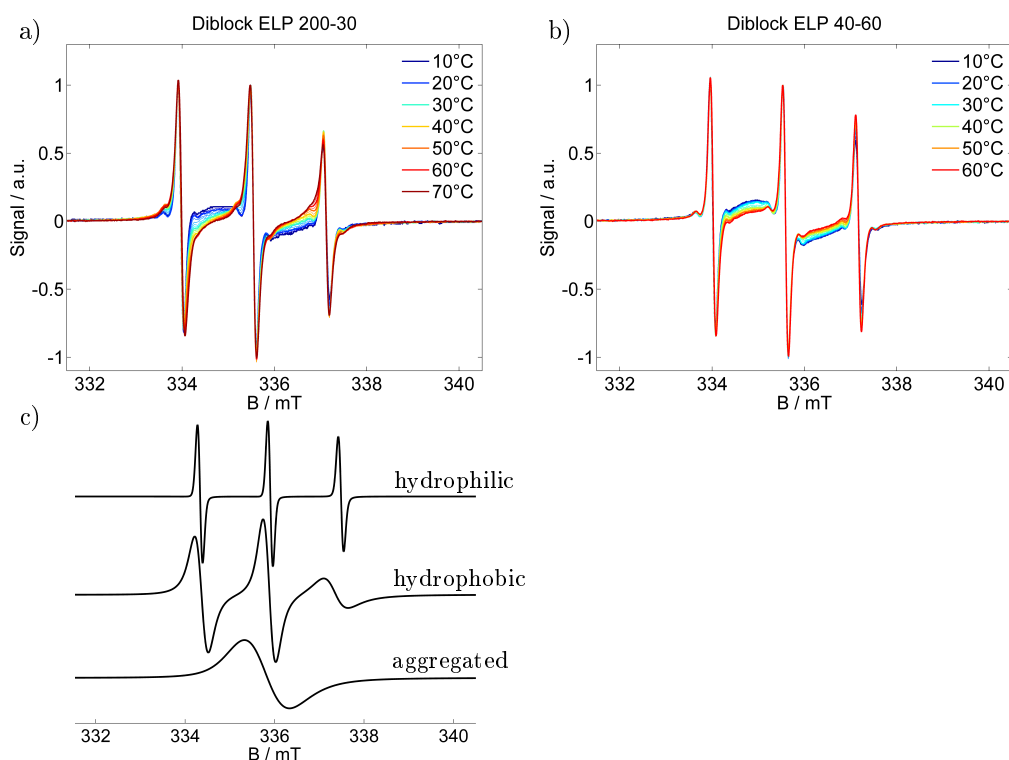


Figure 3.1: CW EPR spectra of 16-DSA in polymer buffer solution. a) Experimental spectra of diblock ELP 200–30, b) experimental spectra of diblock ELP 40–60 and c) simulated spectral components of the multimodal EPR spectra.

3.2.2 Results and discussion

3.2.2.1 EPR spectroscopic changes during the loss of hydration

Temperature-dependent changes of the investigated polymers were detected with CW EPR spectroscopy using the spin probe 16-DSA (16-DOXYL stearic acid; for chemical structure, see Figure 5.1 b). The CW EPR spectra detected during heating of the polymer solutions with 16-DSA are shown in Figures 3.1 a, b and A.1. EPR spectra during cooling are not considered since no differences between heating and cooling spectra have been observed (Figure A.2).

At small T , the EPR spectra show no interaction between probe and polymer (exemplary shown for ELP 200–30 in Figure A.3, 10 and 20 °C). The probe senses merely a slightly higher viscosity. The interaction starts with the aggregation of the polymer. At temperatures above the transition temperature the spectra exhibit temperature-dependent changes that differ from the reference measurement of 16-DSA in pure buffer (exemplary shown for ELP 200–30 in Figure A.3, $T \geq 30$ °C). The spectra are composed of different components of the spin probe. Three components were taken into account for the simulation of the spectra (Figure 3.1 c):

A) hydrophilic component: 16-DSA molecules freely rotating in buffer and showing

no interaction with the polymer. The rotational correlation time τ is in the order of magnitude of 10^{-10} s. The probe senses a polar environment leading to a high hyperfine splitting constant a .

- B) hydrophobic component: 16-DSA molecules located in hydrophobic and apolar regions of the polymer. The probe rotates slower and senses a smaller polarity leading to higher τ ($\approx 10^{-9}$ s) and smaller a .
- C) aggregated component: 16-DSA molecules forming aggregates (e.g. micelles) in buffer. This leads to highly frequent spin probe collisions, which results in high Heisenberg spin exchange frequencies, which as its hallmark shows a collapse of the three peaks into one broad peak with lower amplitude. This component vanishes partly during the increase of temperature and since the fraction of component C is not reproducible, the fractions of the 16-DSA aggregates were subtracted out of the fraction of the depicted hydrophobic component for the sake of comparability.

For simulated spectra, see Figures A.4–A.9.

At temperatures below the transition temperature the spectra are a superposition of the three-peak spectrum of the freely rotating nitroxide molecules and the broad one-peak spectrum of 16-DSA aggregates. In this temperature region the spectra of 16-DSA in polymeric solution are similar to the reference spectra of 16-DSA in pure buffer: no interaction of the spin probe with the polymer is detectable. With reaching the transition temperature of the respective polymer the hydrophobic component appears in the EPR spectra, indicating the formation of polymer-rich nanophases that 16-DSA as an amphiphilic molecule partitions into a large degree. Due to a smaller hyperfine splitting constant and the shift of the hydrophobic component spectrum towards smaller magnetic (B -)fields, the appearance of the hydrophobic component becomes visible next to the high-field peak at smaller B -field values than the third peak of the hydrophilic component. The relative weight of these two spectral contributions changes with increasing temperature. In the case of smaller hydrophilic mass fractions (e.g. ELP 200–30, Figure 3.1 a) the appearance of the hydrophobic component in the spectra is more distinct than for higher hydrophilic mass fractions (e.g. ELP 40–60, Figure 3.1 b).

3.2.2.2 Microscopic phase transition

Since the above described LCST is the minimum of a phase diagram that also takes the concentration of the polymer in the solution into account, the temperature of the here reported phase transition process at constant concentration is denoted as ‘transition temperature’.

The transition temperature $T_{t/EPR}$ of the diblock ELPs is marked by the onset of appearance of the hydrophobic component in the EPR spectra. Since spin probing EPR reports on the first occurrence of polymer-rich, apolar cavities in the polymeric system, the here stated transition temperatures (Table 3.1) have to be discerned from absorbance spectroscopic data. The latter may identify the transition only when much larger aggregates are present to scatter the transmitted light. Figure 3.2 shows the transition temperatures of all measured diblock ELPs as a function of the hydrophilic mass fraction f . The transition temperatures derived from EPR measurements as well as the data of absorbance spectroscopy (Garanger et al.¹⁰³ and Table A.1) show an exponential dependence from the hydrophilic mass fraction. Taking the exponential regression (see Equations A.1 and

Table 3.1: Transition temperatures for all diblock ELP investigated with CW EPR spectroscopy. The transition temperature is indicated by the appearance of the hydrophobic spectral components of 16-DSA.

x_1	x_2	$f_{\text{hydrophilic}}$	T_t/EPR in $^{\circ}\text{C}$
200	30	0.12	22 ± 1
200	S30	0.13	22 ± 1
200	60	0.21	24 ± 1
120	60	0.31	26 ± 1
80	60	0.4	28 ± 1
40	60	0.56	38 ± 1

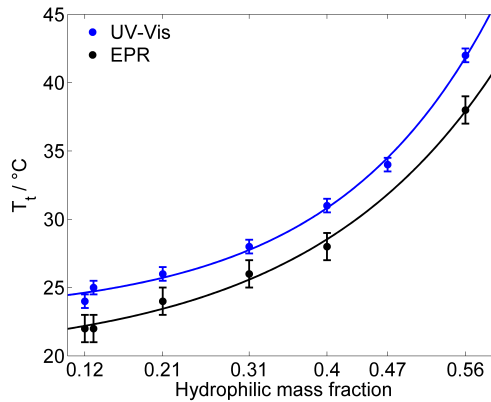


Figure 3.2: Transition temperatures as a function of the hydrophilic mass fraction of all diblock ELPs as measured by EPR and UV-Vis spectroscopy¹⁰³ (see also Table A.1).

A.2) into account, a transition temperature can be determined for $f = 0$ corresponding to the ELP motif (VPGVG). Table 3.2 compares the theoretical values for the transition temperature of (VPGVG) determined by EPR, absorbance spectroscopy and turbidity.¹⁰⁶ Urry et al. assumed a linear dependence for $T_t = f(f)$, but considered only hydrophilic mass fractions of $f < 0.5$. The results of EPR show slightly lower T -values than those of Garanger¹⁰³ and Urry.¹⁰⁶ This could have two reasons: with 16-DSA smaller inhomogeneities can be detected at lower temperatures than with absorbance spectroscopy and turbidity and/or higher concentrations of the polymer lead to smaller transition temperatures. But the former appears less likely because 16-DSA is too big to enter small hydrophobic cavities. The smaller but more hydrophilic spin probe TEMPO (2,2,6,6-Tetramethylpiperidine-1-oxyl) was also tested but did not show any interaction with the diblock ELPs (Figure A.10). Hence, the slightly lower transition temperature is most likely due to the employed higher polymer concentration.

The other extremum, $f = 1$, leading to the motif (VPGAG–VPGGG) would lead to far too high transition temperatures compared to Urry, who stated $T_t = 45^{\circ}\text{C}$ for (VPGAG) and $T_t = 55^{\circ}\text{C}$ for (VPGGG). In conclusion the exponential model is an empirical model to estimate the transition temperature for a given hydrophilic mass fraction f , but it collapses at high hydrophilic mass fractions.

Table 3.2: Extrapolated transition temperatures for diblock ELP with minimal hydrophilic mass fraction.

	T_t/EPR in $^{\circ}\text{C}$ $c = 300 \mu\text{M}$	T_t/CMT in $^{\circ}\text{C}$ $c = 25 \mu\text{M}$	T_t/Urry in $^{\circ}\text{C}$ $c = ?$
$f = 0$ (VPGVG) $_{x_1}$	21.15	23.26	24 ¹⁰⁶

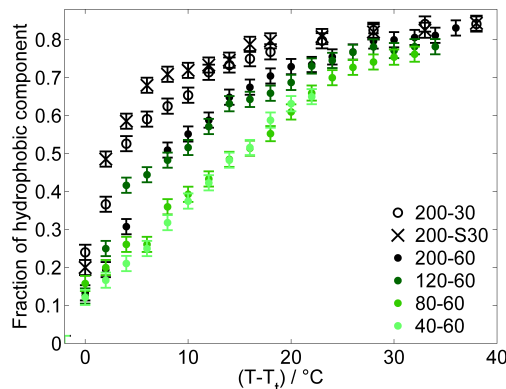


Figure 3.3: Fraction of simulated hydrophobic component of the EPR spectra of the investigated diblock ELPs.

Since the appearance of the hydrophobic component in the EPR spectra of the diblock ELPs marks the temperature of the inverse phase transition on the nanoscale, the fraction of this component mirrors the progression of the transition process. At temperatures near T_t the fraction of 16-DSA molecules located in the polymeric aggregates increases rapidly (Figure 3.3) indicating a sharp transition of the diblock ELPs. The smaller the hydrophilic mass fraction, the faster the increase of the hydrophobic fraction after their appearance. At higher temperatures, the slope of the fraction becomes smaller for all diblock ELPs showing an asymptotic behaviour.

A higher hydrophilicity of a polymer leads to a higher hydration of the polymer chains and less hydrophobic aggregated regions. As a consequence, less 16-DSA molecules are located near to hydrophobic regions. This leads to smaller fractions of hydrophobic component in the spectra and a smaller slope of the fraction increase, since more water molecules around the not-aggregated hydrophilic parts of the polymer make it less likely that the spin probe molecules favouring more non-polar regions actually enter the aggregated regions.

3.2.2.3 Type of inhomogeneities

With spin probing EPR spectroscopy, only one transition could be detected. Garanger et al.¹⁰³ described two transitions for the diblock ELPs x_1 -60. If the loss of water and the densification of the polymer aggregates that they reported between the transitions, could have been detected by EPR, the occurrence of static inhomogeneities would have

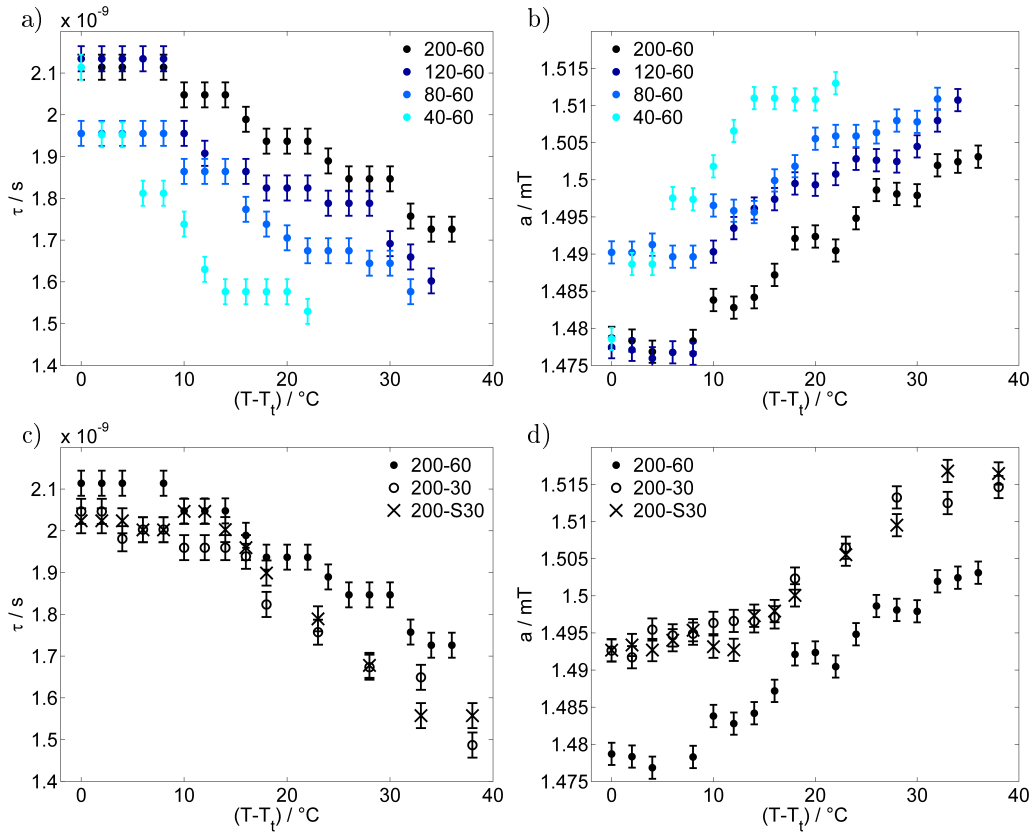


Figure 3.4: Results of simulation of the CW EPR spectra of 16-DSA in a polymer–buffer solution: rotational correlation times (a) and c)) and hyperfine splitting constant (b) and d)) of the hydrophobic component for different hydrophobic block lengths (a) and b)) and different hydrophilic blocks (c) and d)). Hyperfine splitting constants give half of the difference in B field of the high-field and of the low-field peak of the simulated EPR spectra of the respective component.

been seen (see Section 3.1, case 1). In this case, the 16-DSA molecules would stay inside the hydrophobic regions of the polymer sensing the loss of water but not exchanging with the surrounding water-rich phase. The loss of water of the aggregates would be characterised by an increase of the rotational correlation times with increasing temperatures as a consequence of the restricted mobility of the spin probe in the densified aggregate and by a decrease of the polarity at higher temperatures in the spin probes environment.

The simulation results do not support these considerations. As can be seen in Figure 3.4, the rotational correlation times decrease and the hyperfine splitting constant increases during the temperature rise. The increase of mobility of the spin probe molecules and the increase of polarity in their environment characterises the polymer aggregates as dynamic inhomogeneities. The gained mobility due to the temperature rise allows the 16-DSA molecules to diffuse between hydrophobic and hydrophilic regions. The detected values of τ and a are the average over both regions. Due to different a values of the hydrophobic and the hydrophilic component, the high-field peak of the EPR spectra is separated at temperatures just above T_t . Way above the transition temperature of the

polymer further increase of temperature leads to an increasing spin-probe exchange. This becomes visible over the merge of the separated high-field peak of the spectra.

After the hydrophobic component arises in the EPR spectra, a stays constant for a specific temperature interval. The increase of temperature leads to an increase of a only after temperature reached $T_t + 8^\circ\text{C}$ in the case of ELP 200- x_2 , 120-60 and 80-60. ELP 40-60 showed an increase of polarity already at $T_t + 4^\circ\text{C}$. At and above these temperatures, the interface between polymeric aggregate of hydrophobic blocks and the corona of hydrophilic blocks becomes permeable by the spin probes. This and the higher mobility allows the spin probe molecules to diffuse between these two regions. According to Kurzbach et al.⁹⁷ the polymer aggregates and the collapse mechanism represent dynamic inhomogeneities of type II.

3.2.2.4 Influence of the hydrophobic block

Diblock ELPs with different lengths of the hydrophobic block (VPGVG) $_{x_1}$ were investigated by spin probing EPR. Their block length x_1 amounted to 40, 80, 120 and 200, while the hydrophilic block stays constant with the guest residues X = A, G (1:1) and a constant length $x_2 = 60$. Higher x_1 cause smaller transition temperatures due to smaller hydrophilic mass fractions f (Table 3.1). Simulation of the CW EPR spectra yielded information about the environment of the different spin probe components. Since the hydrophilic component represents the 16-DSA molecules freely tumbling in water, only the results of the spin probe molecules located in the hydrophobic polymer aggregates are plotted in Figure 3.4. For simulation results of the hydrophilic component, see Figure A.12.

As can be seen in Figure 3.4 a, diblock ELPs with higher x_1 show higher rotational correlation times τ inside the polymer aggregates. This means that the here located 16-DSA molecules have a smaller mobility and rotate slower than the spin probes in polymer aggregates of ELPs with smaller x_1 . A dependence of the hydrophobic block length is also visible in the progression of the hyperfine splitting constant with increasing temperature (Figure 3.4 b). Smaller x_1 cause higher hyperfine splitting constants. Higher values of a indicate a higher polarity in the environment of the spin probe, often speaking for a higher amount of water. The temperature-dependent progression of both—the rotational correlation time and the hyperfine splitting constant—can be interpreted such that the 16-DSA molecules sense more water inside polymeric aggregates of more hydrophilic polymers. As already stated, the more hydrophilic an ELP is, the more water molecules surround this polymer due to its higher hydration. Hence, a spin probe inside hydrophobic regions of ELP with higher hydrophilicity show higher values of a and smaller values of τ .

Another scenario, which could explain the higher hydrophobicity sensed by the spin probe refers to the contact area of hydrophobic and hydrophilic polymer regions. Changing the length of the hydrophobic block by keeping the molar concentration the same results in different hydrophobic volume fractions per measured diblock ELP. Consequently, the interface between hydrophobic and hydrophilic domains is diminished with higher x_1 . To examine this possible explanation for smaller hyperfine splitting constants in the case of higher x_1 , spectra of different concentrations of polymer and spin probe were recorded and simulated (Figures A.13–A.21). Since the concentration of polymer as well as of spin probe has no significant effect on the rotational correlation time and the hyperfine splitting constant, it can be ruled out that the higher hydrophobicity sensed by the probe

is a result of a diminished contact area between hydrophobic and hydrophilic regions for higher x_1 .

3.2.2.5 Influence of the hydrophilic block

The hydrophilic block of the diblock ELPs was varied with regard to block length x_2 and guest residue in the hydrophilic motif of (VPGXG). x_2 was chosen as either 60 and 30 with the guest residue X = A, G (1:1), in each case with the hydrophobic block (VPGVG)₂₀₀. Another diblock ELP was composed of (VPGVG)₂₀₀ and (VPGSG)₃₀.

As can be expected, the effect of the number of repeat units of the hydrophilic block x_2 on the transition temperature is reverse to the effect of the number of repeat units of the hydrophobic block x_1 . The diblock ELP with $x_2 = 60$ shows a higher transition temperature than the diblock ELPs with $x_2 = 30$ (Table 3.1). This is consistent with the influence of x_1 on the transition temperature, since a higher x_2 causes a larger hydrophilic mass fraction.

The comparison of the diblock ELPs with different guest residues in the hydrophilic block shows no significant differences. The fraction (Figure 3.3), rotational correlation time and hyperfine splitting constant (Figure 3.4 c and d) of the hydrophobic component of the EPR spectra of ELP 200–30 and 200–S30 show similar results for both polymers. Considering only the hydrophobicity of the different pentapeptides, the similarity in behaviour is not surprising. According to the hydrophobicity scale of Urry et al.¹⁰⁶ the transition temperature of (VPGAG) amounts to 45 °C, (VPGGG) to 55 °C and (VPGSG) to 50 °C. Since the transition temperatures are a measure for hydrophobicity and hydrophilicity, respectively, the hydrophilicity of the diblock ELPs 200–30 and 200–S30 is identical within experimental error.

ELPs 200–30 and 200–S30 have similar hydrophilic mass fractions (Table 3.1). Due to their $x_2 = 30$, their hydrophilic mass fraction is smaller than of all other investigated diblock copolymers. According to the former subsection, it was expected that the hydrophobic component of the ELPs 200–30 and 200–S30 shows higher rotational correlation times and smaller hyperfine coupling constants than ELP 200–60. Less hydration of the polymers with $x_2 = 30$ gives rise to the presumption that the spin probe senses less water molecules than in the case of $x_2 = 60$. However, the results (Figure 3.4 c and d) are contradictory to this consideration. The rotational correlation times of the spin probe molecules located in the aggregated regions of the ELPs 200–30 and 200–S30 are slightly smaller than of 200–60. Concomitantly, the polarity in the probes environment is higher for smaller x_2 observable on higher values of a of diblock copolymers with $x_2 = 30$. As the studies of Garanger¹⁰³ on diblock ELPs with a hydrophilic chain length of $x_2 = 60$ showed, the hydrophobic parts of these diblock ELPs collapses into aggregates and the hydrophilic blocks are located around these micelles. This is also in agreement with the EPR-spectroscopic measurements of the ELP x_1 –60 copolymers. Apparently, this does not apply for ELPs with shorter hydrophilic block length of $x_2 = 30$. The short hydrophilic blocks seem not to be capable of forming a nanophase-separated corona and are rather incorporated into the hydrophobic regions during their aggregation. Due to the hydration of the hydrophilic part of the polymer, more water molecules are also incorporated into the polymer aggregates. The higher water content inside the aggregates leads to a higher mobility of the here located spin probe molecules accompanied by smaller rotational correlation times. Moreover, the spin probes sense a more polar environment explaining the higher values of a for ELP 200–30 and 200–S30.

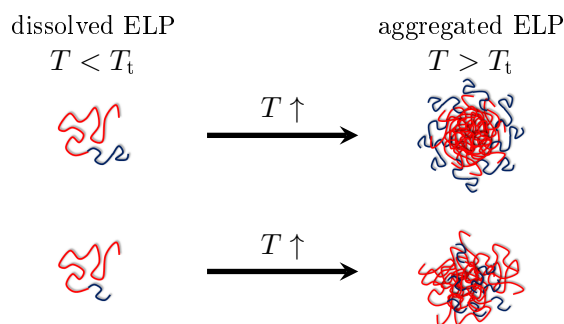


Figure 3.5: Schematic depiction of the different aggregation mechanisms for diblock ELP 200–60 (top) and ELP 200–30 (bottom), blue: hydrophilic polymer block, red: hydrophobic polymer block.

3.2.3 Conclusions

The inverse phase transition behaviour of diblock ELPs with different hydrophobic block length and different hydrophilic blocks were investigated by self-assembly spin probing CW EPR spectroscopy. This study gained new insights into the temperature-responsive transition of the block copolymer that is driven by the hydrophobic block. The thermoresponsive phase behaviour proceeds via structural inhomogeneities on the nanometre scale, similarly to what was found for synthetic and ELP homopolymers. The here observed polymeric aggregates are dynamic inhomogeneities featuring a spin-probe exchange between polymer-rich and water-rich nanophases at specific temperatures above the transition temperature. These specific temperatures are 8 °C and 4 °C above the transition temperature, respectively, depending on the relative hydrophilic mass fractions. At the onset of exchange, the spin probe molecules so far located in the hydrophobic regions diffuse through the permeable interface between hydrophobic aggregate and hydrophilic regions. Kurzbach et al.⁹² already found this type of inhomogeneities for synthetic block copolymers.

A second transition driven by aggregation of the hydrophilic blocks as well as a loss of water leading to the densification of the polymer aggregates was not visible at the molecular level with the here applied EPR-spectroscopic characterisation. Remarkably, EPR spectroscopy becomes a helpful tool if this process is not observed by scattering techniques. As seen here in the diblock copolymers with only 30 repeat units in the (short) hydrophilic block, these hydrophilic blocks cannot form a hydrophilic corona (Figure 3.5) but these short chains are rather incorporated into the hydrophobic aggregates formed at the transition temperature of the polymer. This is in contrast to diblock ELPs with long (60 repeat units) hydrophilic blocks, which are located around the hydrophobic aggregates building a corona (Figure 3.5). This explains why Garanger and co-workers did not observe a second temperature transition and hence nanophase-separation of the diblocks with hydrophilic block length of 30, yet they did observe it at block lengths of 60.

The knowledge of the phase transition behaviour obtained by spin probing EPR is gained in an indirect manner. One has to deduce the behaviour of a host-polymer from the guest molecules' behaviour and one can use EPR spectroscopy to characterise the temperature-induced nanophase-separation and the processes at the interface of polymer- and water-rich nanophase.

3.3 Dehydration and rehydration of hysteretic temperature-responsive peptide polymers

3.3.1 Hysteretic peptide polymers

Most reports of temperature-dependent behaviour of LCST peptide polymers focus on processes taking place with increasing temperature, since no differences could be observed between the behaviour during the heating and the cooling cycle of the thermoresponsive polymer. Only a sparse number of studies reports on a thermal hysteresis. A difference in the response of the polymer to increasing and decreasing temperatures has been reported by Wang¹⁰⁷ and Kujawa¹⁰⁸ for the synthetic polymer PNiPAAm investigated by calorimetric and light scattering techniques. A thermal hysteresis of the ELP (VPGVG)₃ was detected by Ma et al. using NMR spectroscopy.¹⁰⁹ Employing differential scanning calorimetry (DSC) and turbidity measurements, Reguera and co-workers observed a delayed (as compared to the aggregation during heating) resolution during cooling only for the peptide polymer with the (VPAVG) repeat unit but not for (VPGVG).¹¹⁰

Since hysteretic effects offer new opportunities for tuning the phase transition of LCST polymers and for application-driven development of, e.g. drug delivery systems, peptide polymers exhibiting a thermal hysteresis are investigated in this section. To obtain a deeper insight into the molecular details of the phase transition, hysteretic peptide polymers of different motifs and different chain lengths are investigated by CW EPR spectroscopy on amphiphilic spin probes.

For this purpose, 4-Hydroxy-TEMPO benzoate (TB) is used to monitor the polymeric phase as the investigated polymers and the more common spin probes (like TEMPO, 16-DSA) showed no molecular interactions. The temperature-dependent behaviour of the hysteretic polymers of the amino acid motifs (VAPVG) and (TPVAVG) with differing chain lengths is investigated with regard to the influence of the primary sequence of the polymer and the chain length on the temperature-dependent behaviour of the polymers in a buffer solution during the increase and the following decrease of temperature. The analysis of the EPR spectra reveals information about the dehydration and rehydration process of the polymer chains. For the amino acid sequences of the investigated hysteretic polymers and experimental details, see Section 5.1.

3.3.2 Results and discussion

3.3.2.1 EPR spectroscopic changes during the loss of hydration

Temperature-dependent changes of the investigated polymers were detected with CW EPR spectroscopy using the spin probe TB (4-Hydroxy-TEMPO benzoate; for chemical structure, see Figure 5.2 b). EPR spectra of TB in the polymer buffer solutions are shown in Figure 3.6 a, b and A.22 for the heating and the cooling cycle because the polymers showed a thermal hysteretic behaviour. In addition to that other spin probes were tested: 16-DSA (16-DOXYL stearic acid), TEMPO (2,2,6,6-Tetramethylpiperidine 1-oxyl), TEMPOL (4-Hydroxy-TEMPO), Phenyl-TEMPO-4-carboxylate, 4-Methyl-phenyl-TEMPO-4-carboxylate and 4-Ethyl-phenyl-TEMPO-4-carboxylate, none of which showed any interaction with the polymers in the complete temperature range (see Figures A.23–A.28).

At small T , the EPR spectra show no interaction between probe and polymer (exemplary

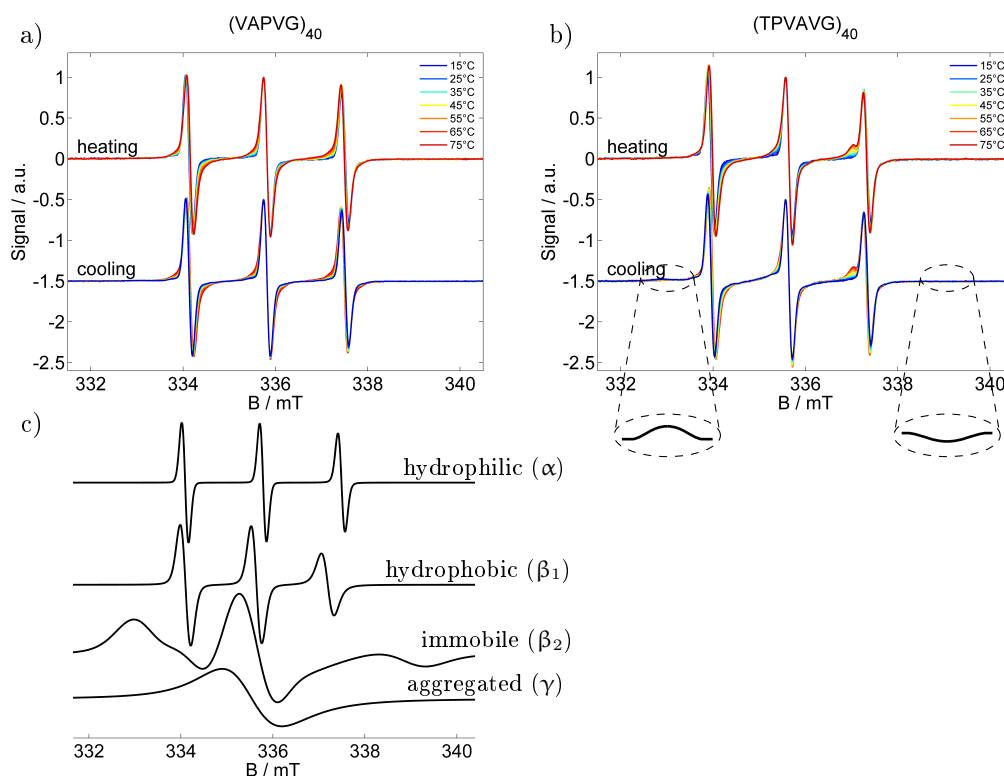


Figure 3.6: CW EPR spectra of TB in polymer buffer solution. a) Experimental spectra of $(\text{VAPVG})_{40}$, b) experimental spectra of $(\text{TPVAVG})_{40}$, c) simulated spectral components of the multimodal EPR spectra.

shown for $(\text{TPVAVG})_{80}$ in Figure A.30, 10 and 20 °C). During heating, the EPR spectra recorded at temperatures below the transition temperature of the respective polymer are composed of two components:

- a) A hydrophilic spectral component of three peaks represents TB molecules freely rotating in buffer, which do not interact with the polymer (component α in Figure 3.6 c). Hence, simulation results of this component are not discussed here (τ and a are shown in Figure A.42). Rotational correlation times τ of this TB species are in the order of magnitude of 10^{-11} s.
- b) Some TB molecules form aggregates in buffer leading to high Heisenberg spin exchange frequencies due to highly frequent spin probe collisions. EPR spectra of aggregated nitroxides are characterised by the collapse of the three peaks into one broad peak with a lower amplitude (component γ in Figure 3.6 c). This spectral component vanishes during the increase of temperature and is not of interest for the characterisation of the polymer behaviour. Hence, the spectral fraction of this component was not taken into account in the further analysis.

At temperatures above the transition temperature the spectra exhibit temperature-dependent changes that differ from the reference measurement of TB in pure buffer (exemplary shown for $(\text{TPVAVG})_{80}$ in Figure A.30, $T \geq 30$ °C). When reaching the transition

temperature T_t the polymers start to aggregate, which is reflected in the EPR spectra by the appearance of two additional spectral components:

- c) A hydrophobic spectral component corresponds to TB molecules close to hydrophobic and apolar regions of the polymer (component β_1 in Figure 3.6 c). The probe rotates slower and senses a lower polarity leading to smaller hyperfine splitting constants a and slower rotational motion due to the presence of the macromolecules as seen in higher τ ($\approx 10^{-10}$ s) than in the case of the hydrophilic component.
- d) Even slower rotating TB molecules ($\tau \approx 10^{-9}$ s) result in an anisotropic spectral component (component β_2 in Figure 3.6 c).

For simulated spectra, see Figures A.31–A.40.

At temperatures below the transition temperature the recorded spectra are a superposition of the three-peak spectrum of the freely rotating TB molecules and the broad one-peak spectrum of the aggregated nitroxide molecules. In this temperature region the peptide polymers are highly hydrated and the amphiphilic spin probes do not interact with the polymers resulting in spectra similar to the reference spectra of TB in pure buffer. The interaction of spin probes and polymers starts with the aggregation process of the polymer. The polymer chains lose their hydration shell and polymer-rich nanophases are formed with TB molecules entering these regions. During this aggregation process the peptide polymers form secondary structures like β -turns or α -helical structures.^{110,111} In previous studies with thermoresponsive peptide polymers⁹² and in the previous section about diblock ELPs, during the aggregation only one hydrophobic spectral component from slowly rotating spin probe molecules was detected. In the present study the aggregation is associated with two spectral components above the transition temperature T_t . Hence, the overall spectra at temperatures above the transition temperature (during heating) are a superposition of three or four components, respectively, since the aggregated TB component vanishes during heating and does not reappear during cooling. The appearance of the hydrophobic three-peak component β_1 is visible in the EPR spectra as having a smaller hyperfine splitting constant a and the shift of the hydrophobic component spectrum towards smaller magnetic (B -)field values (higher g values). As a consequence the hydrophobic spectral component β_1 appears next to the high-field peak at lower B -field values than the high-field peak of the hydrophilic component. The second spectral component indicating aggregation is an immobilised spectral fraction β_2 showing broad anisotropic EPR lineshapes. This anisotropic contribution to the entire spectrum is distinguished by a positive peak at B fields smaller than the low-field peak of the hydrophilic and the hydrophobic peak, respectively, and a negative spectral feature at B fields higher than the high-field peak of the hydrophilic and the hydrophobic component, respectively. The difference between the B values of these two extrema is equal to twice the apparent hyperfine coupling constant A'_{zz} . Due to the weak signal amplitude of the immobilised component (β_2) as compared to the amplitude of the spectral components α and β_1 , component β_2 is only barely visible in the EPR spectra and highlighted in Figure 3.6 b for the spectra of (TPVAVG)₄₀ in the cooling branch of the temperature cycle. For a detailed view of the low field peaks of component β_2 of the recorded EPR spectra, which is clearly visible in spectra of the cooling cycle at low temperatures, see Figure A.41. It should be noted that components β_1 and β_2 always appear together in all investigated polymers.

During the cooling of the polymer solution, the immobilised spectral component β_2 is

Table 3.3: Transition temperatures of the measured polymer buffer solutions investigated by CW EPR spectroscopy. The transition temperature is indicated by the appearance of two spectral components of slowly rotating TB (β_1 and β_2).

Monomer	n	T_t in °C
TPVAVG	80	24 ± 1
TPVAVG	40	24 ± 1
VAPVG	80	26 ± 1
VAPVG	40	30 ± 1
VAPVG	30	34 ± 1

present with a nearly constant fraction in a broad temperature range, while the fraction of the hydrophobic component β_1 decreases monotonically. Both components are observable at temperatures below T_t during the cooling period (see Figures 3.7 and 3.8).

The hydrophobic as well as the immobile spectral component is more prominent in the case of the (TPVAVG) $_n$ polymers without a visible influence of the number of repeats n . For the (VAPVG) $_n$ polymers, a more prominent appearance of the hydrophobic species is obvious for smaller n .

Since the above described LCST is the minimum of a phase diagram that also takes the concentration of the polymer in the solution into account, the temperature of the here reported phase transition process at constant concentration is denoted as ‘transition temperature’. The transition temperatures, which are marked by the onset of appearance of the hydrophobic and the immobilised components (β_1 and β_2) in the EPR spectra, of all investigated polymers are given in Table 3.3. With increasing degree of polymerisation n of the pentapeptide polymers, T_t is shifted to lower temperatures. This behaviour is in accordance with previous studies on peptide polymers⁹² and the results of the hydration behaviour of diblock ELPs (see Section 3.2). The transition temperatures of the two investigated hexapeptide polymers showed no n -dependence. Comparison of the temperature dependence of both polymer types reveals that the discrepancies between the T_t of both polymers at identical n is lowered with increasing n ($\Delta T_t(n = 80) = 2^\circ\text{C}$, $\Delta T_t(n = 40) = 6^\circ\text{C}$). A longer chain lengths leads to an only slightly higher T_t of (VAPVG) $_{80}$ compared to (TPVAVG) $_{80}$.

While the appearance of the components β_1 and β_2 in the EPR spectra indicates the onset temperature of the inverse phase transition on the nanoscale, the temperature-dependent behaviour of the fractions of these components mirrors the progression of the transition process upon heating. The fraction of the immobilised component (β_2) of TB increases rapidly at temperatures near T_t (Figure 3.7 b and Figure 3.8 b). Thus, the aggregated regions occupied by the immobilised TB molecules show a sharp transition. In contrast the fraction of the hydrophobic component shows only a small increase near T_t (Figure 3.7 a and Figure 3.8 a) followed by a monotone increase indicating a smooth transition of the hydrophobic regions represented by this spectral component.

One could argue that during the polymeric aggregation at $T > T_t$, the loss of hydration and the related diffusion of water molecules from the polymer-rich to the water-rich phase should result in a decrease in mobility of the spin probes and in polarity inside the dehydrated and aggregated polymer regions indicated by an increase of the rota-

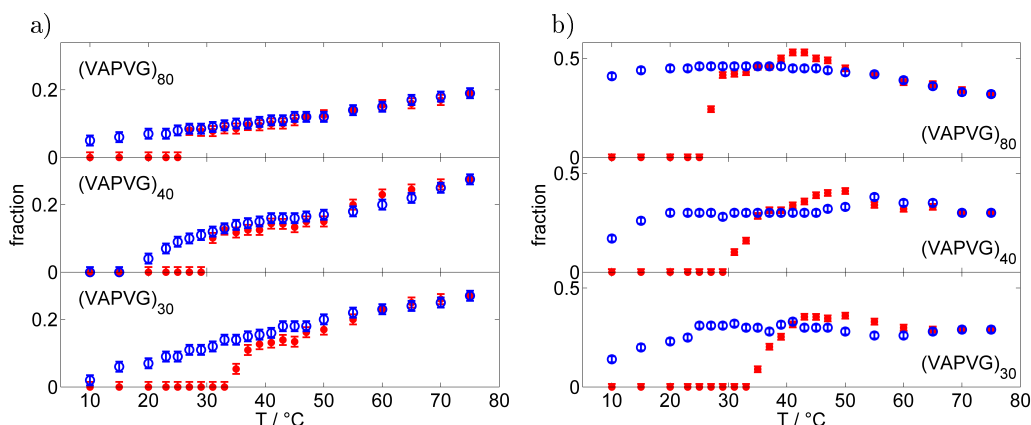


Figure 3.7: Fractions of the components of the EPR spectra of the $(\text{VAPVG})_n$ polymers arising with the transition of the polymer from rigorous spectral simulation. a) Fractions of the hydrophobic component, b) fractions of the immobile component, \bullet heating and \circ cooling.

tional correlation time τ and a decreasing hyperfine splitting constant a . The results of the simulation of the EPR spectra recorded of the hysteretic polymers reveal the opposite situation. All spin probes in the examined polymers feature an increasing hyperfine splitting constant a (i.e. an increase in polarity of the environment) for the hydrophobic component β_1 (Figure 3.10 a). At first glance the decrease of a of the immobilised component β_2 (Figure A.44) points at a decrease in polarity. However, in this case the temperature-dependent behaviour of A'_{zz} is dominated by the increase in mobility of the immobile spin probes due to a gain in kinetic energy at higher temperatures. Consequently, the hyperfine splitting spans values in the transition regime from the anisotropic A_{zz} to the isotropic a_{iso} . The gain in mobility and the increase in polarity in the environment of the hydrophobic spectral component is typical for *dynamic inhomogeneities of type II* during the collapse process (see Section 3.1 case 3, according to Kurzbach et al.⁹⁷), allowing the probes to diffuse between polymer-rich and water-rich regions on the timescale of several nanoseconds. Averaged values of τ and a of these regions then dominate these EPR spectral components.

3.3.2.2 Hysteretic behaviour of (VAPVG) and (TPVAVG)

The EPR spectra of the polymers $(\text{VAPVG})_n$ and $(\text{TPVAVG})_n$ at a given temperature show distinct differences between the spectra depending on whether they were recorded during heating or cooling steps, respectively. The hysteretic behaviour is most obvious in the temperature-dependent fractions of the spectral components arising at the transition temperature during heating (Figure 3.7 and Figure 3.8). Since the hydrophilic component represents the TB molecules freely tumbling in water, this component is not discussed here. For simulation results of the hydrophilic component, see Figure A.42.

Thermal hysteresis is clearly visible for the heating and cooling curves of the fraction of the immobilised component β_2 of the spin probe and is first described in the following, before component β_1 is also taken into account. During heating, all three $(\text{VAPVG})_n$ polymers basically follow the same curve shape, only shifted along the T -axis by the transition temperature of the respective polymer (Figure 3.7 b). After a sharp increase

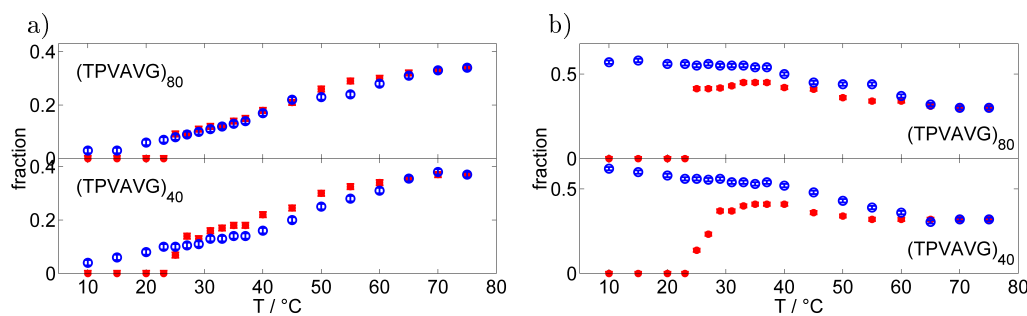


Figure 3.8: Fractions of the components of the EPR spectra of the $(\text{TPVAVG})_n$ polymers arising with the transition of the polymer from rigorous spectral simulation. a) Fractions of the hydrophobic component β_1 , b) fractions of the immobile component β_2 , \bullet heating and \circ cooling.

at T_t , fraction β_2 increases to a maximum at 40 $^\circ\text{C}$ –50 $^\circ\text{C}$ and then slightly decreases at higher temperatures to reach a plateau value at $T > 65$ $^\circ\text{C}$. This decrease possibly stems from the increase in mobility of the immobile TB molecules. As shown in Figure A.43 and Figure A.44, the rotational correlation time and the hyperfine splitting constant A'_{zz} of the immobile component decrease with increasing temperature indicating faster rotating molecules. It is possible that some molecules gain enough thermal energy to leave the strong hydrophobic, water-depleted regions leading to a smaller fraction of the immobile TB molecules.

There is a slight n -dependence of the maximum fraction value attained (0.53, 0.41, 0.36 for $n = 80, 40, 30$, respectively) but the final fraction values in the plateau region above 65 $^\circ\text{C}$ are very similar for all $(\text{VAPVG})_n$ (0.33, 0.3, 0.29 for $n = 80, 40, 30$, respectively). When the polymer solution is then cooled after heating to 75 $^\circ\text{C}$, the fraction of the immobilised component β_2 remains nearly constant down to temperatures of at least 25 $^\circ\text{C}$. Only at temperatures of 25 $^\circ\text{C}$ ($(\text{VAPVG})_{30}$) or 15 $^\circ\text{C}$ ($(\text{VAPVG})_{40}$), the fraction slightly decreases suggesting a saturation of the hysteresis at lower temperatures. Larger n -values lead to higher fractions of the immobilised component β_2 during the heating as well as the cooling phase and in the cooling steps. This is especially true for $n = 80$ as compared with $n = 30, 40$ (Figure A.45 b). The two polymers of shorter chain length show only minute differences.

In the case of the polymers composed of (TPVAVG) the dependence of the immobilised component fraction during heating is qualitatively similar to those of the (VAPVG) polymers but without a distinct dependence on n (Figure A.45 d). The $(\text{TPVAVG})_{80}$ polymer has only slightly higher fractions of the immobilised component than $(\text{TPVAVG})_{40}$. In the cooling phase the (TPVAVG) polymers show a development of the immobilised fractions β_2 that is distinctly different to that of (VAPVG) . Decreasing temperature from 75 $^\circ\text{C}$ to 10 $^\circ\text{C}$ leads to increasing immobilised fractions of all (TPVAVG) polymers.

This temperature hysteresis of the weighted fraction is also observable for the hydrophobic component β_1 —to a lesser degree (Figure 3.8 a). Fractions of this component β_1 have virtually identical temperature behaviour for both, (VAPVG) and (TPVAVG) polymers. Heating up the polymer solution, the hydrophobic component β_1 appears with a steep increase at the transition temperature, which is followed by a monotone increase of the fraction with higher temperatures. The following cooling shows no hysteresis in

the fractions of the hydrophobic component until T_t is reached again. The hydrophobic component β_1 does not disappear when the polymer solution is cooled, yet—the fraction of the hydrophobic component decreases further at temperatures below T_t . Taking the chain length of the polymers into account, a stronger n -dependence is observed for the (VAPVG) polymers (Figure A.45 a). In contrast to the findings in Section 3.2 longer chain lengths lead to smaller fractions of the hydrophobic component β_1 . The same applies to (TPVAVG) but with only a small difference between a chain length of 40 and of 80 motif repetitions (Figure A.45 c). The divergence of this n -dependent behaviour possibly arises from the fact that in former studies only one spectral component characterised the thermoresponsivity, whereas two of them are observed in the present study.

Taking all together it can be stated that the inverse phase transition and the temperature-dependent behaviour of the (VAPVG) and (TPVAVG) polymers can be investigated by CW EPR spectroscopy, specifically by characterising the two spectral components β_1 and β_2 arising at the transition temperature. These hydrophobic and immobile components β_1 and β_2 , respectively, have a remarkably different temperature dependence. The sharp transition indicated by the immobilised component is in contrast to the smooth transition observed for the hydrophobic component. The hysteretic behaviour is observable for all polymers studied here in the plots of the temperature-dependent fraction for both components but is decidedly more distinguished for the immobilised component β_2 . Longer polymer chains result in higher fractions of component β_2 , whereas the fraction of component β_1 drops for longer chain length. These differences indicate different transition processes of different hydrophobic and polymer-rich regions of the aggregating polymers. Nonetheless, the onset of both processes is identical, at the transition temperature. Since LCST-type transitions as for these peptide polymers are driven by changes in hydration, the observed thermal hysteresis may reflect differences in the rehydration process during cooling when compared to the dehydration of the polymer chains during heating. In the case of the well-studied ELPs, neither the immobilised component nor a thermal hysteresis was observed. Hence, one can connect the hysteresis observed in the two spectral components β_1 and β_2 and the individual differences of the temperature dependence of the two components with different nanoscopic processes during the transition of the (VAPVG) and (TPVAVG) polymers.

For ELPs, Kurzbach et al. were able to describe an amino-acid (residue X) tuning of either a coupled or a decoupled state of main chain and side chain hydration of these polypeptides.⁹² The coupled hydration state featured only one transition temperature, while the decoupled state was characterised by two transition temperatures stemming from the dehydration of the main chain and of the side chains individually. In this study of (VAPVG) and (TPVAVG) the dehydration of main chain and side chain during heating happens simultaneously at the same temperature, since no second temperature transition could be detected, but the process of the rehydration during cooling shows a delay between the rehydration of two aggregated regions—assumably the main chain and the side chain region. As can be seen in Figure 3.9, when the polymer solution is heated up to the transition temperature (process ① in Figure 3.9), the hydration shell of the main chain (depicted in cyan) vanishes as well as the hydration shell of the side chain (depicted in blue) leading to the collapse of the polymer, forming intra- and intermolecular physical crosslinks (through H-bonding) that lead to the macroscopically observable polymeric aggregates. During the following cooling (process ② in Figure 3.9), the side

chains are more easily and gradually rehydrated while the main chain stays dehydrated. Hence, the polymer–polymer contacts and the secondary structures formed during the transition stabilise the polymer-rich phase and thus persist even when cooled below the transition temperature. As a result, the polymer is not fully resolubilised at the transition temperature. Main chain and parts of the side chains stay dehydrated. This is reflected in the fraction of the immobilised component β_2 remaining constant and that of the hydrophobic component β_1 not vanishing (but decreasing) at temperatures below the transition temperature.

The temperature hysteresis and the difference in the dehydration and rehydration processes are obviously related to the amino acid sequence of the peptide polymers. Classical ELPs with repeat units built on the (VPGXG) motif have at least two glycines in the sequence, i.e. at least two of five amino acids have no side chains, precluding a hysteresis in hydration. The (VAPVG) and (TPVAVG) polymers contain only one side-chain free amino acid (glycine) so that one can assume that the remaining four or five, respectively, amino acids are capable of forming a compact side chain hydration shell. This side chain hydration layer seems to be able to protect the aggregated main chains from rehydration by impeding the diffusion of water molecules into the dense hydrophobic aggregates, which were formed when heating the polymer solution above the transition temperature. Considering the described insights in de- and rehydration, one can interpret the physical origin of the two spectral components arising at the inverse phase transition. Denoted TB molecules representing the hydrophobic component β_1 (● in Figure 3.9) are probably situated close to side chains, which undergo a smooth dehydration. The slower rotating TB molecules of the immobilised component β_2 (• in Figure 3.9) are located in the water-depleted, strongly hydrophobic regions of the dehydrated main chains, which undergo a fast, sharp dehydration process. Overall, this can hence be characterised as a complete decoupling of main-chain and side-chain rehydration, while the onset of the dehydration process is coupled (T_i for components β_1 and β_2 are identical). Nonetheless the process of dehydration of both hydration layers nansocopically (inspecting the different sharp vs. smooth transition curves) are somehow decoupled.

3.3.2.3 Stabilisation of aggregates by a hydrophilic amino acid

The amino acid sequence of the polymer has an impact on the transition as well as on the hysteretic behaviour. The (TPVAVG)-based polymers show higher fractions of the immobilised component β_2 during cooling. Furthermore, one observes higher fractions of the hydrophobic component. In the case of (TPVAVG) it is also remarkable that the hyperfine splitting constant a of the hydrophobic component is smaller than in the case of (VAPVG) (Figure 3.10 c and d). Since a is a measure of the polarity of the local environment of the spin probe, a smaller a of TPVAVP indicates a lower polarity around the hydrophobic component of the TB molecules and concomitantly less water in their environment despite the fact that the additional amino acid threonine (T) is a highly hydrophilic amino acid¹⁰⁶ with a hydroxyl group side chain. In contrast, it has been shown for diblock ELPs that a higher hydrophilicity leads to a higher polarity in the environment of spin probes located in the aggregated regions (see Section 3.2).

The additional amino acid threonine apparently also influences the thermal hysteresis as can be seen in Figure 3.8 b compared to Figure 3.7 b. The fraction of the immobilised component β_2 as compared to that in (VAPVG) is much larger and ever-increasing with decreasing temperatures.

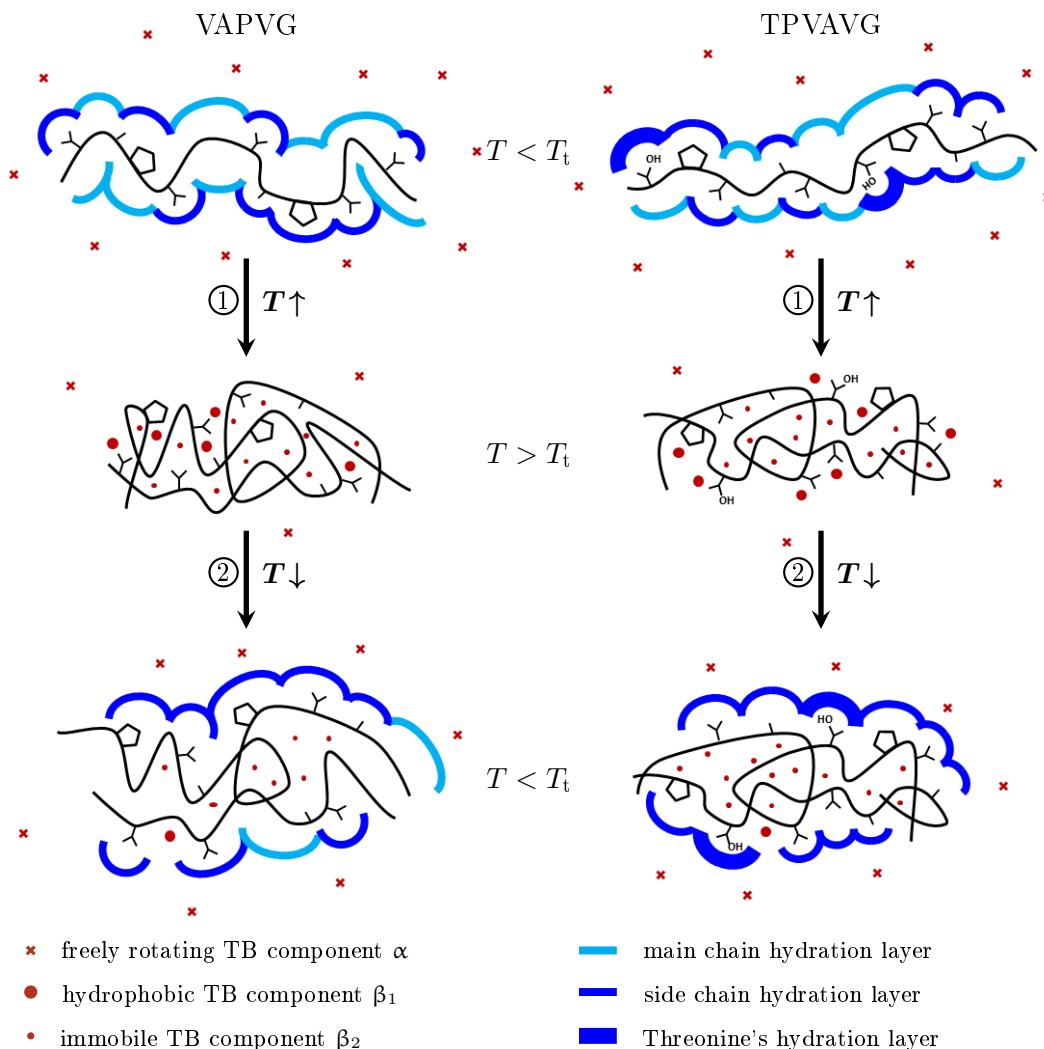


Figure 3.9: Schematic representation of the supposed hydration process of the hysteretic peptide polymers (VAPVG) (left) and (TPVAVG) (right). Side and main chains of the polymers are hydrated at temperatures below the transition temperature and dehydrated at temperatures above the transition temperature. If the temperature is decreased afterwards to temperatures below the transition temperature, the side chains are rehydrated, while for (VAPVG) the main chains are only partially rehydrated and for (TPVAVG) a hydration layer of threonine-bound water prevents main chain rehydration almost completely.

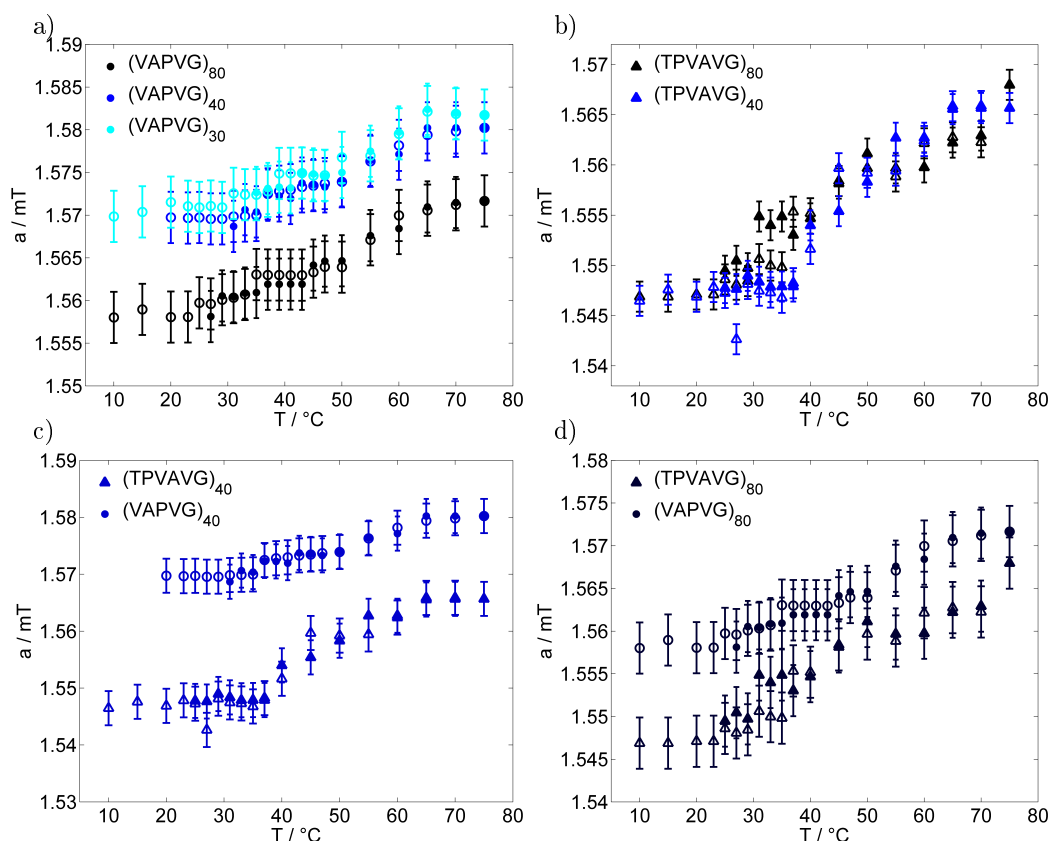


Figure 3.10: Results of simulation of the CW EPR spectra of TB in a polymer–buffer solution: hyperfine splitting constants of the simulated hydrophobic component compared for the same motif (a) (VAPVG) and b) (TPVAVG)) and for the same chain length (c) $n = 40$ and d) $n = 40$). \bullet and \blacktriangle : heating, \circ and \triangle : cooling. Hyperfine splitting constants give half of the difference in B field of the high-field and of the low-field peak of the simulated EPR spectra of the respective component.

Spectral simulation of the CW EPR spectra allows for an even more detailed and differentiated characterisation of the processes leading to thermal hysteresis than just obtaining the fractions of the individual spectral components. The isotropic hyperfine coupling values a also give detailed insights in the surrounding polarity.

The results of the simulation of the EPR spectra reveal that the rehydration process differs for (VAPVG) and (TPVAVG) polymers. The side chains of the (VAPVG)-polymers are rehydrated almost completely at temperatures clearly below T_t , as the fraction of the hydrophobic component β_1 reaches values of $f \approx 0$ (Figure 3.7 a). The fraction of the immobilised component β_2 of these polymers slightly decreases during cooling at temperatures below T_t but remains significantly above $f = 0$. Apparently, the mostly hydrated and resoluted side chains of this type of peptide polymer do not shield the still aggregated main chains from the surrounding water any more. Consequently, water molecules can reach the main chain regions, where the immobilised fraction β_2 of the TB molecules is situated, leading to the polymer and TB molecules being resoluted and the destruction of the secondary structure elements formed during the inverse phase

transition. The hydrophobic component β_1 close to the side chains of the (TPVAVG) polymers vanishes, too, but there is no concomitant decrease in the fraction of the immobilised component β_2 . Thus, the surrounding water does not reach the regions of the aggregated main chains, where the immobilised TB molecules are located.

Assumingly, slight difference in the order of the amino acids beyond the addition of the very hydrophilic threonine in the repeat units does not lead to such drastic effects. Thus, the different hysteretic behaviour of the (VAPVG) and (TPVAVG) polymers can be traced back to the OH group of threonine and its ability to form hydrogen bonds. The hydroxyl group of threonine can interact with the surrounding water molecules, being incorporated in the aqueous H-bond network. Due to its hydrophilicity threonine prefers to be localised at the interface of the polymer aggregates with the water-rich regions rather than in the hydrophobic, water-depleted regions of the polymeric aggregates. Hence, rather rigid and local H-bonding networks may form around the side chains of the threonines (depicted as thick blue shell in Figure 3.9). As a consequence and somehow counterintuitive, the hydration shells of the main chain and of the side chains of the amino acids other than threonine may be perturbed in comparison to the polymers not containing threonine. These polymers may always have more water molecules close to the non-polar amino acid side chains and the main chain. This explanation is in fact supported by the transition temperatures of the polymers, which are lower in the case of the T-containing polymers (Table 3.3) and the smaller values of a of the hydrophobic component indicating a smaller polarity in the surrounding of the side chains (Figure 3.10 c, d). The T-side chain hydration therefore expedites the dehydration of the polymer chain, potentially by acting as an efficient trap for water molecules leaving the polymer chains above T_t .

When the polymer solution is cooled after the heating cycle, the localised water structure/hydration shell forming around threonines together with the hydration shell of the rehydrated amino acid side chains may shield the strongly hydrophobic, water-depleted and still dehydrated main chains of (TPVAVG) from penetrating water. This can be viewed as a hydration layer of rather localised water molecules that prevent water molecules from reaching the main chain. Thus, the main chain aggregates exist during the cooling cycle even at small temperatures (as can be seen in Figure 3.9 (right) at $T < T_t$ after process ②) indicated by the not decreasing fraction of the immobile spectral component.

3.3.2.4 Chain length dependence

The comparison of EPR spectroscopic parameters for (VAPVG) and (TPVAVG) polymers reveals different dependences of the chain length n . While the parameters for (TPVAVG) polymers virtually display no n -dependence, for (VAPVG) polymers a clear n -dependence for the fractions of the hydrophobic (β_1) and the immobilised components (β_2) and in the hyperfine splitting constant a of the hydrophobic component (Figures 3.7, 3.8 and 3.10). Since a is inversely proportional to n , shorter polymer chains are apparently hydrated more strongly, which is also reflected in the higher transition temperatures for smaller n (Table 3.3). On the contrary (TPVAVG)₄₀ and (TPVAVG)₈₀ have very similar T_t . It seems that threonine or the hydration shell of threonine's side chain, respectively, counteracts the impact of the chain lengths on the thermal behaviour of the peptide polymers also with regard to the transition temperatures.

The phase transition for both polymers seems to proceed nearly identically as can be seen in the temperature-dependent fractions of the immobilised component β_2 (Figures 3.7 and 3.8). The development of spectral fractions of this component in (VAPVG) and (TPVAVG) show a similar behaviour, only shifted along the temperature axis through their different T_t s. Additionally, for $n = 80$ a higher fraction of the immobilised component was observed for VAPVG.

Already for entropic reasons, the chain length of the pentapeptide polymers strongly determines the size of the polymeric aggregates. Short (VAPVG) $_n$ polymers ($n = 30, 40$) apparently form small very hydrophobic aggregates containing the immobilised TB molecules and less hydrophobic, more water containing regions located around these extremely water-depleted regions. The higher fraction of component β_2 and the smaller fraction of component β_1 in case of longer (VAPVG) $_n$ polymers ($n = 80$) indicates preferential formation of the highly water-depleted regions in which the immobilised TB molecules reside. Since the ratio of the spectral fractions of components β_1 and β_2 in the EPR spectra is reduced with higher degree of polymerisation, it is concluded that dehydrated side chains partake into the very hydrophobic, water-depleted aggregates hosting the immobilised TB molecules.

While the fraction of the immobilised component β_2 shows similar values for both polymer types, the fraction of the hydrophobic component β_1 is significantly higher for the hexapeptide polymers. Since the temperature-dependent development of the fractions of the spectral components interacting with the dehydrated chains of (TPVAVG) $_n$ is nearly independent of n it can be suggested that the ratio of hydrophobic regions to very hydrophobic regions does not change with the chain length of the polymer. This is in contrast to the aggregation behaviour of (VAPVG) $_n$ and leads to the assumption that the (TPVAVG) $_n$ polymers form very hydrophobic (main chain) aggregates, where the immobilised component β_2 is located, while the side chains independently form the hydrophobic regions containing the hydrophobic spectral component β_1 . This is schematically depicted in Figure 3.9, where the side chains of (VAPVG) (left part of the picture) are situated mostly inside the main chain aggregates and the side chains of (TPVAVG) (right part of the picture) outside the main chain aggregates. The located water structure around threonine seems to be coupled to the hydration shell of the side chains of the other amino acids of (TPVAVG). This results in a more prominent distinction of the hydrophobic and the immobile regions than in the case of (VAPVG) leading to a nearly n -independent ratio of the hydrophobic to the immobile fractions. As described above, threonine assumingly leads to structural different polymer-rich regions, where the dehydrated main chain regions and the dehydrated side chain regions are more separated. They are coupled upon heating but the hydration layer of water coupled to threonine decouples the rehydration upon cooling. All this is not the case for any peptide polymer without threonine.

3.3.3 Conclusions

Peptide polymers of two different motifs and varying chain lengths were investigated by self-assembly spin probing CW EPR spectroscopy. This study sheds light upon the nanoscale of the temperature-dependent behaviour of the polymers (VAPVG) $_n$ and (TPVAVG) $_n$ in a buffer solution during heating and subsequent cooling.

In contrast to previous findings of the phase transition behaviour of peptide polymers, the transition of these polymers leading to the aggregation of the polymer chains is

hallmarked by the appearance of two components in the EPR spectra: a slow rotating component with a hydrophobic environment and an even slower rotating component in a strongly water-depleted, very hydrophobic region showing an immobilised spectral contribution. The analysis of the spectra with respect to the amino acid sequence of the polymers allows the conclusion that the immobilised probe molecules of spectral component β_2 are situated near the dehydrated main chain regions and the slightly faster rotating probe molecules of spectral component β_1 near the dehydrated side chains. The dehydration of both polymer regions starts at the same temperature. Although their onset upon heating is coupled, the dehydration process of their hydration layers appear to be somehow decoupled since the immobilised spectral component displays a sharp transition, whereas the development of the fraction of the hydrophobic component with increasing temperature denotes a smoother, more gradual transition.

Both polymer types exhibit a thermal hysteresis. The rehydration process, when the polymers were cooled down, differs from the dehydration process, when the polymer solution was heated up. The different hydration states are summarised in Figure 3.9. The rehydration of the side and the main chains proceeds differently. The side chains are gradually hydrated with decreasing temperature, while the main chain stays dehydrated over an extended temperature interval. This is surprising, since such a hysteresis was not observed for the structurally similar, well-studied ELPs. It can be assumed, that in the case of $(VAPVG)_n$ and $(TPVAVG)_n$ the rehydrated side chains shield the dehydrated main chain regions from penetrating water. This effect is amplified for the threonine-containing sequence. The measurements revealed that the OH group of threonine forms its own shell of water molecules, which strengthens the shielding of the water-depleted, aggregated regions from penetrating water molecules. Furthermore, the very hydrophilic amino acid threonine decreases the transition temperature and cancels the influence of the chain length on the phase transition behaviour of these peptide polymers.

3.4 Outlook

The study of diblock ELP consisting of a hydrophobic and a hydrophilic block by CW EPR spectroscopy based on a former study applying light and neutron scattering techniques. With the approach used in this thesis, further insight into the nanoscopic phase transition of the diblock ELPs was gained. However, only the transition of the hydrophobic block could be detected. The subsequent loss of water and transition of the hydrophilic block, which was stated by Garanger et al.¹⁰³ for this type of polypeptides, was indiscernible with spin probing EPR. These limitations may be overcome with the binding of a spin label covalently to the polymer. By site-directed spin labelling, a nitroxide radical such as MTSSL ((1-oxyl-2,2,5,5-tetramethyl-D-pyrroline-3-methyl)methanethiosulfonate) could be bound covalently to the cysteine located in the leader sequence near to the hydrophobic block of the diblock ELPs. Consequently, the loss of water inside the aggregated hydrophobic block may be detectable by CW EPR since the nitroxide radical would not exchange between polymer-rich and water-rich phases of the aggregated polymer in solution as observed with the spin probing approach. By comparing the CW EPR results of the spin probing with the CW EPR results of the spin labelling experiments, it could be investigated if the spin label has a significant influence on the temperature-dependent phase separation of the polymers.

The results of EPR measurements on peptide polymers showing a thermal hysteresis revealed differences in the rehydration process of side and main chains of the amino acids, which are amplified by the OH group of an additional threonine. In this thesis, only two different sequences were studied. To verify the interpretation of the EPR data, more relevant sequences have to be investigated. Results of polymers with the motif (VPGVG) as an example for non-hysteretic behaviour¹¹⁰ should be involved. This motif was already investigated with CW EPR by Kurzbach et al.⁹² but without taking the hydration behaviour during cooling into consideration and using 16-DSA instead of TB, which was used in this thesis. Thus, CW EPR results of TB and of 16-DSA, respectively, should be compared for ELP known as non-hysteretic. Furthermore, EPR measurements of the sequence (VPAVG) should be implemented, which is one of the first described hysteretic peptide polymer.¹¹⁰ Since the amino acid compositions of (VPAVG) and (VAPVG), which was investigated in this thesis, are identical, the comparison of the dehydration and rehydration processes during heating and cooling of these polymers would facilitate the interpretation of the effects governing the hysteresis from the perspective of main and side chain hydration.

EPR measurements in the presence of urea may help to gain further insights. Urea is known to increase the transition temperature of ELPs¹¹² and can significantly decrease the degree of hysteresis of (VAPVG) but has a lower effect on the degree of hysteresis of (TPVAVG) (unpublished data by F. G. Quiroz and A. Chilkoti). Adding urea in different concentrations to the solutions of (VAPVG), (TPVAVG), (VPAVG) and (VPGVG), respectively, may reveal further comprehension of the behaviour of the different spin probe fractions upon cooling due to possibly different effects of urea on the main chain hydration and on the side chain hydration.

CHAPTER 4

Myelin basic protein

4.1 Introduction

The myelin sheath—a multilamellar lipid membrane—is wrapped concentrically around the nerve axons in the central nervous system (CNS).^{33,113} Thereby, it accomplishes the task of insulating the nerve fibres and facilitating rapid nerve impulse transmission by saltatory conduction.^{114–116} To increase the efficiency of transmission of electric nerve signals, a low capacitance and, concomitantly, a low effective dielectric constant of the myelin are necessary. This requirement is enabled by a relatively high lipid content of 70–80 % in the myelin sheath¹¹⁷ (compared to 20 % for most cell membranes¹¹⁸) and a dielectric constant of the lipid acyl chains $\epsilon_{\text{Lipid}} \approx 2$.⁷⁸ For an optimal application of ϵ_{Lipid} , the myelin sheath has to be compact and tightly wrapped around the nerve fibre. Myelinated axons transmit nerve impulses much faster than axons without a compact myelin sheath.¹¹⁹

The myelin basic protein (MBP; for amino acid sequence of human, bovine and recombinant murine charge variants of MBP, see Table 4.1) is a structural protein that associates with opposing leaflets of the cytoplasmic side of the oligodendrocyte membrane like a ‘molecular glue’ to ensure a high compaction of the myelin sheath.^{113,120,121} The 18.5 kDa splice isoform is the major structural protein of the myelin sheath in the adult human and bovine brain.¹²² MBP is an intrinsically disordered peripheral membrane protein with a net positive charge of +19 (at pH 7). In aqueous solution, MBP has long been known to have an extended conformation. It interacts with diverse binding partners like divalent cations^{123,124} (e.g. Zn^{2+} , Cu^{2+}),^{125–127} molecules of the immune system^{128,129} and proteins like MBP itself^{121,130} and proteolipid protein.^{131,132} The protein’s interaction with most of its binding partners, but especially lipids, causes it to undergo conformational changes and form ordered secondary structures at the binding site.^{35,113,133,134} In particular, three amphipathic α -helices exist in the protein bound to the myelin membrane, located at the N- and C-termini, and in the central region: T33–D46, V83–T92 and Y142–L154 (murine 18.5 kDa sequence numbering, Table 4.1).^{113,135} The binding of MBP to the cytoplasmic membrane is driven by electrostatic and hydrophobic interactions^{120,136,137} with an assumed absolute requirement of the electrostatic interaction between negatively charged lipids and the positively charged MBP.¹³⁸ The conformational transition of MBP from an extended conformation into a self-assembled protein with elements of ordered secondary structures is assumed to be triggered by the lower dielectric constant of the membrane surface¹³⁹ and fixed by charge neutralisation of the

Table 4.1: Amino acid sequences of 18.5 kDa human (h)MBP C1,¹²² bovine (b)MBP,¹²² recombinant murine (rm)MBP C1 and C8.¹⁴³ Highlighted amino acids indicate the basic residues (**K**, **R**) of rmMBP C1 that are replaced by glutamine (**Q**) to yield rmMBP C8.

	1	11	21	31
hMBP C1	ASQKRPSQRH	GSKYLATAST	MDHARHGFLP	RHRDTGILDS
bMBP	AAQKRPSQRS	KYLASASTMD	HARHGFLPRH	RDTGILDSLGL
rmMBP C1	ASQKRPSQRS	KYLATASTMD	HARHGFLPRH	RDTGILDSIG
rmMBP C8	ASQKRPSQRS	KYLATASTMD	HAQHGF LPRH	QDTGILDSIG
	41	51	61	71
hMBP C1	IGRFFGGDRG	APKRGSGKDS	HHPARTAHYG	SLPQKSHGRT
bMBP	RFFGSDRGAP	KRGSKGKDGHH	AARTTHYGSL	PQKAQGHRPQ
rmMBP C1	RFFSGDRGAP	KRGSKGKDSHT	RTTHYGSLPQ	KSQHGRTQDE
rmMBP C8	RFFSGDRGAP	KRGSKGKDSHT	RTTHYGSLPQ	KSQHGRTQDE
	81	91	101	111
hMBP C1	QDENPVVHFF	KNIVTPRTPP	PSQGKGRGLS	LSRFSWGAEG
bMBP	DENPVVHFFK	NIIVTPRTPPP	SQGKGRGLSL	SRFSWGAEGQ
rmMBP C1	NPVVHFFKNI	VTPRTPPPSQ	GKGRGLSLSR	FSWGAEG QKP
rmMBP C8	NPVVHFFKNI	VTPRTPPPSQ	GKGRGLSLSR	FSWGAEG QQP
	121	131	141	151
hMBP C1	QRPGFGYGGR	ASDYKSAHKG	FKGVDAQGTL	SKIFKLGGRD
bMBP	KPGFGYGGRA	SDYKSAHKGL	KGHDAQGTLS	KIFKLGGRDS
rmMBP C1	GFGYGG R ASD	YKSAHKGFKG	AYDAQGTLSK	IFKLG G RDSR
rmMBP C8	GFGYGG Q ASD	YKSAHKGFKG	AYDAQGTLSK	IFKLG G Q DSR
	161			
hMBP C1	SRSGSPMARR			
bMBP	RSGSPMARR			
rmMBP C1	SGSPMA RR			
rmMBP C8	SGSPMA RQ			

positively charged amino acid residues of MBP by negatively charged lipids.^{140,141} The strong interaction of MBP and the oligodendrocyte membrane leads to the tightly packed multilamellar structure of the myelin sheath.¹⁴² MBP is also a candidate autoantigen in multiple sclerosis.^{144,145} Binding to a membrane, the amino acid segment V83–T92 of the murine MBP sequence (corresponding to V86–T95 in the case of human MBP) assumes an α -helical conformation and is known as immunodominant epitope for B and T cells.^{145–147} MBP-specific autoantibodies bind to this region, if it is exposed from the membrane. In the human disease MS, active destruction of the myelin sheath and resultant demyelination of the axons¹⁴⁸ lead to sensory and motor impairments that are a basis for diagnosis.¹⁴⁹ There is no animal model of MS that fully recapitulates its manifestation in humans. The induced inflammatory disease experimental autoimmune encephalomyelitis (EAE) in rodents (mainly) as well as in primates, such as marmosets, nevertheless, shows many similarities to MS in its later stages and is therefore commonly used as a model system for diseased myelin.^{150,151} Myelin lipids derived from brains of EAE-afflicted animals have increased amounts of negatively charged phosphatidylserine (PS), decreased amounts of phosphatidylcholine (PC) and sphingomyelin (SM), and

a greater degree of acyl chain unsaturation, compared to healthy controls.^{150,152} Although it is contentious as to whether these changes reflect an underlying mechanism of degradation or are a consequence of it, it is nonetheless intriguing that protein–lipid adsorption isotherms are altered using EAE-mimetic monolayers and that fatty acyl chain unsaturation has effects independent of lipid headgroup composition.¹⁵⁰ More recently, the small-angle X-ray scattering (SAXS) and cryogenic transmission electron microscopy (cryo-TEM) measurements conducted by Shaharabani and co-workers have revealed that instabilities in the myelin membrane in the form of an inverted hexagonal phase occurred in membranes with lipid compositions similar to those observed in EAE-mimetic myelin, in contrast to the multilamellar phase characteristic of membranes like those in healthy myelin.¹⁵¹ These changes in abnormal adsorption of MBP to a membrane of altered lipid composition may be an additional mechanism that contributes to destabilising myelin and might be operative in human MS.

Since the molecular mechanisms of the MBP–lipid interactions are still not completely understood, the initial stages of myelin degeneration at the cellular level are unknown.¹⁵³ For such reasons, there is still no therapeutic option for MS patients that will result in full recovery.^{154,155} A large number of partly unconnected (so far) pieces of the puzzle ‘multiple sclerosis’ exist, all yielding attempts to explain the molecular origin of this disease: Most commonly, researchers have investigated the autoimmune character of the disease mediated by the response of T cells against proteins of the myelin sheath.^{145,156,157} In other studies, a relation of MS and iron in MS plaques coming from extracellular hemoglobin has been discovered.^{158–160} Effects of a post-translational deimination of MBP C1 to MBP C8 have already been studied.^{35,121,147,161–164} This short list can in addition be expanded to include genetic approaches.¹⁶⁵ Changes in the biophysical properties of the myelin membrane are suggested as a key factor in the development of demyelinated diseases.¹⁶⁶ Thus, a better understanding of the binding of the MBP to the myelin lipids may lead to a more detailed picture of the processes causing the loss of myelination and to newer therapeutic strategies.

MBP as an intrinsically disordered protein (IDP) undergoes conformational changes from an extended conformation in aqueous solution into a self-assembled protein with elements of ordered secondary structure caused by the interaction with lipids.^{20,139,167} Thus, lipid monolayer adsorption experiments are a useful tool to investigate these interactions. Representing half of a bilayer,^{62,168} lipid monolayers at the air–water interface are useful model systems for investigating the specific interactions of proteins to a membrane.^{169,170} In monolayer adsorption measurements, the change in area per molecule or the surface pressure can be easily determined. Here, monolayer adsorption experiments and the analysis of the maximum insertion pressures (MIPs) of the protein adsorbed to monolayers formed by several lipid combinations reveal the importance of hydrophobic and especially electrostatic interactions leading to the high compaction of the myelin sheath. (The MIP represents the initial surface pressure above which no protein incorporation into the lipid monolayer occurs.) An MIP of 30 to 35 mN/m speaks of a well-incorporated protein. At smaller values, there is nearly no incorporation.¹⁷¹

In the following sections, the interaction of MBP and the major lipids of the cytoplasmic side of the oligodendrocyte membrane is investigated in detail by using monolayer methods. A better understanding of the molecular mechanisms of the MBP–lipid interactions may be helpful for obtaining deeper insights into the processes leading to the MS-related loss of myelin. For experimental details, see Section 5.2.

4.2 Interaction of bovine myelin basic protein with lipid monolayers

This section is already published in:

Widder et al. Interaction of myelin basic protein with myelin-like lipid monolayers at air–water interface. *Langmuir*, 34:6095–6108, 2018.

4.2.1 MBP–lipid interactions

Diverse previous studies of the interaction of MBP and lipid monolayers and bilayers by atomic force microscopy, surface pressure measurements, calorimetry, and scattering measurements^{119, 120, 137, 172} have revealed that the stability of the myelin sheath is maintained by a balance of the forces between the protein and the components of the myelin layer.¹⁶⁷ The myelin sheath loses its stable structure if this balance is disturbed by, for example, changes in the lipid composition. Many of these previous studies on the interaction of MBP and lipids have used model lipids like phosphatidylglycerol (PG),^{136, 137, 173} phosphatidic acid (PA),^{136, 137, 174} dipalmitoylphosphatidylserine (DPPS),^{172, 175} or dipalmitoylphosphatidylcholine (DPPC).¹⁷² However, interpretation of the results should be done with caution, especially in the case of PA or PG, for example, since these lipids are not relevant in the environment of MBP. Furthermore, most of the studies do not include the whole lipid composition of the cytoplasmic membrane leaflets, and it remains to ascertain how the separate components interact synergistically.

The following investigations shed further light on the role of each of the major single brain lipids found on the cytoplasmic side of the oligodendrocyte membrane, for the association of MBP to it. To elucidate this role, monolayer experiments were done of bovine MBP (bMBP) interacting with the whole lipid composition of the cytoplasmic side of the oligodendrocyte membrane (further referred to as ‘normal’ composition) and with the single lipids. Importantly, the negative image—the normal lipid composition of the myelin without the indicated lipid—was also evaluated. For example, in the case of cholesterol, additionally, the normal composition without cholesterol was investigated by adjusting the ratio of all other lipids to make them equal to what they would be in the normal composition. In situations of removal of highly represented lipids, like cholesterol or phosphatidylethanolamine (PE), the impact of negatively charged lipids increases. This approach enables to focus on their electrostatic interactions with positively charged MBP and their key role in facilitating MBP folding and membrane binding.¹⁴¹ By considering all lipids of the cytoplasmic leaflet of the myelin membrane systematically, the results of the monolayer adsorption measurements reveal more clearly the specific impact of every lipid in the natural environment of MBP on the lipid–protein interaction. MBP extracted from bovine brain contains different charge variants of MBP. Using bMBP allows to focus on the role of the single lipids leaving influences of the charge of MBP in this section aside.

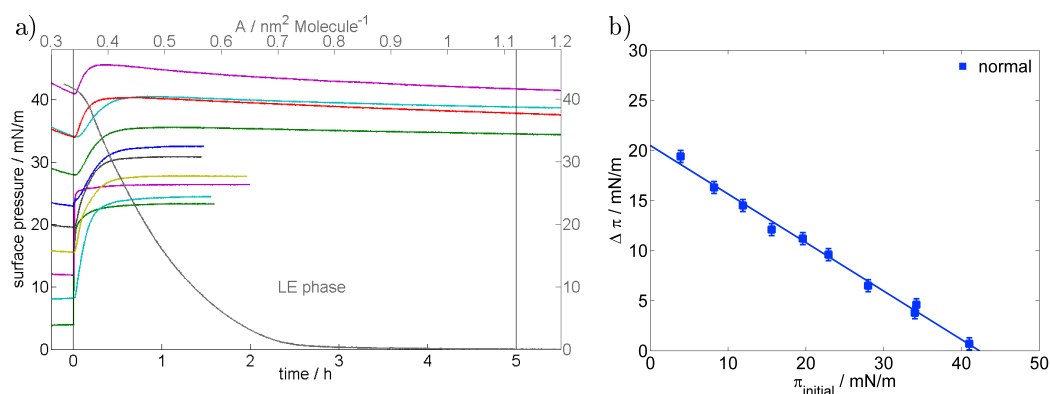


Figure 4.1: a) Time-dependent surface pressure of bMBP ($c = 100$ nM) injected at $t = 0$ h below a monolayer of constant surface area. The top scale refers to the surface pressure–area isotherm of the lipid monolayer at 20 °C (grey curve). b) Difference of surface pressure $\Delta\pi(\pi_{\text{ini}})$ after maximal 5 h of adsorption of bMBP ($c = 100$ nM) to lipid monolayers with a lipid composition similar to the cytoplasmic leaflet of the myelin sheath (cholesterol, PE, PS, PC, SM, and PI in a mole ratio of 44:27:13:11:3:2) at different initial surface pressures. Regression curve is included.

Subphase: 20 °C, 20 mM HEPES and 10 mM NaCl at pH 7.4.

4.2.2 Results and discussion

4.2.2.1 Monolayers of the normal myelin composition

To investigate the interaction of myelin basic protein with the myelin-like lipid monolayer, chloroform solutions of cholesterol, PE, PS, PC, SM, and PI were prepared in a mole ratio of 44:27:13:11:3:2 (further referred to as ‘normal’ composition). Thus, the lipid mixture consists of 56 % amphiphilic phospholipids and sphingomyelin and 44 % cholesterol. This composition corresponds to that of the cytoplasmic leaflet of the myelin sheath.^{176,177} Different amounts of lipid solution, spread onto the buffer surface, resulted in different initial surface pressures. Small π_{ini} up to 20 mN/m remain constant after several minutes. Higher π_{ini} are not constant even after the waiting time of 30 min, by which time the chloroform evaporates. It is possible that an ongoing reorientation of the unsaturated lipids results in a decreasing surface pressure of the film.

Injecting the protein–buffer solution below the monolayer leads to an increase of the surface pressure $\pi(t)$ depending on π_{ini} (Figure 4.1a). The increase of surface pressure results from the incorporation of bMBP into the lipid monolayer driven by hydrophobic interactions. If proteins or only parts of the proteins are incorporated into a monolayer, either they can be inserted into the lipid layer to interact with the acyl chain region or they can interact with the lipid headgroups and occupy space at the air–water interface.¹⁷⁸ In either case, the surface pressure increases at a constant total area. Higher initial surface pressures cause smaller increases in π than small π_{ini} because the monolayer is in a more condensed liquid-expanded (LE) state at higher pressures. It is interesting that after injecting the protein below a monolayer of a high π_{ini} , the surface pressure increases well above the collapse pressure (≈ 43 mN/m) and then decreases to a pressure

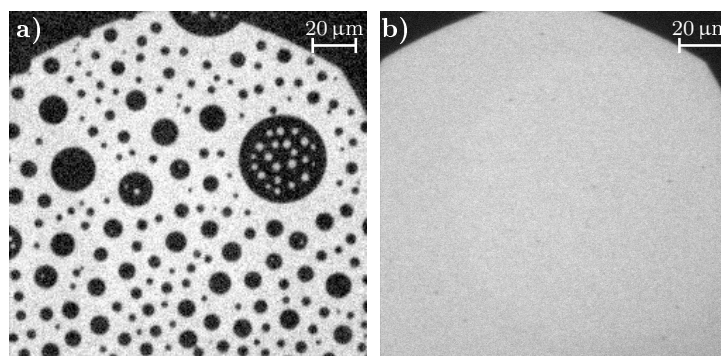


Figure 4.2: Fluorescence microscopy images of a monolayer composed of a) the normal composition and b) the normal composition without cholesterol at a pressure of ca. 5 mN/m. (The image of the normal composition without cholesterol has been recorded by Jennica Träger in the course of her Master’s thesis ‘Wechselwirkung zwischen divalenten Metallionen und basischem Myelin-Protein in Myelin-artigen Lipidmonoschichten’, Martin-Luther-Universität Halle Wittemberg, 2016, advised by the author of the present thesis.)
Lipid dye: 0.05 mol-% Rh-DHPE, subphase: 20 °C, 20 mM HEPES and 10 mM NaCl at pH 7.4.

region where the lipid film is stable. MBP seems to stabilise the myelin monolayer to prevent it from collapsing.

The change in surface pressure $\Delta\pi = \pi_{\text{end}} - \pi_{\text{ini}}$ as a function of π_{ini} shows a linear behaviour for this lipid composition (Figure 4.1 b). As mentioned before, the MIP of a protein or peptide well incorporated into the monolayer lies between 30 and 35 mN/m. The maximum insertion pressure of bMBP adsorbed to the normal myelin lipid monolayer amounts to 42.3 mN/m. This relatively high value well above a well-incorporated protein speaks for a strong interaction between bMBP and the myelin-like monolayer. As the surface pressure–molecular area curve shows, the monolayer is in the LE phase over all areas (Figure 4.1 a, grey curve).

A phase separation is visible in the results of epifluorescence microscopy (Figure 4.2 a). Defined, well-separated, domains are visible even at small surface pressures. McConnell et al.¹⁷⁹ previously described a phase separation of lipid mixtures of cholesterol and phospholipids. Here, taking this study into account, it is concluded that the monolayer phase separates in a dark cholesterol-rich phase and a bright phospholipid-rich phase. The multicomponent system of four phospholipids, sphingomyelin, and cholesterol thus behaves here as a pseudobinary system,¹⁸⁰ where the phospholipids are assumed to be homogeneously distributed between the cholesterol domains. Since the fluorescent dye (0.05 mol-% Rh-DHPE) is preferentially located in LE phases, the cholesterol-rich domains show darker regions because cholesterol inclines to the higher-ordered liquid-condensed (LC) phase behaviour. Indeed, the phase separation into cholesterol-rich and phospholipid-rich domains has already been reported for purified myelin from bovine spinal cord by Oliveira and Maggio¹⁸¹ and for lipid compositions similar to the white matter of marmosets by Min et al.,¹⁸² supporting the relevance of the here adopted experimental system.

If bMBP is adsorbed to the lipid monolayer of the normal composition, small grey regions are visible in the fluorescent microscopy images (blue arrows in Figure 4.3). As

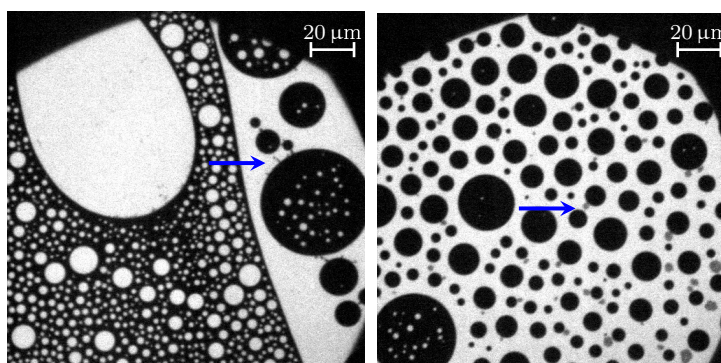


Figure 4.3: Fluorescence microscopy images of bMBP adsorbed to a monolayer composed of the normal composition at a pressure of ca. 5 mN/m. (The images have been recorded by Jennica Träger in the course of her Master’s thesis ‘Wechselwirkung zwischen divalenten Metallionen und basischem Myelin-Protein in Myelin-artigen Lipidmonoschichten’, Martin-Luther-Universität Halle Wittenberg, 2016, advised by the author of the present thesis.) The blue arrows highlight small regions arising from the adsorption of bMBP to the myelin-like monolayer.

Lipid dye: 0.05 mol-% Rh-DHPE, subphase: 20 °C, 20 mM HEPES and 10 mM NaCl at pH 7.4.

these regions did not occur in the monolayer without adsorbed protein, they must represent the MBP incorporated into the lipid film. Remarkably, bMBP is mostly visible in the phospholipid-rich domain near the cholesterol-rich phase. DeBruin and Harauz suggested the localisation of MBP at the boundary of the cholesterol-rich domains¹⁸³ and the here shown data provide direct experimental evidence for this conjecture. It is possible that MBP is also incorporated into cholesterol-rich phases, but this cannot be detected with the approach used here, and this event is not considered to be likely.

4.2.2.2 Various combinations of brain lipids of the myelin-like monolayers

Adsorption experiments of bMBP to a monolayer of the respective brain lipid and of the normal composition without this specific lipid by keeping the ratio of all other lipids constant (the ‘negative’ scenario; for lipid ratios, see Table 5.1) were performed to investigate the specific role of each lipid, by observing the effect of the protein on the physical state of every lipid during its incorporation into the monolayer. Table 4.2 shows the determined maximum insertion pressures (MIPs). The difference in surface pressure $\Delta\pi(\pi_{\text{ini}})$ as a function of the initial pressure π_{ini} is shown for PE and PS in Figure 4.4 and for cholesterol, PC, SM, and PI and the normal composition without the respective lipids in Figure B.1. For $\pi(t)$ diagrams, see Figure B.2.

In the following, the series of experiments with the individual lipids are described.

Cholesterol (Chol) The most abundant lipid in the cytoplasmic leaflet of the myelin sheath is slightly amphiphilic due to a single OH group and is known to modulate the fluidity of

Table 4.2: Maximum insertion pressures for binding of bMBP to the different brain lipids of myelin. Compared are the values of monolayers of the several lipids alone, the normal composition, and the normal composition without the respective lipid. In the case of PS, PI, and the mixture without PE, the given value is the apparent maximum insertion pressure MIP_{app} as the $\Delta\pi(\pi_{ini})$ behaviour is not linear.

Monolayer	MIP in mN/m					
	Chol	PE	PS	PC	SM	PI
Lipid alone	35.9	36.5	41.8 [#]	26.0	19.5	36.6 [#]
	± 1.1	± 1.3	± 2.5	± 1.2	± 1.0	± 3.9
Normal	42.3					
	± 1.4					
Without indicated lipid	54.9	41.8 [#]	32.6 [*]	45.6	47.3	32.6 [*]
	± 1.9	± 3.7	± 1.9	± 1.4	± 1.6	± 1.9

* without PS and PI

MIP_{app}

membranes because its planar nature allows it to intercalate between fatty acyl chains. Molecules with small polar groups, like cholesterol, have reduced degrees of freedom and tend to be in a condensed phase on their own.¹⁸⁴ This statement is supported by the surface pressure–area isotherms obtained here, which for cholesterol monolayers shows a direct transition from the gas-analogue state into the liquid-condensed (LC) phase (Figure B.1).

For cholesterol, the change in surface pressure $\Delta\pi(\pi_{ini})$ relative to π_{ini} shows a linear decreasing curve. The same applies for the adsorption of bMBP to a monolayer of the normal composition without cholesterol. The MIP of bMBP injected below a cholesterol monolayer is in the range of a well-incorporated protein: 35.9 mN/m. If the normal composition without cholesterol is determined, the MIP of 54.9 mN/m is even higher than that for the normal lipid composition. Comparing the MIPs, it is assumed that cholesterol slightly impedes the incorporation of the protein into the myelin monolayer.

Analysing the phase behaviour of the mix without cholesterol with epifluorescence microscopy reveals that cholesterol leads to the occurrence of cholesterol-rich and phospholipid-rich phases, as already assumed above. Without cholesterol, the lipid monolayer is nearly homogeneous (Figure 4.2 b).

Phosphatidylcholine (PC) With its cylindrical shape, PC is ideally suited to serve as the bulk structural element of eukaryotic biological membranes. Previous measurements on dipalmitoylphosphatidylcholine (DPPC) monolayers¹⁷⁵ and vesicles of PC^{117, 185, 186} indicated no significant interaction between MBP and PC. Some earlier studies, however, suggested a weak interaction, i.e., a non-negligible one so the point might simply represent differences in semantics.^{187, 188}

Injecting bMBP below a brain PC monolayer causes only small increases of surface pres-

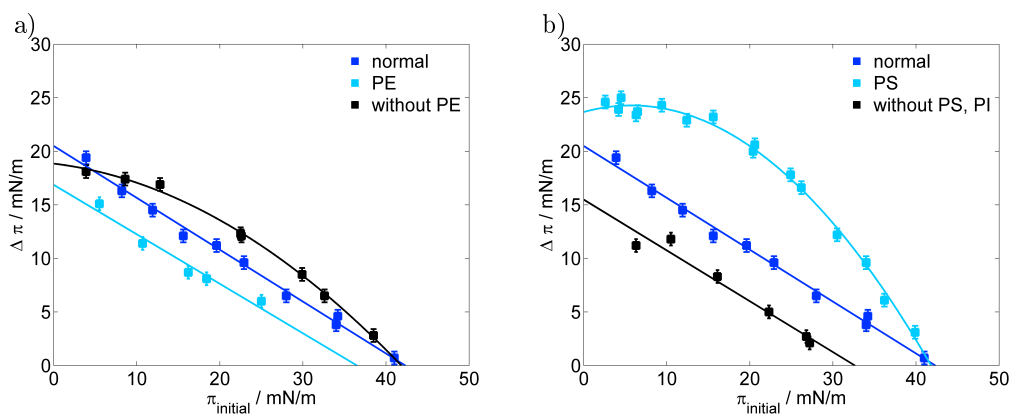


Figure 4.4: Difference of surface pressure $\Delta\pi(\pi_{\text{ini}})$ after maximal 5 h of adsorption of bMBP ($c = 100 \text{ nM}$) to lipid monolayers as a function of the initial surface pressure π_{ini} . a) Normal composition, only PE and the normal composition without PE with all other lipids in the same ratio as in the normal composition. b) Normal composition, only PS and the normal composition without PS with all other lipids in the same ratio as in the normal composition. Regression curves are included.

Subphase: 20°C , 20 mM HEPES and 10 mM NaCl at pH 7.4.

sure. The $\Delta\pi(\pi_{\text{ini}})$ curve shows a linear behaviour with an MIP of 26.0 mN/m , which is similar to the MIP of the model lipid DPPC of 27 mN/m measured by Polverini et al.¹⁷⁵ This relatively low pressure indicates a very low affinity of bMBP for the headgroup of PC. Since the incorporation of bMBP into the lipid monolayer without PC results in a higher MIP (45.6 mN/m) than in the case of the normal myelin composition, it can be concluded that PC reduces the maximum insertion pressure of bMBP incorporated into the monolayer.

Sphingomyelin (SM) SM and cholesterol have a high affinity for each other via van der Waals interaction. They are usually thought to be located together in the so-called lipid rafts.¹⁸⁹

Since SM has the same headgroup as PC, the adsorption behaviour of bMBP to an SM monolayer is similar to that of a PC monolayer. The small MIP of 19.5 mN/m highlights the poor affinity of bMBP to interact with the headgroup of PC and SM. But due to its interaction with cholesterol, it can be assumed that sphingomyelin plays a role in the formation of lipid domains in myelin.¹⁹⁰ Compared to the MIP of bMBP adsorbed to the normal composition, the MIP for a monolayer of the normal composition without SM is slightly higher. This will be further investigated and discussed in Section 4.3.

Phosphatidylethanolamine (PE) In membranes, PE modulates the curvature due to its small headgroup and the resulting cone shape of the lipid. At very high pH, it is mostly deprotonated, whereas 99 % of PE molecules (due to a pK_a of 9.6^{191}) are in the protonated form at a pH of 7.4 used in this study.

The $\Delta\pi(\pi_{\text{ini}})$ linearly decreasing dependence of the adsorption of bMBP to a PE monolayer has a zero crossing at 36.5 mN/m , indicating good protein incorporation (Figure 4.4). In contrast to this result, though poor penetration of MBP into PE monolayers

or vesicles has been reported in the literature.^{117,192} Here, it is postulated that the high MIP arises from the polar interaction of the MBP with the lipid headgroups rather than from a hydrophobic interaction with the acyl chains.^{117,137} For a schematic depiction, see Figure 4.5 b(II).

Intriguingly, the change in surface pressure is not in a linear relation to the initial surface pressure if the normal lipid composition without PE is examined (Figure 4.4 a). For small π_{ini} up to ≈ 15 mN/m, the $\Delta\pi(\pi_{\text{ini}})$ is roughly constant. If π_{ini} is higher than 20 mN/m, then $\Delta\pi(\pi_{\text{ini}})$ decreases more sharply than in the case of the normal monolayer. Fitting the experimental data with the quadratic curve $\Delta\pi(\pi_{\text{ini}}) = c + d \cdot \pi_{\text{ini}} - e \cdot \pi_{\text{ini}}^2$ is a helpful and well-suited tool to characterise and compare the nonlinear behaviour of different lipid compositions, and a quadratic regression matches well with the experimental data of the adsorption to the monolayer without PE yielding a quadratic term of $e = 0.0085$ m/NM. Since the maximum insertion pressure is defined for linear $\Delta\pi(\pi_{\text{ini}})$ graphs, the zero of the quadratic function may not represent the true MIP per se. Hence, the value of 41.8 mN/m should be described as the apparent maximum insertion pressure MIP_{app} . The real initial pressure, at which no incorporation occurs any more, should be higher. Taking this into account, it can be stated that PE slightly lowers the MIP of bMBP adsorbing to the myelin monolayer. The reasons leading to the nonlinear behaviour of $\Delta\pi(\pi_{\text{ini}})$ are explained further in the next paragraph.

Phosphatidylserine (PS) PS is the most abundant anionic phospholipid in the cytoplasmic leaflet of the myelin sheath and therefore makes the biggest contribution to nonspecific electrostatic interactions in the membrane.

The adsorption of bMBP to a PS monolayer leads to a high increase in surface pressure, which is approximately constant with ≈ 23.9 mN/m up to an initial surface pressure of 15.6 mN/m. After this plateau phase, $\Delta\pi$ decreases steeply with increasing π_{ini} (Figure 4.4 b). In accordance with former studies on the interaction of MBP with monolayers of the negatively charged model lipids dipalmitoylphosphatidylserine (DPPE)¹⁷⁵ and dipalmitoylphosphatidylglycerol (DPPG)¹⁷³ and with vesicles composed of negatively charged lipids like PS, dimyristoylphosphatidic acid (DMPA), and DPPG,¹³⁶ two counteracting processes lead to this special behaviour of the change in surface pressure:

- i) protein incorporation driven by hydrophobic interactions leading to an increase of the surface pressure π and
- ii) lipid condensation due to electrostatic interactions leading to a decrease of π ,

where i) predominates over the measured range of π_{ini} leading to a positive surface pressure.

Native MBP in its most abundant isoform has a net positive charge of +19 (at pH 7) due to its abundance of positively charged arginine and lysine residues. The electrostatic interactions between these residues of the cationic protein and the negatively charged headgroups of PS result in a shielding of the negative charges and a concomitant reduction of the repulsive forces between the PS molecules. As a consequence, the area occupied by the lipid molecules is reduced because there is better acyl chain packing (Figure 4.5 a). It is known that MBP adopts α -helical structures during hydrophobic interaction with the myelin membrane^{113,140,141} (shown in a simplified illustration in Figure 4.5). The incorporation of the protein, or even parts of the protein (particularly the three amphipathic α -helices), in opposition, disturbs the order of the acyl chains and

leads to an increasing surface pressure.

Epifluorescence microscopy shows small grey regions in the mostly homogeneous lipid film of PS upon adsorption of bMBP (Figure B.3), interpreted to be regions of higher order than the LE phase of PS alone. Apparently, these dark regions represent lipid condensed parts of the PS film induced (as only observed when bMBP is present) by protein–PS interactions.

A deviation from the linear behaviour of $\Delta\pi(\pi_{\text{ini}})$, if positively charged peptides are adsorbed to negatively charged monolayers, has already been observed before.^{193–196} A separate analysis of the kinetics of the two superimposed processes, as described by Hädicke and Blume¹⁹⁵ is not applicable here for the time-dependent change of the surface pressure if bMBP is adsorbed to charged monolayers. Both processes proceed with similar time constants and cannot be separated in the time-dependent surface pressure graphs (Figure B.2).

The definition of the MIP, described above, cannot be applied for the binding of bMBP to PS monolayers. Since the increasing and the decreasing parts of the $\pi(t)$ curves cannot be separated, it cannot be detected if the condensing process occurs over the whole range of π_{ini} . Thus, it is not possible to ascertain whether the value of $\Delta\pi(\pi_{\text{ini}}) = 0$ mN/m describes the maximum pressure of insertion or the superposition pressure. At this point, the contributions of the protein incorporation and the lipid condensation are in an equilibrium. The real maximum insertion pressure could be higher. Again, that is why, π_{ini} of $\Delta\pi(\pi_{\text{ini}}) = 0$ mN/m is here called ‘apparent maximum insertion pressure’ MIP_{app}. Compared to an MIP of 32.6 mN/m for the lipid composition without the charged lipids PS and PI, PS increases the MIP of the myelin monolayer significantly, speaking for a better incorporation of bMBP into the monolayer.

Phosphatidylinositol (PI) PI is another negatively charged lipid of the myelin. With PI, the ratio of negatively charged lipids to neutral lipids can be modified by phosphorylation of PI to PIP or PIP₂.¹⁹⁷

The interaction of bMBP with a pure PI monolayer results in a high increase of the surface pressure. The $\Delta\pi(\pi_{\text{ini}})$ curve of bMBP adsorbed to PI (Figure B.1) shows a similar behaviour to the adsorption to PS. At small π_{ini} up to 13.8 mN/m, the change in surface pressure is nearly independent of the initial pressure with a value of ≈ 25.7 mN/m. A steep decrease of $\Delta\pi(\pi_{\text{ini}})$ is observed for higher π_{ini} . The nonlinear $\Delta\pi(\pi_{\text{ini}})$ curve of PI is attributed to the same processes as in the case of PS: the surface pressure $\pi(t)$ is a superposition of protein incorporation and lipid condensation as a result of electrostatic interaction between positively charged MBP and negatively charged PI molecules. The former process leads to an increase of surface pressure, and the latter to a decrease. Both effects apparently occur with the same time constant. Therefore, the maximum insertion pressure cannot be determined reliably and the value $\pi_{\text{ini}} = 36.6$ mN/m of $\Delta\pi(\pi_{\text{ini}}) = 0$ mN/m is only an apparent MIP.

Again, a suitable regression curve of the $\Delta\pi(\pi_{\text{ini}})$ graph is a quadratic fit with the downward opened function $\Delta\pi(\pi_{\text{ini}}) = c + d \cdot \pi_{\text{ini}} - e \cdot \pi_{\text{ini}}^2$. The quadratic term e can then be used for the characterisation and comparison of the quadratic course of the curve and of the electrostatic interaction. The higher the value of e , the higher is the deviation from a linear function. The $\Delta\pi(\pi_{\text{ini}})$ is linear if e is close to 0 m/mN, in consideration of the error Δe . The change in surface pressure as a function of the initial surface pressure of bMBP injected below a PI monolayer yields a quadratic term of 0.0285 m/mN (Table 4.3). In

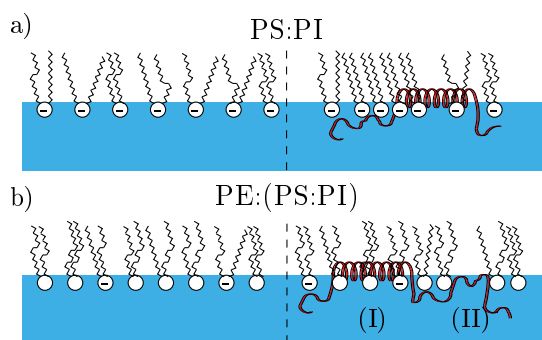


Figure 4.5: Schematic depiction of the adsorption of MBP to a lipid monolayer of a) the charged lipids PS and PI and b) the lipid mixture PE:(PS:PI) at the air–water interface before the injection of MBP below the monolayer (left) and a few hours after injection of MBP below the monolayer (right). In b) the two possibilities of protein incorporation are sketched: (I) parts of the protein interact with the acyl chain region, (II) parts of the protein interact with the lipid headgroups of PE at the air–water interface. The depiction of the protein and lipids is simplified.

the the case of PS, e amounts to 0.0187 m/mN. The higher quadratic term of the PI monolayer measurements implies a higher slope of $\Delta\pi(\pi_{\text{ini}})$ at higher π_{ini} indicating a stronger electrostatic attraction between bMBP and PI than between bMBP and PS.

In monolayers without the charged lipids PS and PI, the MIP of bMBP is in the range of a well-incorporated protein. Thus, with PS and PI present in the monolayer, the electrostatic interactions increase the maximum insertion pressure of bMBP to a myelin-like monolayer.

4.2.2.3 Electrostatic interaction

Change of surface pressure

These investigations of the adsorption of MBP to the lipids of the cytoplasmic monolayer of the myelin sheath showed a special adsorption behaviour of charged lipids (PS and PI), as sketched in Figure 4.5 a. Due to a superposition of protein incorporation into the monolayer and lipid condensation as a result of electrostatic interaction, the change of surface pressure does not decrease linearly with increasing initial surface pressures, as observed for uncharged lipid films. The nonlinear behaviour of the $\Delta\pi(\pi_{\text{ini}})$ graphs of MBP adsorbed to PS and PI monolayers is also present if the normal composition is used but without the neutral lipid PE. It is possible to ascribe this fact to a higher amount of negatively charged lipids in the composition without PE (21 % of PS and PI together) compared to the normal lipid composition (15 % of PS and PI). However, the lipid composition without cholesterol, which has an even higher proportion of negative charges (27 % of PS and PI), shows the same linear $\Delta\pi(\pi_{\text{ini}})$ behaviour as with uncharged monolayers (Table 4.3). One may assume that PE shields the electrostatic attraction between negatively charged lipids and the positively charged protein. This assumption was tested with different lipid compositions of cholesterol, PE, PC, PS, and PI with different ratios of uncharged to charged lipids. The ratio of PS to PI was in all cases the same

as in the natural composition (13:2). The same applies for the ratio of cholesterol to PE (44:27). PC was used to test the ‘anti-nonlinear’ role of PE. Therefore, in compositions with cholesterol and PC, their ratio was equal to that of cholesterol to PE in the normal composition (44:27). For detailed information about the composition of the lipid mixtures, see Table 5.2.

Tables 4.3 and 4.4 summarise the quadratic terms and apparent maximum insertion pressures of the adsorption of bMBP to all tested lipid compositions relevant for electrostatic analysis. For $\Delta\pi(\pi_{\text{ini}})$ and $pi(t)$ diagrams, see Figures B.4 and B.5.

Chol:(PS:PI) Due to the domain-building effect of cholesterol to the brain lipids of the myelin sheath, its effect on the nonlinear behaviour of negatively charged monolayers was tested with different ratios of cholesterol to PS and PI.

As can be seen in Table 4.3, higher amounts of cholesterol lower the quadratic term e . A mere mixture of PS and PI exhibits a nonlinear $\Delta\pi(\pi_{\text{ini}})$ behaviour with an e of 0.0209 m/mN, which decreases to 0.0092 m/mN if cholesterol and the negatively charged lipids are in an equal amount. Even a lipid composition with 80 % cholesterol shows clearly a quadratic $\Delta\pi(\pi_{\text{ini}})$ curve. Thus, cholesterol seems to have only a small effect on the electrostatic interactions between protein and lipid monolayer, which possibly relies on the smaller amount of negatively charged lipids at a high percentage of cholesterol.

PE:(PS:PI) As discussed above, the nonlinear $\Delta\pi(\pi_{\text{ini}})$ graph of bMBP adsorbed to the monolayer of normal myelin composition without PE suggests a shielding of the electrostatic attraction between the positively charged protein and the negative charges of PS and PI.

An increasing lipid content of PE results in a decrease of the quadratic term e coming close to zero and a concomitant decreasing influence of lipid condensation on $\Delta\pi(\pi_{\text{ini}})$. Spreading a lipid mixture of PE, PS, and PI in a ratio of 50:50 (uncharged to charged lipids) on the buffer surface and injecting bMBP below the monolayer show with a quadratic term of 0.0087 m/mN a similar $\Delta\pi(\pi_{\text{ini}})$ behaviour to the 50:50 mixture of cholesterol with PS and PI. But higher amounts of PE show a stronger effect on the curve shape. Although the function of the change in surface pressure is only slightly quadratic with $e = 0.0055$ m/mN for the 65:35 mixture of PE:(PS:PI), it is linear if the content of PE is 80 %. Consequently, the influence of PE on the quadratic behaviour of $\Delta\pi(\pi_{\text{ini}})$ is higher than that of cholesterol.

(Chol:PE):(PS:PI) Replacing parts of PE by cholesterol gaining the same ratio of cholesterol to PE as in the normal composition slightly lowers the shielding effect of PE. The quadratic term is significantly higher if the amount of cholesterol and PE is 80 %. This composition leads to a change in surface pressure that still shows a nonlinear dependence on the initial surface pressure. Without cholesterol and with the same amount of negatively charged lipids, the graph was already linear at this point.

PC:(PS:PI) To test a possible influence on the lipid condensing process of a phospholipid with an unattractive headgroup for the adsorption of bMBP, different proportions of the uncharged PC and charged lipids PS and PI were investigated.

As previously observed for lipid compositions of PE, PS, and PI, a decreasing amount of charged lipids results in an decrease of the quadratic term e . The same relation was found

Table 4.3: Quadratic terms e of the quadratic regression $\Delta\pi(\pi_{\text{ini}}) = c + d \cdot \pi_{\text{ini}} - e \cdot \pi_{\text{ini}}^2$ of different mole ratios of the lipid mixtures $(x):(y)$ tested for electrostatic investigations, with x referring to uncharged lipids and y to charged lipids. In the case of $(e \pm \Delta e) \geq 0$ m/mN, $\Delta\pi(\pi_{\text{ini}})$ can be assumed as linear. The values with linear behaviour $\Delta\pi(\pi_{\text{ini}})$ are written in blue. For detailed composition of lipid mixtures, see Table 5.2.

Monolayer (x):(y)	e in m/mN					
	0:100	20:80	50:50	65:35	80:20	100:0
Chol:(PS:PI)	0.0209 ± 0.0028	-	0.0092 ± 0.0014	-	0.0071 ± 0.0019	0
PE:(PS:PI)	0.0209 ± 0.0028	0.0164 ± 0.0010	0.0087 ± 0.0016	0.0055 ± 0.0013	0.0012 ± 0.0029	0
(Chol:PE): (PS:PI)	0.0209 ± 0.0028	0.0166 ± 0.0014	0.0099 ± 0.0009	0.0050 ± 0.0010	0.0050 ± 0.0019	0
PC:(PS:PI)	0.0209 ± 0.0028	0.0143 ± 0.0013	0.0040 ± 0.0014	-	-0.0003 ± 0.0010	0
(Chol:PC): (PS:PI)	0.0209 ± 0.0028	-	0.0091 ± 0.0023	-0.0003 ± 0.0010	0.0008 ± 0.0017	0
PS	0.0187 ± 0.0013					
PI	0.0285 ± 0.0037					
(Chol:PC:SM): (PS:PI)*					0.0085 ± 0.0012	
(PE:PC:SM): (PS:PI)#				0		
(Chol:PE:PC:SM): (PS:PI)‡					0	

* normal composition without PE (79:21)

normal composition without cholesterol (73:27)

‡ normal composition (85:15)

Table 4.4: Apparent maximum insertion pressures MIP_{app} of different mole ratios of the lipid mixtures $(x):(y)$ tested for electrostatic investigations, with x referring to uncharged lipids and y to charged lipids. In the case of $(e \pm \Delta e) \geq 0 \text{ m/mN}$ (Table 4.3), $\Delta\pi(\pi_{\text{ini}})$ can be assumed as linear and the given MIP (written in blue) is obtained from linear regression. For detailed composition of lipid mixtures, see Table 5.2.

Monolayer $(x):(y)$	MIP_{app} in mN/m					
	0:100	20:80	50:50	65:35	80:20	100:0
Chol:(PS:PI)	40.3 ± 4.7	-	45.6 ± 4.2	-	41.9 ± 5.6	35.9 ± 1.1
PE:(PS:PI)	40.3 ± 4.7	42.1 ± 2.0	45.9 ± 5.3	45.9 ± 5.4	44.2 ± 1.5	36.5 ± 1.3
(Chol:PE): (PS:PI)	40.3 ± 4.7	42.1 ± 2.9	45.6 ± 2.6	48.8 ± 4.5	43.5 ± 7.8	36.2 ± 1.2
PC:(PS:PI)	40.3 ± 4.7	42.5 ± 3.0	45.9 ± 6.5	-	45.1 ± 1.7	26.0 ± 1.2
(Chol:PC): (PS:PI)	40.3 ± 4.7	-	44.5 ± 7.0	47.8 ± 1.3	43.6 ± 1.3	29.4 ± 0.9
PS	41.8 ± 2.5					
PI	36.6 ± 3.9					
(Chol:PC:SM): (PS:PI)*					41.8 ± 3.7	
(PE:PC:SM): (PS:PI) [‡]				54.9 ± 1.9		
(Chol:PE:PC:SM): (PS:PI) [‡]					42.3 ± 1.4	

* normal composition without PE (79:21)

[‡] normal composition without cholesterol (73:27)

[‡] normal composition (85:15)

for the lipid mixtures of PC, PS, and PI, albeit not to the same extent. The effect of PC on the nonlinear behaviour of $\Delta\pi(\pi_{\text{ini}})$ is significantly higher than of PE and cholesterol. This trend already delineates at a composition of PC to the charged lipids of 20:80 and is clearly visible at the ratio of 50:50. An equal amount of uncharged and charged lipids results, in the case of PC as an uncharged phospholipid, in a nearly linear $\Delta\pi(\pi_{\text{ini}})$ function. The higher impact of PC on the quadratic behaviour of $\Delta\pi(\pi_{\text{ini}})$ compared to PE results partly from a small amount of protonated PE molecules. At pH 7.4, only 99% of PE molecules are deprotonated, whereas PC is deprotonated completely. But this small fraction of protonated PE shifts the uncharged to charged ratios only slightly to higher contents of charged lipids. A bigger impact could result from the fact that PC's headgroup is larger than the headgroup of PE, leading to a greater overall area of uncharged lipids at the air-water interface in the case of PC.

(Chol:PC):(PS:PI) The effect of cholesterol on the curve behaviour of the change in surface pressure is consistent for lipid mixtures with PC and for lipid mixtures with PE. The addition of cholesterol lowers the 'anti-nonlinear' effect of PC, especially if uncharged and charged lipids are in balance. At a ratio of 50:50, the change in surface pressure is still a quadratic function of the initial surface pressure. Nevertheless, if the content of PS and PI only amounts to 20%, cholesterol does not prevent the linear behaviour of $\Delta\pi(\pi_{\text{ini}})$.

Combining these results with the findings of the individual lipids and the normal composition without the respective lipid gives deeper insights into the specific roles of the brain lipids that constitute myelin. The normal composition without cholesterol with a ratio of uncharged to charged lipids of 73:27, shows a linear $\Delta\pi(\pi_{\text{ini}})$ curve. This observation is in accordance with the results of the adsorption measurements with PC:(PS:PI) and PE:(PS:PI), for which quadratic regression of $\Delta\pi(\pi_{\text{ini}})$ yielded quadratic terms e near 0 m/mN. It becomes apparent that SM, if cholesterol is lacking, does not influence the shielding impact of PE and PC on the lipid condensation process resulting from electrostatic interaction between the spread lipids and the adsorbed protein. The quadratic behaviour of the change in surface pressure after injecting bMBP below the normal lipid composition without PE results from the small content of PC in contrast to a comparatively high cholesterol content. The ratio of uncharged to charged lipids in the normal mix without PE is 79:21, the quadratic factor of which is 0.0085 m/mN, a value slightly higher than that of the 80:20 mixture of Chol:(PS:PI). Probably, the high affinity of SM to cholesterol, thereby building more condensed lipid domains, leads here to a lowered shielding of the electrostatic interactions by uncharged lipids and a concomitant higher deviation of a linear relationship between the change in surface pressure and initial surface pressure during adsorption of bMBP to a monolayer of the normal myelin composition without PE.

The linear $\Delta\pi(\pi_{\text{ini}})$ curve of the adsorption of bMBP to the normal lipid composition fits well into these considerations. The content of PS and PI of 15% is insufficient to cause a quadratic dependency between $\Delta\pi$ and π_{ini} . The shielding effect of PE and PC is strong enough to be not abolished by the domains built by cholesterol. As shown above, PC has a stronger impact than PE on suppressing the lipid condensation resulting from electrostatic interaction with the protein. But this effect is compensated by a higher amount of PE in the myelin monolayer. So the anti-nonlinear effect is a collaboration of PE and PC.

Taking a look at the maximum insertion pressures of the examined lipid compositions with and without charged lipids (Table 4.4), it becomes apparent that even small amounts of PS and PI result in an increased incorporation of bMBP into the monolayer indicated by higher MIPs. In the case of PE, the MIP increases from 36.5 mN/m to 44.2 mN/m if 20 % PS and PI are added. This increase in protein incorporation is exceeded by adding the same content of charged lipids to PC. Due to weak interactions between bMBP and the headgroup of PC, the adsorption measurements revealed an MIP of 26.0 mN/m. But even a small amount of PS and PI (20 %) raised the MIP to 45.1 mN/m. Hence, the negatively charged lipids foster the hydrophobic interaction of MBP and the acyl chains of the uncharged lipids PC and PE, with which MBP interacts only barely or just via polar interaction with the lipid headgroup (schematically depicted in Figure 4.5 b). It is not possible to assess a trend of the MIP over the course of increasing content of charged lipids since the real MIP could not be calculated for the change in surface pressure being a nonlinear function of the initial surface pressure. Nonetheless, the apparent maximum insertion pressures convey an impression of values in the region of the MIP of the normal composition and possibly higher. The myelin basic protein shows a strong selectivity of interaction with PI and PS, which is the major anionic lipid component of the myelin sheath. A visual electron microscopic demonstration of MBP forming higher-order assemblies on monolayers comprising PS or PI was previously published by Ishiyama et al.¹⁶²

The area related distances in subphase (TARDIS)

The results of different compositions of PC and PE with the charged myelin lipids PS and PI led to the supposition that the bigger headgroup of PC results in a higher anti-quadratic effect than the smaller headgroup of PE, which should be verifiable by the area–surface pressure isotherms of these lipid compositions.

The area–surface pressure graph reveals the mean area that every molecule occupies at the air–water interface at a certain pressure. Assuming that the phospholipids of the PE:(PS:PI) and PC:(PS:PI) mixtures are homogeneously distributed and that a lipid molecule occupies a square area, it is possible to calculate the mean distance between charged lipids depending on the surface pressure as the square root of the area per molecule. The area–surface pressure isotherms of all PE:(PS:PI) and PC:(PS:PI) compositions were measured, as well as of PS:PI and PE, PC, PS, and PI alone. The distances derived from the measured isotherms of the lipid mixes are compared to the calculated distances of the isotherms of the specific mixture by the weighted average of the several lipids. The distances of charges $s^-(\pi)$ in the PE:(PS:PI) mixes are calculated in three ways:

$$s_{\text{PE:(PS:PI)}}^-(\pi) = \frac{s_{\text{PE:(PS:PI)}}(\pi)}{n_{\text{PS}} + n_{\text{PI}}} \quad (4.1)$$

$$s_{\text{PE+(PS:PI)}}^-(\pi) = \frac{n_{\text{PE}} s_{\text{PE}}(\pi) + (n_{\text{PS}} + n_{\text{PI}}) s_{\text{PS:PI}}(\pi)}{n_{\text{PS}} + n_{\text{PI}}} \quad (4.2)$$

$$s_{\text{PE+PS+PI}}^-(\pi) = \frac{n_{\text{PE}} s_{\text{PE}}(\pi) + n_{\text{PS}} s_{\text{PS}}(\pi) + n_{\text{PI}} s_{\text{PI}}(\pi)}{n_{\text{PS}} + n_{\text{PI}}}, \quad (4.3)$$

where s_x represents the distance between two lipids in the lipid film x and n_x is the mole fraction of the respective lipid in the mixture. Equation 4.1 calculates the charge distance

from the measured area–surface pressure isotherm of the lipid mixtures PE:(PS:PI) (in Figure B.7 referred to as ‘measured’, symbol: +). With Equation 4.2, the charge distance is calculated by the weighted addition of the surface pressure-dependent area of a PE monolayer and a monolayer of the (PS:PI) mixture (in Figure B.7 referred to as ‘PE+PSPI’, symbol: ∇). By weighing the area of a PE, a PS, and a PI monolayer with the respective mole ratios, the charge distance is calculated by Equation 4.3 (in Figure B.7 referred to as ‘PE+PS+PI’, symbol: o). The same equations apply for the PC:(PS:PI) compositions. The small deviations of the $s^-(\pi)$ graphs from each other indicate a homogeneous distribution of the lipids, and a similar behaviour of the lipids alone and in a mixture of different phospholipids. The graphs of $s^-(\pi)$ derived with Equations (4.1)–(4.3) are compared in Figure B.7. Since they show no big differences (except slightly bigger differences in the case of a ratio of 80:20), Figure 4.6 shows only the graphs of Equation 4.1 for the sake of clarity.

As can be seen in Figure 4.6, a higher amount of uncharged lipids in the PE:(PS:PI) and PC:(PS:PI) mixes lead to bigger distances between charged lipids. These bigger distances are reflected in the bigger quadratic terms e of the nonlinear $\Delta\pi(\pi_{\text{ini}})$ graphs. Analogous to Equations (4.1)–(4.3), the distances between charged lipids in the (Chol:PE):(PS:PI) mixtures were calculated with:

$$s_{(\text{Chol:PE}):(\text{PS:PI})}^-(\pi) = \frac{s_{(\text{Chol:PE}):(\text{PS:PI})}(\pi)}{n_{\text{PS}} + n_{\text{PI}}} \quad (4.4)$$

$$s_{(\text{Chol:PE})+(\text{PS:PI})}^-(\pi) = \frac{(n_{\text{Chol}} + n_{\text{PE}}) s_{\text{Chol:PE}}(\pi) + (n_{\text{PS}} + n_{\text{PI}}) s_{\text{PS:PI}}(\pi)}{n_{\text{PS}} + n_{\text{PI}}} \quad (4.5)$$

$$s_{\text{Chol+PE+PS+PI}}^-(\pi) = \frac{n_{\text{Chol}} s_{\text{Chol}}(\pi) + n_{\text{PE}} s_{\text{PE}}(\pi) + n_{\text{PS}} s_{\text{PS}}(\pi) + n_{\text{PI}} s_{\text{PI}}(\pi)}{n_{\text{PS}} + n_{\text{PI}}} \quad (4.6)$$

and similarly for (Chol:PC):(PS:PI).

In these compositions, the distance of the charged lipids outside the cholesterol-rich domains is pivotal for the nonlinear $\Delta\pi(\pi_{\text{ini}})$ behaviour. But the calculation of the distance between charges from the area–surface pressure isotherms is error-prone due to the domain building caused by cholesterol. Equations (4.4)–(4.6) require that the cholesterol-rich domains include no phospholipids. However, the cholesterol-rich phase also includes, for example, PS¹⁸¹ and saturated lipids.¹⁸² It is not known how many phospholipid molecules are located in the cholesterol-rich phase and how many cholesterol molecules the phospholipid-rich phase contains. This uncertainty is reflected in the large deviations of the $s^-(\pi)$ graphs (Figure B.9) calculated with Equations (4.4)–(4.6). But a trend can be read from the charge distances of (Chol:PE):(PS:PI) compared to those of PE:(PS:PI) (Figure B.10) and (Chol:PC):(PS:PI) compared to those of PC:(PS:PI) (Figure B.11). As already assumed, the charged lipid molecules experience a reduced accessible area since parts of the water surface are occupied by the cholesterol-rich domains. This leads to higher values of the quadratic term e for compositions with cholesterol, compared to compositions without cholesterol with the same ratio of uncharged to charged lipids.

Since PC has the larger headgroup, its quadratic terms are closer to zero than for the same amount of PE and thus greater distances between charged lipids were expected for the mixtures containing PC. This effect is reflected in the mean distance between the lipids in monolayers of PE and PC (Figure B.6). There is a larger distance between

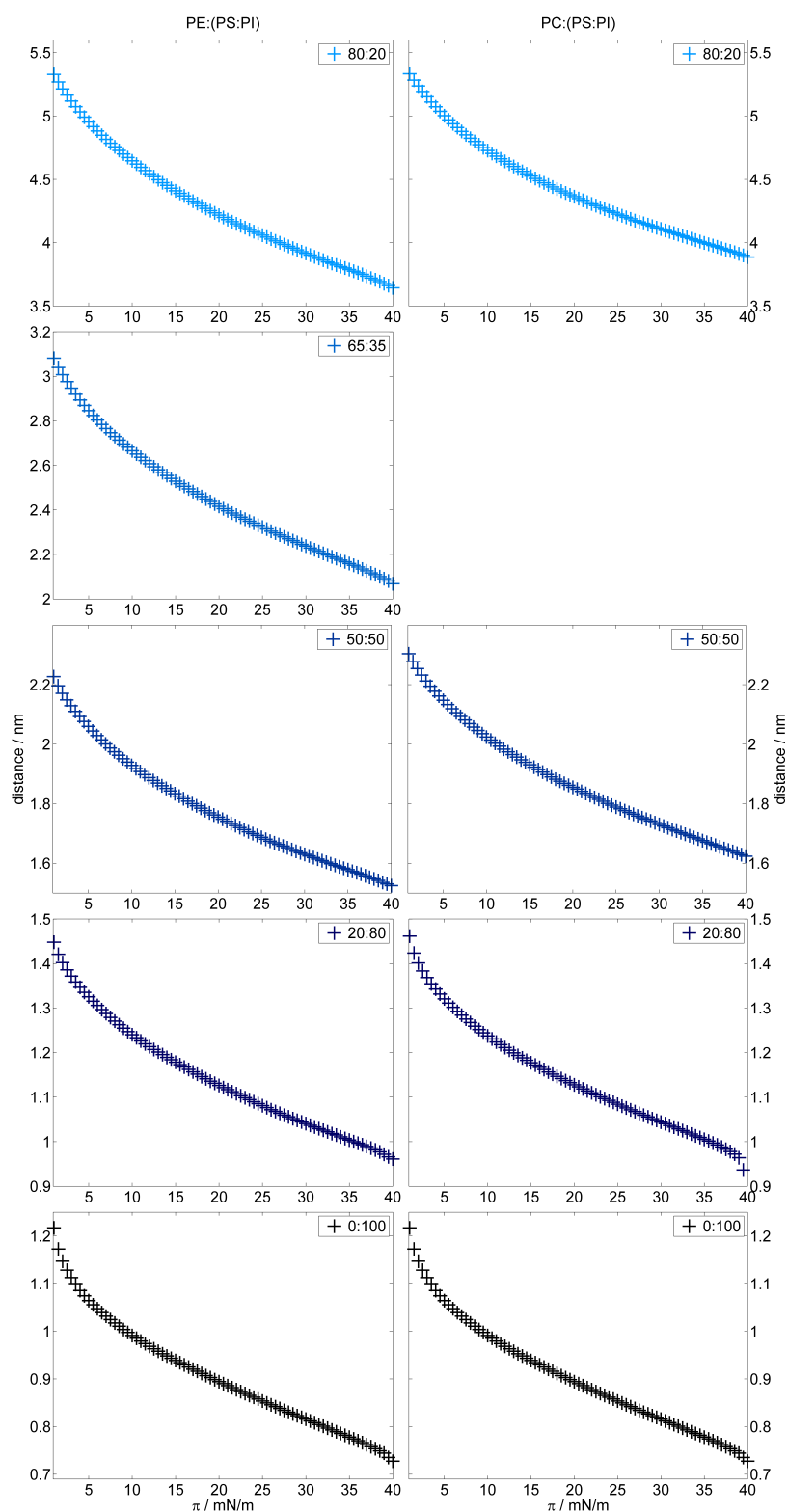


Figure 4.6: Distances between two charged lipids in all compositions of PE:(PS:PI) (left) and PC:(PS:PI) (right) derived from their area–surface pressure isotherms applying Equation 4.1. Error bars are not visible since they are identical to the marker size.

Subphase: 20 °C, 20 mM HEPES and 10 mM NaCl at pH 7.4.

PC molecules than between PE molecules, as stated. But if the monolayers also contain charged lipids, significantly higher distances are only apparent if there is no cholesterol and if the proportion of uncharged lipids is at least 50 % (Figures 4.6 and B.8). In the case of the 20:80 ratio of uncharged to charged lipids, the surface pressure-dependent charge distances are in a nearly identical interval. The only slightly smaller distances in the 50:50 mixtures of PE:(PS:PI) and PC:(PS:PI), despite the different quadratic term of the $\Delta\pi(\pi_{\text{ini}})$ graphs of these mixtures make it clear that the bigger headgroup leading to a bigger charge distance is not the only reason for the higher antiquadratic effect of PC. Consequently, the shielding of the electrostatic interaction of the positively charged MBP and the negatively charged lipids of the myelin may be also influenced by the smaller number of double bonds of brain PC tails compared to brain PE (Figure B.13) and the higher attraction between the MBP and PE monolayers than for PC monolayers.

4.2.3 Conclusions

In this section, the role of major lipids of the cytoplasmic leaflet of the oligodendrocyte for the binding and incorporation of bovine MBP, as modelled by myelin-like lipid monolayers, was investigated by measuring parameters such as maximum insertion pressure. bMBP adsorbed to a lipid monolayer that is similar to the lipid composition of the cytoplasmic leaflet shows values of high incorporation into the myelin-like monolayer (MIP = 42.3 mN/m). A strategy of scrutinising each major lipid in turn systematically for a comparative analysis distinguishes this study from most previous ones in which a particular lipid composition has been selected. In this thesis it has been confirmed that the headgroups of PC and SM appear to have minor attraction for bMBP, even though SM is associated with the domain-building properties of cholesterol, with bMBP seemingly attracted to domain boundaries. The anionic phospholipids PS and PI have the strongest influence on cationic bMBP's association with the membrane, as evidenced by the high maximum insertion pressures, showing the overriding importance of electrostatic interactions. Importantly, though, monolayers of PE alone or the normal composition without the charged lipids PS and PI, also show large maximum insertion pressures (between 30 and 35 mN/m), indicating a well-incorporated protein. Thus, electrostatic associations are not the only driving force for bMBP association with the membrane. The lowering effect of cholesterol and PE on the MIP of bMBP to myelin monolayers results mostly from higher amounts of charged lipids if the normal lipid composition without the indicated uncharged lipid is measured, maintaining the same ratios of all other lipids. The cationic protein association with anionic lipids is associated presumably with lipid condensation, which lowers the fluidity of the lipid layer. Since the lipid condensation partly depends on the distance between charged lipids, the uncharged lipids PE and PC attenuate it without preventing the electrostatic protein-lipid attractions. Taking all observations into consideration, it is clear that each of the major myelin lipids act synergistically, and their balanced composition is essential for the normal condensation of myelin leaflets (molecular events, as discussed in former studies^{35,141}). Moreover, a disruption of this fine balance may exacerbate demyelination as observed in MS. Here, lipid compositions putatively associated with model EAE myelin are also studied, viz., higher amounts of PS and lower amounts of PC, resulting in increased electrostatic interactions but lowered shielding by uncharged lipids. More lipid-condensed regions occur, making the diseased myelin less stable.

Addressing the protein preparation, it has to be noted that bMBP differs from protein derived from human brain.¹⁹⁸ Especially, the balance of post-translational modifications of MBP is altered in MS, possibly as one of the earlier molecular events, resulting in a preponderance of hyper-deiminated MBP of reduced net positive charge.^{199–201} The pattern of modifications results in different modes of protein association with myelin-like membranes.^{20, 161, 202} Pure recombinant forms representing the unmodified and deiminated forms of MBP have been used for many previous biophysical studies.^{35, 121, 147, 161–164} Their analysis represents the next step for exploitation of the experimental system established here.

4.3 Interaction of myelin basic protein charge variants with lipid monolayers

4.3.1 MBP C1 and MBP C8

The charge isomer MBP C1 with a net positive charge of +19 (at pH 7) is the predominant form of MBP in the healthy adult brain. A post-translational modification by the enzyme peptidylarginine deiminase of six arginine to citrulline^{122, 203} (for chemical structures, see Figure 4.7) results in the charge-reduced variant MBP C8 (+13 at pH 7). The deimination of MBP results in the loss of one positive charge for each citrullinated arginine affecting the interaction with lipids and diminishing the compaction of the myelin sheath.³³ The less cationic form of MBP is less able to aggregate lipid vesicles.^{204–206} The amphipatic α -helix of the immunodominant epitope (mentioned in Section 4.1) of MBP C8 is shorter and more surface exposed than the one of MBP C1¹⁴⁷ although no citrulline is located in the region of this epitope.²⁰⁷ Furthermore, MBP C8 adopts a more opened structure than MBP C1.^{208, 209} Due to that and the higher surface exposure, the deiminated form of MBP is more susceptible to degradation by proteases.^{122, 210} A well-studied example is the digestion by cathepsin D, which digested MBP C8 significantly faster than the higher charged MBP C1.^{147, 211}

It is suggested that the deimination of MBP is a mechanism related to MS.²¹² In the healthy adult brain the ratio of MBP C8 to MBP C1 amounts to 0.82.¹⁴⁴ The adult MS brain as well as the normal developing brain shows higher amounts of this highly deiminated C8 form of MBP as compared to MBP C1 with a ratio of 2.45.¹⁴⁴ In the Marburg type, a rare form of MS, an MBP C19 with 18 of the 19 arginine deiminated was found in a ratio of MBP C19/MBP C1 of 6.7.²¹² Patients suffering from this acute type of MS survive only a few month after the disease outbreak.²¹³

MBP extracted from a natural source contains post-translational modifications in addition to deimination as for example methylation²¹⁴ and phosphorylation.²¹⁵ This hampers the study of the influence of deimination on the interaction of MBP and the lipids of the myelin sheath. Thus, recombinant produced proteins have been used in the following investigations. It has already been shown that the recombinant murine 18.5 kDa form of MBP (rmMBP, for amino acid sequences, see Table 4.1) is comparable to protein extracted from bovine brain.²¹⁶ Since citrulline cannot be synthesised recombinantly by translation from a specific codon, recombinant MBP C8, used in this work, contains glutamine instead, which is uncharged and its structure is similar to the structure of citrulline^{122, 217} (Figure 4.7). Another difference is the change of five arginines and one lysin to the uncharged glutamine. The lysin–glutamine mutation of K119 corresponds to

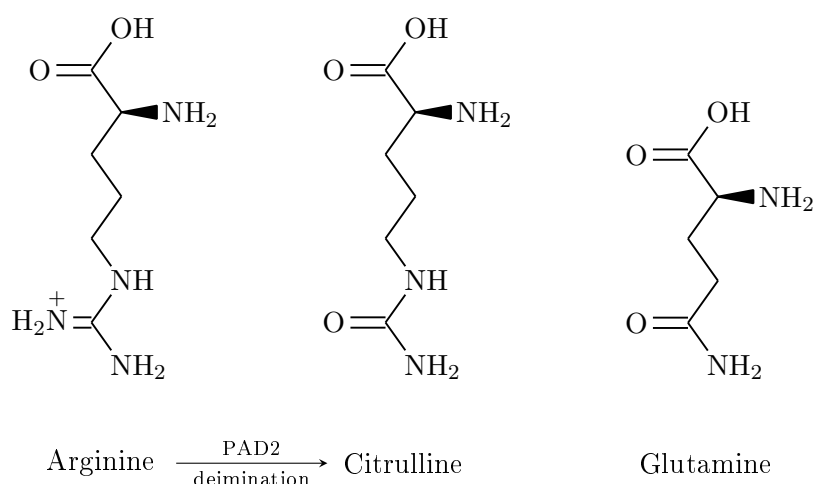


Figure 4.7: Chemical structures of the amino acids arginine, citrulline and glutamine. The enzyme peptidylarginine deiminase 2 (PAD2) leads to deimination of arginine to citrulline. In recombinant produced proteins the similar, codon-specified amino acid glutamine is inserted instead of citrulline.

the arginine–citrulline mutation of R122 in the human form of MBP.

Based on the results of the previous section systematically quantifying the effect of each of the major single brain lipids of the cytoplasmic side of the oligodendrocyte membrane on bovine (mixed charge state) MBP–lipid interaction, here the behaviour of the single charge variants MBP C1 and MBP C8 injected below monolayers of several lipid combinations is compared. The analysis of the phase-separating behaviour of the myelin-like lipid composition is visualised by epifluorescence microscopy and quantified by the maximum insertion pressures (MIPs) of the proteins adsorbed to monolayers of different lipid composition.

4.3.2 Results and discussion

4.3.2.1 Monolayers of the normal myelin composition

To compare the interaction of rmMBP C1 and rmMBP C8 with myelin-like lipid monolayers, chloroform solutions of cholesterol, PE, PS, PC, SM and PI were used in a molar ratio of 44:27:13:11:3:2 (further referred to as ‘normal’ composition), corresponding to the lipid composition of the cytoplasmic leaflet of the myelin sheath.^{176,177}

The lipid solution was spread onto the buffer surface, adjusting different initial surface pressures π_{ini} by different amounts of solution. The incorporation of the protein, which is injected into the buffer subphase below the lipid monolayer, leads to an increase of the surface pressure (Figure B.14). This incorporation is characterised by the insertion of parts of the protein into the lipid layer, where they interact with the acyl chain region, or the interaction of the protein with the lipid headgroups, occupying space at the air–water interface. Both processes cause an increase in surface pressure at a constant total area. Higher initial surface pressures imply a more condensed liquid-expanded (LE) state of the monolayer. Thus, at higher π_{ini} , the increase in surface pressure resulting from protein incorporation is smaller than in the case of smaller π_{ini} .

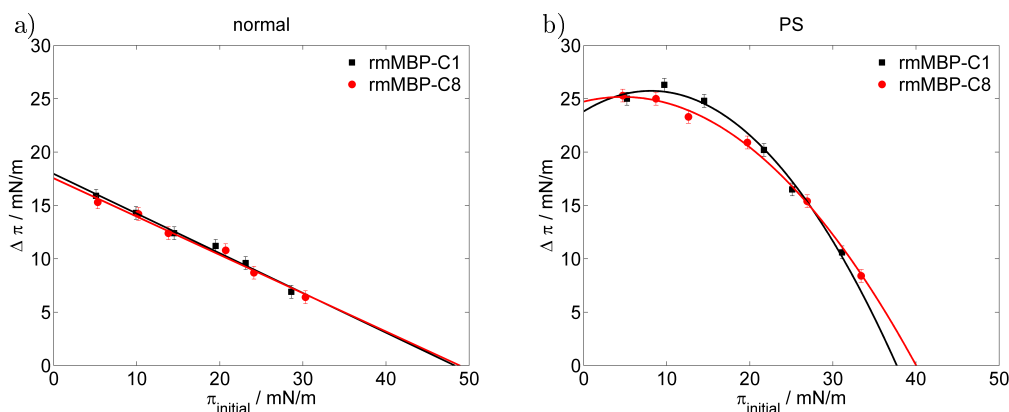


Figure 4.8: Difference of surface pressure $\Delta\pi(\pi_{\text{ini}})$ after maximal 5 h of adsorption of myelin basic protein charge variants C1 and C8 ($c = 100$ nM) to lipid monolayers a) of the normal composition and b) of PS as a function of the initial surface pressure π_{ini} . Regression curves are included.

Subphase: 20 °C, 20 mM HEPES and 10 mM NaCl at pH 7.4.

In the case of injecting MBP below lipid monolayers of the normal composition, the change in surface pressure $\Delta\pi(\pi_{\text{ini}}) = \pi_{\text{end}}(\pi_{\text{ini}}) - \pi_{\text{ini}}$ shows a linear behaviour (Figure 4.8). The MIPs of the two tested charge variants of MBP are nearly equal with 48.3 mN/m for C1 and 48.9 mN/m for C8 adsorbed to the normal lipid composition. These values indicate a strong incorporation of both MBP types into the myelin-like monolayer. (Proteins with MIPs above 30 to 35 mN/m are usually considered to be well-incorporated.¹⁷¹) MBP C1 and MBP C8 show almost identical interactions with the native/normal myelin lipid monolayer. Thus, the reduced net positive charge of MBP C8 alone seems not to be enough to weaken this interaction with the monolayer, necessary for a compact myelin sheath.

Epifluorescence microscopy of a lipid monolayer with normal composition shows defined, well-separated domains of cholesterol-rich (dark regions) and phospholipid-rich (bright regions) phases (Figure 4.9 a). Small grey regions (blue arrows in Figures 4.9 b, c, B.16 and B.17) occur after protein is injected below the lipid monolayer. They represent clusters of MBP incorporated into the lipid film, since these regions are not visible in the fluorescent images of the monolayer without adsorbed protein as already discussed in Section 4.2. Such clustering of both MBP charge variants in myelin-like membrane vesicles has also been found using nanoscale distance measurements with the electron paramagnetic resonance (EPR) spectroscopic method double electron-electron resonance (DEER).^{121,164} MBP C1 as well as MBP C8 thus adsorb to phospholipid-rich domains in close vicinity to cholesterol-rich domains. A possible incorporation of MBP into cholesterol-rich phases is not considered to be likely¹⁸³ and cannot be detected with the approach used here, because the fluorescent dye (0.05 mol % Rh-DHPE) is preferentially located in liquid expanded (LE) phases leading to the dark appearance of cholesterol-rich phases, which are of the higher-ordered liquid condensed (LC) phase.

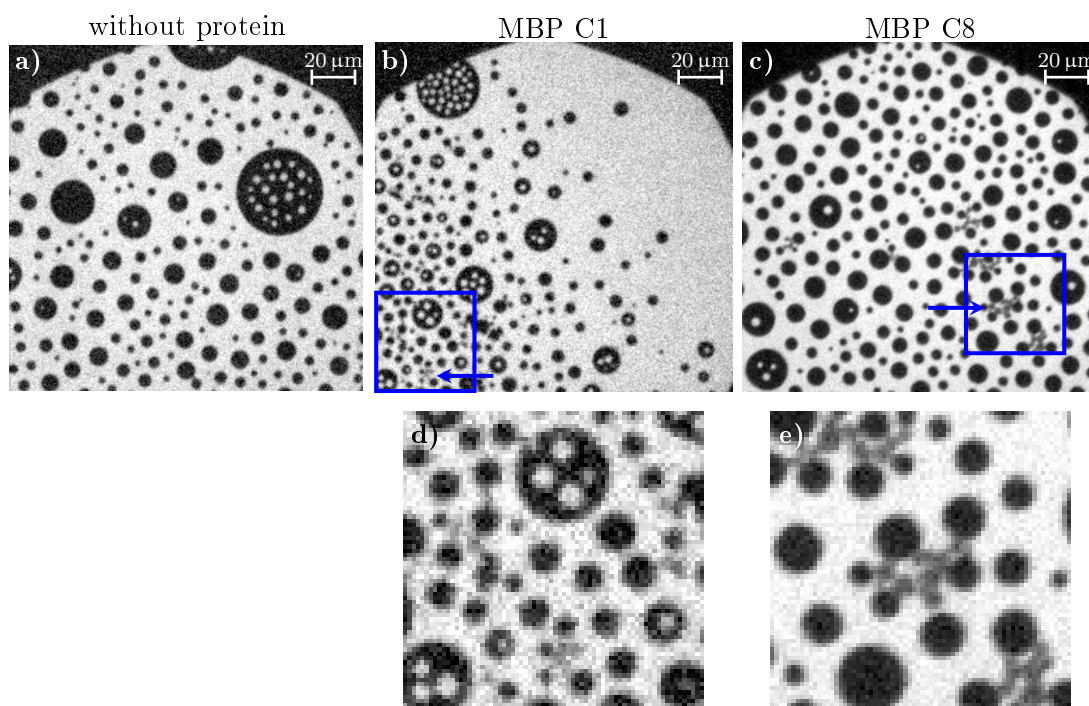


Figure 4.9: a)–c) Fluorescence microscopy images of a monolayer composed of the normal composition and MBP C1 and MBP C8 adsorbed to a monolayer composed of the normal composition at a pressure of ca. 5 mN/m. The blue arrows and squares highlight exemplary small regions arising from the adsorption of MBP to the myelin-like monolayer. d), e) Regions of interest magnified 3 times.

Lipid dye: 0.05 mol-% Rh-DHPE, subphase: 20 °C, 20 mM HEPES and 10 mM NaCl at pH 7.4.

4.3.2.2 Various combinations of brain lipids of the myelin-like monolayers

To investigate if the individual types of lipids of the normal composition have different influences on the interaction between the monolayer and MBP C1 and C8, respectively, the adsorption behaviours of MBP C1 and MBP C8 to monolayers of the respective lipids are compared. Table 4.5 summarises the MIPs of both MBP charge variants adsorbed to a monolayer of the specific lipid. For area–surface pressure diagrams, see Figure B.1 (right).

Injecting the proteins below monolayers of cholesterol, PE, PC, or SM, respectively, leads to a linear behaviour of the $\Delta\pi(\pi_{ini})$ graph (Figure B.18; for $\pi(t)$ diagrams, see Figure B.19). In these cases the increase in surface pressure after injecting the protein results from the interaction of MBP with the lipid, driven by hydrophobic interactions. Regarding the lipids PC and SM, whose headgroups are identical, it becomes obvious that neither MBP C1 nor MBP C8 show strong affinities to incorporate into PC or SM monolayers indicated by MIPs of 25 mN/m (PC) and 20 mN/m (SM), respectively. Since the MIPs of C1 and C8 are small and show no significant differences, the MBP variants do not seem to interact significantly to full PC and SM monolayers at the air–water interface. The MIPs for MBP C1 and C8 after injection below monolayers of uncharged cholesterol

Table 4.5: Maximum insertion pressures for binding of rmMBP C1 and rmMBP C8 to the different brain lipids of myelin and the normal composition. In the case of PS and PI the given value is the apparent maximum insertion pressure MIP_{app} as the $\Delta\pi(\pi_{ini})$ behaviour is not linear.

Protein	MIP in mN/m						
	Chol	PE	PS	PC	SM	PI	normal
rmMBP C1	40.1	36.2	37.7 [#]	25.1	19.9	35.6 [#]	48.3
	± 1.5	± 1.3	± 3.8	± 1.3	± 1.1	± 5.7	± 1.7
rmMBP C8	37.5	38.2	40.0 [#]	25.3	20.2	36.8 [#]	48.9
	± 1.3	± 1.4	± 3.7	± 1.4	± 1.1	± 5.7	± 1.7

[#] MIP_{app}

Table 4.6: Quadratic terms e of the quadratic regression $\Delta\pi(\pi_{ini}) = c + d \cdot \pi_{ini} - e \cdot \pi_{ini}^2$ of MBP C1 and MBP C8 adsorbed to myelin-like lipid monolayers.

Protein	e in m/mN		
	PS	PI	without PE
rmMBP C1	0.0294	0.0312	0.0095
	± 0.0022	± 0.0053	± 0.0042
rmMBP C8	0.0202	0.0212	0.0120
	± 0.0022	± 0.0057	± 0.0062

or PE are much higher than for PC and SM and are in the range and even above values of well-incorporated proteins (see Table 4.5, MIPs between 36 and 40 mN/m). Also for these two lipids, there is no significant difference in the MIPs between MBP C1 and C8.

The negatively charged lipids PS and PI caused a quadratic dependence of $\Delta\pi(\pi_{ini})$ (Figures 4.8, B.18 and B.20), which arises from the superposition of two processes: a) increase of surface pressure π due to protein incorporation driven by hydrophobic interaction and b) decrease of surface pressure π due to lipid condensation as a consequence of electrostatic interactions between positively charged MBP and negatively charged PS and PI. The influence of the electrostatic interactions on the protein–lipid association has already been investigated in detail in Section 4.2.2.3. The definition of the MIP as the initial surface pressure above which no incorporation into the monolayer occurs cannot be applied in the case of nonlinear $\Delta\pi(\pi_{ini})$. The zero of the quadratic $\Delta\pi(\pi_{ini})$ of MBP adsorbed to negatively charged monolayers either marks the maximum insertion pressure or the superposition pressure, at which the contribution of protein incorporation and lipid condensation are equal. As a consequence, $\pi_{ini}(\Delta\pi = 0)$ is an apparent maximum insertion pressure MIP_{app} . The two counteracting processes leading to the quadratic behaviour of $\Delta\pi(\pi_{ini})$ cannot be separated since they proceed with similar time constants in the time-dependent surface pressure graphs (Figure B.19). Thus, the MIP_{app} cannot

Table 4.7: Maximum insertion pressures for binding of rmMBP C1 and rmMBP C8 to the the normal composition and the normal composition without the respective lipid. In the case of the mixture without PE the given value is the apparent maximum insertion pressure MIP_{app} as the $\Delta\pi(\pi_{ini})$ behaviour is not linear.

Protein	MIP in mN/m						
	Normal composition without						normal
	Chol	PE	PS*	PC	SM	PI*	
rmMBP C1	59.4	40.7 [‡]	32.7	49.0	57.4	32.7	48.3
	± 2.1	± 4.7	± 1.4	± 1.6	± 1.7	± 1.4	± 1.7
rmMBP C8	50.6	38.8 [‡]	33.9	48.4	49.7	33.9	48.9
	± 2.1	± 4.8	± 1.5	± 1.5	± 1.7	± 1.5	± 1.7

* without PS and PI

[‡] MIP_{app}

be employed for comparing MBP C1 and C8. Fitting the nonlinear $\Delta\pi(\pi_{ini})$ graphs of MBP adsorbed to negatively charged lipid monolayers with a quadratic regression curve is a helpful and well-suited tool to characterise the nonlinear behaviour. The quadratic term e of the downward opened function $\Delta\pi(\pi_{ini}) = c + d \cdot \pi_{ini} - e \cdot \pi_{ini}^2$ can be used for comparing the strength of electrostatic interaction between positively charged proteins and negatively charged lipids. Higher e indicate a stronger deviation from the linear behaviour and stronger electrostatic interaction between protein and monolayer. Due to the higher net positive charge of MBP C1 (+19 at pH 7) compared to MBP C8 (+13 at pH 7), a stronger electrostatic interaction is expected for MBP C1 injected below monolayers of negatively charged lipids. This assumption is confirmed by the quadratic terms e (Table 4.6), which show significant differences for MBP C1 and MBP C8. Injected below monolayers of PS as well as of PI, MBP C1 induces higher quadratic terms than MBP C8 indicating a stronger electrostatic interaction between the negative lipids and the more highly charged MBP variant.

To get further information about possibly different influences of the specific lipid on the interaction of the MBP charge variants and myelin-like monolayers, adsorption experiments of MBP and monolayers composed of the normal composition without the respective lipid were performed by keeping the ratio of all other lipids constant. This strategy was introduced in Section 4.2. The $\Delta\pi(\pi_{ini})$ diagrams are shown in Figure B.20. For $\pi(t)$ diagrams, see Figure B.21. The MIPs of MBP C1 and MBP C8 adsorbed to these monolayers are summarised in Table 4.7. For area–surface pressure diagrams, see Figure B.1 (right).

Examining the normal composition without PE leads to a quadratic $\Delta\pi(\pi_{ini})$ behaviour, which was discussed in detail for the charge variant mixtures of bovine MBP (Section 4.2.2.2). Here, with a specific look at pure charge variants it becomes apparent that the charge of MBP seems to have no significant influence on the interaction with this monolayer, since there is no significant difference in the quadratic term e of the re-

gression curve of $\Delta\pi(\pi_{\text{ini}})$ (Table 4.6). Again, the real MIP is not determinable due to the nonlinear behaviour. The MIPs of MBP C1 and C8 adsorbed to monolayers of the normal composition without the negatively charged lipids PS and PI are 32.7 mN/m for MBP C1 and 33.9 mN/m for MBP C8 and nearly equal and in the range of a well-incorporated protein but well below the values of the normal composition. Thus, electrostatic interactions are not essential for the binding of MBP to the myelin-like monolayers but strengthen this binding.

A huge difference between MBP C1 and MBP C8 becomes visible if these proteins are injected below monolayers of the normal composition without cholesterol. The MIP of MBP C1 (59.4 mN/m) is much higher than of MBP C8 (50.6 mN/m) adsorbed to the myelin lipids without cholesterol. Compared to the normal composition, where the ratio of uncharged to charged lipids is 85:15, the normal myelin-like monolayer without cholesterol has a smaller ratio of 73:27. Hence, a possible explanation of the higher MIP in the case of MBP C1 could be the enhanced electrostatic interaction due to the increased proportion of negatively charged lipid molecules in the monolayer. It was already shown for bovine MBP that even a small increase in the overall negative charge of the lipid monolayer raises the MIP significantly (see Table 4.4 in the previous section).

Surprisingly, the MIPs of MBP C1 and C8 adsorbed to the normal mix without SM show differences of a similar large extent. If MBP C8 is injected below a monolayer of this composition, the reached maximum insertion pressure is 49.7 mN/m, which is very high and still in the range observed for MBP C8 or C1, respectively, adsorbed to the monolayer of normal composition. However, the interaction of MBP C1 and the monolayer without SM leads to a MIP of 57.4 mN/m, which is well above the value of MBP C1 or C8 and the normal composition, and the value of MBP C8 and the mixture without SM. These results are surprising, since the normal composition contains only 3 % SM. Thus, the amount of negatively charged lipids is not significantly increased if SM is left out. At first glance, a difference in the electrostatic interaction between the MBP charge variants and the normal myelin-like composition without SM seems unlikely. SM, together with cholesterol, is thought to be involved in the building of cholesterol-rich microdomains.^{189,190,218,219} Hence, epifluorescence microscopy is used to visualise changes in the microstructure induced by the 3 % SM, or lack thereof, in the myelin-like monolayers.

Regarding the normal composition without SM investigated by epifluorescence microscopy, a phase separation into phospholipid-rich and cholesterol-rich regions similar to that of the normal lipid monolayer is visible (Figure 4.10 a and d). As described above, in the normal composition, both charged variants are found (in larger aggregates) in the bright phospholipid-rich regions at the interface to the cholesterol-rich microdomains. On the contrary, in the lipid composition lacking SM, a difference in the adsorption behaviours could be detected for MBP C1 and C8. As can be seen in Figures 4.10 e and B.23, highlighted by the blue rectangles, MBP C1 is not incorporated into the lipid monolayer near to cholesterol-rich domains like it does if it is injected below a monolayer of the normal composition. Instead, MBP C1 is found in the phospholipid-rich phase clearly remote from the cholesterol-rich domains, which are also visible in the monolayer without SM. It is probable that the distance between negatively charged lipids in these regions is smaller (and hence the negative charge density is higher) than in regions close to the cholesterol-rich phase. As a consequence, the electrostatic interaction with the highly positively charged MBP C1 is increased. This interpretation is substantiated through the

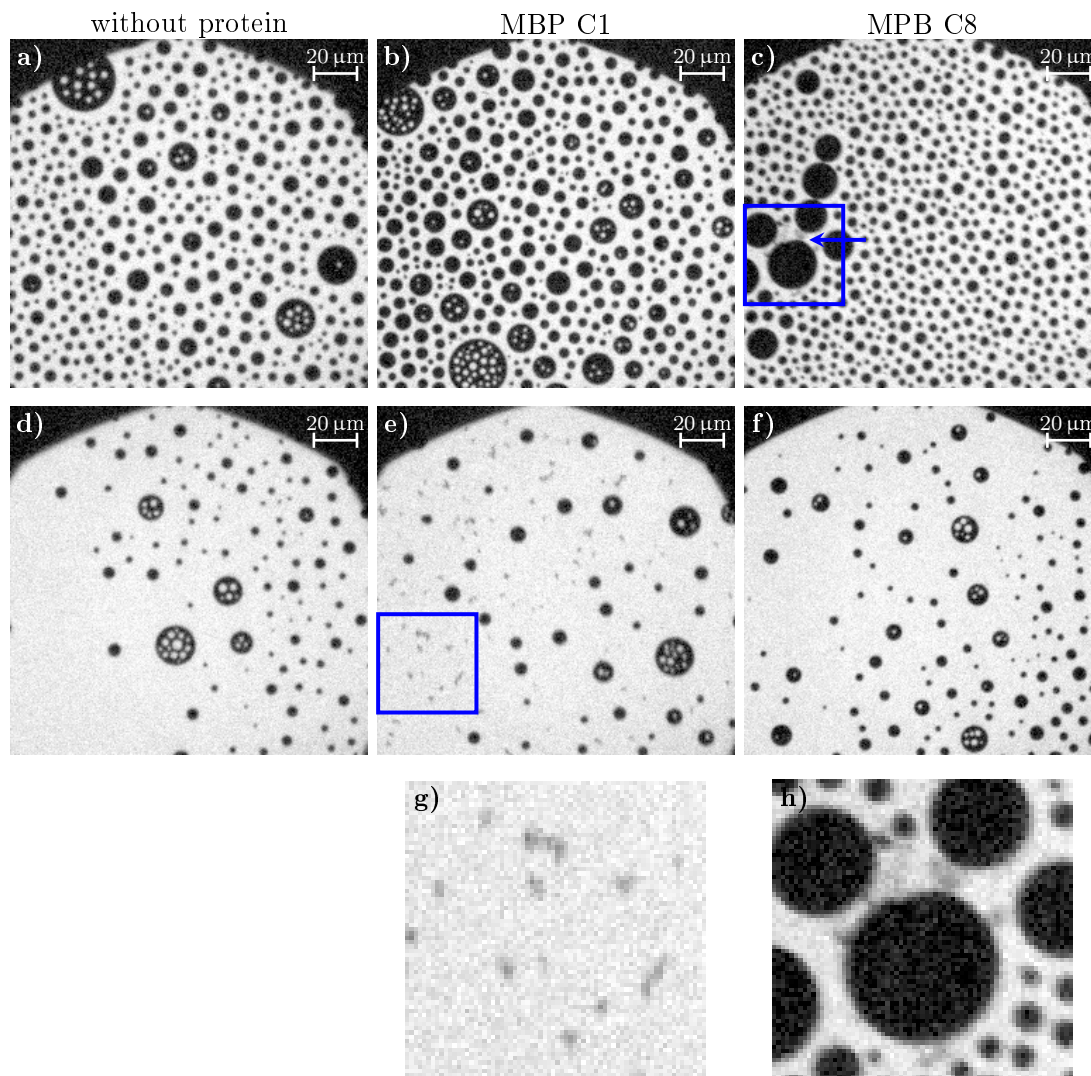


Figure 4.10: Fluorescence microscopy images of a monolayer composed of the normal composition without SM and MBP adsorbed to a monolayer composed of the normal composition without SM at a pressure of ca. 5 mN/m. The blue arrow and the blue squares highlight exemplary small regions arising from the adsorption of MBP to the myelin-like monolayer. a)–c): regions with a high density of cholesterol-rich domains, d)–f): regions with a low density of cholesterol-rich domains, g), h) regions of interest magnified 3 times. Lipid dye: 0.05 mol-% Rh-DHPE, subphase: 20 °C, 20 mM HEPES and 10 mM NaCl at pH 7.4.

higher MIP of C1 adsorbed to the lipid composition without SM compared to the value for the normal composition (Table 4.7), since stronger electrostatic interactions increase the MIP. If MBP C8 is injected below the lipid monolayer without SM, the protein is still visible close to cholesterol-rich domains (Figures 4.10 c and B.24) like in the case of the normal monolayer.

4.3.2.3 Line tension vs. electrostatic attraction

The lipid domains of either cholesterol-rich or phospholipid-rich regions tend to exhibit a circular shape to minimize the length of the boundary and concomitantly the line tension between the two phases. This line tension at the domain interface comes at an energetic cost, partly arising from the height mismatch between the more ordered cholesterol-rich and the less ordered phospholipid-rich domain.^{220,221} Other parameters influencing the line tension are e.g. the lipid composition or proteins interacting with the lipid layer.²²¹ In the case of the positively charged MBP interacting with microphase-separated monolayers, which contain negatively charged phospholipids, the line tension, with the free energy

$$E_{\text{line}} = \gamma \int dC \quad (4.7)$$

with line tension γ and the contour $\int dC$ around the domain, competes with the electrostatic interaction with Coulomb energy

$$E_{\text{elec}} = \int \rho_p(r-x)\varphi_{\text{ext}}(x)dx \quad (4.8)$$

with the distance between protein and monolayer r , the charge density of the protein ρ_p and the external electrostatic potential φ_{ext} (see Chapter 2.2.4).

The prospective gain in energy determines the preferential interaction leading to the incorporation of the protein into the monolayer since higher energy is less favourable. It can be supposed that the incorporation of MBP into the lipid monolayer near domain boundaries decreases the line tension leading to a gain in energy. A decreasing effect on the line tension has already been reported for several proteins.^{222,223} The energy difference ΔE of the protein adsorbing to the monolayer either near a domain boundary, or in regions enriched in negatively charged phospholipids, determines the preferential adsorption mechanism. Injecting MBP C1 below the normal myelin-like lipid monolayer without SM, the (additional) electrostatic attraction between the negative lipids and the highly positive MBP C1 when the protein is attached within the charged domains is larger than the gain in energy when attaching close to the domain boundary and reducing the line tension of the domains (Figure 4.11 b). It should be noted that all MBP variants, even when inserting at the domain boundaries, are in electrostatic contact with the phospholipid-rich regions. For MBP C1 in the monolayers of the normal composition without SM, the additional gain in electrostatic energy by attaching remotely to the domain boundaries is now larger than the reduction in line tension at the boundaries. The situation is different in the case of MBP C8: the lower charge of MBP C8 only leads to an energy gain through ‘pure’ electrostatic interactions in the phospholipid-rich domains

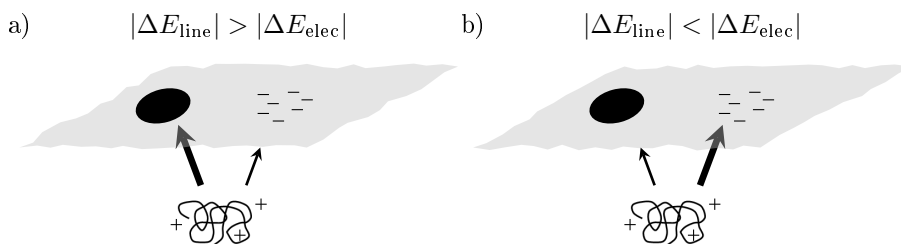


Figure 4.11: Schematic depiction of the competing adsorption mechanisms. The dominating mechanism is a gain in energy due to a) a decrease in line tension and b) electrostatic interaction between negatively charged lipids and positively charged MBP.

Table 4.8: Energy relations characterising the different incorporation mechanisms of MBP C1 and MBP C8 injected below myelin-like lipid monolayers.

Protein	Energetic relation	
	normal mix	normal mix without SM
MBP C1	$ \Delta E_{\text{line}} > \Delta E_{\text{elec}} $	$ \Delta E_{\text{line}} < \Delta E_{\text{elec}} $
MBP C8	$ \Delta E_{\text{line}} > \Delta E_{\text{elec}} $	$ \Delta E_{\text{line}} > \Delta E_{\text{elec}} $

remote from the microdomain boundaries that does not outweigh the reduction in line tension. In this case, the decrease of the line tension is stronger than the additional electrostatic interaction (Figure 4.11 a). SM seems to increase the line tension between the cholesterol-rich and the phospholipid-rich regions, since even the incorporation of MBP C1 into regions near the cholesterol-rich phase leads to a higher gain in energy than the electrostatic interaction with regions enriched in negatively charged lipids, when it is adsorbed to the normal composition containing 3% SM. For a summary of the energetic relations, see Table 4.8.

These experimental findings and simple energetic interpretations may certainly not be transferred to the situation in actual myelin, yet it may help to shed light on some of the fundamental physical-chemical reasons for large scale changes of lipid and protein compositions in diseased or in developing myelin. To this end, one may speculate what the physiological consequences of the difference in interaction between the two different charge variants and the monolayers with and without SM may be. When looking at processes leading to less compact myelin, different chronological orders of events are possible: i) The SM metabolism may get altered in response to the deimination of MBP C1 to charge-reduced variants even down to MBP C8. ii) Deimination to charge-reduced variants could be an adjustment to a lowered SM content. The *in vitro* experiments in myelin-like monolayers discussed here are certainly strongly simplified models of myelin, yet the data would be in good agreement with the second physiological case. If deimination is assumed as the first event, this were reflected in adsorption experiments with the normal composition. However, both MBP types incorporate near the cholesterol-rich domains

leading to a nearly equal MIP. Thus, if the lipid layer is ‘healthy’, for both protein variants nearly identical situations are found. In fact, very similar distributions and interactions of MBP C1 and MBP C8 with myelin-like large unilamellar vesicles (LUVs) were found using DEER spectroscopy.^{121,164} In the second case, if SM is lacking, too strong electrostatic attraction between the lipids and an MBP isomer of high charge could lead to lipid condensation, which lowers the fluidity of the myelin-like monolayer. Then, reducing the net positive charge of the protein, leading to MBP C8, may be an appropriate choice to ensure that lipid condensation is impeded to maintain the fluidity of the lipid layer. This ‘emergency turn’ then may have the consequence that the immunodominant epitope of MBP C8 is less deeply penetrating the membrane and more exposed to the cytosolic space making it more susceptible to proteolysis.^{147,200} This may then result in a loss of compaction of myelin and autoimmune responses against myelin components, both related to the demyelinating disease MS.¹⁴⁷

These findings may also aid in understanding the rather enigmatic protein composition in the developing brain.^{144,201} Unlike in healthy adult myelin, in the developing brain myelin larger amounts of charge-reduced MBP variants are found. This may also lead to situations, in which relative composition of brain lipids is such that it lacks SM and/or cholesterol.²²⁴ To ensure initial compaction during myelination, more charge-reduced variants may be needed, which in the course of development are replaced by high-charge variants like MBP C1 once the final adult composition is reached.^{144,201}

4.3.3 Conclusions

The interaction of different charge variants of MBP with myelin-like lipid monolayers at the air–water interface has been investigated with monolayer adsorption experiments and epifluorescence microscopy. As was expected due to the lower net positive charge of MBP C8 compared to MBP C1, differences in the electrostatic interaction between protein and lipid monolayer have been observed. These become obvious during the interaction of MBP with pure PS or PI monolayers and with monolayers of sufficient high contents of the negatively charged lipids PS and PI, here observed in the case of the normal monolayer without cholesterol (27% negatively charged lipids).

Due to the relatively low amount of sphingomyelin (SM) in the cytoplasmic side of the oligodendrocyte membrane (3%),¹⁷⁶ little attention has so far been paid to the role of SM, despite that its important role for myelination is known.²²⁵ A hyperactivation of the SM metabolism was found in MS^{226,227} and is already targeted by the therapy with Fingolimod (FTY720).^{228,229} Surprisingly, a difference in the adsorption behaviour of the proteins of different net charge to a lipid monolayer composed of the normal myelin-like composition without SM was visible in the maximum adsorption pressure as well as in the epifluorescence microscopy images. This is related to the electrostatic interaction, too, although a content of only 3% of SM in the normal mix does not lead to significantly higher amounts of negatively charged lipids in the lipid composition without SM. These results can be understood as reflecting two energetic effects competing during the adsorption of MBP to myelin-like lipid monolayers: i) reducing the line tension at the phase boundaries of cholesterol-rich and phospholipid-rich domains and ii) electrostatic attraction. The relative energetic gain of these effects decides on the predominant incorporation mechanism. If a decrease of the line tension outweighs the additional electrostatic attraction, MBP incorporates into the monolayer near cholesterol-rich domains and vice versa into regions of higher contents of negatively charged lipids in phospholipid-rich regions.

The latter is the case if the monolayer contains no SM and the protein has a sufficiently high positive charge, e.g. in form of MBP C1, then the electrostatic attraction prevails over the attraction to cholesterol-rich regions.

The differences observed here between MBP C1 and C8 interacting with a monolayer of the normal composition without SM may be related to higher amounts of MBP C8 in the infant brain and in the MS brain. The ratio of MBP C8 to MBP C1 in an adult normal brain amounts to 0.82. This ratio is increased to 2.45 in brains of MS patients. In the brain of healthy children a similar ratio is received.¹⁴⁴ Higher amounts of the deiminated form of MBP may be correlated with lower amounts of SM. In the infant brain^{224,230,231} and in the brain of MS patients^{226,232,233} the SM content is reduced over the healthy adult brain. This may indicate that deimination of MBP C1 to the less charged MBP C8 is an adjustment to lacking SM.

4.4 Outlook

Another monolayer-related technique to study lipid–protein interactions is infrared reflection–absorption spectroscopy (IRRAS) on monolayers. Information on the molecular conformation, orientation and thickness of the monolayer at the air–water interface can be obtained. Furthermore, changes in the secondary structure of the proteins that occur upon binding to a lipid monolayer can be determined using IRRAS.^{234,235} To calculate a reflectance absorbance spectrum RA according to

$$RA = -\log\left(\frac{I}{I_0}\right) \quad (4.9)$$

with single beam reflectivity of pure water or pure buffer surface (I_0), respectively, and of the water or buffer surface covered by a lipid monolayer (I) is recorded using a shuttle technique with a reference trough and a sample trough. This approach minimises the influence of rotational–vibrational bands of water vapour in the light beam on the IRRA spectra.²³⁶ Recording IRRA spectra at different angles of incidence with parallel (p) and perpendicular (s) polarised light may enable the determination of the orientation of secondary structure elements.²³⁷ The analysis of the spectra focusses on band intensities and wavenumbers of the different vibrational modes of the sample at the air–water interface. Spectra recorded at different angles of incidence can be simulated and fitted as described by Schwieger et al.²³⁷ If the adsorption of proteins to monolayers is investigated, the amide I and amide II bands are of particular interest.

For this thesis, IRRA spectra were measured to compare the adsorption of MBP C1 and MBP C8 to a monolayer of the normal myelin-like lipid composition (Figure 4.12), to a monolayer of PS:PI = 13:2 (Figure B.25) and to a monolayer of the normal composition without SM (Figure B.26). The respective protein solution was injected below a monolayer at a surface pressure of 30 mN/m due to similar physical characteristics to a bilayer at this surface pressure.²³⁸ Figure 4.12 shows the reflectance absorption spectrum of a lipid monolayer of the normal composition (green curve), as well as of MBP C1 (black curve) and MBP C8 (red curve) adsorbed to this lipid layer. The amide I and amide II bands of the adsorbed protein are overlapped by the lipid spectrum. Subtracting the lipid IRRA spectrum from the spectrum of the protein adsorbed to the monolayer visualises the amide bands of MBP C1 (blue curve) and MBP C8 (purple curve). The wavenumbers of these bands (amide I: 1662 cm⁻¹, amide II: 1541 cm⁻¹) are identical for both MBP

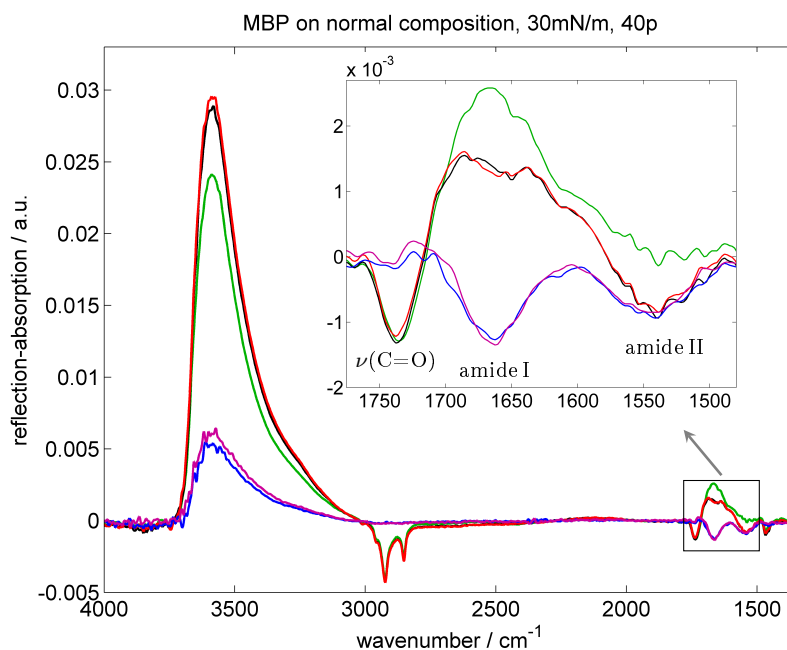


Figure 4.12: IRRAS spectrum of (A) a monolayer of normal composition at 30 mN/m (green curve), (B) MBP C1 adsorbed to a monolayer of normal composition at 30 mN/m (black curve), (C) MBP C8 adsorbed to a monolayer of normal composition at 30 mN/m (red curve), (D) differential spectrum of (B) and (A) (blue curve) and (E) differential spectrum of (C) and (A) (purple curve). Spectra were recorded with p-polarised IR radiation at an angle of incidence of 40° .

Subphase: 20°C , 20 mM HEPES and 10 mM NaCl at pH 7.4.

variants and indicate a α -helical structure (amide I: $1648\text{--}1657\text{ cm}^{-1}$, amide II: $1545\text{--}1550\text{ cm}^{-1}$)²³⁹ and the absence of β -sheets (amide I: $1623\text{--}1641\text{ cm}^{-1}$, $1674\text{--}1695\text{ cm}^{-1}$, amide II: $1525\text{--}1532\text{ cm}^{-1}$).²³⁹ The fact that the wavenumbers of the amide bands are slightly out of the typical intervals speak for contributions of disordered protein parts. The same applies for MBP adsorbed to a monolayer of PS:PI = 13:2 and to a monolayer of the normal composition without SM. In the case of MBP adsorbed to the negatively charged lipids PS and PI (Figure B.25), the amide bands are more prominent than in the case of monolayers of a lower surface charge density due to the stronger interaction between MBP and monolayer resulting from electrostatic interactions.

Angle-dependent measurements of MBP C1 and MBP C8 adsorbed to the respective monolayers have been recorded for angles of incidence $\varphi = \{26^\circ, 30^\circ, 34^\circ, 38^\circ, 42^\circ, 46^\circ, 62^\circ, 66^\circ, 70^\circ\}$.^{*} Despite all efforts, simulation and fitting of the angle-dependent spectra to extract the tilt angle of the α -helix of MBP inside the monolayer are not likely to lead to success since MBP adsorbed to lipids forms three α -helices. The extracted tilt angle would be an error-prone average of the tilt angle of all helices. IRRAS measurement and

^{*}Angles near the Brewster angle $\varphi_B = 53,1^\circ$ (air-water interface) have not been taken into account due to a minimum of the reflectivity of p-polarised light at φ_B leading to a low signal-to-noise ratio.

Table 4.9: Maximum insertion pressures for adsorption of bMBP to monolayers of the normal composition after incubation with FeCl₃ and H₂O₂.

Incubation time in h	MIP in mN/m			
	bMBP	bMBP + FeCl ₃	bMBP + H ₂ O ₂	bMBP + FeCl ₃ + H ₂ O ₂
0	42.3	42.0	42.5	49.9
	± 1.4	± 0.9	± 1.2	± 1.7
25	44.9	43.7	42.4	49.1
	± 1.4	± 2.3	± 1.9	± 1.5

analysis would be more reasonable if only the central segment of MBP comprising one α -helix (so-called immunodominant epitope¹⁴⁵⁻¹⁴⁷) is investigated as it has already been done with NMR spectroscopy^{240,241} and molecular dynamics simulation.^{241,242} A comparison of rmMBP C1 and rmMBP C8 is still not possible with this approach since none of the arginine to glutamine deiminations are located near the central segment. However, the tilt angle of this α -helix could be determined for monolayers of the several lipids of the cytoplasmic leaflet of the myelin sheath using IRRAS to investigate the influence of every lipid on the tilt angle. Prior to this, one has to make certain with monolayer adsorption measurements that these lipids affect the interaction between monolayers and the MBP segment in a similar manner as in case of the whole protein since a segment of a protein may behave completely different than the whole protein.

A potential role in the pathogenesis of MS is attributed to haemoglobin in combination with other factors, such as oxidative stress,¹⁶⁰ due to abnormal accumulations of iron in brains of MS patients, e.g. near demyelinated plaques.^{158,159,243,244} Bamm et al. have performed oxidation experiments with MBP, haemoglobin and H₂O₂ in the presence of cytoplasmic large unilamellar vesicles dependent on various times of incubation.¹⁷⁷ In accordance to this study, preliminary experiments have been carried out to investigate the role of iron for the interaction of MBP and myelin-like lipid monolayers. Bovine MBP has been incubated with FeCl₃ (74 nM), with H₂O₂ (18.5 nM) and with FeCl₃ and H₂O₂, respectively, for incubation times of 0 h and 25 h at 37°. H₂O₂ was added to simulate oxidative stress. The MIPs of all bMBP-mixtures adsorbed to monolayers of the normal composition have been determined with monolayer adsorption experiments (Table 4.9) at 20 °C on 20 mM HEPES and 10 mM NaCl at pH 7.4 (for $\Delta\pi(\pi_{ini})$ and $\pi(t)$ diagrams, see Figures B.33 and B.34). The incubation time, as well as the addition of FeCl₃ or H₂O₂ has no significant effect on the MIP of bMBP adsorbing to a monolayer of the normal composition. However, the addition of both substances, FeCl₃ and H₂O₂, leads to a significant increase of the MIP of 7.6 mN/m (0 h incubation) and 4.2 mN/m (25 h incubation time). These preliminary experiments already show an influence of iron on the MBP-lipid interaction in the presence of H₂O₂. It remains to examine the reason for the increase of the MIP. A possible increase of electrostatic interactions could be considered with monolayer adsorption experiments with monolayers of negatively charged

lipids. Furthermore, the mixtures of bMBP, FeCl₃ and H₂O₂ should be injected below monolayers of the normal composition without SM due to the important role of SM revealed in Chapter 4.3. Fluorescence microscopy may yield further insights.

The potential role of iron for the pathogenesis of MS may be related to three pathways: i) the reactivity of free iron, ii) the activity of haeme and iii) the activity of haemoglobin.¹⁷⁷

As a consequence the above suggested experiments have to be compared to measurements using haemin chloride and haemoglobin, respectively, instead of FeCl₃. In addition to that, measurements with protoporphyrin IX may help with the separation of effects on the MBP–lipid interaction arising on one hand from the iron and on the other hand from the porphyrin part of the haemoglobin. Since haemoglobin is surface active,²⁴⁵ too, all experiments have to be repeated without bMBP.

To compare the influence of iron and iron-containing substances on different charge variants of MBP, recombinant produced proteins used in this thesis are not suitable since they contain a His-tag. This His-tag facilitates the purification of the protein after its expression in *E. coli*. However, its metal-affinity would distort the investigation of the iron–MBP interaction. For these measurement, untagged rmMBP should be produced.

CHAPTER 5

Experimental

5.1 Thermoresponsive peptide polymers

5.1.1 Materials

All diblock ELPs are composed of a hydrophobic block $(\text{VPGVG})_{x_1}$ at the N-terminal end of the polypeptide and a hydrophilic block $(\text{VPGXG})_{x_2}$ located at the C-terminal end. The so-called leader sequence MGCGWPG (for $x_2 = 60$) or GCGWPG (for $x_2 = 30$), respectively, was encoded at the N-terminus and the respective trailer sequence PGGG at the C-terminus (see Figure 5.1 a). In case of the hydrophilic block with guest residue $X = \text{A, G}$ (1:1) and $x_2 = 60$, the hydrophobic block lengths were varied within $x_1 \in \{40, 80, 120, 200\}$. Two additional diblocks were investigated with a hydrophobic block length of $x_1 = 200$ and a hydrophilic block length of $x_2 = 30$: one with the previous guest residue $X = \text{A, G}$ (1:1) and the second one with $X = \text{S}$. In summary, the investigated diblock ELP are composed of the following amino acid sequences:

- i) ELP 40–60: MGCGWPG–(VGVPG)₄₀–(AGVPGGGVPG)₃₀–PGGS
- ii) ELP 80–60: MGCGWPG–(VGVPG)₈₀–(AGVPGGGVPG)₃₀–PGGS
- iii) ELP 120–60: MGCGWPG–(VGVPG)₁₂₀–(AGVPGGGVPG)₃₀–PGGS
- iv) ELP 200–60: MGCGWPG–(VGVPG)₂₀₀–(AGVPGGGVPG)₃₀–PGGS
- v) ELP 200–30: GCGWPG–(VGVPG)₂₀₀–(AGVPGGGVPG)₁₅–PGGS
- vi) ELP 200–S30: GCGWPG–(VGVPG)₂₀₀–(SGVPG)₃₀–PGGS.

These diblock compositions lead to hydrophilic mass fractions between 0.12 and 0.56 (Table 3.3 in Section 3.2). Following the established nomenclature, it will be referred to the diblock ELPs as 'ELP x_1 – x_2 ' with the hydrophobic block length x_1 and the hydrophilic block length x_2 . In case of serine as the guest residue of the hydrophilic block the polymer is called 'ELP 200–S30'.

The diblock ELPs were cloned and produced in *Escherichia coli* by Sarah MacEwan (Chilkoti Lab, Duke University). They were received from Elisabeth Garanger (Université de Bordeaux), who already described their synthesis, expression and purification.¹⁰³

The hysteretic peptide polymers were cloned and produced in *Escherichia coli* by Felipe García Quiroz (Chilkoti Lab, Duke University), who already investigated their hysteretic

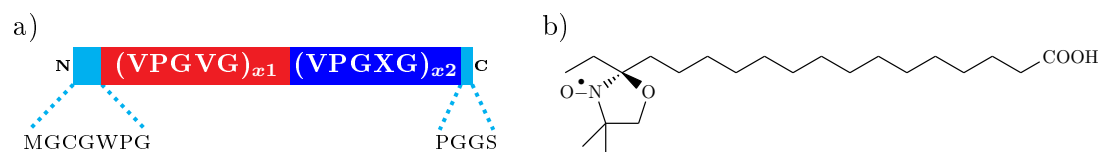


Figure 5.1: a) Schematic depiction of the sequence of the diblock ELPs $(VPGVG)_{x1}$ - $(VPGXG)_{x2}$ with $X = A,G (1:1) \cup X = S$, b) structural formula of 16-DOXYL stearic acid (16-DSA).

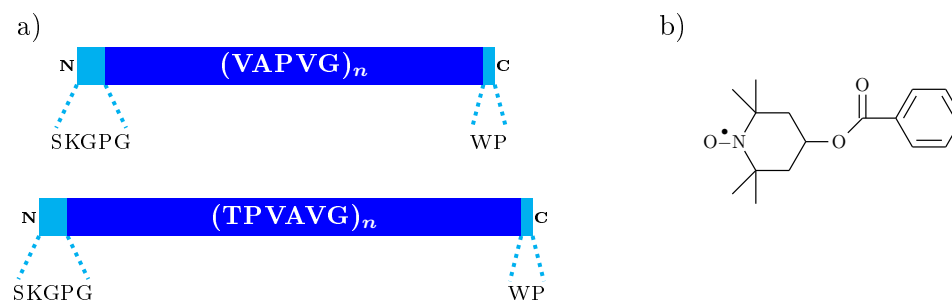


Figure 5.2: a) Schematic depiction of the sequence of the hysteretic polymers $(VAPVG)_n$ and $(TPVAVG)_n$, b) structural formula of 4-Hydroxy-TEMPO benzoate (TB).

behaviour with the use of turbidimetry measurements (unpublished data). Synthesis, expression and purification of these peptide polymers has been reported in detail by Quiroz and Chillkoti.²⁴

Two different polymer sequences were investigated (see Figure 5.2 a): i) composed of the amino acid sequence $(VAPVG)_n$ with $n \in \{30, 40, 80\}$ and ii) composed of the amino acid sequence $(TPVAVG)_n$ with $n \in \{40, 80\}$. The so-called leader sequence SKGPG is encoded at the N-terminus and the respective trailer sequence WP at the C-terminus.

5.1.2 Methods

For the measurement with CW EPR the diblock ELPs were dissolved in PBS (pH 7.4) cooled by ice to avoid an early phase transition. The amphiphilic spin probe 16-DSA (16-DOXYL stearic acid, purchased from Sigma-Aldrich Co. LLC., St. Louis, USA, Figure 5.1 b), dissolved in ethanol, was added. Different concentrations of polymer and spin probe were tested to find the most suitable approach. The final samples contained 300 μM polymer and 1 mM 16-DSA. Micropipettes (BLAUBRAND intraMARK, Wertheim, Germany) were filled with about 15 μl of the solution and sealed with CRITOSEAL (Leica Microsystems, Wetzlar, Germany) for subsequent EPR measurements. Temperatures were adjusted with the Temperature Controller H03 (Magnettech, Berlin, Germany) with an accuracy of $\pm 0.2^\circ\text{C}$ and a heating rate of $1^\circ\text{C}/\text{min}$. To distinguish the effects of the temperature on the probe from the effects of the polymer aggregates on the probe, reference spectra of 1 mM 16-DSA in pure buffer were measured.

For the measurement with CW EPR the hysteretic polymers were dissolved in PBS

(pH 7.4) and cooled by ice to avoid an early phase transition. The nitroxide spin probe TB (4-Hydroxy-TEMPO benzoate, purchased from Sigma-Aldrich Co. LLC., St. Louis, USA, Figure 5.2 b), dissolved in ethanol, was added. Different concentrations of polymer and spin probe were tested to find the most suitable molar ratio. The final samples contained 300 μM polymer and 1 mM TB. Micropipettes (BLAUBRAND intraMARK, Wertheim, Germany) were filled with about 15 μl of the solution and sealed with CRITOSEAL (Leica Microsystems, Wetzlar, Germany) for subsequent EPR measurements. Using the Temperature Controller H03 (Magnettech, Berlin, Germany) with an accuracy of $\pm 0.2^\circ\text{C}$ and a heating/cooling rate of $1^\circ\text{C}/\text{min}$, the samples were first heated from 10 to 75°C . After an equilibration time of 10 min, the samples were cooled to 10°C . To distinguish the effects of the temperature on the probe from the effects of the polymer aggregates on the probe, reference spectra of 1 mM TB in pure buffer were measured.

CW EPR spectra were detected using a MiniScope MS400 (Magnettech, Berlin, Germany) spectrometer with a frequency of approximately $\nu = 9.4$ GHz and a magnetic field sweep of 15 mT centred around 336 mT. The exact frequency was recorded using a frequency counter (Racal Dana 2101, Neu-Isenburg, Germany).

EPR spectra were analysed by spectral simulation with MATLAB R2014a using the program package EasySpin for EPR spectroscopy. The simulation parameters diffusion tensor \mathbf{D} (rotational correlation time $\tau = \frac{1}{6}(D_{xx}D_{yy}D_{zz})^{-1/3}$) and hyperfine splitting tensor \mathbf{A} (hyperfine splitting constant $a = \frac{1}{3}(A_{xx} + A_{yy} + A_{zz})$) of the spin probe as well as the weighted fractions of 2 to 4 components of the nitroxide spectra were extracted in an iterative manual procedure. Parameters were obtained partly from literature and by adjusting them reasonable little by little until the difference between the measured and the simulated spectra was minimised. Starting parameters for the values of the \mathbf{g} tensor and for the hyperfine splitting tensor \mathbf{A} were chosen considering Ge et al.²⁴⁶ for 16-DSA spectra and Cramer et al.²⁴⁷ for TB. In the latter case literature values of the spin probe TEMPO were adjusted for TB.

In case of spectra of 16-DSA, g values of the hydrophilic spectral component were chosen as $\mathbf{g} = [g_{xx} \ g_{yy} \ g_{zz}] = [2.0086 \ 2.0063 \ 2.0025]$. Taking into account that the difference of g_{xx} between polar and apolar regions is not higher than 0.0004,^{48,248} for the hydrophobic spectral component of 16-DSA g values were chosen as $\mathbf{g} = [g_{xx} \ g_{yy} \ g_{zz}] = [2.0089 \ 2.0063 \ 2.0025]$.

TB spectra were simulated with $\mathbf{g} = [g_{xx} \ g_{yy} \ g_{zz}] = [2.0103 \ 2.0069 \ 2.0030]$ for the hydrophilic component, $\mathbf{g} = [g_{xx} \ g_{yy} \ g_{zz}] = [2.0107 \ 2.0071 \ 2.0032]$ for the hydrophobic component and $\mathbf{g} = [g_{xx} \ g_{yy} \ g_{zz}] = [2.0107 \ 2.0071 \ 2.0032]$ for the immobile component. It has to be noted that these g values are only of a qualitative character and can only be measured by a W-Band spectrometer for higher accuracy.

5.2 Myelin basic protein

5.2.1 Materials

Lyophilised bovine myelin basic protein (18.5 kDa isoform predominating) was purchased from Sigma-Aldrich Co. LLC. (St. Louis, MO, U.S.A.). Expression constructs containing 18.5 kDa recombinant murine MBP (rmMBP) C1 and C8 sequence (with a C-terminal

LEH₆ tag; for amino acid sequences, see Figure 4.1) in the vector pET-22b(+) were received from George Harauz (University of Guelph). With these constructs, rmMBP was expressed and purified following instructions based on Bates et al.:²¹⁶ The constructs were transformed into *Escherichia coli* RosettaTM(DE3). Cultures were grown in LB (lysogeny broth) medium containing ampicillin and chloramphenicol. Protein expression was induced by IPTG (isopropyl β -D-1-thiogalactopyranoside). For protein purification expression culture was centrifugated and redissolved in a lysis buffer containing 8 M urea, 100 mM NaH₂PO₄, 5 mM Tris-HCl, 500 mM NaCl, 100 mM imidazole and 1% Tween-20, pH 8. By applying the material to a Ni-NTA agarose resin column (Qiagen, Venlo, Netherlands) non-specifically bound proteins were removed by washing with lysis buffer. rmMBP was eluted with lysis buffer (without Tween-20) of pH 4.5 and afterwards dialysed with buffer containing 6 M urea, 80 mM glycine at pH 10. The rmMBP containing fractions were loaded on a HiTrap CM FF column (VWR, PA, Radnor, U.S.A.) and eluted with dialyse buffer in a linear gradient of 0–0.2 mM NaCl. Salt and the denaturant urea were removed stepwise by slow dialysis in buffer containing 50 mM TRIS and 250 mM NaCl at pH 7.4 (2 steps), afterwards in buffer containing 100 mM NaCl at pH 7.4 (2 steps) and finally in distilled water (4 steps). The protein solution was then lyophilised.

The lyophilised protein was dissolved in a buffer solution of 20 mM HEPES (N-(2-hydroxyethyl)-piperazine-N-ethanesulfonic acid) and 10 mM NaCl, which was adjusted with NaOH to pH 7.4. Buffer was prepared with ultrapure water from Milli-Q Advantage A10 (Millipore S.A.S., Molsheim Cédex, France) with a conductivity lower than 0.055 μ S/cm and a TOC (total organic carbon) below 4 ppb. L- α -phosphatidylethanolamine (brain, porcine) (PE), L- α -phosphatidylserine (brain, porcine) (PS), L- α -phosphatidylcholine (brain, porcine) (PC), sphingomyelin (brain, porcine) (SM), and L- α -phosphatidylinositol (liver, bovine) (PI) dissolved in chloroform were purchased from Avanti Polar Lipids Inc. (Alabaster, AL, USA) as well as cholesterol (ovine wool). The brain lipids PE and PC contain plasmalogens in an amount similar to that in brain myelin. For the chemical structures of all used lipids, see Figure 5.3. The lipids were diluted with chloroform (Carl Roth GmbH & Co. KG, Karlsruhe, Germany). All given ratios of lipid compositions (Tables 5.1 and 5.2) represent the mole ratio.

The fluorescent dye 1,2-dihexadecanoyl-*sn*-glycero-3-phosphoethanolamine-N-(lissamine rhodamine B sulfonyl) (Rh-DHPE) was purchased from Life Technologies GmbH (Darmstadt, Germany).

All chemicals were used as received without further purification.

5.2.2 Methods

Monolayer adsorption measurements

All adsorption experiments were performed in home-built circular PTFE troughs, covered by a plastic hood to prevent contamination and to keep the temperature and humidity around the troughs constant. By keeping the temperature at $20\text{ }^{\circ}\text{C} \pm 0.1\text{ }^{\circ}\text{C}$ with a circulating water bath (Thermostat F6, Haake, Karlsruhe, Germany) and small water-filled bowls, which ensured a high humidity around the troughs, the evaporation of subphase-water was minimised and thus ensured constant concentration of protein in the subphase. Surface pressure was recorded using a microbalance (Riegler und Kirstein GmbH, Berlin, Germany) equipped with a Wilhelmy plate. Prior to every experiment, the troughs were

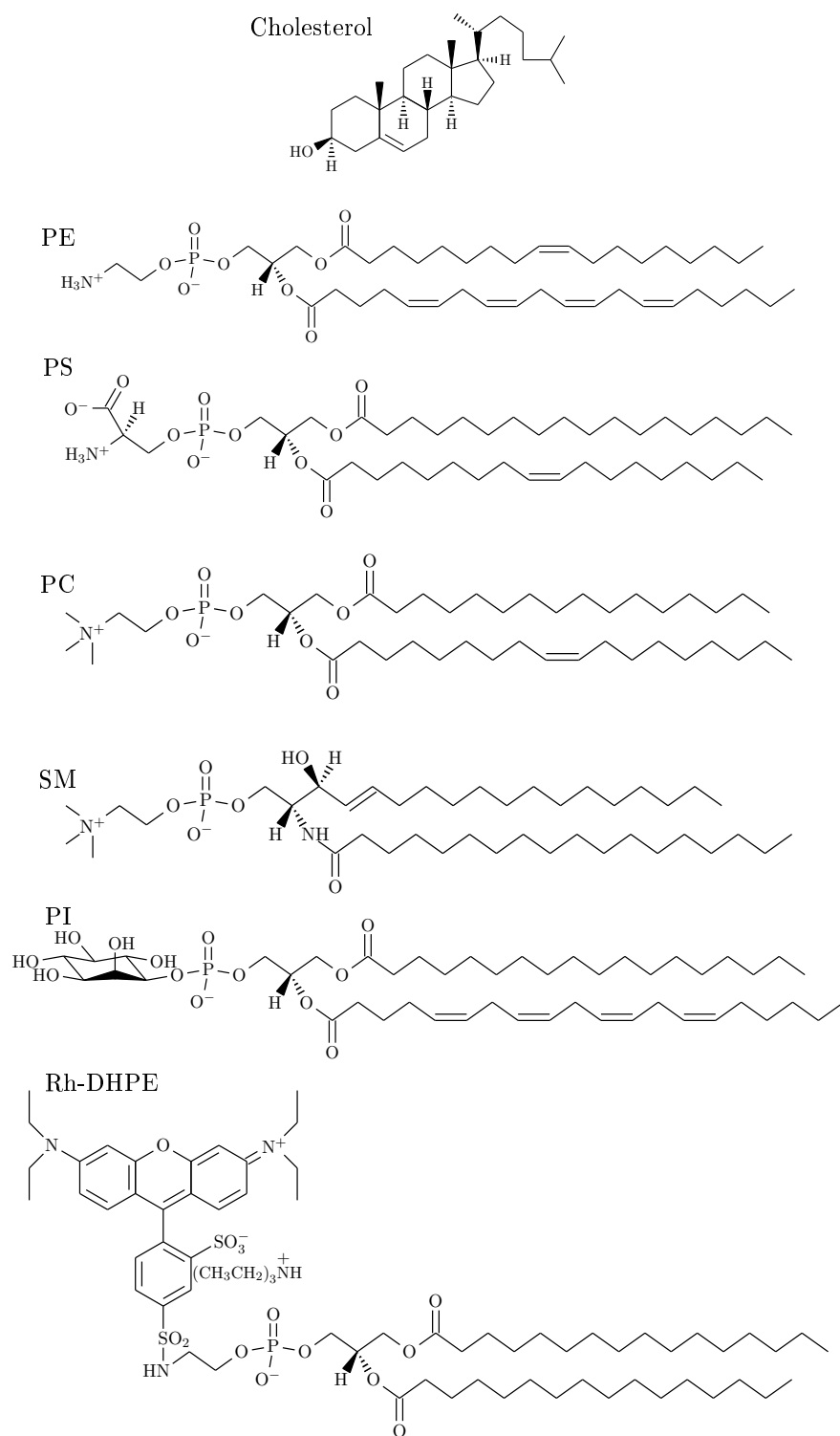


Figure 5.3: Chemical structures of the used brain lipids. The depicted structure is only one of many possible structures. See Figure B.13 for the fatty acid distributions.

Table 5.1: Compositions of the measured lipid mixtures of the normal composition and the normal composition without the respective lipid.

Lipid mixture	Chol	PE	PS	PC	SM	PI
normal	44	27	13	11	3	2
without Chol	0	48.2	23.2	19.6	5.4	3.6
without PE	60.3	0	17.8	15.1	4.1	2.7
without PS, PI	51.8	31.8	0	12.9	3.5	0
without PC	49.5	30.3	14.6	0	3.4	2.2
without SM	45.4	27.8	13.4	11.3	0	2.1

Table 5.2: Compositions of different mole ratios of the lipid mixtures $(x):(y)$ tested for electrostatic investigations, with x referring to uncharged lipids and y to charged lipids, $p \in \{\text{Chol, PE, PC}\}$, $q \in \{\text{PE, PC}\}$.

$(x):(y)$	$p:(\text{PS:PI})$	$(\text{Chol:}q):(\text{PS:PI})$
0:100	0:(86.7:13.3)	(0: 0):(86.7:13.3)
20: 80	20:(69.3:10.7)	(12.4: 7.6):(69.3:10.7)
50: 50	50:(43.3: 6.7)	(31.0:19.0):(43.3: 6.7)
65: 35	65:(30.3: 4.7)	(40.3:24.7):(30.3: 4.7)
80: 20	80:(17.3: 2.7)	(49.6:30.4):(17.3: 2.7)
100: 0	100:(0: 0)	(62.0:38.0):(0: 0)

cleaned with the cleaning concentrate HellmanexTM (Hellma Analytics, Müllheim, Germany) and ultrapure water, and a fresh Wilhelmy plate was mounted. The pressure sensor was calibrated using the surface pressure of ultrapure water (72.8 mN/m)^{61,62} and that of air (0 mN/m) as reference points.

For adsorption measurements, the troughs were filled with HEPES–NaCl buffer (20 mM HEPES, 10 mM NaCl) of pH 7.4. After the lipids were spread, a waiting period of 30 min was abided for complete solvent evaporation and lipid equilibration. The MBP buffer solution was injected below the monolayer using a feed-through from the edge of the trough, reaching a final protein concentration of $c = 100$ nM. During the adsorption experiment, the subphase was stirred by a small stirring magnet to accelerate diffusion of the added solutes.

Primarily, monolayer adsorption measurements were here used to determine the maximum insertion pressure (MIP). For calculating the MIP of a protein that is incorporated into a lipid monolayer at the air–water interface, the change in surface pressure $\Delta\pi = \pi_{\text{end}} - \pi_{\text{ini}}$ is plotted as a function of the initial surface pressure π_{ini} . The final pressure π_{end} is the constant value the surface pressure reached. To ensure, that evaporation of water of the subphase has no influence on this value, π_{end} is taken not later than 5 hours after injection of the protein solution. If $\Delta\pi(\pi_{\text{ini}})$ follows the linear relationship $\Delta\pi(\pi_{\text{ini}}) = a + b \cdot \pi_{\text{ini}}$, the MIP can be calculated with $\text{MIP} = -a/b$ resulting from the definition of the MIP: $\Delta\pi(\pi_{\text{ini}}) = 0$ mN/m.

Area–surface pressure isotherms

The area-dependent surface pressure was measured with a film balance equipped with moveable computer-controlled Teflon barriers for the variation of the area per molecule and a Wilhelmy plate for measuring the surface pressure. Prior to every experiment, the troughs were cleaned with HellmanexTM and ultrapure water and a fresh Wilhelmy plate was mounted. The pressure sensor was calibrated using the surface pressure of ultrapure water (72.8 mN/m)^{61,62} and that of air (0 mN/m) as reference points.

The trough was filled with HEPES–NaCl buffer (20 mM HEPES, 10 mM NaCl) of pH 7.4. Temperature was kept constant at 20 °C ± 0.1 °C by a circulating water bath (Thermostat F6, Haake, Karlsruhe, Germany). A certain volume of lipid solution in chloroform was spread onto the surface forming the myelin-like monolayer. After a waiting period of 30 min for complete solvent evaporation, the monolayer was compressed at a rate of $v = 2 \text{ \AA}^2/(\text{molecule}\cdot\text{min})$.

Epifluorescence Microscopy of Lipid Monolayers

Fluorescence microscopy images of monolayers at the air-water interface were taken using an Axio Scope A1 Vario epifluorescence microscope (Carl Zeiss MicroImaging, Jena, Germany). A home-built Langmuir Teflon trough with moveable computer-controlled Teflon barriers was located underneath the microscope on a x-y stage (Märzhauser, Wetzlar, Germany) for moving the film surface to any desired position below the objective lens. The stage was controlled by a MAC5000 system (Ludl Electronic Products, Hawthorne, NY, USA). Surface pressure was recorded using a microbalance (Riegler und Kirstein GmbH, Berlin, Germany) equipped with a Wilhelmy plate. Prior to every experiment, the troughs were cleaned with the cleaning concentrate HellmanexTM (Hellma Analytics, Müllheim, Germany) and ultrapure water, and a fresh Wilhelmy plate was mounted. The pressure sensor was calibrated using the surface pressure of ultrapure water (72.8 mN/m)^{61,62} and that of air (0 mN/m) as reference points. The trough was filled with HEPES–NaCl buffer (20 mM HEPES, 10 mM NaCl) of pH 7.4. Temperature was kept constant at 20 °C ± 0.1 °C by a circulating water bath (Thermostat F6, Haake, Karlsruhe, Germany). The air-water surface was illuminated by a 100 W mercury arc lamp (HXP 120 C) combined with a long working distance objective (LD EC Epiplan-NEOFLUAR 50x) and a filter/beam splitter combination to select appropriate wavelengths for the excitation and detection of the used fluorescent dye Rh-DHPE. Image data were recorded by an EMCCD camera (ImageEM C9100-13, Hamamatsu, Herrsching, Germany) and acquired by the software AxioVision (Carl Zeiss MicroImaging, Jena, Germany).

The fluorescent dye Rh-DHPE was added to the lipid-chloroform solution gaining a mole ratio of 0.05 mol-% by reducing the amount of brain PE by 0.05 mol-%. The monolayers were spread and the protein was injected as described above.

CHAPTER 6

Summary

Intrinsically disordered proteins (IDPs) do not adopt a well-defined tertiary protein structure in solution. They undergo a disorder-to-order transition depending on environmental conditions such as temperature or the presence of binding partners. Two types of IDPs were investigated in this thesis to scrutinise their aggregation behaviour: i) thermoresponsive peptide polymers exhibiting an inverse phase transition and ii) myelin basic protein (MBP) adopting a tertiary structure during the interaction with lipids.

Amino acid-derived thermoresponsive polymers are promising prototypes representing model systems of IDPs. The temperature-driven behaviour of these peptide polymers in aqueous solution was studied as a function of the amino acid sequence with spin probing continuous wave (CW) electron paramagnetic resonance (EPR) spectroscopy. The incorporation of EPR-active molecules into the systems of interest allowed the examination of the local structure of the peptide polymers from the perspective of the hosted guest molecules, which is of high interest due to a possible application as e.g. drug delivery systems.

To understand the complex nanoscale dehydration process during the aggregation of the polymers undergoing an inverse phase transition, two classes of thermoresponsive biopolymers were examined in this thesis. First, the temperature-dependent phase transition of diblock elastin-like polypeptide (ELP) copolymers composed of a hydrophobic block and a hydrophilic block was studied. Analysing the spectral parameters obtained with spectral simulation revealed different mechanisms of a temperature-driven phase transition. It was shown that the phase transition temperature is a function of the hydrophobic mass fraction of the diblock ELPs, whereas the hydrophilic block length determines the molecular structure of the polymer aggregates formed above the transition temperature. Diblock ELPs with weight ratios of hydrophilic block length to hydrophobic block length above a particular value form aggregates consisting of a core of aggregated hydrophobic blocks and a corona of hydrophilic blocks. Ratios below this value result in aggregates of the hydrophobic parts that enclose the hydrated hydrophilic blocks.

Second, thermoresponsive peptide polymers with differing dehydration and rehydration mechanisms during heating and subsequent cooling of the polymers were investigated. The thermal hysteresis of these polymers is characterised by the rehydration of the amino acid during decreasing temperature that proceeds different for the side and the main chains of the amino acid sequence. The continual rehydrated side chains shield the main chains from penetrating water maintaining their dehydration over a broad temperature interval. If the repeat unit of the hysteretic polymer contains additionally the hydrophilic

amino acid threonine, the shielding of the main chain from hydration is strengthened. The larger extend of the hysteresis of the threonine-containing polymers indicates an additional hydration shell forming a water-impermeable water layer around threonine's OH group.

Analysing the phase transition of the different peptide polymers monitored by the hydration of the amino acid chains revealed that the aggregation behaviour strongly depends on the amino acid sequence. Extending the findings of this thesis with further investigations will help to precisely tune the biophysical properties of thermoresponsive peptide polymers for the desired applications in biotechnology and medicine.

An IDP that is involved in physiological and pathological processes is myelin basic protein (MBP), whose interaction with the cytoplasmic leaflets of the oligodendrocyte membrane is essential for the formation of a compact myelin sheath. MBP is implicated in the pathogenesis of neurodegenerative diseases like multiple sclerosis (MS). To gain more-detailed insights into the interaction of MBP and the lipids of the myelin sheath, the adsorption of MBP to model lipid monolayers of similar composition to the myelin of the central nervous system was studied at the air-water interface with monolayer adsorption experiments. In a first step, the maximum insertion pressures of bovine MBP adsorbed to different myelin-like lipid monolayers provided detailed information about the specific role of each of the single lipids in the myelin. It became apparent that electrostatic interactions between the negatively charged lipids phosphatidylserine (PS) and phosphatidylinositol (PI) and the positively charged MBP are of particular importance for the protein-lipid interaction. Depending on the ratio of negatively charged lipids to uncharged lipids and the distance between charges, the adsorption process was found to be determined by two counteracting effects: i) protein incorporation, and ii) lipid condensation due to electrostatic interaction between the positively charged protein and negatively charged lipids. The presence of the uncharged phospholipids phosphatidylethanolamine (PE) and phosphatidylcholine (PC) in the lipid layer results in an increase of the distance between negatively charged lipids and may prevent lipid condensation, which is related to a lower fluidity of the lipid monolayer. Cholesterol, the most abundant lipid in the cytoplasmic side of the myelin sheath, induces the building of cholesterol-rich and phospholipid-rich domains in the lipid film. MBP seems to be attracted to the boundaries of these domains. Based on these results, in the next step, the interaction of the charge variants MBP C1 (charge: +19) and MBP C8 (charge: +13) with lipid monolayers similar to the composition of the cytoplasmic leaflet of the oligodendrocyte membrane was compared to reveal differences arising from the charge of MBP that may be related to the pathogenesis of MS. Concerning the role of the single lipids for the protein-lipid interaction, monolayer adsorption experiments yielded comparable results to the investigations with bovine MBP of mixed charge. In addition to these results, it was found with the help of epifluorescence microscopy that the electrostatic attraction between the positively charged proteins and negatively charged lipids in the myelin-like monolayers competes with the incorporation of MBP into regions near cholesterol-rich domains. The incorporation of MBP into regions of high contents of negatively charged lipids is not favoured due to additional lipid condensation, which would lead to a lower fluidity of the lipid layer. In this regard, a major role of sphingomyelin (SM) was found, which was unexpected due to the low content of SM (3 %) in the lipid composition similar to the myelin. If SM is absent, the highly charged MBP C1 variant does not incorporate near the cholesterol-rich domains

into the monolayer as opposed to MBP C8, which is still incorporated into these regions. It is concluded, that MBP C1 requires a specific interaction with SM that outweighs the electrostatic interaction. The incorporation of MBP C8 near cholesterol-rich domains is ensured due to its reduced net positive charge. This connection may be relevant for the correlation of higher amounts of MBP C8 and reduced amounts of SM in brains of adult MS patients and healthy children compared to healthy adults. The charge reduction of MBP C1 to MBP C8 seems to be a reaction to a lack of SM.

The systematic investigation of the interaction of MBP with the single lipids of the cytoplasmic side of the myelin revealed the importance of the synergy of the lipids to ensure MBP's physiologic role for the compaction of the myelin sheath and may further the understanding of pathological processes related to neurodegenerative diseases.

Zusammenfassung

Intrinsisch unstrukturierte Proteine (engl. *intrinsically disordered proteins*, IDP) haben in Lösung keine bestimmte Tertiärstruktur inne. Es kann eine Aggregation von ungeordneter zu geordneter Struktur erfolgen, die abhängig von Umgebungsbedingungen wie beispielsweise Temperatur oder die Anwesenheit von Bindungspartnern ist. In dieser Arbeit wird das Aggregationsverhalten zweier verschiedener IDP-Systeme untersucht:

i) thermoresponsive Polypeptide, die einen inversen Phasenübergang aufweisen und ii) basisches Myelinprotein (engl. *myelin basic protein*, MBP), das durch die Wechselwirkung mit Lipiden eine Tertiärstruktur einnimmt.

Aminosäuren-basierte thermoresponsive Polymere stellen vielversprechende Modellsysteme für IDPs dar. Das biophysikalische Verhalten dieser Peptidpolymere wurde in Abhängigkeit von ihrer Aminosäuresequenz mit *continuous wave* (CW) Elektronenspinresonanz-(engl. *electron paramagnetic resonance*, EPR) Spektroskopie untersucht. Das Einbringen eines EPR-aktiven Moleküls in das zu untersuchende System ermöglicht die Untersuchung der Lokalstruktur der Peptidpolymere aus Sicht des aufgenommenen Sondenmoleküls. Dies ist von besonderem Interesse, da thermoresponsive Polymere unter anderem Anwendung als Wirkstofftransportsysteme finden.

Um den im Nanobereich stattfindenden Dehydratisierungsprozess, der die Aggregation der Polymere während des inversen Phasenübergangs bestimmt, zu verstehen, wurden in dieser Arbeit zwei Arten thermoresponsiver Peptidpolymere untersucht. Zum einen wurde der temperaturabhängige Phasenübergang von Diblock-Copolymeren untersucht, die den elastin-artigen Polypeptiden (engl. *elastin-like polypeptides*, ELP) zugeordnet sind. Diese Copolymere setzen sich aus einem hydrophoben und einem hydrophilen Block zusammen. Die Analyse der spektralen Parameter, die mithilfe der Simulation der EPR-Spektren erhalten wurden, ergab verschiedene Mechanismen des Temperatur-abhängigen Übergangs, bedingt durch die Primärstruktur der Diblock-ELPs. Es wurde gezeigt, dass die Übergangstemperatur abhängig vom hydrophoben Massenanteil des Diblock-ELPs ist, wohingegen die Länge des hydrophilen Blocks die molekulare Struktur der Aggregate bestimmt, die oberhalb der Übergangstemperatur ausgebildet werden. Diblock-ELPs, deren Verhältnis von hydrophiler Blocklänge zu hydrophober Blocklänge über einem bestimmten Wert liegt, bilden Aggregate, die aus einem Kern aus aggregierten hydrophoben Blöcken und einer den Kern umgebenden Korona aus hydrophilen Blöcken bestehen. Ist das Verhältnis kleiner als dieser Wert, schließen die Aggregate der hydrophoben Blöcke die hydratisierten hydrophilen Blöcke ein.

Zum anderen wurden thermoresponsive Peptidpolymere untersucht, deren Dehydratisierungs- und Rehydratisierungsmechanismen während des Heizens bzw. während des anschließenden Abkühlens der Polymere sich voneinander unterscheiden. Die thermische Hysterese dieser Polymere ist durch die Rehydratation der Aminosäuren während des

Abkühlens charakterisiert. Diese erfolgt für die Seitenketten und die Hauptketten der Aminosäuresequenzen nicht gleichzeitig. Die kontinuierlich rehydratisierten Seitenketten schirmen die Hauptketten vor dem Eindringen von Wassermolekülen ab, sodass die Dehydratation der Hauptketten über ein breites Temperaturintervall aufrecht erhalten bleibt. Die Abschirmung der Hauptketten vor Hydratisierung wird verstärkt, wenn die Repetiereinheit des hysteretischen Polymers die hydrophile Aminosäure Threonin enthält. Eine stärker ausgeprägte Hysterese der Threonin-beinhaltenen Polymere weist auf eine zusätzliche Hydratisierungshülle hin, die eine wasserundurchlässige Wasserschicht um die OH-Gruppe von Threonin bildet.

Aus der Auswertung des Phasenübergangs verschiedener Peptidpolymere anhand der Hydratisierung der Aminosäureketten lässt sich schlussfolgern, dass das jeweilige Aggregationsverhalten stark von der Aminosäuresequenz abhängig ist. Das Vertiefen der Erkenntnisse dieser Arbeit mit weiteren Untersuchungen wird die präzise Einstellung gewünschter Eigenschaften für vorgesehene Anwendungen in Biotechnologie und Medizin unterstützen.

Ein IDP, das in physiologische und pathologische Prozesse involviert, ist MBP, dessen Wechselwirkung mit dem zytoplasmatischen Teil der Oligodendrozytmembran für die Bildung einer kompakten Myelinscheide erforderlich ist. Es besteht ein enger Zusammenhang zwischen MBP und der Entstehung neurodegenerativer Krankheiten wie Multipler Sklerose (MS). Um nähere Informationen über die Wechselwirkung zwischen MBP und den Lipiden der Myelinscheide zu erhalten, wurde die Adsorption von MBP an Modelllipidmonoschichten mit Monoschicht-Adsorptions-Experimenten an der Luft-Wasser-Grenzfläche untersucht. Die Lipidzusammensetzung der Monoschichten orientierte sich hierbei an derjenigen des Myelins des zentralen Nervensystems. Der erste Schritt bestand darin, anhand des maximalen Einbaudruckes von Rinder-MBP in verschiedene Myelin-ähnliche Lipidmonoschichten Informationen über die spezifische Rolle jedes der im Myelin vorhandenen Lipids zu erhalten. Dabei wurde deutlich, dass elektrostatische Wechselwirkungen zwischen den negativ geladenen Lipiden Phosphatidylserin (PS) und Phosphatidylinositol (PI) und dem positiv geladenen MBP von besonderer Bedeutung für die Protein-Lipid-Wechselwirkung sind. Abhängig vom Verhältnis zwischen negativ geladenen Lipiden zu ungeladenen Lipiden und des Abstandes zwischen den geladenen Lipiden, wird der Adsorptionsprozess von zwei entgegengesetzt wirkenden Effekten bestimmt:

i) Proteineinbau und ii) Lipidkondensation infolge elektrostatischer Wechselwirkung zwischen negativ geladenen Lipiden und dem positiv geladenen Protein. Das Vorhandensein der ungeladenen Phospholipide Phosphatidylethanolamin (PE) and Phosphatidylcholin (PC) in der Lipidschicht bewirkt eine Vergrößerung des Abstands zwischen geladenen Lipiden und kann Lipidkondensation, welche die Fluidität der Lipidmonoschicht senkt, verhindern. Das am häufigsten in der Myelinscheide vorkommende Lipid Cholesterol sorgt für das Ausbilden Cholesterol-reicher und Phospholipid-reicher Domänen im Lipidfilm. MBP scheint sich bevorzugt an der Grenze dieser Domänen in die Lipidschicht einzubauen.

Basierend auf diesen Erkenntnissen wurde im nächsten Schritt die Wechselwirkung der geladenen MBP-Varianten MBP C1 (Ladung: +19) und MBP C8 (Ladung: +13) mit Lipidmonoschichten Myelin-ähnlicher Zusammensetzung verglichen, um Unterschiede zu finden, die auf die unterschiedliche Ladung der Proteine zurückzuführen sind und im

Zusammenhang mit der Entstehung von MS stehen könnten. Die Rolle eines jeden Lipids betreffend wurden mit Monoschicht-Adsorptions-Experimenten vergleichbare Ergebnisse wie zuvor mit Rinder-MBP, welches eine Mischung der MBP-Ladungsvarianten enthält, erhalten. Zusätzlich hierzu wurde mit Fluoreszenzmikroskopie herausgefunden, dass die elektrostatische Anziehung zwischen dem positiv geladenen Protein und negativ geladenen Lipiden in den Monoschichten mit dem Einbau des MBPs in Regionen nahe Cholesterol-reichen Domänen konkurriert. Der Einbau des MBPs in Bereiche mit hohen Anteilen an geladenen Lipiden wird nicht bevorzugt, da die daraus resultierende Lipidkondensation die Fluidität der Lipidschicht herabsetzt. In diesem Zusammenhang stellte sich heraus, dass Sphingomyelin (SM) eine wichtige Rolle bei der Protein-Lipid-Wechselwirkung spielt, was nicht zu erwarten war, da SM nur zu 3 % in der Myelin-ähnlichen Schicht vorkommt. Fehlt SM in der Lipidmonoschicht, wird die stark geladene Variante MBP-C1 nicht in der Nähe von Cholesterol-reichen Domänen eingebaut. Demgegenüber wird MBP-C8 auch bei fehlendem SM in dieser Regionen eingebaut. Daraus kann geschlussfolgert werden, dass für MBP-C1 eine bestimmte Wechselwirkung mit SM erforderlich ist, die gegenüber der elektrostatischen Wechselwirkung überwiegt. Der Einbau von MBP-C8 nahe Domänengrenzen wird durch die geringere Nettoladung sichergestellt. Diese Eigenschaft könnte einen Zusammenhang zwischen den höheren Mengen an MBP-C8 und geringeren Mengen an SM in Gehirnen von erwachsenen MS-Patienten sowie von gesunden Kindern verglichen mit den Mengen in Gehirnen gesunder Erwachsener herstellen. Die Ladungsminderung von MBP-C1 zu MBP-C8 scheint somit eine Reaktion auf das Fehlen von SM zu sein.

Die systematische Untersuchung der Wechselwirkung des MBPs mit den einzelnen Lipiden der zytoplasmatischen Lipidschicht des Myelins zeigte die Bedeutung des Zusammenwirkens der Lipide für die physiologische Rolle des MBPs, die Kompaktheit der Myelinscheide sicherzustellen. Dies erlaubt Rückschlüsse für die Aufklärung pathologischer Prozesse im Zusammenhang mit neurodegenerativen Erkrankungen.

Bibliography

- (1) P. E. Wright and H. J. Dyson. Intrinsically unstructured proteins: Re-assessing the protein structure–function paradigm. *Journal of Molecular Biology*, 293:321–331, 1999.
- (2) A. K. Dunker, J. D. Lawson, C. J. Brown, R. M. Williams, P. Romero, J. S. Oh, C. J. Oldfield, A. M. Campen, C. M. Ratliff, K. W. Hipps, J. Ausio, M. S. Nissen, R. Reeves, C. Kang, C. R. Kissinger, R. W. Bailey, M. D. Griswold, W. Chiu, E. C. Garner, and Z. Obradović. Intrinsically disordered protein. *Journal of Molecular Graphics and Modelling*, 19:26–59, 2001.
- (3) P. Tompa. The interplay between structure and function in intrinsically unstructured proteins. *FEBS Letters*, 579:3346–3354, 2005.
- (4) M. Z. Atassi. Antigenic structures of proteins. Their determination has revealed important aspects of immune recognition and generated strategies for synthetic mimicking of protein binding sites. *European Journal of Biochemistry*, 145:1–20, 1984.
- (5) S. J. Benkovic and S. Hammes-Schiffer. A perspective on enzyme catalysis. *Science*, 301:1196–1202, 2003.
- (6) A. Ren, X. C. Wang, C. A. Kellenberger, K. R. Rajashankar, R. A. Jones, M. C. Hammond, and D. J. Patel. Structural basis for molecular discrimination by a 3',3'-cGAMP sensing riboswitch. *Cell Reports*, 11:1–12, 2015.
- (7) A. K. Dunker, C. J. Brown, J. D. Lawson, L. M. Iakoucheva, and Z. Obradović. Intrinsic disorder and protein function. *Biochemistry*, 41:6573–6582, 2002.
- (8) J. J. Ward, J. S. Sodhi, L. J. McGuffin, B. F. Buxton, and D. T. Jones. Prediction and functional analysis of native disorder in proteins from the three kingdoms of life. *Journal of Molecular Biology*, 337:635–645, 2004.
- (9) L. M. Iakoucheva, C. J. Brown, J. D. Lawson, Z. Obradović, and A. K. Dunker. Intrinsic disorder in cell-signaling and cancer-associated proteins. *Journal of Molecular Biology*, 323:573–584, 2002.
- (10) P. Tompa and P. Csermely. The role of structural disorder in the function of RNA and protein chaperones. *FASEB Journal*, 18:1169–1175, 2004.
- (11) P. Tompa. Intrinsically disordered proteins: A 10-year recap. *Trends in Biochemical Sciences*, 37:509–516, 2012.
- (12) V. N. Uversky. What does it mean to be natively unfolded? *European Journal of Biochemistry*, 269:2–12, 2002.
- (13) M. Fuxreiter, I. Simon, P. Friedrich, and P. Tompa. Preformed structural elements feature in partner recognition by intrinsically unstructured proteins. *Journal of Molecular Biology*, 338:1015–1026, 2004.
- (14) P. Tompa. Intrinsically unstructured proteins. *Trends in Biochemical Sciences*, 27:527–533, 2002.

- (15) S. Roberts, M. Dzuricky, and A. Chilkoti. Elastin-like polypeptides as models of intrinsically disordered proteins. *FEBS Letters*, 589:2477–2486, 2015.
- (16) W.-L. Hsu, C. Oldfield, J. Meng, F. Huang, B. Xue, V. N. Uversky, P. Romero, and A. K. Dunker. Intrinsic protein disorder and protein–protein interactions. *Pacific Symposium on Biocomputing*, 17:116–127, 2012.
- (17) V. N. Uversky. Intrinsically disordered proteins from A to Z. *International Journal of Biochemistry and Cell Biology*, 43:1090–1103, 2011.
- (18) V. N. Uversky, J. R. Gillespie, and A. L. Fink. Why are “natively unfolded” proteins unstructured under physiologic conditions? *Proteins: Structure, Function, and Genetics*, 41:415–427, 2000.
- (19) P. Tompa. *Structure and Function of Intrinsically Disordered Proteins*. Chapman and Hall/CRC Press, 2009.
- (20) G. Harauz and J. M. Boggs. Myelin management by the 18.5-kDa and 21.5-kDa classic myelin basic protein isoforms. *Journal of Neurochemistry*, 125:334–361, 2013.
- (21) V. N. Uversky. Targeting intrinsically disordered proteins in neurodegenerative and protein dysfunction diseases: Another illustration of the D² concept. *Expert Review of Proteomics*, 7:543–564, 2010.
- (22) M. M. Babu, R. van der Lee, N. S. de Groot, and J. Gsponer. Intrinsically disordered proteins: Regulation and disease. *Current Opinion in Structural Biology*, 21:1–9, 2011.
- (23) V. N. Uversky. A decade and a half of protein intrinsic disorder: Biology still waits for physics. *Protein Science*, 22:693–724, 2013.
- (24) F. G. Quiroz and A. Chilkoti. Sequence heuristics to encode phase behaviour in intrinsically disordered protein polymers. *Nature Materials*, 14:1164–1171, 2015.
- (25) S. Rauscher, S. Baud, M. Miao, F. W. Keeley, and R. Pomès. Proline and glycine control protein self-organization into elastomeric or amyloid fibrils. *Structure*, 14:1667–1676, 2006.
- (26) D. E. Meyer, B. C. Shin, G. A. Kong, M. W. Dewhirst, and A. Chilkoti. Drug targeting using thermally responsive polymers local and hyperthermia. *Journal of Controlled Release*, 74:213–224, 2001.
- (27) J. R. McDaniel, D. J. Callahan, and A. Chilkoti. Drug delivery to solid tumors by elastin-like polypeptides. *Advanced Drug Delivery Reviews*, 62:1456–1467, 2010.
- (28) D. L. Nettles, A. Chilkoti, and L. A. Setton. Applications of elastin-like polypeptides in tissue engineering. *Advanced Drug Delivery Reviews*, 62:1479–1485, 2010.
- (29) J. M. Caves, W. Cui, J. Wen, V. A. Kumar, C. A. Haller, and E. L. Chaikof. Elastin-like protein matrix reinforced with collagen microfibers for soft tissue repair. *Biomaterials*, 32:5371–5379, 2011.
- (30) D. W. Urry, T. M. Parker, M. C. Reid, and D. C. Gowan. Biocompatibility of the bioelastic materials, poly(GVGVP) and its γ -irradiation cross-linked matrix: Summary of generic biological test results. *Journal of Bioactive and Compatible Polymers*, 6:263–282, 1991.
- (31) M. F. Shamji, H. Betre, V. B. Kraus, J. Chen, A. Chilkoti, R. Pichika, K. Masuda, and L. A. Setton. Development and characterization of a fusion protein between thermally responsive elastin-like polypeptide and interleukin-1 receptor antagonist. *Arthritis and Rheumatism*, 56:3650–3661, 2007.
- (32) K. Trabbic-Carlson, L. Liu, B. Kim, and A. Chilkoti. Expression and purification of recombinant proteins from *Escherichia coli*: Comparison of an elastin-like polypeptide fusion with an oligohistidine fusion. *Protein Science*, 13:3274–3284, 2004.

-
- (33) G. Harauz, N. Ishiyama, C. M. Hill, I. R. Bates, D. S. Libich, and C. Farès. Myelin basic protein—diverse conformational states of an intrinsically unstructured protein and its roles in myelin assembly and multiple sclerosis. *Micron*, 35:503–542, 2004.
- (34) W. R. Krigbaum and T. S. Hsu. Molecular conformation of bovine A1 basic protein, a coiling macromolecule in aqueous solution. *Biochemistry*, 14:2542–2546, 1975.
- (35) K. A. Vassall, V. V. Bamm, and G. Harauz. Myelstones: The executive roles of myelin basic protein in myelin assembly and destabilization in multiple sclerosis. *Biochemical Journal*, 472:17–32, 2015.
- (36) M. A. Keniry and R. Smith. Dependence on lipid structure of the coil-to-helix transition of bovine myelin basic protein. *Biochimica et Biophysica Acta (BBA) - Protein Structure*, 668:107–118, 1981.
- (37) E. Polverini, A. Fasano, F. Zito, P. Riccio, and P. Cavatorta. Conformation of bovine myelin basic protein purified with bound lipids. *European Biophysics Journal*, 28:351–355, 1999.
- (38) J. A. Weil and J. R. Bolton. *Electron Paramagnetic Resonance - Elementary theory and practical applications*. John Wiley & Sons, 2. edition, 2007.
- (39) A. Schweiger and G. Jeschke. *Principles of pulse electron paramagnetic resonance*. Oxford University Press, 2001.
- (40) A. Kumar, R. R. Ernst, and K. Wüthrich. A two-dimensional nuclear Overhauser enhancement (2D NOE) experiment for the elucidation of complete proton-proton cross-relaxation networks in biological macromolecules. *Biochemical and Biophysical Research Communications*, 95:1–6, 1980.
- (41) G. Jeschke. Determination of the nanostructure of polymer materials by electron paramagnetic resonance spectroscopy. *Macromolecular Rapid Communications*, 23:227–246, 2002.
- (42) Y. N. Molin, K. M. Salikhov, and K. I. Zamaraev. *Spin Exchange - Principles and applications in chemistry and biology*, volume 8 of *Chemical Physics*. Springer-Verlag, 1980.
- (43) M. P. Eastman, M. R. Kooser, M. R. Das, and J. H. Freed. Studies of Heisenberg spin exchange in ESR spectra. I. Linewidth and saturation effects. *Journal of Chemical Physics*, 51:2690–2709, 1969.
- (44) R. A. Martin, M. Pannier, F. Diederich, V. Gramlich, M. Hubrich, and H. W. Spiess. Determination of end-to-end distance in a series of TEMPO diradicals of up to 2.8 nm length with a new four-pulse double electron electron resonance experiment. *Angewandte Chemie International Edition*, 37:2833–2837, 1998.
- (45) M. Pannier, S. Veit, A. Godt, G. Jeschke, and H. W. Spiess. Dead-time free measurement of dipol-dipol interactions between electron spins. *Journal of Magnetic Resonance*, 142:331–340, 2000.
- (46) D. Sezer, J. H. Freed, and B. Roux. Simulating electron spin resonance spectra of nitroxide spin labels from molecular dynamics and stochastic trajectories. *Journal of Chemical Physics*, 128:165106:1–16, 2008.
- (47) C. Wegener, A. Savitsky, M. Pfeiffer, K. Möbius, and H.-J. Steinhoff. High-field EPR-detected shifts of magnetic tensor components of spin label side chains reveal protein conformational changes: The proton entrance channel of bacteriorhodopsin. *Applied Magnetic Resonance*, 21:441–452, 2001.
- (48) K. Möbius, A. Savitsky, C. Wegener, M. Plato, M. Fuchs, A. Schnegg, A. A. Dubinskii, Y. A. Grishin, I. A. Grigor’ev, M. Kühn, D. Duché, H. Zimmermann, and H.-J. Steinhoff. Combining high-field EPR with site-directed spin labeling reveals unique information on proteins in action. *Magnetic Resonance in Chemistry*, 43:S4–S19, 2005.

- (49) F. Perrin. Mouvement brownien d'un ellipsoïde—I. Dispersion diélectrique pour des molécules ellipsoïdales. *Journal de Physique et le Radium*, 5:497–511, 1934.
- (50) D. Kivelson. Theory of ESR linewidths of free radicals. *Journal of Chemical Physics*, 33:1094–1106, 1960.
- (51) J. H. Freed and G. K. Fraenkel. Theory of linewidths in electron spin resonance spectra. *Journal of Chemical Physics*, 39:326–348, 1963.
- (52) S. Stoll and A. Schweiger. Easyspin, a comprehensive software package for spectral simulation and analysis in EPR. *Journal of Magnetic Resonance*, 178:42–55, 2006.
- (53) J. H. Freed. Theory of slow tumbling ESR spectra for nitroxides. In L. J. Berliner, editor, *Spin labeling - Theory and application*. Academic Press, 1976.
- (54) D. J. Schneider and J. H. Freed. Calculating slow motional magnetic resonance spectra. A user's guide. In L. J. Berliner and J. Reuben, editors, *Spin Labeling. Theory and Application*, volume 8 of *Biological Magnetic Resonance*. Springer US, 1989.
- (55) S. Stoll and A. Schweiger. EasySpin: Simulating cw ESR spectra. *Biological Magnetic Resonance*, 27:299–321, 2007.
- (56) E. Meirovitch, D. Igner, E. Igner, G. Moro, and J. H. Freed. Electron-spin relaxation and ordering in smectic and supercooled nematic liquid crystals. *Journal of Chemical Physics*, 77:3915–3938, 1982.
- (57) H. Möhwald. Phospholipid and phospholipid-protein monolayers at the air/water interface. *Annu. Rev. Phys. Chem.*, 41:441–76, 1990.
- (58) R. Winter and F. Noll. *Methoden der biophysikalischen Chemie*. Teubner Studienbücher, 1998.
- (59) R. A. Demel. Monolayers—description and use of interaction. *Methods in Enzymology*, 32:539–544, 1974.
- (60) H.-D. Dörfler. *Grenzflächen und kolloid-disperse Systeme*. Springer, 2002.
- (61) R. Breslow and T. Guo. Surface tension measurements show that chaotropic salting-in denaturants are not just water-structure breakers. *Proceedings of the National Academy of Sciences of the United States of America*, 87:167–169, 1990.
- (62) R. Maget-Dana. The monolayer technique: A potent tool for studying the interfacial properties of antimicrobial and membrane-lytic peptides and their interactions with lipid membranes. *Biochimica et Biophysica Acta (BBA) - Biomembranes*, 1462:109–140, 1999.
- (63) H. Möhwald. Phospholipid monolayers. In R. Lipowsky and E. Sackmann, editors, *From Cells to Vesicles*, volume 1A of *Structure and Dynamics of Membranes*. North Holland, 1995.
- (64) S. A. Akimov, P. I. Kuzmin, J. Zimmerberg, F. S. Cohen, and Y. A. Chizmadzhev. An elastic theory for line tension at a boundary separating two lipid monolayer regions of different thickness. *Journal of Electroanalytical Chemistry*, 564:13–18, 2004.
- (65) B. L. Stottrup, A. M. Heussler, and T. A. Bibelniaks. Determination of line tension in lipid monolayers by fourier analysis of capillary waves. *Journal of Physical Chemistry B*, 111:11091–11094, 2007.
- (66) P. Debye and E. Hückel. Zur Theorie der Elektrolyte. I. Gefrierpunktserniedrigung und verwandte Erscheinungen. *Physikalische Zeitschrift*, 24:185–206, 1923.
- (67) L. G. Gouy. Sur la constitution de la charge électrique à la surface d'un électrolyte. *Journal de Physique Théorique et Appliquée*, 9:457–468, 1910.

-
- (68) D. L. Chapman. A contribution to the theory of electrocapillarity. *London, Edinburgh, and Dublin Philosophical Magazin and Journal of Science*, 25:475–481, 1913.
- (69) S. L. Carnie and G. L. Torrie. The statistical mechanics of the electrical double layer. In I. Prigogine and S. A. Rice, editors, *Advances in Chemical Physics*, volume 56. John Wiley & Sons, 1984.
- (70) S. McLaughlin. The electrostatic properties of membranes. *Annual Review of Biophysics and Biochemistry*, 18:113–136, 1989.
- (71) G. Cevc. Membrane electrostatics. *Biochimica et Biophysica Acta*, 1031:311–382, 1990.
- (72) J. Israelachvili. *Intermolecular & Surface Forces*. Academic Press, London, San Diego, 2. edition, 1992.
- (73) M. Langner and K. Kubica. The electrostatics of lipid surfaces. *Chemistry and Physics of Lipids*, 101:3–35, 1999.
- (74) O. Stern. Zur Theorie der elektrolytischen Doppelschicht. *Zeitschrift für Elektrochemie*, 30:508–516, 1924.
- (75) H. von Helmholtz. Studien über electriche Grenzschichten. In G. Wiedemann, editor, *Annalen der Physik und Chemie*, volume 243. Verlag von Johann Ambrosius Barth, 1879.
- (76) B. H. Honig, W. L. Hubbell, and R. F. Flewelling. Electrostatic interactions in membranes and proteins. *Annual Review of Biophysics and Biophysical Chemistry*, 15:163–193, 1986.
- (77) D. R. Lide. Properties of water in the range 0–100 °C. In *CRC Handbook of Chemistry and Physics*. CRC Press, 85. edition, 2004.
- (78) J. P. Dilger, L. R. Fisher, and D. A. Haydon. A critical comparison of electrical and optical methods for bilayer thickness determination. *Chemistry and Physics of Lipids*, 30:159–176, 1982.
- (79) J. J. Bellucci, M. Amiram, J. Bhattacharyya, D. McCafferty, and A. Chilkoti. “Three-in-one” chromatography-free purification, tag removal, and site-specific modification of recombinant fusion proteins using Sortase A and elastin-like polypeptides. *Angewandte Chemie International Edition*, 52:3703–3708, 2013.
- (80) W. Hassouneh, T. Christensen, and A. Chilkoti. Elastin-like polypeptides as a purification tag for recombinant proteins. *Current Protocols in Protein Science*, 6:11.1–11.16, 2010.
- (81) B. Helms and J. M. J. Fréchet. The dendrimer effect in homogeneous catalysis. *Advanced Synthesis & Catalysis*, 348:1125–1148, 2006.
- (82) M. J. N. Junk, U. Jonas, and D. Hinderberger. EPR spectroscopy reveals nanoinhomogeneities in the structure and reactivity of thermoresponsive hydrogels. *Small*, 4:1485–1493, 2008.
- (83) T. Wolf, J. Hunold, J. Simon, C. Rosenauer, D. Hinderberger, and F. R. Wurm. Temperature responsive poly(phosphonate) copolymers: from single chain to macroscopic coacervates. *Polymer Chemistry*, 9:490–498, 2018.
- (84) A. Chilkoti, M. R. Dreher, D. E. Meyer, and D. Raucher. Targeted drug delivery by thermally responsive polymers. *Advanced Drug Delivery Reviews*, 54:613–630, 2002.
- (85) S. R. MacEwan and A. Chilkoti. Elastin-like polypeptides: Biomedical applications of tunable biopolymers. *Biopolymers*, 94:60–77, 2010.
- (86) L. D. Muiznieks and F. W. Keeley. Proline periodicity modulates the self-assembly properties of elastin-like polypeptides. *Journal of Biological Chemistry*, 285:39779–39789, 2010.

- (87) N. K. Dutta, M. Y. Truong, S. Mayavan, N. R. Choudhury, C. M. Elvin, M. Kim, R. Knott, K. M. Nairn, and A. J. Hill. A genetically engineered protein responsive to multiple stimuli. *Angewandte Chemie International Edition*, 50:4428–4431, 2011.
- (88) J. C. M. van Hest and D. A. Tirrell. Protein-based materials, toward a new level of structural control. *Chemical Communications*, 19:1897–1904, 2001.
- (89) A. Chilkoti, M. R. Dreher, and D. E. Meyer. Design of thermally responsive, recombinant polypeptide carriers for targeted drug delivery. *Advanced Drug Delivery Reviews*, 54:1093–1111, 2002.
- (90) J. A. MacKay, D. J. Callahan, K. N. FitzGerald, and A. Chilkoti. Quantitative model of the phase behavior of recombinant pH-responsive elastin-like polypeptides. *Biomacromolecules*, 11:2873–2879, 2010.
- (91) Y. Chen and Z. Guan. Bioinspired modular synthesis of elastin-mimic polymers to probe the mechanism of elastin elasticity. *Journal of the American Chemical Society*, 132:4577–4579, 2010.
- (92) D. Kurzbach, W. Hassouneh, J. R. McDaniel, E. A. Jaumann, A. Chilkoti, and D. Hinderberger. Hydration layer coupling and cooperativity in phase behavior of stimulus responsive peptide polymers. *Journal of the American Chemical Society*, 135:11299–11308, 2013.
- (93) N. K. Li, F. G. Quiroz, C. K. Hall, A. Chilkoti, and Y. G. Yingling. Molecular description of the LCST behavior of an elastin-like polypeptide. *Biomacromolecules*, 15:3522–3530, 2014.
- (94) D. W. Urry. Entropic elastic processes in protein mechanisms. I. Elastic structure due to an inverse temperature transition and elasticity due to internal chain dynamics. *Journal of Protein Chemistry*, 7:1–34, 1988.
- (95) B. Li, D. O. V. Alonso, and V. Daggett. The molecular basis for the inverse temperature transition of elastin. *Journal of Molecular Biology*, 305:581–592, 2001.
- (96) D. Schmaljohann. Thermo- and pH-responsive polymers in drug delivery. *Advanced Drug Delivery Reviews*, 58:1655–1670, 2006.
- (97) D. Kurzbach, M. J. N. Junk, and D. Hinderberger. Nanoscale inhomogeneities in thermoresponsive polymers. *Macromolecular Rapid Communications*, 34:119–134, 2013.
- (98) M. J. N. Junk, W. Li, A. D. Schlueter, G. Wegner, H. W. Spiess, A. Zhang, and D. Hinderberger. EPR spectroscopic characterization of local nanoscopic heterogeneities during the thermal collapse of thermoresponsive dendronized polymers. *Angewandte Chemie International Edition*, 49:5683–5687, 2010.
- (99) D. Kurzbach, M. Schoemer, V. S. Wilms, H. Frey, and D. Hinderberger. How structure-related collapse mechanisms determine nanoscale inhomogeneities in thermoresponsive polymers. *Macromolecules*, 45:7535–7548, 2012.
- (100) J. Reichenwallner, A. Thomas, L. Nuhn, T. Johann, A. Meister, H. Frey, and D. Hinderberger. Tunable dynamic hydrophobic attachment of guest molecules in amphiphilic core-shell polymers. *Polymer Chemistry*, 7:5783–5798, 2016.
- (101) A. N. Cimato, L. L. Piehl, G. B. Facorro, H. B. Torti, and A. A. Hager. Antioxidant effects of water- and lipid-soluble nitroxide radicals in liposomes. *Free Radical Biology and Medicine*, 37:2042–2051, 2004.
- (102) D. W. Urry, T. L. Trapane, and K. U. Prasad. Phase-structure transitions of the elastin polypentapeptide–water system within the framework of composition–temperature studies. *Biopolymers*, 24:2345–2356, 1985.

-
- (103) E. Garanger, S. R. MacEwan, O. Sandre, A. Brûlet, L. Bataille, A. Chilkoti, and S. Lecommandoux. Structural evolution of a stimulus-responsive diblock polypeptide micelle by temperature tunable compaction of its core. *Macromolecules*, 48:6617–6627, 2015.
- (104) T. Asakura, J. Ashida, and K. Ohgo. Conformational characterization of (Val-Pro-Gly-Val-Gly)₆ with ¹³C solid state NMR. *Polymer Journal*, 35:293–296, 2003.
- (105) M. Hong, D. Isailovic, R. A. McMillan, and V. P. Conticello. Structure of an elastin-mimetic polypeptide by solid-state NMR chemical shift analysis. *Biopolymers*, 70:158–168, 2003.
- (106) D. W. Urry, D. C. Gowda, T. M. Parker, C.-H. Luan, M. C. Reid, C. M. Harris, A. Patanaik, and R. D. Harris. Hydrophobicity scale for proteins based on inverse temperature transitions. *Biopolymers*, 32:1243–1250, 1992.
- (107) X. Wang, X. Qiu, and C. Wu. Comparison of the coil-to-globule and the globule-to-coil transitions of a single poly(N-isopropylacrylamide) homopolymer chain in water. *Macromolecules*, 31:2972–2976, 1998.
- (108) P. Kujawa, V. Aseyev, H. Tenhu, and F. M. Winnik. Temperature-sensitive properties of poly(N-isopropylacrylamide) mesoglobules formed in dilute aqueous solutions heated above their demixing point. *Macromolecules*, 39:7686–7693, 2006.
- (109) X. Ma, C. Sun, J. Huang, and G. S. Boutis. Thermal hysteresis in the backbone and side chain dynamics of the elastin mimetic peptide [VPGVG]₃ revealed by ²H NMR. *Journal of Physical Chemistry B*, 116:555–564, 2012.
- (110) J. Reguera, J. M. Lagarón, M. Alonso, V. Reboto, B. Calvo, and J. C. Rodríguez-Cabello. Thermal behavior and kinetic analysis of the chain unfolding and refolding and of the concomitant nonpolar solvation and desolvation of two elastin-like polymers. *Macromolecules*, 36:8470–8476, 2003.
- (111) D. W. Urry. Molecular machines: How motion and other functions of living organisms can result from reversible chemical changes. *Angewandte Chemie International Edition*, 32:819–841, 1993.
- (112) C.-H. Luan and D. W. Urry. Solvent deuteration enhancement of hydrophobicity: DSC study of the inverse temperature transition of elastin-based polypeptides. *Journal of Physical Chemistry*, 95:7896–7900, 1991.
- (113) M. A. Ahmed, V. V. Bamm, G. Harauz, and V. Ladizhansky. Solid-state NMR spectroscopy of membrane-associated myelin basic protein—conformation and dynamics of an immunodominant epitope. *Biophysical Journal*, 99:1247–1255, 2010.
- (114) E. J. Arroyo and S. S. Scherer. On the molecular architecture of myelinated fibers. *Histochemistry and Cell Biology*, 113:1–18, 2000.
- (115) N. Baumann and D. Pham-Dinh. Biology of oligodendrocyte and myelin in the mammalian central nervous system. *Physiological Reviews*, 81:871–927, 2001.
- (116) E.-M. Krämer, A. Schardt, and K.-A. Nave. Membrane traffic in myelinating oligodendrocytes. *Microscopy Research and Technique*, 52:656–671, 2001.
- (117) J. M. Boggs and M. A. Moscarello. Structural organization of the human myelin membrane. *Biochimica et Biophysica Acta (BBA) - Reviews on Biomembranes*, 515:1–21, 1978.
- (118) D. D. Wood and M. A. Moscarello. Is the myelin membrane abnormal in multiple sclerosis? *Journal of Membrane Biology*, 79:195–201, 1984.
- (119) Y. Hu, I. Doudevski, D. Wood, M. Moscarello, C. Husted, C. Genain, J. A. Zasadzinski, and J. Israelachvili. Synergistic interactions of lipids and myelin basic protein. *Proceedings of the National Academy of Sciences of the United States of America*, 101:13466–13471, 2004.

- (120) Y. Min, K. Kristiansen, J. M. Boggs, C. Husted, J. A. Zasadzinski, and J. Israelachvili. Interaction forces and adhesion of supported myelin lipid bilayers modulated by myelin basic protein. *Proceedings of the National Academy of Sciences of the United States of America*, 106:3154–3159, 2009.
- (121) D. R. Kattnig, T. Bund, J. M. Boggs, G. Harauz, and D. Hinderberger. Lateral self-assembly of 18.5-kDa myelin basic protein (MBP) charge component-C1 on membranes. *Biochimica et Biophysica Acta (BBA) - Biomembranes*, 1818:2636–2647, 2012.
- (122) G. Harauz and A. A. Musse. A tale of two citrullines—structural and functional aspects of myelin basic protein deimination in health and disease. *Neurochemical Research*, 32:137–158, 2007.
- (123) H. H. Berlet, H. Bischoff, and F. Weinhardt. Divalent metals of myelin and their differential binding by myelin basic protein of bovine central nervous system. *Neuroscience Letters*, 179:75–78, 1994.
- (124) C. Baran, G. S. Smith, V. V. Bamm, G. Harauz, and J. S. Lee. Divalent cations induce a compaction of intrinsically disordered myelin basic protein. *Biochemical and Biophysical Research Communications*, 391:224–229, 2010.
- (125) C. Earl, A. Chantry, N. Mohammed, and P. Glynn. Zinc ions stabilise the association of basic protein with brain myelin membranes. *Journal of Neurochemistry*, 51:718–724, 1988.
- (126) G. S. T. Smith, L. Chen, V. V. Bamm, J. R. Dutcher, and G. Harauz. The interaction of zinc with membrane-associated 18.5 kDa myelin basic protein: an attenuated total reflectance-Fourier transform infrared spectroscopic study. *Amino Acids*, 39:739–750, 2010.
- (127) T. Bund, J. M. Boggs, G. Harauz, N. Hellmann, and D. Hinderberger. Copper uptake induces self-assembly of 18.5 kDa myelin basic protein (MBP). *Biophysical Journal*, 99:3020–3028, 2010.
- (128) P. Dharmasaroja. Specificity of autoantibodies to epitopes of myelin proteins in multiple sclerosis. *Journal of the Neurological Sciences*, 206:7–16, 2003.
- (129) A. Facchinetti, P. Gallo, P. Perini, S. Mezzalana, F. Ronchese, and G. Biasi. The MBP-reactive repertoire is shaped by recognition of minor histocompatibility antigens. *Journal of Neuroimmunology*, 148:154–161, 2004.
- (130) E. E. Golds and P. E. Braun. Cross-linking studies on the conformation and dimerization of myelin basic protein in solution. *Journal of Biological Chemistry*, 253:8171–8177, 1978.
- (131) A. M. Edwards, N. W. Ross, J. B. Ulmer, and P. E. Braun. Interaction of myelin basic protein and proteolipid protein. *Journal of Neuroscience Research*, 22:97–102, 1989.
- (132) A. T. Campagnoni and R. P. Skoff. The pathobiology of myelin mutants reveal novel biological functions of the MBP and PLP genes. *Brain Pathology*, 11:74–91, 2001.
- (133) R. Smith. The basic protein of CNS myelin: Its structure and ligand binding. *Journal of Neurochemistry*, 59:1589–1608, 1992.
- (134) P. Riccio, A. Fasano, N. Borenshtein, T. Blevé-Zacheo, and D. A. Kirschner. Multilamellar packing of myelin modeled by lipid-bound MBP. *Journal of Neuroscience Research*, 59:513–521, 2000.
- (135) D. S. Libich and G. Harauz. Backbone dynamics of the 18.5 kDa isoform of myelin basic protein reveals transient α -helices and a calmodulin-binding site. *Biophysical Journal*, 94:4847–4866, 2008.
- (136) J. M. Boggs, D. D. Wood, and M. A. Moscarello. Hydrophobic and electrostatic interactions of myelin basic protein with lipid. Participation of N-terminal and C-terminal portions. *Biochemistry*, 20:1065–1073, 1981.

-
- (137) J. M. Boggs, L. S. Chia, G. Rangaraj, and M. A. Moscarello. Interaction of myelin basic protein with different ionization states of phosphatidic acid and phosphatidylserine. *Chemistry and Physics of Lipids*, 39:165–184, 1986.
- (138) M. B. Sankaram, P. J. Brophy, and D. Marsh. Selectivity of interaction of phospholipids with bovine spinal cord myelin basic protein studied by spin-label electron spin resonance. *Biochemistry*, 28:9699–9707, 1989.
- (139) K. A. Vassall, A. D. Jenkins, V. V. Bamm, and G. Harauz. Thermodynamic analysis of the disorder-to- α -helical transition of 18.5-kDa myelin basic protein reveals an equilibrium intermediate representing the most compact conformation. *Journal of Molecular Biology*, 427:1977–1992, 2015.
- (140) S. Aggarwal, N. Snaidero, G. Pähler, S. Frey, P. Sánchez, M. Zweckstetter, A. Janshoff, A. Schneider, M.-T. Weil, I. A. T. Schaap, J. Görlich, and M. Simons. Myelin membrane assembly is driven by a phase transition of myelin basic proteins into a cohesive protein meshwork. *PLoS Biology*, 11:e1001577:1–14, 2013.
- (141) A. Raasakka, S. Ruskamo, J. Kowal, R. Barker, A. Baumann, A. Martel, J. Tuusa, M. Myllykoski, J. Bürck, A. Ulrich, H. Stahlberg, and P. Kursula. Membrane association landscape of myelin basic protein portrays formation of the myelin major dense line. *Scientific Reports*, 7:1–18, 2017.
- (142) G. W. Brady, N. S. Murthy, and D. B. Fein. The effect of basic myelin protein on multilayer membrane formation. *Biophysical Journal*, 34:345–350, 1981.
- (143) I. R. Bates, J. M. Boggs, J. B. Feix, and G. Harauz. Membrane-anchoring and charge effects in the interaction of myelin basic protein with lipid bilayers studied by site-directed spin labeling. *Journal of Biological Chemistry*, 278:29041–29047, 2003.
- (144) M. Moscarello, D. Wood, C. Ackerley, and C. Boulias. Myelin in multiple sclerosis is developmentally immature. *Journal of Clinical Investigation*, 94:146–154, 1994.
- (145) K. W. Wucherpfennig, I. Catz, S. Hausmann, J. L. Strominger, L. Steinman, and K. G. Warren. Recognition of the immunodominant myelin basic protein peptide by autoantibodies and HLA-DR2-restricted T cell clones from multiple sclerosis patients. Identity of key contact residues in the B-cell and T-cell epitopes. *Journal of Clinical Investigation*, 100:1114–1122, 1997.
- (146) K. G. Warren, I. Catz, and L. Steinman. Fine specificity of the antibody response to myelin basic protein in the central nervous system in multiple sclerosis: The minimal B-cell epitope and a model of its features. *Proceedings of the National Academy of Sciences of the United States of America*, 92:11061–11065, 1995.
- (147) A. A. Musse, J. M. Boggs, and G. Harauz. Deimination of membrane-bound myelin basic protein in multiple sclerosis exposes an immunodominant epitope. *Proceedings of the National Academy of Sciences of the United States of America*, 103:4422–4427, 2006.
- (148) H. Lassmann. Mechanisms of white matter damage in multiple sclerosis. *GLIA*, 62:1816–1830, 2014.
- (149) B. D. Trapp and K.-A. Nave. Multiple sclerosis: An immune or neurodegenerative disorder? *Annual Review of Neuroscience*, 31:247–269, 2008.
- (150) B. Ohler, K. Graf, R. Bragg, T. Lemons, R. Coe, C. Genain, J. Israelachvili, and C. Husted. Role of lipid interactions in autoimmune demyelination. *Biochimica et Biophysica Acta (BBA) - Molecular Basis of Disease*, 1688:10–17, 2004.
- (151) R. Shaharabani, M. Ram-On, R. Avinery, R. Aharoni, R. Arnon, Y. Talmon, and R. Beck. Structural transition in myelin membrane as initiator of multiple sclerosis. *Journal of the American Chemical Society*, 138:12159–12165, 2016.

- (152) D. W. Lee, X. Banquy, K. Kristiansen, Y. Kaufman, J. M. Boggs, and J. N. Israelachvili. Lipid domains control myelin basic protein adsorption and membrane interactions between model myelin lipid bilayers. *Proceedings of the National Academy of Sciences of the United States of America*, 111:E768–E775, 2014.
- (153) P. K. Stys, G. W. Zampono, J. van Minnen, and J. J. G. Geurts. Will the real multiple sclerosis please stand up? *Nature Reviews Neuroscience*, 13:507–514, 2012.
- (154) A. Compston and A. Coles. Multiple sclerosis. *Lancet*, 359:1221–1231, 2002.
- (155) A. Lewin, S. Hamiton, A. Witkover, P. Langford, R. Nicholas, J. Chataway, and C. R. M. Bangham. Free serum haemoglobin is associated with brain atrophy in secondary progressive multiple sclerosis. *Wellcome Open Research*, 1, 2016.
- (156) L. Steinman. Multiple sclerosis: A coordinated review immunological attack against myelin in the central nervous system. *Cell*, 85:299–302, 1996.
- (157) S. L. Hauser and J. R. Oksenberg. The neurobiology of multiple sclerosis: Genes, inflammation, and neurodegeneration. *Neuron*, 52:61–76, 2006.
- (158) C. W. M. Adams. Perivascular iron deposition and other vascular damage in multiple sclerosis. *Journal of Neurology, Neurosurgery and Psychiatry*, 51:260–265, 1988.
- (159) E. M. Haacke, M. Makki, Y. Ge, M. Maheshwari, V. Sehgal, J. Hu, M. Selvan, Z. Wu, Z. Latif, Y. Xuan, O. Khan, J. Garbern, and R. I. Grossmann. Characterizing iron deposition in multiple sclerosis lesions using susceptibility weighted imaging. *Journal of Magnetic Resonance Imaging*, 29:537–544, 2009.
- (160) V. V. Bamm and G. Harauz. Hemoglobin as a source of iron overload in multiple sclerosis: Does multiple sclerosis share risk factors with vascular disorders? *Cellular and Molecular Life Sciences*, 71:1789–1798, 2014.
- (161) J. M. Boggs, P. M. Yip, G. Rangaraj, and E. Jo. Effect of posttranslational modifications to myelin basic protein on its ability to aggregate acidic lipid vesicles. *Biochemistry*, 36:5065–5071, 1997.
- (162) N. Ishiyama, I. R. Bates, C. M. Hill, D. D. Wood, P. Matharu, N. J. Viner, M. A. Moscarello, and G. Harauz. The effects of deimination of myelin basic protein on structures formed by its interaction with phosphoinositide-containing lipid monolayers. *Journal of Structural Biology*, 136:30–45, 2001.
- (163) S. Suresh, C. Wang, R. Nanekar, P. Kursula, and J. M. Edwardson. Myelin basic protein and myelin protein 2 act synergistically to cause stacking of lipid bilayers. *Biochemistry*, 49:3456–3463, 2010.
- (164) K. A. Vassall, V. V. Bamm, A. D. Jenkins, C. J. Velte, D. R. Kattnig, J. M. Boggs, D. Hinderberger, and G. Harauz. Substitutions mimicking deimination and phosphorylation of 18.5-kDa myelin basic protein exert local structural effects that subtly influence its global folding. *Biochimica et Biophysica Acta (BBA) - Biomembranes*, 1858:1262–1277, 2016.
- (165) J. D. Lutton, R. Winston, and T. C. Rodman. Multiple sclerosis: Etiological mechanisms and future directions. *Experimental Biology and Medicine*, 229:12–20, 2004.
- (166) I. Micu, J. R. Plemel, C. Lachance, J. Proft, A. J. Jansen, K. Cummins, J. van Minnen, and P. K. Stys. The molecular physiology of the axo-myelinic synapse. *Experimental Neurology*, 276:41–50, 2016.
- (167) G. Harauz, V. Ladizhansky, and J. M. Boggs. Structural polymorphism and multifunctionality of myelin basic protein. *Biochemistry*, 48:8094–8104, 2009.
- (168) H. Brockman. Lipid monolayers: Why use half a membrane to characterize protein–membrane interactions? *Current Opinion in Structural Biology*, 9:438–443, 1999.

- (169) A. Giehl, T. Lemm, O. Bartelsen, K. Sandhoff, and A. Blume. Interaction of the GM2-activator protein with phospholipid-ganglioside bilayer membranes and with monolayers at the air–water interface. *European Journal of Biochemistry*, 261:650–658, 1999.
- (170) P. Calvez, E. Demers, E. Boisselier, and C. Salesse. Analysis of the contribution of saturated and polyunsaturated phospholipid monolayers to the binding of proteins. *Langmuir*, 27:1373–1379, 2011.
- (171) P. Calvez, S. Bussi eres,  eric Demers, and C. Salesse. Parameters modulating the maximum insertion pressure of proteins and peptides in lipid monolayers. *Biochimie*, 91:718–733, 2009.
- (172) P. Rispoli, R. Carzino, T. Svaldo-Lanero, A. Relini, O. Cavalleri, A. Fasano, G. Liuzzi, G. Carlone, P. Riccio, A. Gliozzi, and R. Rolandi. A thermodynamic and structural study of myelin basic protein in lipid membrane models. *Biophysical Journal*, 93:1999–2010, 2007.
- (173) L. Cristofolini, M. P. Fontana, F. Serra, A. Fasano, P. Riccio, and O. Kononov. Microstructural analysis of the effects of incorporation of myelin basic protein in phospholipid layers. *European Biophysics Journal*, 34:1041–1048, 2005.
- (174) H. Haas, R. Steitz, A. Fasano, G. M. Liuzzi, E. Polverini, P. Cavatorta, and P. Riccio. Lamellar order within langmuir-blodgett multilayers from phospholipid and myelin basic protein: A neutron reflectivity study. *Langmuir*, 23:8491–8496, 2007.
- (175) E. Polverini, S. Arisi, P. Cavatorta, T. Berzina, L. Cristofolini, A. Fasano, P. Riccio, and M. P. Fontana. Interaction of myelin basic protein with phospholipid monolayers: Mechanism of protein penetration. *Langmuir*, 19:872–877, 2003.
- (176) H. Inouye and D. A. Kirschner. Membrane interactions in nerve myelin, II. Determination of surface charge from biochemical data. *Biophysical Journal*, 53:247–260, 1988.
- (177) V. V. Bamm, D. K. Lanthier, E. L. Stephenson, G. S. Smith, and G. Harauz. In vitro study of the direct effect of extracellular hemoglobin on myelin components. *Biochimica et Biophysica Acta (BBA) - Molecular Basis of Disease*, 1852:92–103, 2015.
- (178) A. Blume and A. Kerth. Peptide and protein binding to lipid monolayers studied by FT-IRRA spectroscopy. *Biochimica et Biophysica Acta (BBA) - Biomembranes*, 1828:2294–2305, 2013.
- (179) A. Radhakrishnan, T. G. Anderson, and H. M. McConnell. Condensed complexes, rafts, and the chemical activity of cholesterol in membranes. *Proceedings of the National Academy of Sciences of the United States of America*, 97:12422–12427, 2000.
- (180) H. M. McConnell and A. Radhakrishnan. Condensed complexes of cholesterol and phospholipids. *Biochimica et Biophysica Acta (BBA) - Biomembranes*, 1610:159–173, 2003.
- (181) R. G. Oliveira and B. Maggio. Compositional domain immiscibility in whole myelin monolayers at the air–water interface and Langmuir–Blodgett films. *Biochimica et Biophysica Acta (BBA) - Biomembranes*, 1561:238–250, 2002.
- (182) Y. Min, T. F. Alig, D. W. Lee, J. M. Boggs, J. Israelachvili, and J. A. Zasadzinski. Critical and off-critical and miscibility transitions and in model and extracellular and cytoplasmic myelin and lipid monolayers. *Biophysical Journal*, 100:1490–1498, 2011.
- (183) L. S. DeBruin and G. Harauz. White matter rafting—membrane microdomains in myelin. *Neurochemical Research*, 32:213–228, 2007.
- (184) C. M. Rosetti, B. Maggio, and R. G. Oliveira. The self-organization of lipids and proteins of myelin at the membrane interface. Molecular factors underlying the microheterogeneity of domain segregation. *Biochimica et Biophysica Acta (BBA) - Biomembranes*, 1778:1665–1675, 2008.

- (185) M. A. Keniry and R. Smith. Circular dichroic analysis of the secondary structure of myelin basic protein and derived peptides bound to detergents and to lipid vesicles. *Biochimica et Biophysica Acta (BBA) - Protein Structure*, 578:381–391, 1979.
- (186) M. B. A. ter Beest and D. Hoekstra. Interaction of myelin basic protein with artificial membranes. Parameters governing binding, aggregation and dissociation. *European Journal of Biochemistry*, 211:689–696, 1993.
- (187) B. D. Kelley, D. I. Wang, and T. A. Hatton. Affinity-based reversed micellar protein extraction: 1. Principles and protein-ligand systems. *Biotechnology and Bioengineering*, 42:1199–1208, 1993.
- (188) N. K. Menon, R. E. Williams, K. Kampf, and A. T. Campagnoni. An analysis of the regions of the myelin basic protein that bind to phosphatidylcholine. *Neurochemical Research*, 15:777–783, 1990.
- (189) A. V. Samsonov, I. Mihalyov, and F. S. Cohen. Characterization of cholesterol-sphingomyelin domains and their dynamics in bilayer membranes. *Biophysical Journal*, 81:1486–1500, 2001.
- (190) D. N. Arvanitis, W. Min, Y. Gong, Y. M. Heng, and J. M. Boggs. Two types of detergent-insoluble, glycosphingolipid/cholesterol-rich membrane domains from isolated myelin. *Journal of Neurochemistry*, 94:1696–1710, 2005.
- (191) F. C. Tsui, D. M. Ojcius, and W. L. Hubbell. The intrinsic pK_a values for phosphatidylserine and phosphatidylethanolamine in phosphatidylcholine host bilayers. *Biophysical Journal*, 49:459–468, 1986.
- (192) J. G. Stollery, J. M. Boggs, and M. A. Moscarello. Variable interaction of spin-labeled human myelin basic protein with different acidic lipids. *Biochemistry*, 19:1219–1226, 1980.
- (193) C. Schwieger and A. Blume. Interaction of poly(L-arginine) with negatively charged DPPG membranes: Calorimetric and monolayer studies. *Biomacromolecules*, 10:2152–2161, 2009.
- (194) M. Hoernke, C. Schwieger, A. Kerth, and A. Blume. Binding of cationic pentapeptides with modified side chain lengths to negatively charged lipid membranes: Complex interplay of electrostatic and hydrophobic interactions. *Biochimica et Biophysica Acta (BBA) - Biomembranes*, 1818:1663–1672, 2012.
- (195) A. Hädicke and A. Blume. Binding of short cationic peptides $(KX)_4K$ to negatively charged DPPG monolayers: Competition between electrostatic and hydrophobic interactions. *Langmuir*, 31:12203–12214, 2015.
- (196) A. Hädicke and A. Blume. Binding of the cationic peptide $(KL)_4K$ to lipid monolayer at the air–water interface: Effect of lipid headgroup charge, acyl chain length and acyl chain saturation. *Journal of Physical Chemistry B*, 120:3880–3887, 2016.
- (197) J. M. Boggs, G. Rangaraj, and A. Dicko. Effect of phosphorylation of phosphatidylinositol on myelin basic protein-mediated binding of actin filaments to lipid bilayers in vitro. *Biochimica et Biophysica Acta (BBA) - Biomembranes*, 1818:2217–2227, 2012.
- (198) J. McLaurin, C. Hew, and M. A. Moscarello. Myelin basic protein does not contain a phosphatidylinositol anchor. *Biochemical Journal*, 269:278–279, 1990.
- (199) J. K. Kim, F. G. Mastronardi, D. D. Wood, D. M. Lubman, R. Zand, and M. A. Moscarello. Multiple sclerosis: An important role for post-translational modifications of myelin basic protein in pathogenesis. *Molecular and Cellular Proteomics*, 2:453–462, 2003.
- (200) G. Harauz. Turning white matter “inside-out” by hyper-deimination of myelin basic protein. In A. P. Nicholas, S. K. Bhattacharya, and P. R. Thompson, editors, *Protein Deimination in Human Health and Disease*. Springer International Publishing, 2. edition, 2017.

- (201) B. Sarg, K. Faserl, and H. H. Lindner. Identification of novel site-specific alterations in the modification level of myelin basic protein isolated from mouse brain at different ages using capillary electrophoresis–mass spectrometry. *Proteomics*, 17:1700269:1–8, 2017.
- (202) E. Jo and J. M. Boggs. Aggregation of acidic lipid vesicles by myelin basic protein: Dependence on potassium concentration. *Biochemistry*, 34:13705–13716, 1995.
- (203) P. R. Finch, D. D. Wood, and M. A. Moscarello. The presence of citrulline in a myelin protein fraction. *FEBS Letters*, 15:145–148, 1971.
- (204) D. D. Wood and M. A. Moscarello. The isolation, characterization, and lipid-aggregating properties of a citrulline containing myelin basic protein. *Journal of Biological Chemistry*, 264:5121–5127, 1989.
- (205) J. M. Boggs, G. Rangaraj, K. M. Koshy, C. Ackerley, D. D. Wood, and M. A. Moscarello. Highly deiminated isoform of myelin basic protein from multiple sclerosis brain causes fragmentation of lipid vesicles. *Journal of Neuroscience Research*, 57:529–535, 1999.
- (206) L. V. Shanshiashvili, N. C. Suknidze, G. G. Machaidze, D. G. Mikeladze, and J. J. Ramsden. Adhesion and clustering of charge isomers of myelin basic protein at model myelin membranes. *Archives of Biochemistry and Biophysics*, 419:170–177, 2003.
- (207) J. M. Boggs. Myelin basic protein: A multifunctional protein. *Cellular and Molecular Life Sciences*, 63:1945–1961, 2006.
- (208) D. R. Beniac, D. D. Wood, N. Palaniyar, F. P. Ottensmeyer, M. A. Moscarello, and G. Harauz. Cryoelectron microscopy of protein–lipid complexes of human myelin basic protein charge isomers differing in degree of citrullination. *Journal of Structural Biology*, 129:80–95, 2000.
- (209) L. B. Pritzker, S. Joshi, J. J. Gowan, G. Harauz, and M. A. Moscarello. Deimination of myelin basic protein. 1. Effect of deimination of arginyl residues of myelin basic protein on its structure and susceptibility to digestion by cathepsin D. *Biochemistry*, 39:5374–5381, 2000.
- (210) M. A. Moscarello, F. G. Mastronardi, and D. D. Wood. The role of citrullinated proteins suggests a novel mechanism in the pathogenesis of multiple sclerosis. *Neurochemical Research*, 32:251–256, 2007.
- (211) L. Cao, R. Goodin, D. D. Wood, M. A. Moscarello, and J. N. Whitaker. Rapid release and unusual stability of immunodominant peptide 45–89 from citrullinated myelin basic protein. *Biochemistry*, 38:6157–6163, 1999.
- (212) D. D. Wood, J. M. Bilbao, P. O’Connors, and M. A. Moscarello. Acute multiple sclerosis (Marburg type) is associated with developmentally immature myelin basic protein. *Annals of Neurology*, 40:18–24, 1996.
- (213) D. R. Beniac, D. D. Wood, N. Palaniyar, F. P. Ottensmeyer, M. A. Moscarello, and G. Harauz. Marburg’s variant of multiple sclerosis correlates with a less compact structure of myelin basic protein. *Molecular Cell Biology Research Communications*, 1:48–51, 1999.
- (214) L. B. Pritzker, S. Joshi, G. Harauz, and M. A. Moscarello. Deimination of myelin basic protein. 2. Effect of methylation of MBP on its deimination by peptidylarginine deiminase. *Biochemistry*, 39:5382–5388, 2000.
- (215) R. Zand, M. X. Li, J. Xiaoying, and D. Lubman. Determination of the sites of posttranslational modifications in the charge isomers of bovine myelin basic protein by capillary electrophoresis–mass spectroscopy. *Biochemistry*, 37:2441–2449, 1998.
- (216) I. R. Bates, P. Matharu, N. Ishiyama, D. Rochon, D. D. Wood, E. Polverini, M. A. Moscarello, N. J. Viner, and G. Harauz. Characterization of a recombinant murine 18.5-kDa myelin basic protein. *Protein Expression and Purification*, 20:285–299, 2000.

- (217) I. R. Bates, D. S. Libich, D. D. Wood, M. A. Moscarello, and G. Harauz. An Arg/Lys \rightarrow Gln mutant of recombinant murine myelin basic protein as a mimic of the deiminated form implicated in multiple sclerosis. *Protein Expression and Purification*, 25:330–341, 2002.
- (218) C. M. Taylor, T. Coetzee, and S. E. Pfeiffer. Detergent-insoluble glycosphingolipid/cholesterol microdomains of the myelin membrane. *Journal of Neurochemistry*, 81:993–1004, 2002.
- (219) L. S. DeBruin, J. D. Haines, L. A. Wellhauser, G. Radeva, V. Schonmann, D. Bienzle, and G. Harauz. Developmental partitioning of myelin basic protein into membrane microdomains. *Journal of Neuroscience Research*, 80:211–225, 2005.
- (220) P. I. Kuzmin, S. A. Akimov, Y. A. Chizmadzhev, J. Zimmerberg, and F. S. Cohen. Line tension and interaction energies of membrane rafts calculated from lipid splay and tilt. *Biophysical Journal*, 88:1120–1133, 2005.
- (221) A. J. García-Sáez, S. Chiantia, and P. Schwille. Effect of line tension on the lateral organization of lipid membranes. *Journal of Biological Chemistry*, 282:33537–33544, 2007.
- (222) C. Nicolini, J. Baranski, S. Schlummer, J. Palomo, M. Lumbierres-Burgues, M. Kahms, J. Kuhlmann, S. Sanchez, E. Gratton, H. Waldmann, and R. Winter. Visualizing association of N-Ras in lipid microdomains: Influence of domain structure and interfacial adsorption. *Journal of the American Chemical Society*, 128:192–201, 2006.
- (223) G. Staneva, M. I. Angelova, and K. Koumanov. Phospholipase A₂ promotes raft budding and fission from giant liposomes. *Chemistry and Physics of Lipids*, 129:53–62, 2004.
- (224) H. C. Kinney, J. Karthigasan, N. I. Borenshteyn, J. D. Flax, and D. A. Kirschner. Myelination in the developing human brain: Biochemical correlates. *Neurochemical Research*, 19:983–996, 1994.
- (225) K. Oshida, T. Shimizu, M. Takase, Y. Tamura, T. Shimizu, and Y. Yamashiro. Effects of dietary sphingomyelin on central nervous system myelination in developing rats. *Pediatric Research*, 53:589–593, 2003.
- (226) D. Wheeler, V. V. R. Bandaru, P. A. Calabresi, A. Nath, and N. J. Haughey. A defect of sphingolipid metabolism modifies the properties of normal appearing white matter in multiple sclerosis. *Brain*, 131:3092–3102, 2008.
- (227) A. Jana and K. Pahan. Sphingolipids in multiple sclerosis. *Neuromolecular Medicine*, 12:351–361, 2010.
- (228) V. Brinkmann, A. Billich, T. Baumruker, P. Heining, R. Schmouder, G. Francis, S. Aradhye, and P. Burtin. Fingolimod (FTY720): Discovery and development of an oral drug to treat multiple sclerosis. *Nature Reviews Drug Discovery*, 9:883–897, 2010.
- (229) J. Chun and H.-P. Hartung. Mechanism of action of oral fingolimod (FTY720) in multiple sclerosis. *Clinical Neuropharmacology*, 33:91–101, 2010.
- (230) M. A. Fishman, H. C. Agrawal, A. Alexander, J. Golterman, R. E. Martenson, and R. F. Mitchell. Biochemical maturation of human central nervous system myelin. *Journal of Neurochemistry*, 24:689–694, 1975.
- (231) C. M. Deber and S. J. Reynolds. Central nervous system myelin: Structure, function and pathology. *Clinical Biochemistry*, 24:113–134, 1991.
- (232) A. N. Davison and M. Wajda. Cerebral lipids in multiple sclerosis. *Journal of Neurochemistry*, 9:427–432, 1962.
- (233) J. N. Cumings and H. Goodwin. Sphingolipids and phospholipids of myelin in multiple sclerosis. *Lancet*, 292:664–665, 1968.

- (234) A. Meister, C. Nicolini, H. Waldmann, J. Kuhlmann, A. Kerth, R. Winter, and A. Blume. Insertion of lipidated Ras proteins into lipid monolayers studied by infrared reflection absorption spectroscopy (IRRAS). *Biophysical Journal*, 91:1388–1401, 2006.
- (235) C. Schwieger, A. Meister, S. Daum, A. Blume, and K. Bacia. Binding of the GTPase Sar1 to a lipid membrane monolayer: Insertion and orientation studied by infrared reflection-absorption spectroscopy. *Polymers*, 9:1–25, 2017.
- (236) C. R. Flach, J. W. Brauner, J. W. Taylor, R. C. Baldwin, and R. Mendelsohn. External reflection FTIR of peptide monolayer films in situ at the air/water interface: Experimental design, spectra–structure correlations, and effects of hydrogen–deuterium exchange. *Biophysical Journal*, 67:402–410, 1994.
- (237) C. Schwieger, B. Chen, C. Tschierske, J. Kressler, and A. Blume. Organization of T-shaped facial amphiphiles at the air/water interface studied by infrared reflection absorption spectroscopy. *Journal of Physical Chemistry B*, 116:12245–12256, 2012.
- (238) A. Blume. A comparative study of the phase transitions of phospholipid bilayers and monolayers. *Biochimica et Biophysica Acta (BBA) - Biomembranes*, 557:32–44, 1979.
- (239) E. Goormaghtigh, V. Cabiaux, and J.-M. Ruyschaert. Determination of soluble and membrane protein structure by fourier transform infrared spectroscopy. III. Secondary structures. In H. J. Hilderson and G. B. Ralston, editors, *Physicochemical Methods in the Study of Biomembranes*, volume 23 of *Subcellular Biochemistry*. Plenum Press, 1994.
- (240) C. Farès, D. S. Libich, and G. Harauz. Solution NMR structure of an immunodominant epitope of myelin basic protein. Conformational dependence on environment of an intrinsically unstructured protein. *FEBS Journal*, 273:601–614, 2006.
- (241) M. A. M. Ahmed, M. De Avila, E. Polverini, K. Bessonov, V. V. Bamm, and G. Harauz. Solution nuclear magnetic resonance structure and molecular dynamics simulations of a murine 18.5 kDa myelin basic protein segment (S72–S107) in association with dodecylphosphocholine micelles. *Biochemistry*, 51:7475–7487, 2012.
- (242) E. Polverini, E. P. Coll, D. P. Tielemann, and G. Harauz. Conformational choreography of a molecular switch region in myelin basic protein—Molecular dynamics shows induced folding and secondary structure type conversion upon threonyl phosphorylation in both aqueous and membrane-associated environments. *Biochimica et Biophysica Acta (BBA) - Biomembranes*, 1808:674–683, 2011.
- (243) F. Bagnato, S. Hametner, B. Yao, P. van Gelderen, H. Merkle, F. K. Cantor, H. Lassmann, and J. H. Duyn. Tracking iron in multiple sclerosis: A combined imaging and histopathological study at 7 Tesla. *Brain*, 134:3602–3615, 2011.
- (244) C. A. Habib, M. Liu, N. Bawany, J. Garbern, I. Krumbein, H.-J. Mentzel, J. Reichenbach, C. Magnano, R. Zivadinov, and E. M. Haacke. Assessing abnormal iron content in the deep gray matter of patients with multiple sclerosis versus healthy controls. *American Journal of Neuroradiology*, 33:252–258, 2012.
- (245) D. Elbaum, J. Harrington, E. F. Roth, and R. L. Nagel. Surface activity of hemoglobin S and other human hemoglobin variants. *Biochimica et Biophysica Acta (BBA) - Protein Structure*, 427:57–69, 1976.
- (246) M. Ge, S. B. Ranavavare, and J. H. Freed. ESR studies of stearic acid binding to bovine serum albumin. *Biochimica et Biophysica Acta*, 1036:228–236, 1990.
- (247) S. E. Cramer, C. Bauer, G. Jeschke, and H. W. Spiess. High-field epr studies on polymer film formation from colloidal dispersions. *Applied Magnetic Resonance*, 21:495–506, 2001.
- (248) Y. Akdogan, J. Heller, H. Zimmermann, and D. Hinderberger. The solvation of nitroxide radicals in ionic liquids studied by high-field EPR spectroscopy. *Physical Chemistry Chemical Physics*, 12:7874–7882, 2010.

APPENDIX A

Thermoresponsive peptide polymers

A.1 Diblock ELP

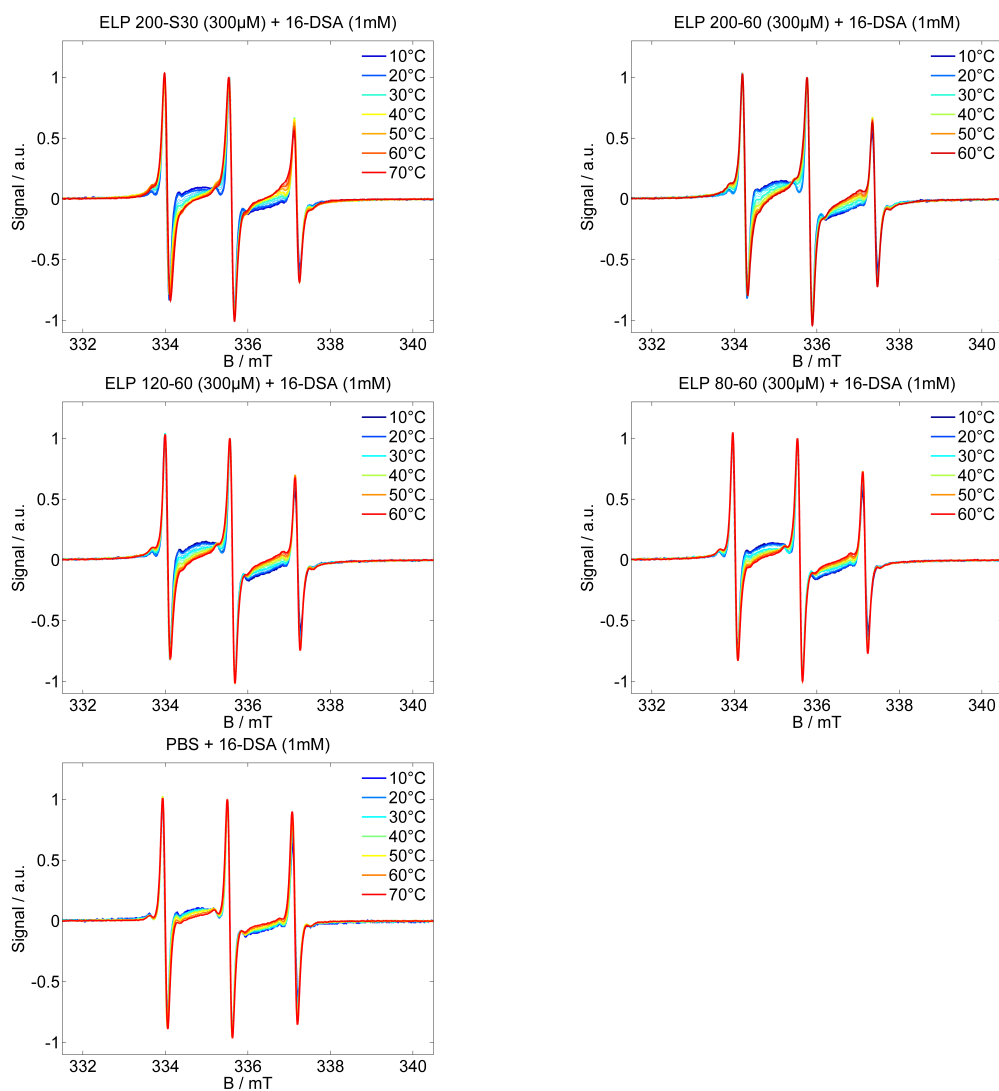


Figure A.1: CW EPR spectra of the polymers with spin probe 16-DSA and of 16-DSA in pure buffer (reference measurement).

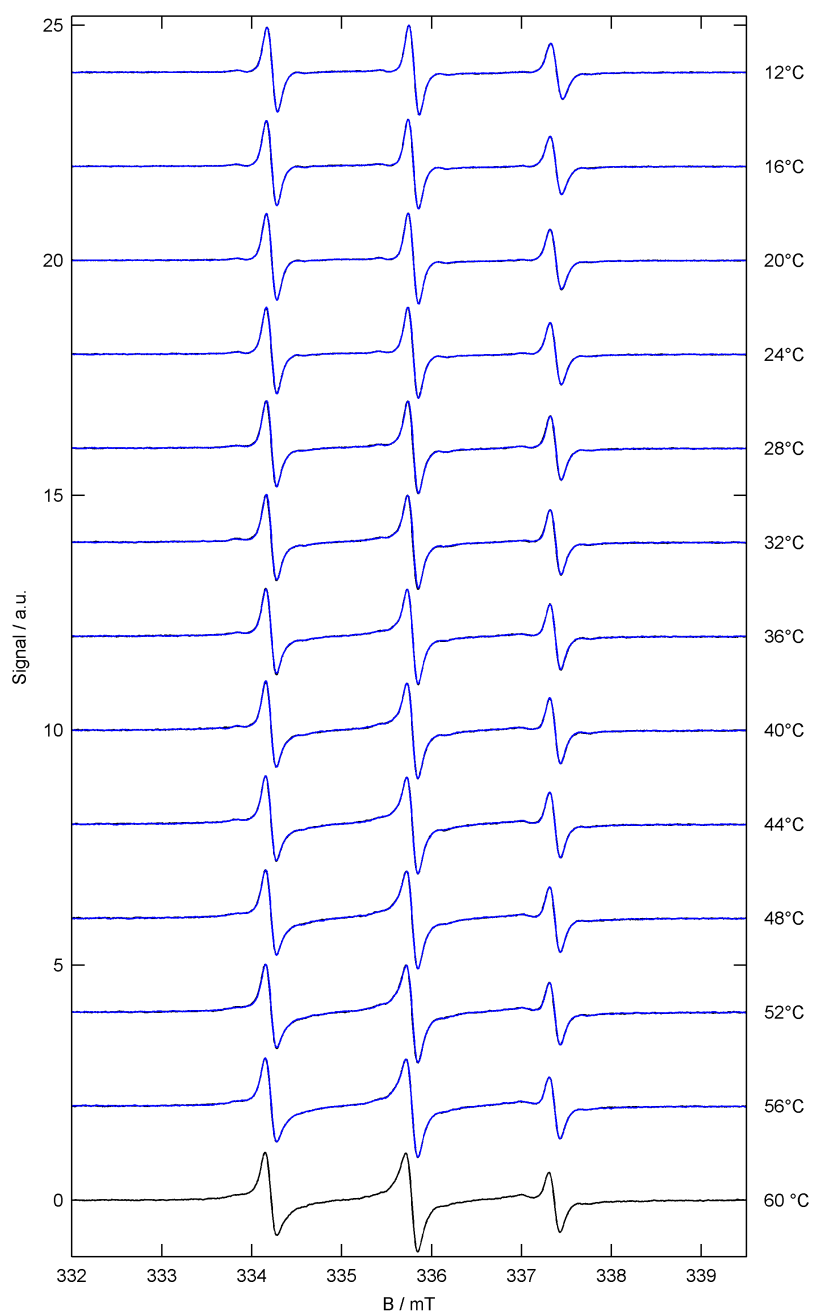


Figure A.2: Superposition of EPR spectra of ELP 200–60 (300 μ M) with 16-DSA (1 mM) during heating (black) and during subsequent cooling (blue) at temperatures between 10 and 60 $^{\circ}$.

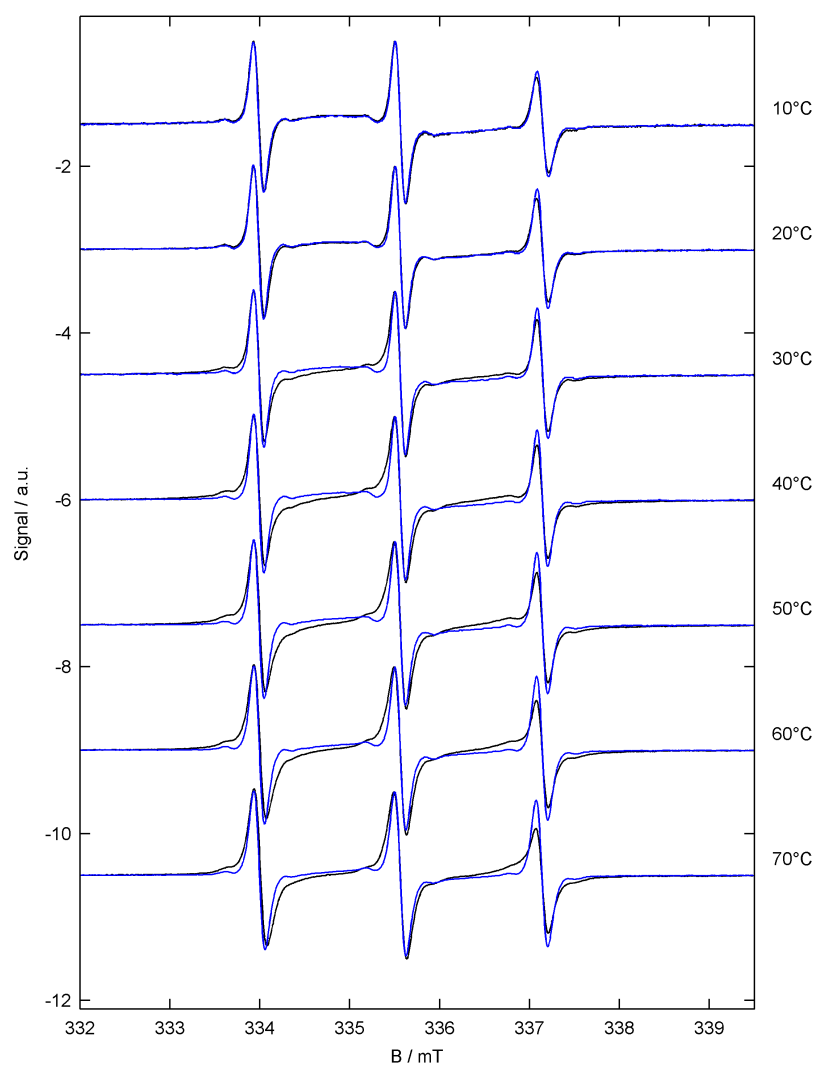


Figure A.3: Superposition of EPR spectra of 16-DSA in pure buffer (blue) and of ELP 200–30 (300 μ M) with 16-DSA (1 mM) (black) at temperatures between 10 and 70 $^{\circ}$.

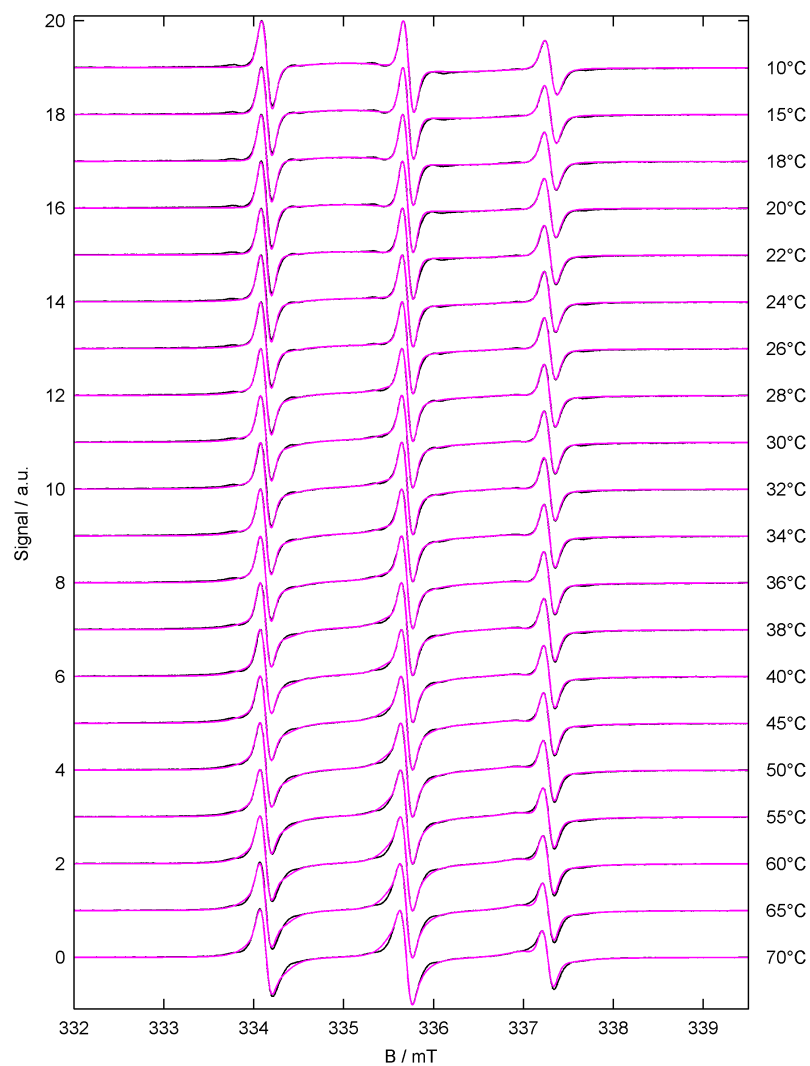


Figure A.4: All EPR spectral simulations of ELP 200–S30 (300 μ M) with 16-DSA (1 mM) at temperatures between 10 and 70 °C. Experimental data is shown in black, simulated data in magenta.

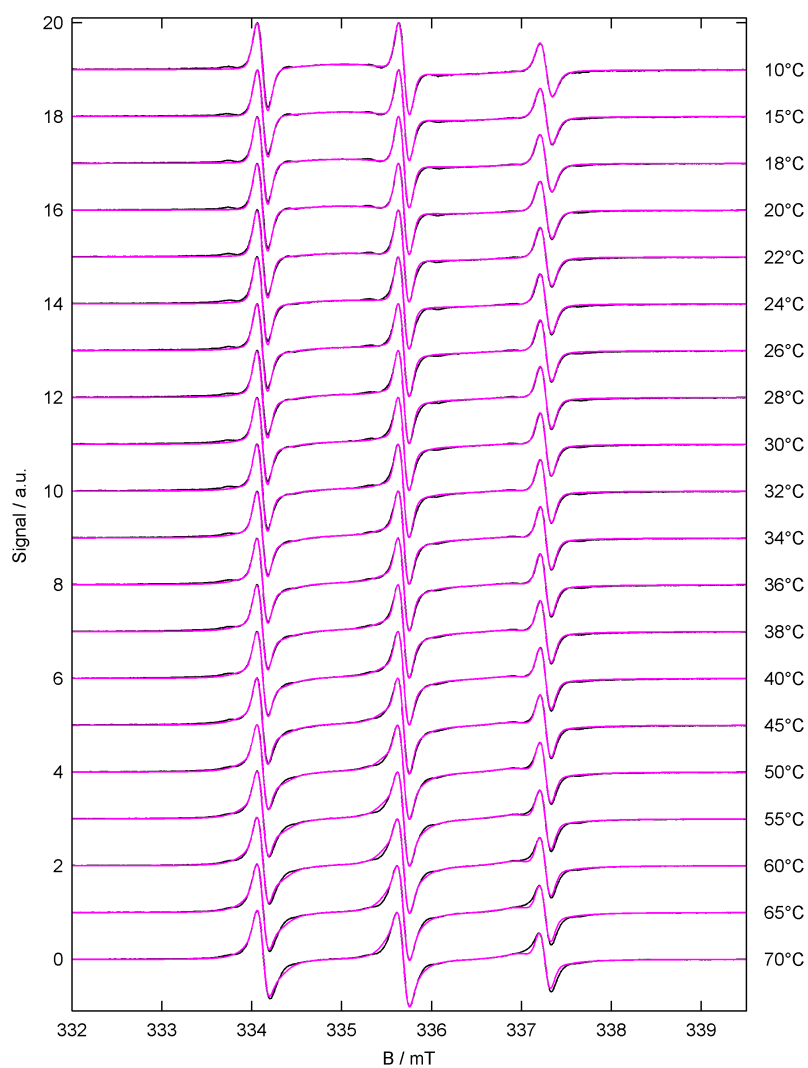


Figure A.5: All EPR spectral simulations of ELP 200–30 ($300\ \mu\text{M}$) with 16-DSA ($1\ \text{mM}$) at temperatures between 10 and $70\ ^\circ\text{C}$. Experimental data is shown in black, simulated data in magenta.

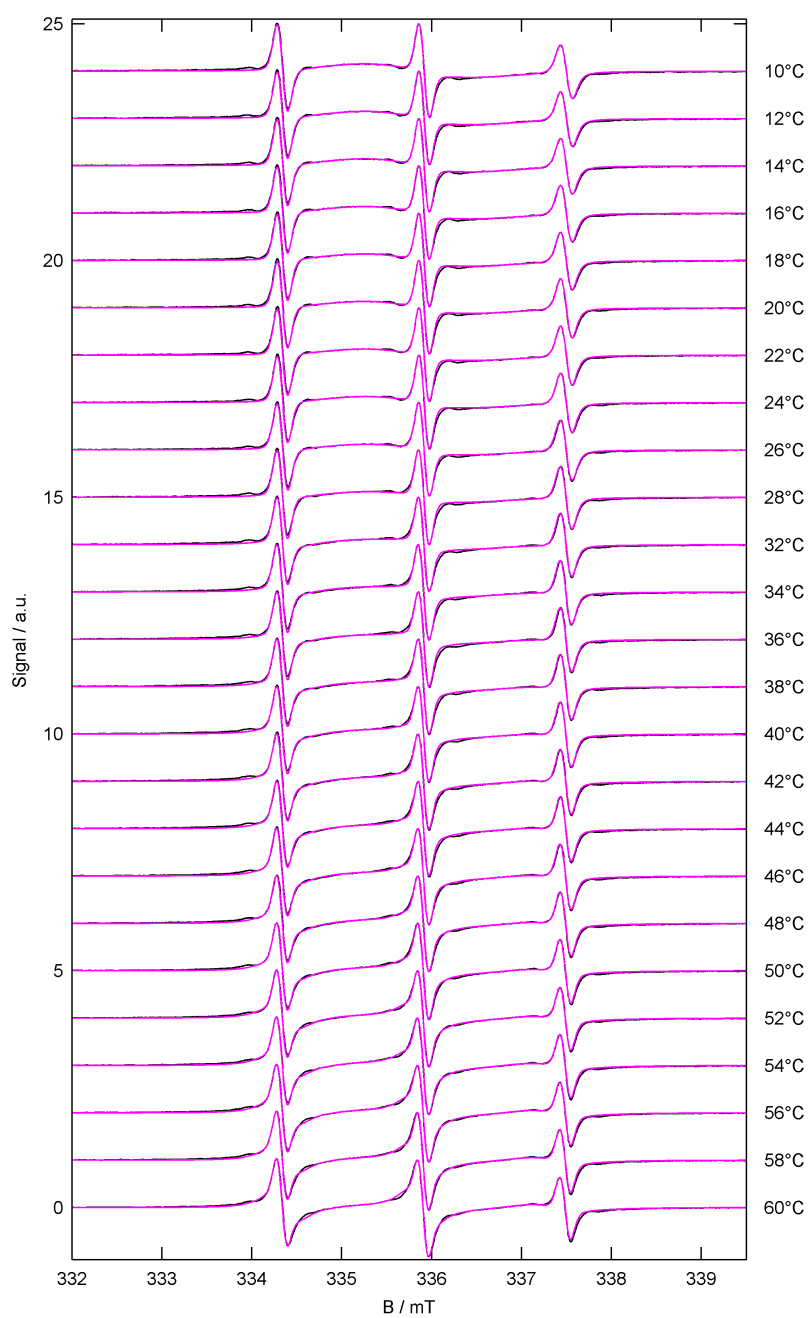


Figure A.6: All EPR spectral simulations of ELP 200–60 (300 μ M) with 16-DSA (1 mM) at temperatures between 10 and 60 °C. Experimental data is shown in black, simulated data in magenta.

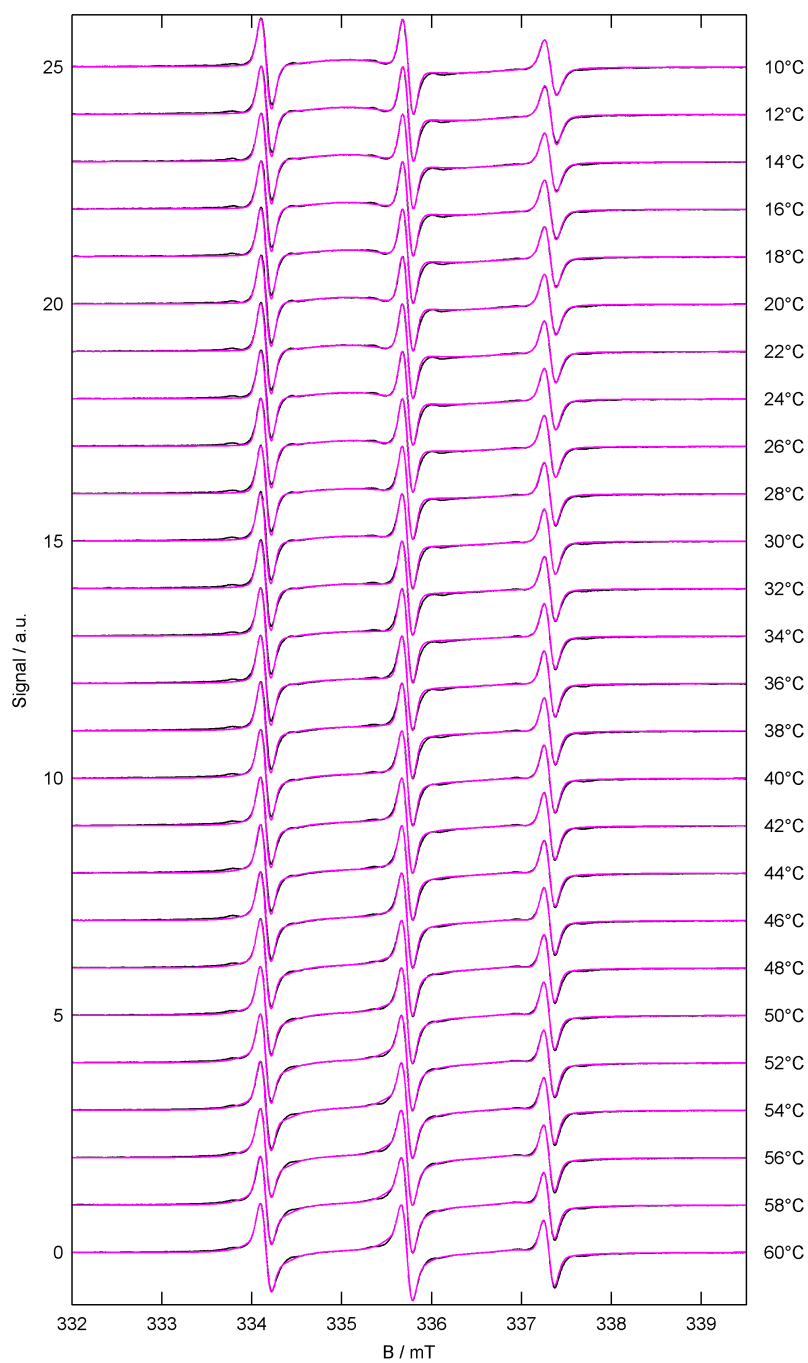


Figure A.7: All EPR spectral simulations of ELP 120–60 (300 μM) with 16-DSA (1 mM) at temperatures between 10 and 60 $^{\circ}\text{C}$. Experimental data is shown in black, simulated data in magenta.

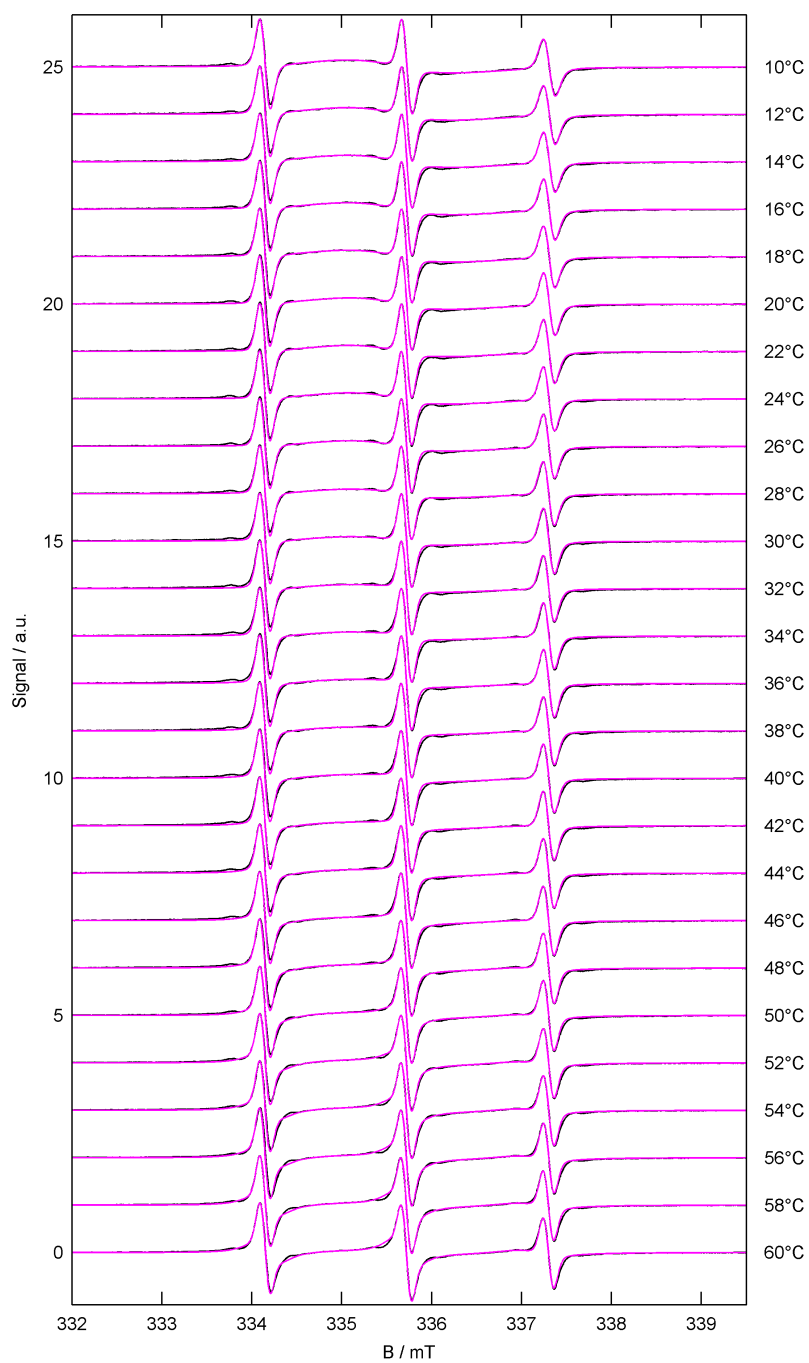


Figure A.8: All EPR spectral simulations of ELP 80–60 (300 μ M) with 16-DSA (1 mM) at temperatures between 10 and 60 °C. Experimental data is shown in black, simulated data in magenta.

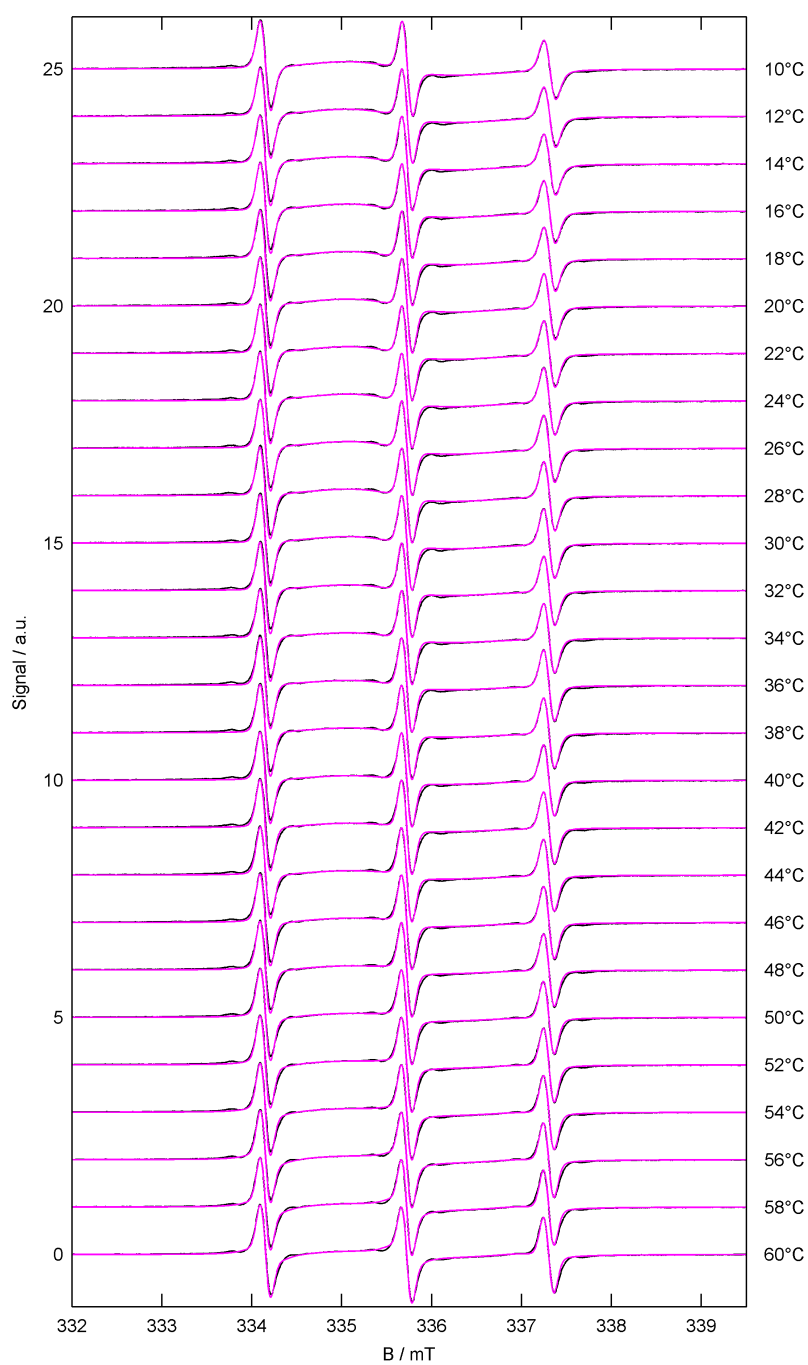


Figure A.9: All EPR spectral simulations of ELP 40–60 (300 μ M) with 16-DSA (1 mM) at temperatures between 10 and 60 $^{\circ}$ C. Experimental data is shown in black, simulated data in magenta.

Table A.1: Characteristics of diblock ELPs 200–30 and 200–S30. Values of $T_{t/UV-vis}$ were received from Elisabeth Garanger.

ELP	MW in kDa	$f_{\text{hydrophilic}}$	$T_{t/UV-vis}$ in °C ($c = 25 \mu\text{M}$)
200–30	94.0	0.12	24
200–S30	94.7	0.13	25

Equations of the exponential regression of the transition temperatures in Figure 3.2 (Section 3.2):

$$T_t(f) = 19.71 \text{ K} + 1.44 \text{ K} \cdot \exp(4.53 \cdot f) \quad (\text{A.1})$$

$$T_t(f) = 22.90 \text{ K} + 0.90 \text{ K} \cdot \exp(5.44 \cdot f). \quad (\text{A.2})$$

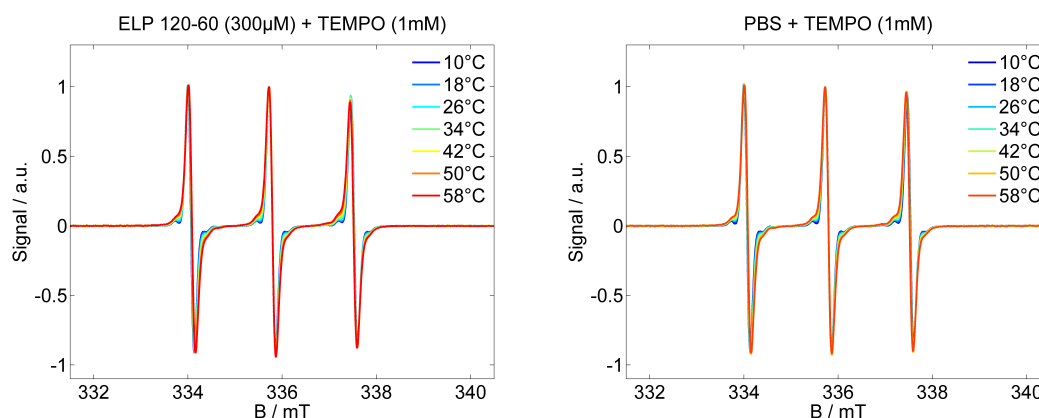


Figure A.10: Test measurements with spin probe TEMPO (for chemical structure, see Figure A.11): ELP 120–60 with TEMPO and reference measurement in PBS without polymer.

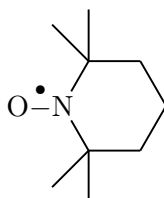


Figure A.11: Structural formula of 2,2,6,6-Tetramethylpiperidine-1-oxyl (TEMPO).

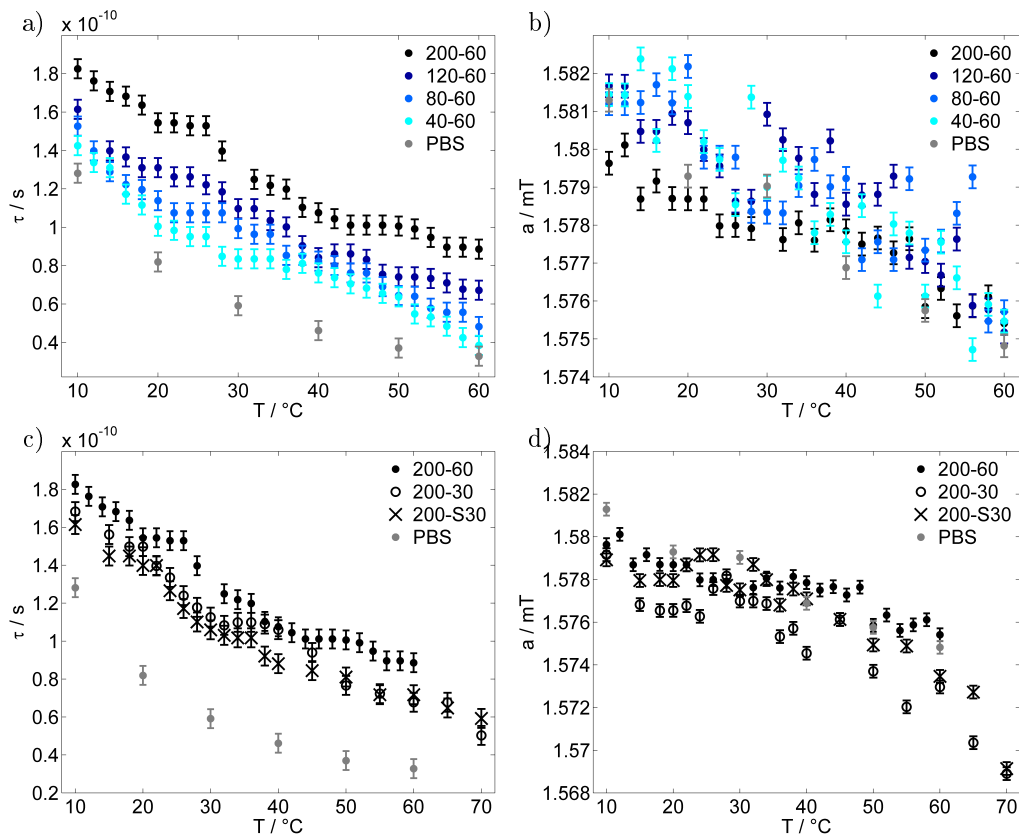


Figure A.12: Results of simulation of 16-DSA in buffer solution of diblock ELPs: rotational correlation times (a) and c)) and hyperfine splitting constant (b) and d)) of the hydrophilic spectral component for different hydrophobic block lengths (a) and b)) and different hydrophilic blocks (c) and d)). Hyperfine splitting constants give half of the difference in B field of the high-field and of the low-field peak of the simulated EPR spectra of the respective component.

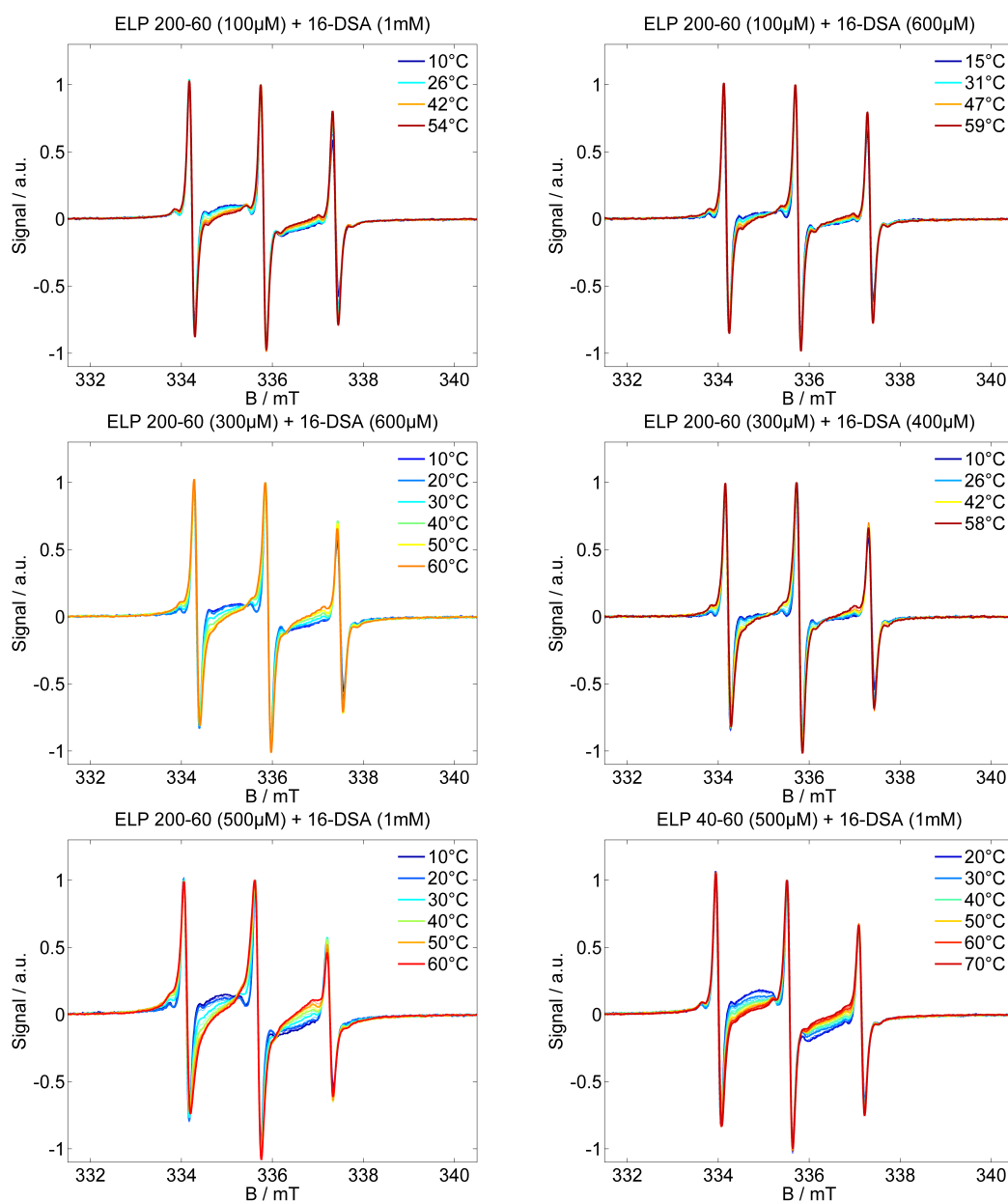


Figure A.13: CW EPR spectra of different polymer concentrations with different concentrations of the spin probe 16-DSA.

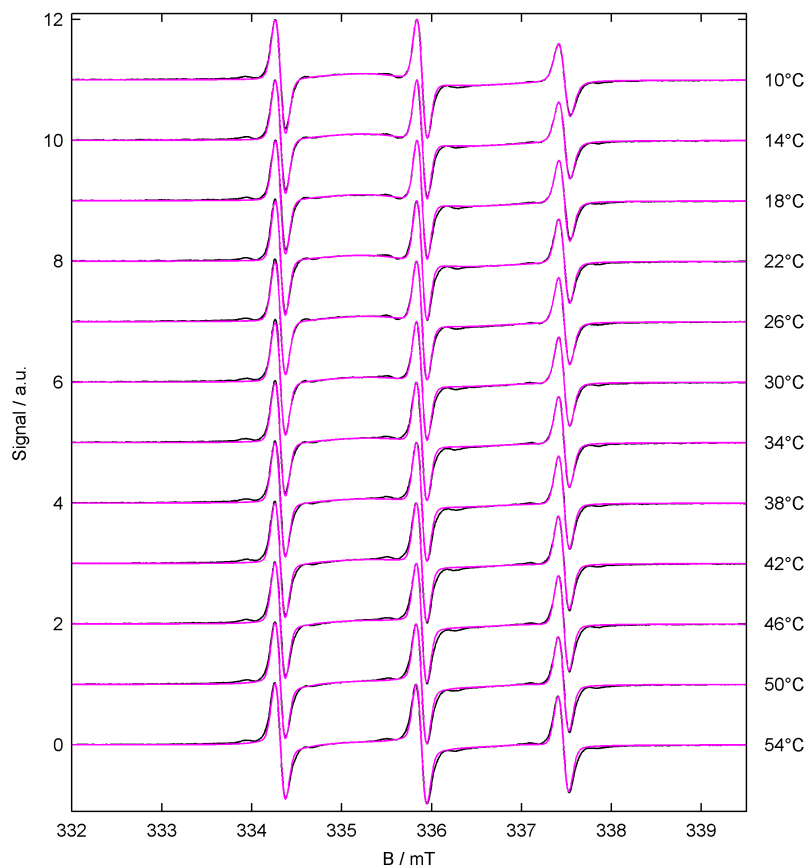


Figure A.14: All EPR spectral simulations of ELP 200–60 (100 μM) with 16-DSA (1 mM) at temperatures between 10 and 54 $^{\circ}\text{C}$. Experimental data is shown in black, simulated data in magenta.

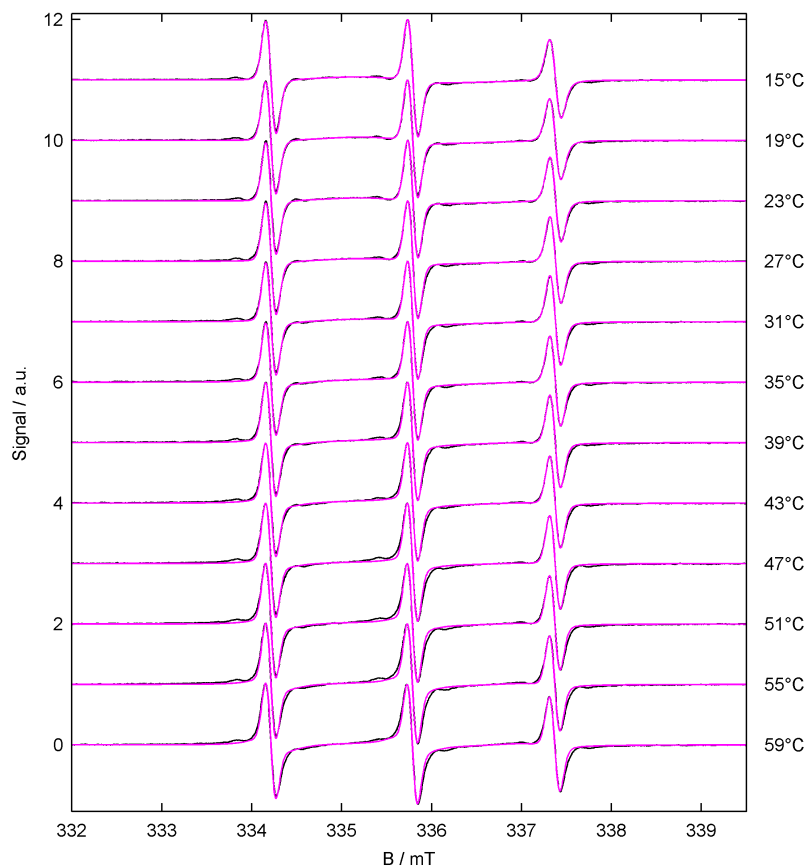


Figure A.15: All EPR spectral simulations of ELP 200–60 ($100\ \mu\text{M}$) with 16-DSA ($600\ \mu\text{M}$) at temperatures between 15 and $59\ ^\circ\text{C}$. Experimental data is shown in black, simulated data in magenta.

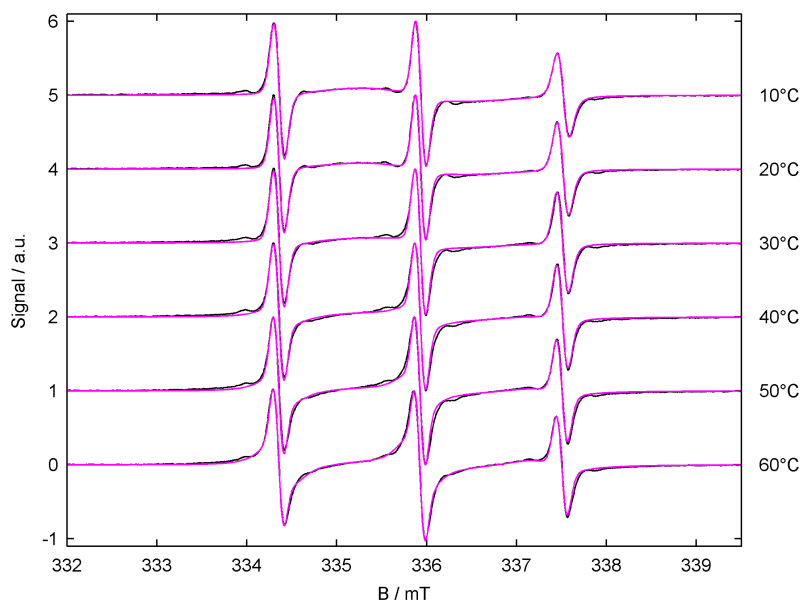


Figure A.16: All EPR spectral simulations of ELP 200-60 (300 μM) with 16-DSA (600 μM) at temperatures between 10 and 60 °C. Experimental data is shown in black, simulated data in magenta.

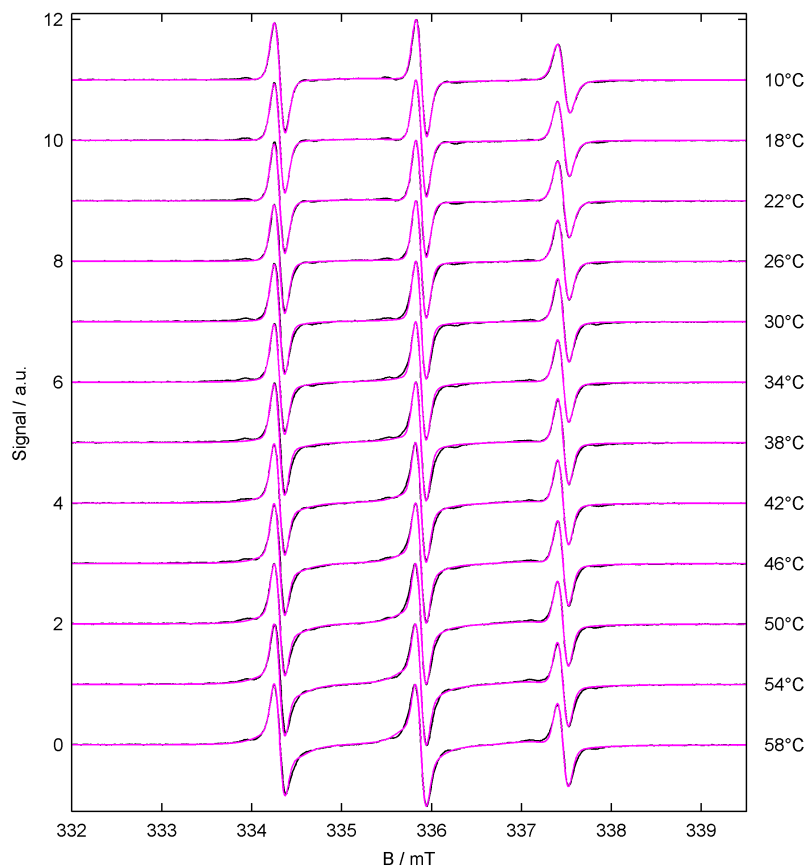


Figure A.17: All EPR spectral simulations of ELP 200–60 ($300\ \mu\text{M}$) with 16-DSA ($400\ \mu\text{M}$) at temperatures between 10 and 58°C . Experimental data is shown in black, simulated data in magenta.

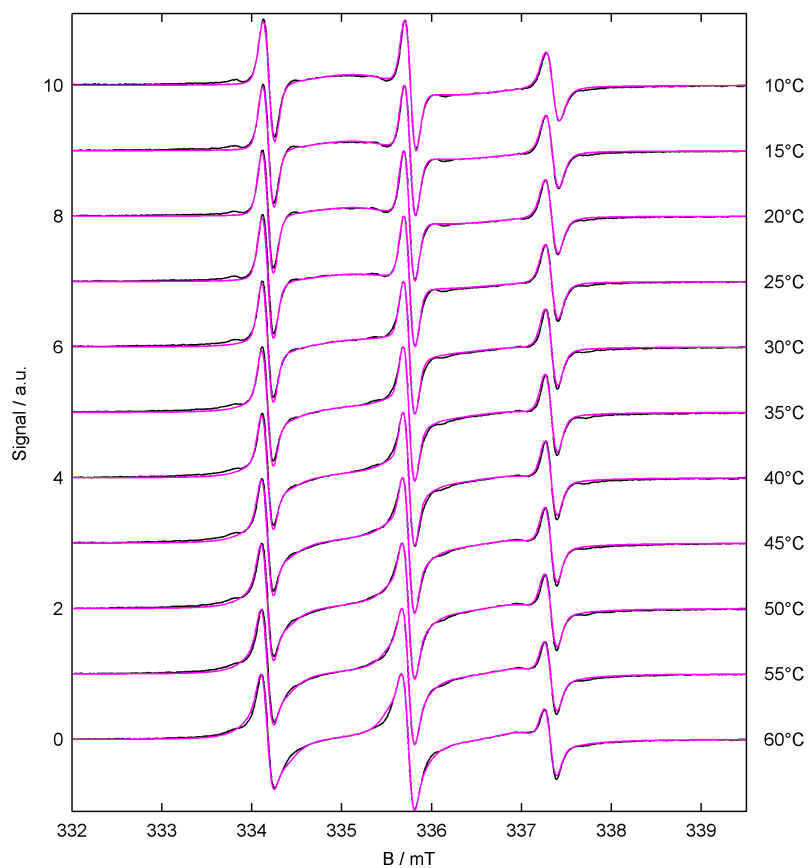


Figure A.18: All EPR spectral simulations of ELP 200–60 (500 μM) with 16-DSA (1 mM) at temperatures between 10 and 60 $^{\circ}\text{C}$. Experimental data is shown in black, simulated data in magenta.

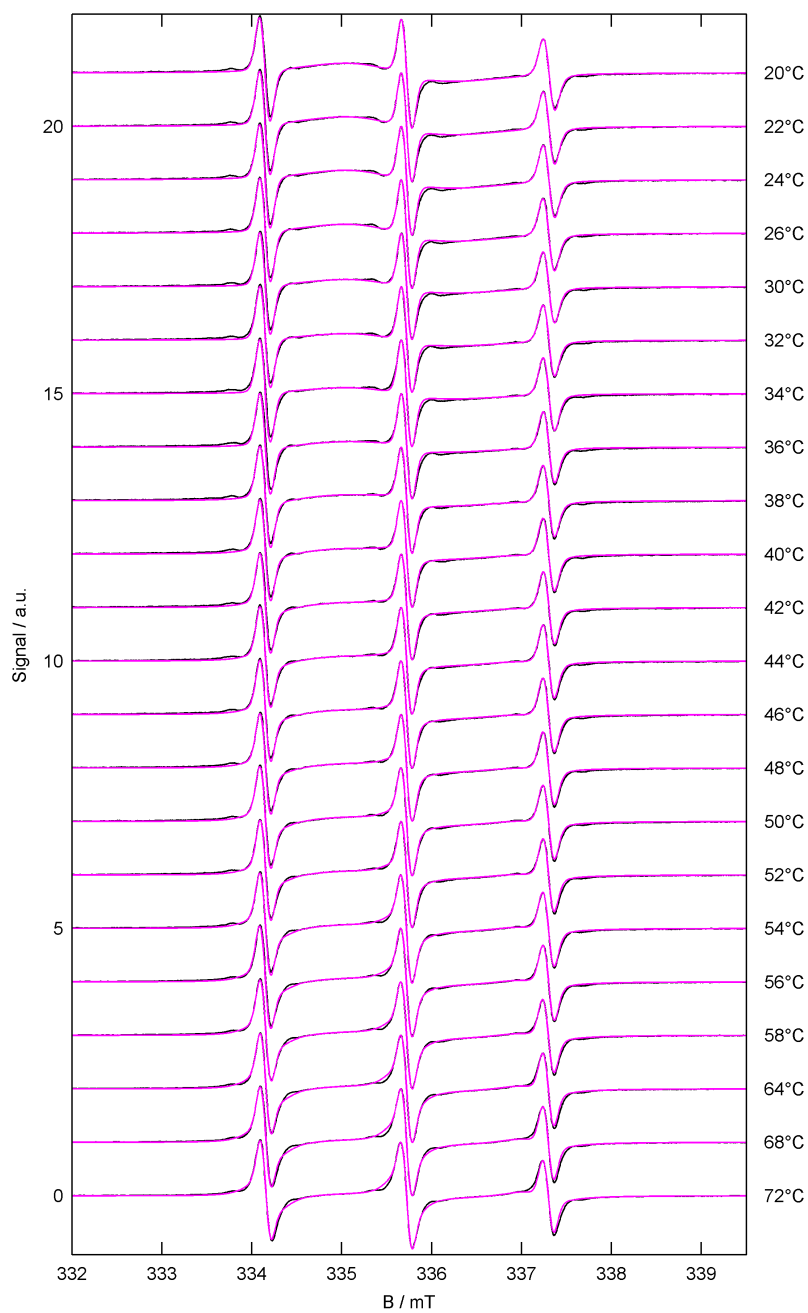


Figure A.19: All EPR spectral simulations of ELP 40–60 (500 μ M) with 16-DSA (1 mM) at temperatures between 20 and 72 $^{\circ}$ C. Experimental data is shown in black, simulated data in magenta.

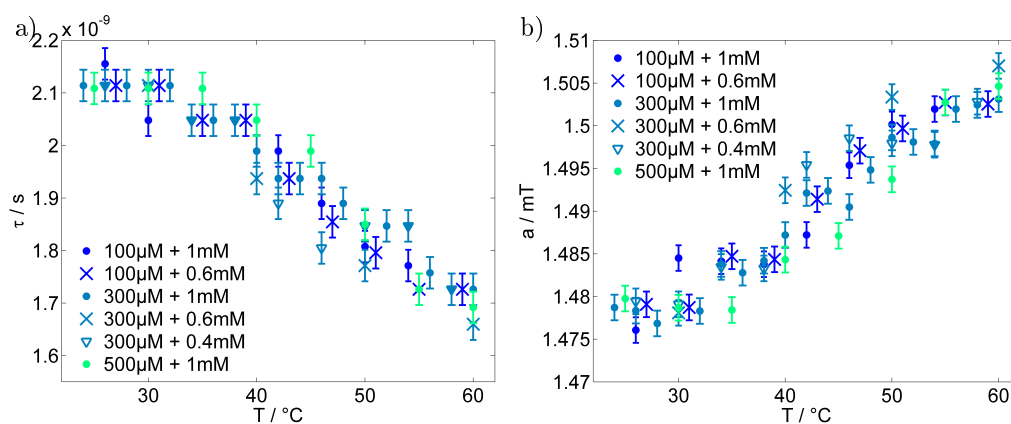


Figure A.20: Results of simulation of diblock ELP 200–60 (various concentrations) with 16-DSA (various concentrations): rotational correlation times a) and hyperfine splitting constant b) of the hydrophobic spectral component. Hyperfine splitting constants give half of the difference in B field of the high-field and of the low-field peak of the simulated EPR spectra of the respective component.

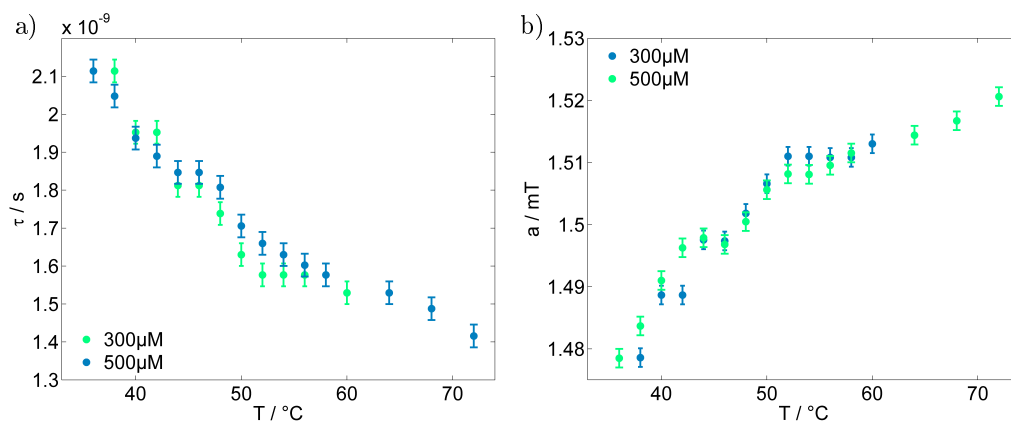


Figure A.21: Results of simulation of diblock ELP 40–60 (various concentrations) with 16-DSA (various concentrations): rotational correlation times a) and hyperfine splitting constant b) of the hydrophobic spectral component. Hyperfine splitting constants give half of the difference in B field of the high-field and of the low-field peak of the simulated EPR spectra of the respective component.

A.2 Hysteretic polymers

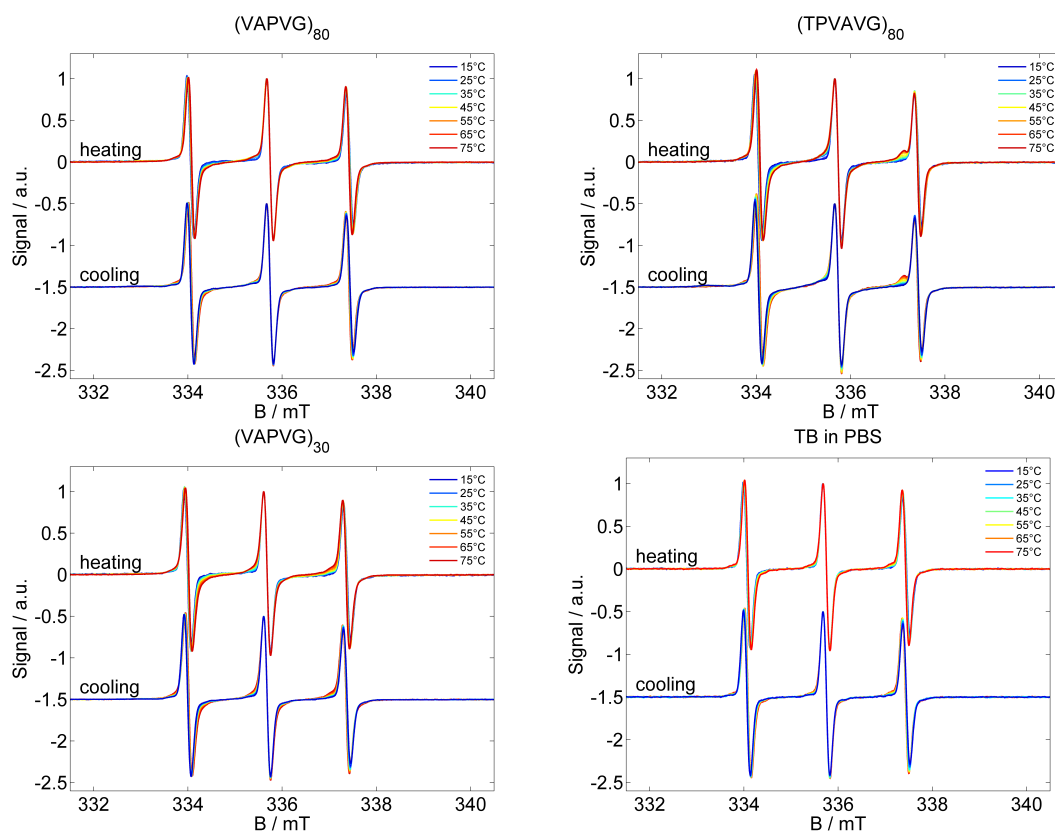


Figure A.22: CW EPR spectra of TB in a polymer buffer solution and reference spectra of TB in PBS

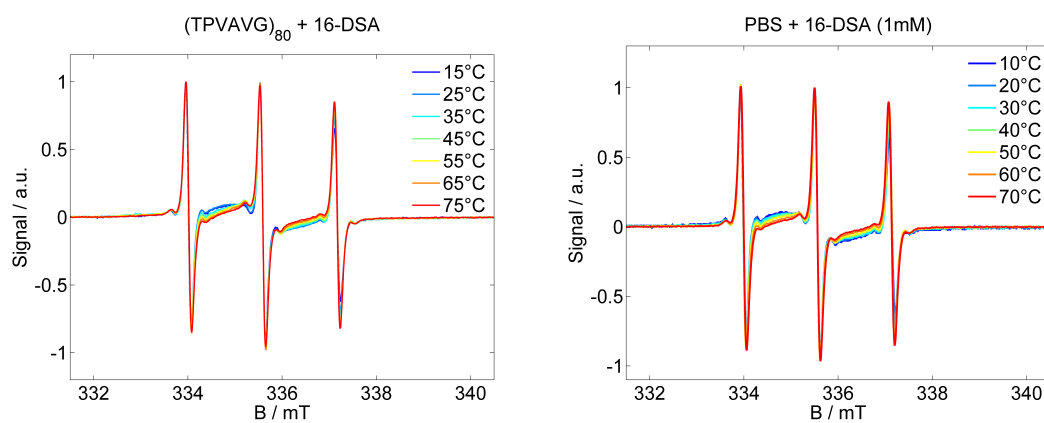


Figure A.23: CW EPR spectra of 16-DSA (for chemical structure, see Figure 5.1 b) (1 mM) in a (TPVAVG)₈₀ buffer solution (300 μM) and reference spectra of 16-DSA (1 mM) in PBS.

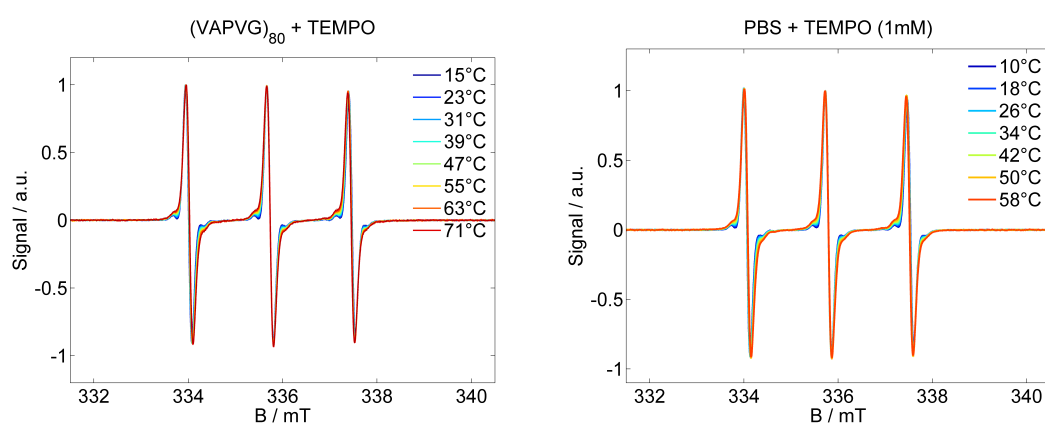


Figure A.24: CW EPR spectra of TEMPO (for chemical structure, see Figure A.11) ($400\ \mu\text{M}$) in a $(\text{VAPVG})_{80}$ buffer solution ($200\ \mu\text{M}$) and reference spectra of TEMPO ($1\ \text{mM}$) in PBS.

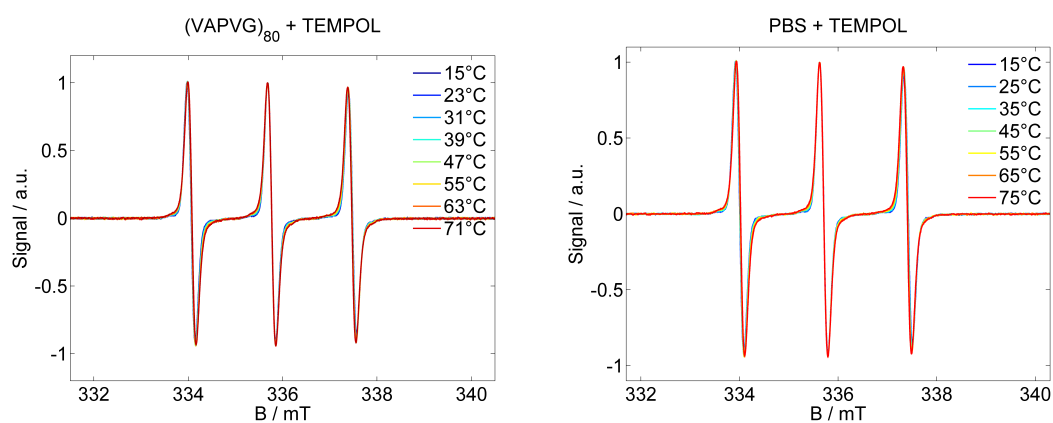


Figure A.25: CW EPR spectra of TEMPOL (for chemical structure, see Figure A.29 a) ($400\ \mu\text{M}$) in a $(\text{VAPVG})_{80}$ buffer solution ($200\ \mu\text{M}$) and reference spectra of TEMPOL ($1\ \text{mM}$) in PBS.

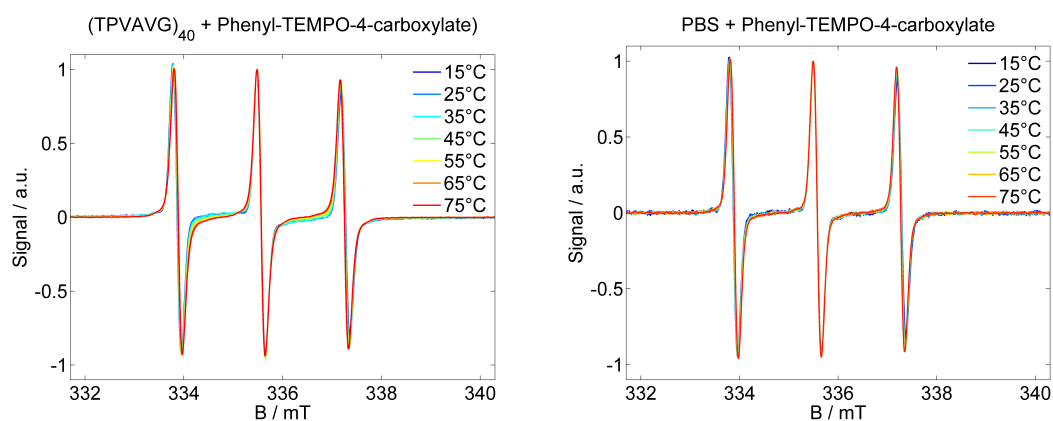


Figure A.26: CW EPR spectra of Phenyl-TEMPO-4-carboxylate (for chemical structure, see Figure A.29 b) ($1\ \text{mM}$) in a $(\text{TPVAVG})_{40}$ buffer solution ($300\ \mu\text{M}$) and reference spectra of Phenyl-TEMPO-4-carboxylate ($1\ \text{mM}$) in PBS.

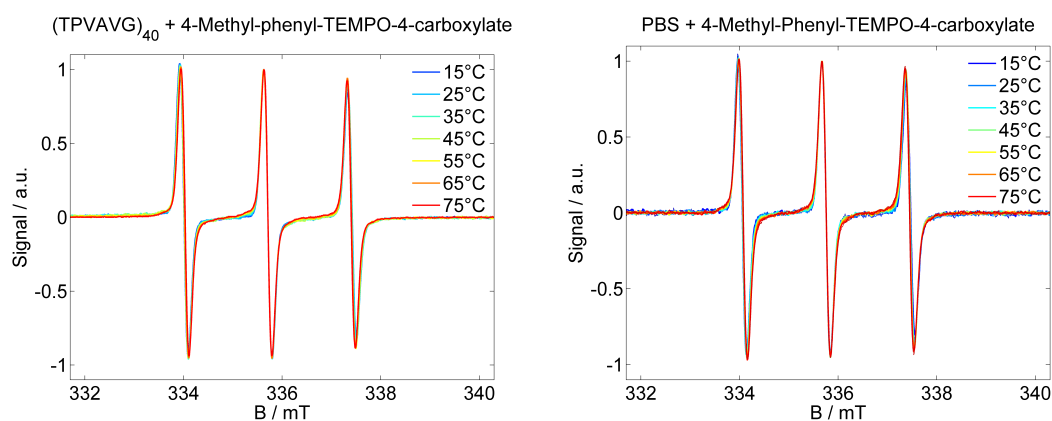


Figure A.27: CW EPR spectra of 4-Methyl-phenyl-TEMPO-4-carboxylate (for chemical structure, see Figure A.29 c) (1 mM) in a (TPVAVG)₄₀ buffer solution (300 μM) and reference spectra of 4-Methyl-phenyl-TEMPO-4-carboxylate (1 mM) in PBS.

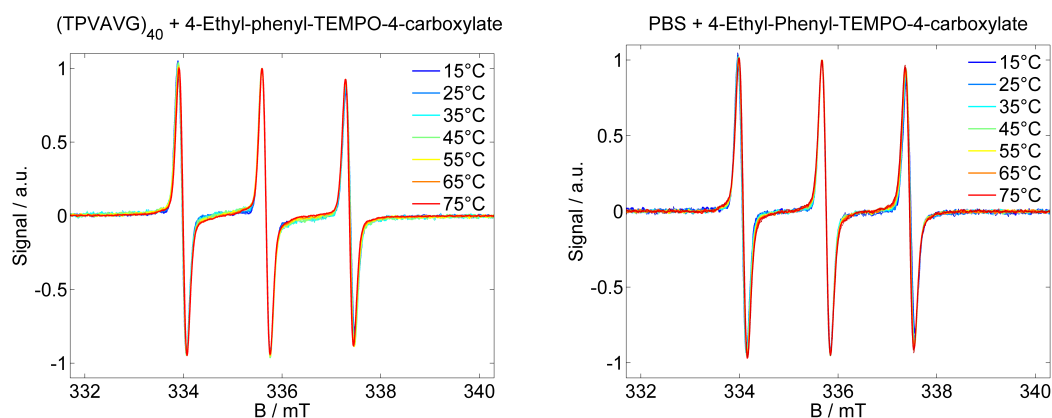


Figure A.28: CW EPR spectra of 4-Ethyl-phenyl-TEMPO-4-carboxylate (for chemical structure, see Figure A.29 d) (1 mM) in a (TPVAVG)₄₀ buffer solution (300 μM) and reference spectra of 4-Ethyl-phenyl-TEMPO-4-carboxylate (1 mM) in PBS.

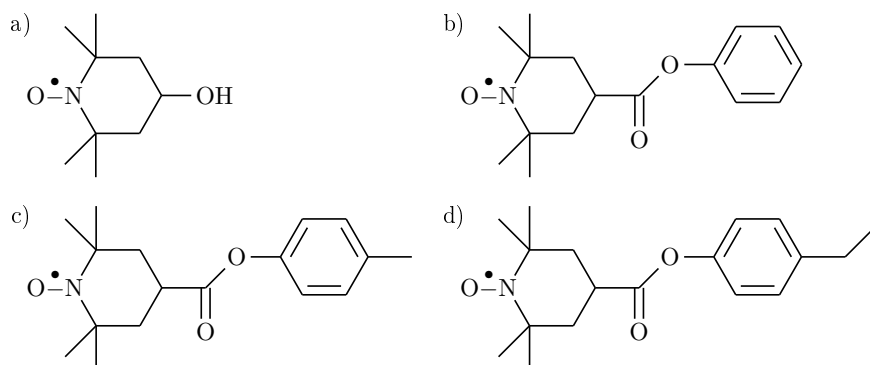


Figure A.29: Structural formula of a) 4-Hydroxy-TEMPO (TEMPOL), b) Phenyl-TEMPO-4-carboxylate, c) 4-Methyl-phenyl-TEMPO-4-carboxylate and d) 4-Ethyl-phenyl-TEMPO-4-carboxylate.

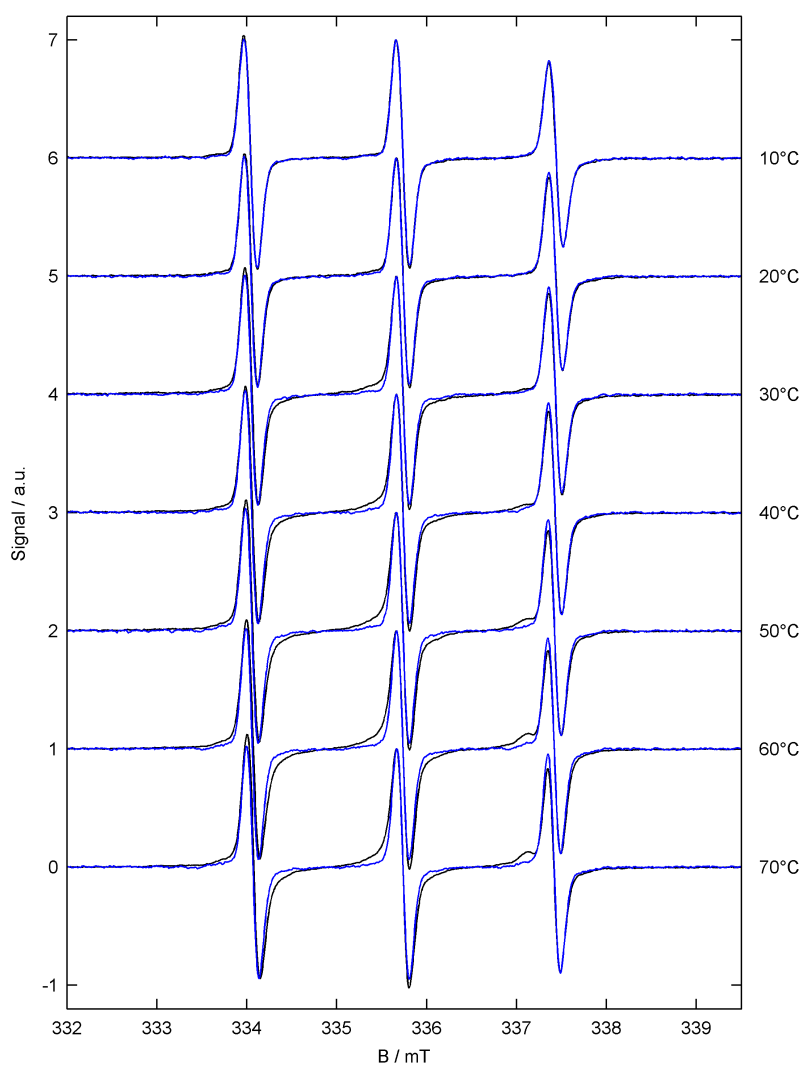


Figure A.30: Superposition of EPR spectra of TB in pure buffer (blue) and of (TPVAVG)₈₀ (300 μM) with TB (1 mM) (black) at temperatures between 10 and 70 °.

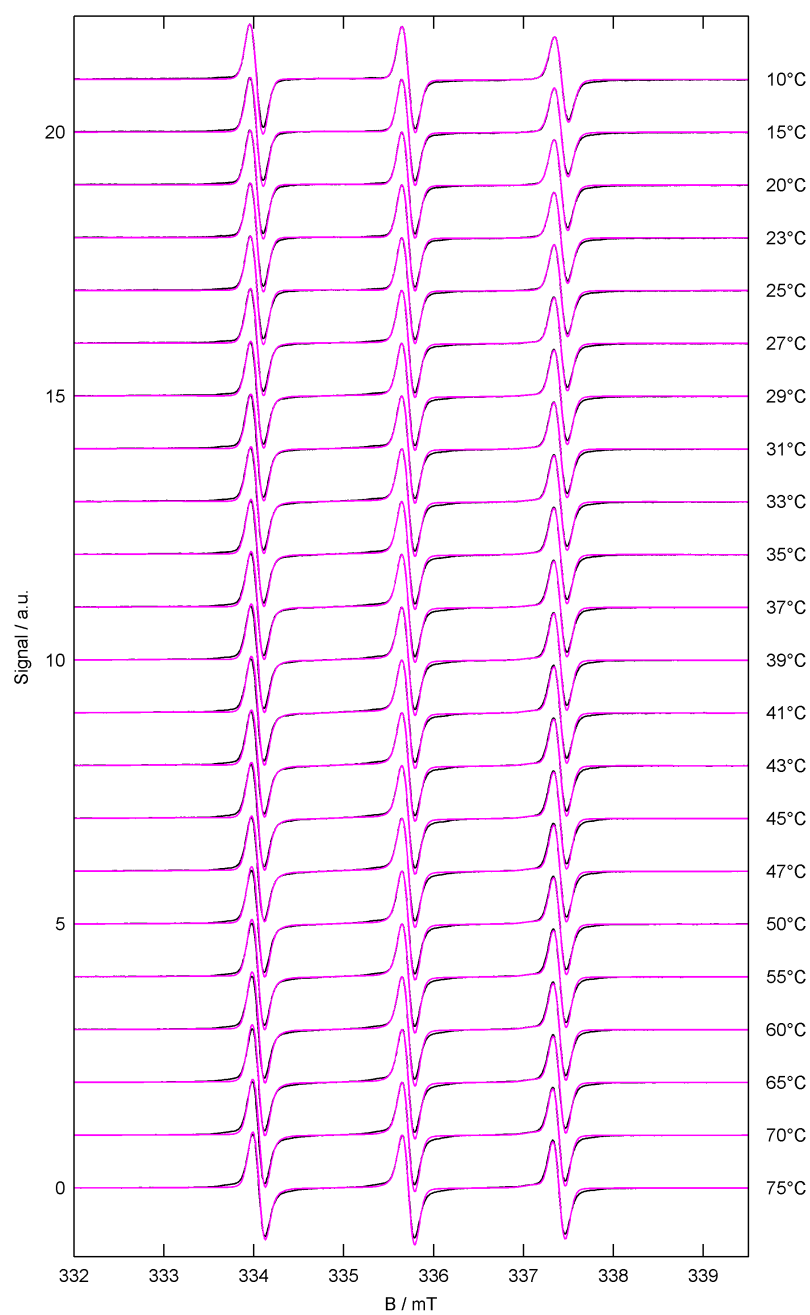


Figure A.31: All EPR spectral simulations of (VAPVG)₈₀ (300 μM) with TB (1 mM) at temperatures between 10 and 75 °C during heating. Experimental data is shown in black, simulated data in magenta.

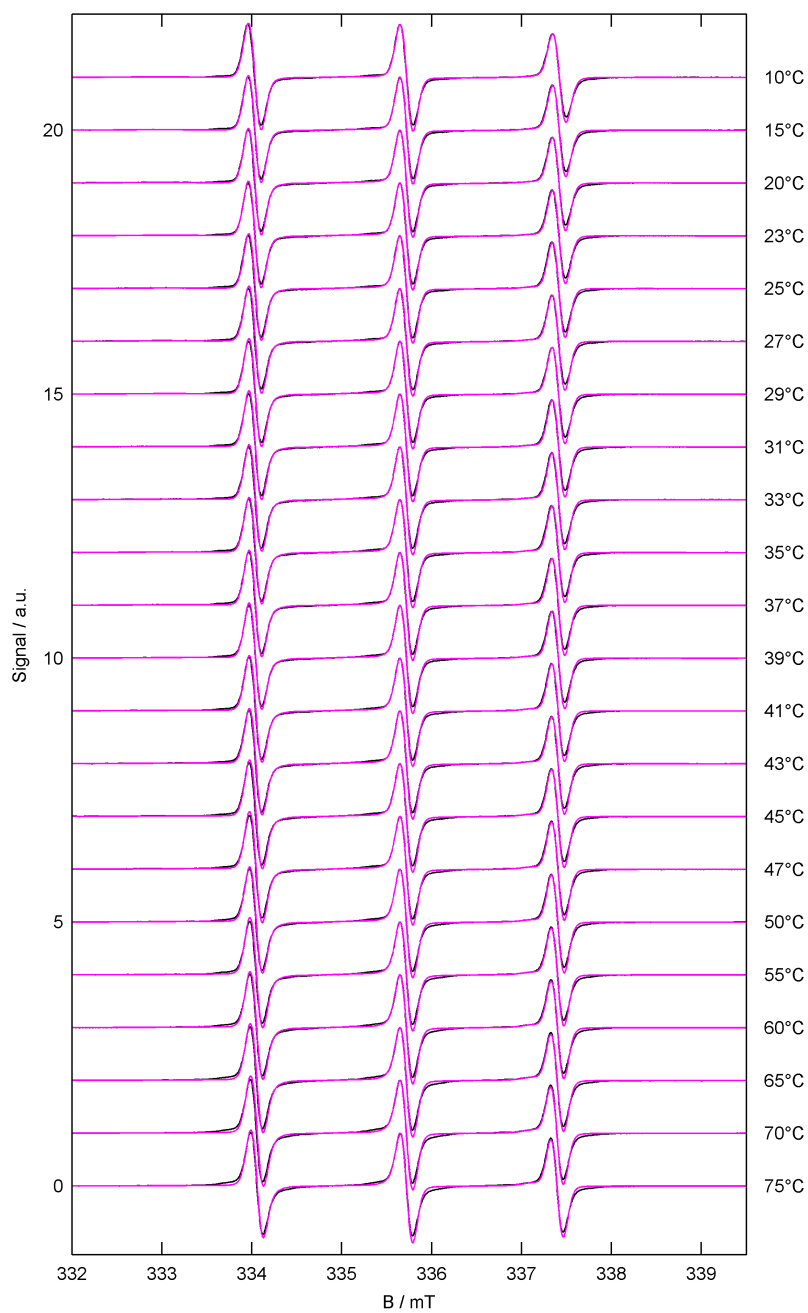


Figure A.32: All EPR spectral simulations of (VAPVG)₈₀ (300 μM) with TB (1 mM) at temperatures between 10 and 75 °C during cooling. Experimental data is shown in black, simulated data in magenta.

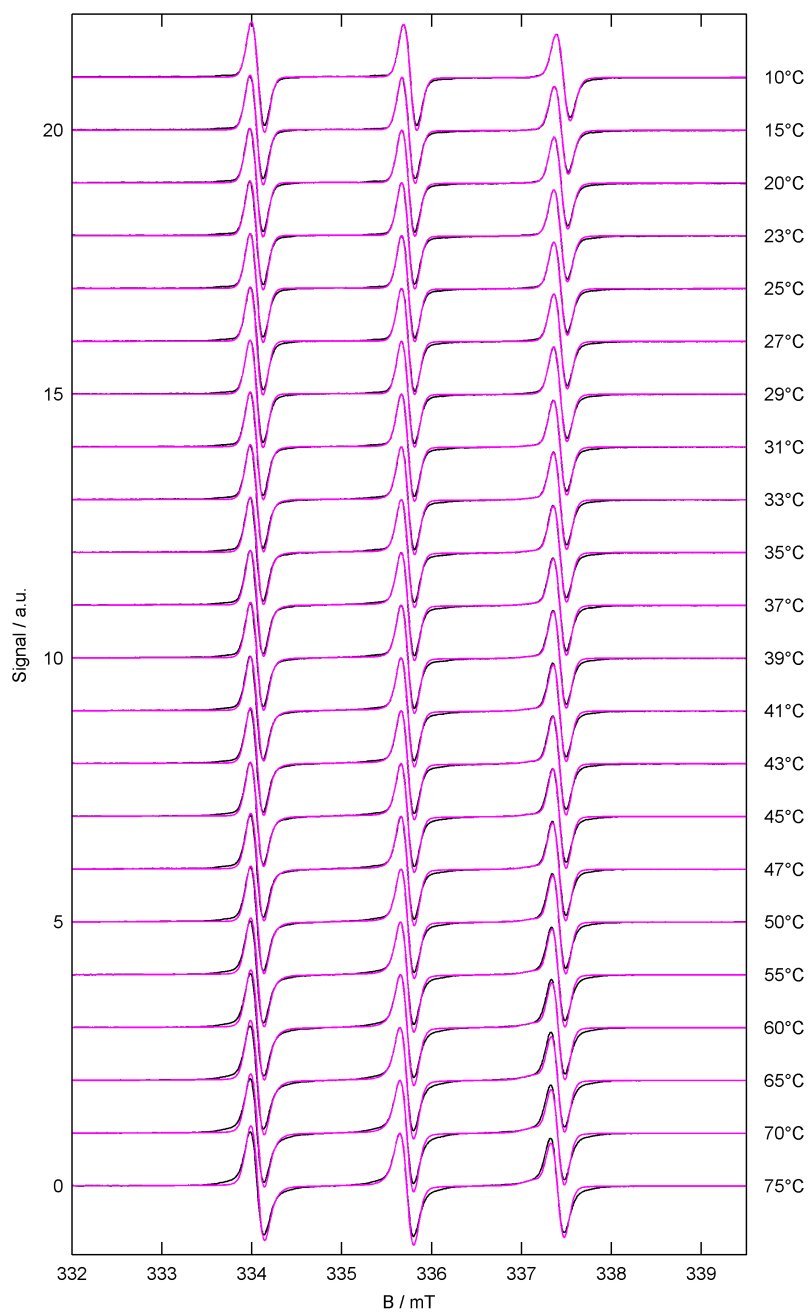


Figure A.33: All EPR spectral simulations of $(\text{VAPVG})_{40}$ ($300 \mu\text{M}$) with TB (1 mM) at temperatures between 10 and 75°C during heating. Experimental data is shown in black, simulated data in magenta.

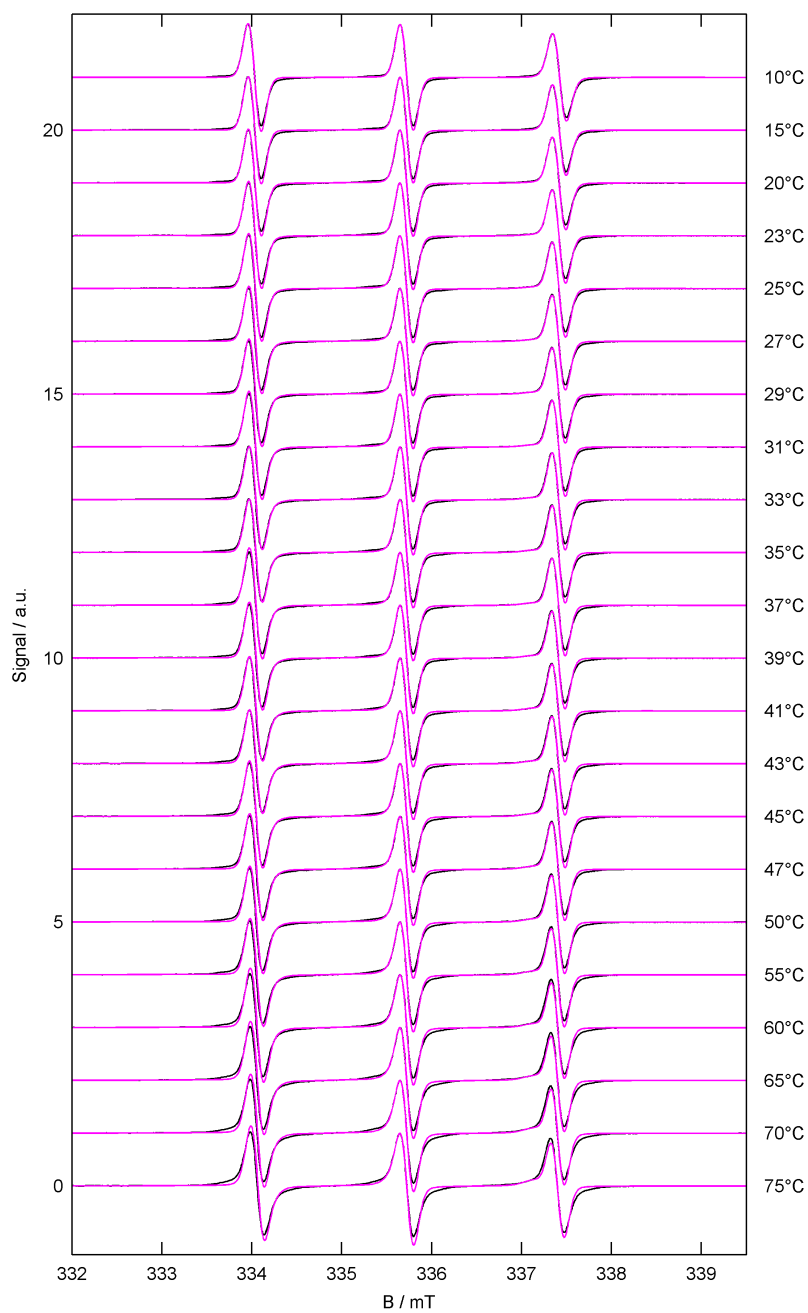


Figure A.34: All EPR spectral simulations of (VAPVG)₄₀ (300 μM) with TB (1 mM) at temperatures between 10 and 75 °C during cooling. Experimental data is shown in black, simulated data in magenta.

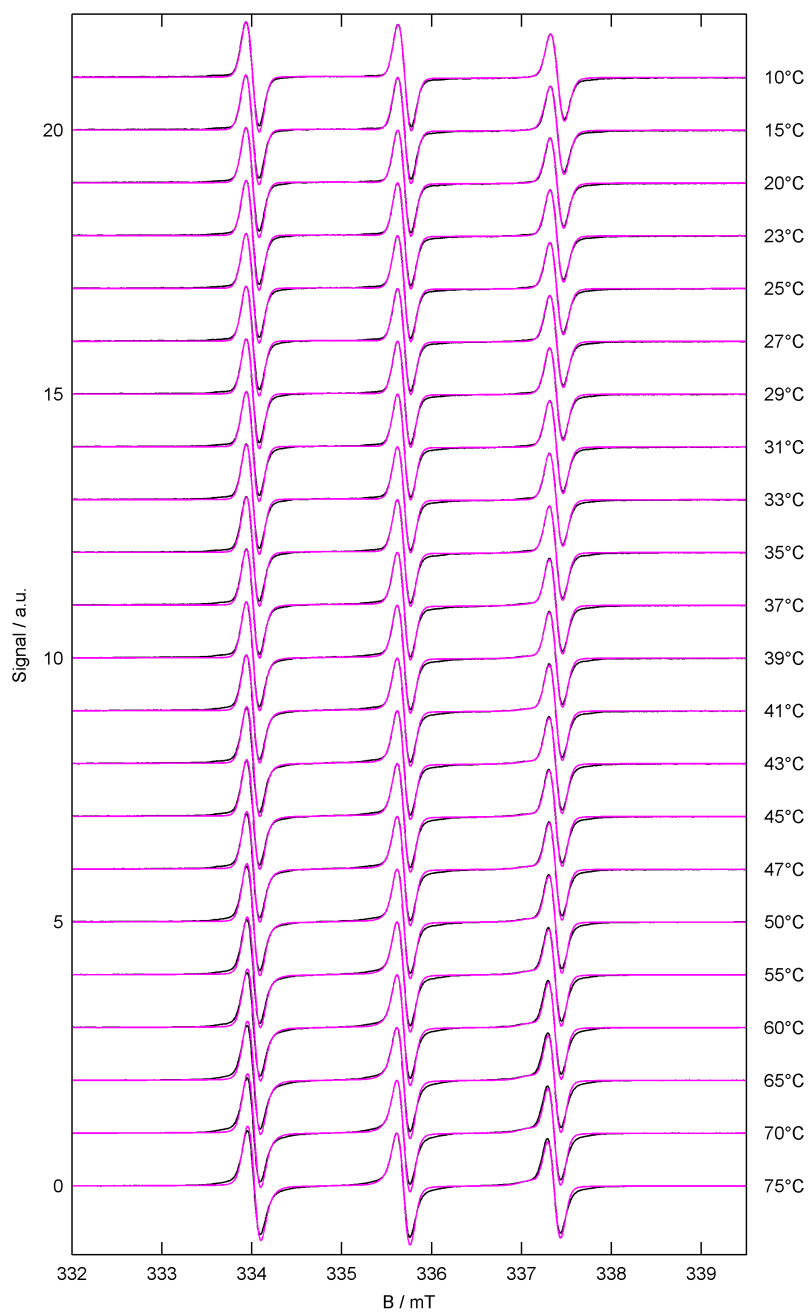


Figure A.35: All EPR spectral simulations of (VAPVG)₃₀ (300 μM) with TB (1 mM) at temperatures between 10 and 75 °C during heating. Experimental data is shown in black, simulated data in magenta.

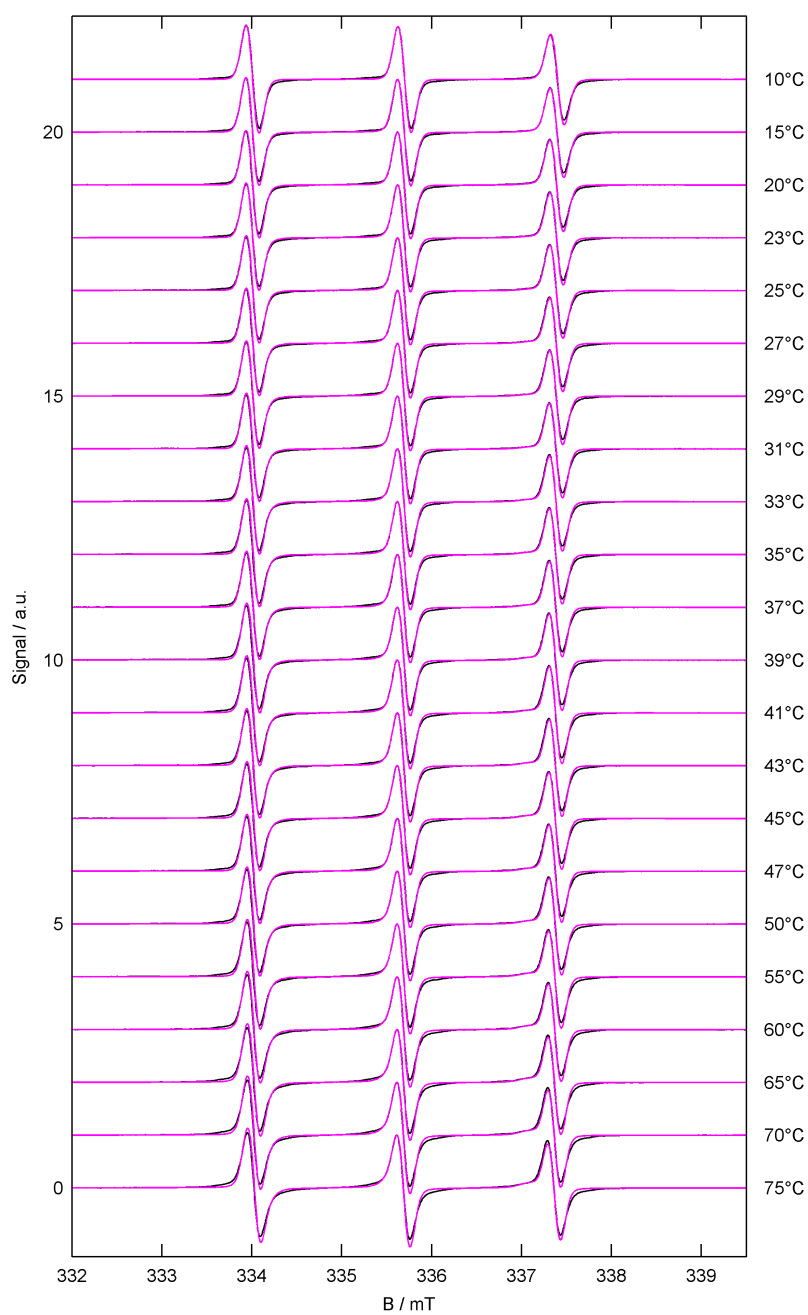


Figure A.36: All EPR spectral simulations of (VAPVG)₃₀ (300 μM) with TB (1 mM) at temperatures between 10 and 75 °C during cooling. Experimental data is shown in black, simulated data in magenta.

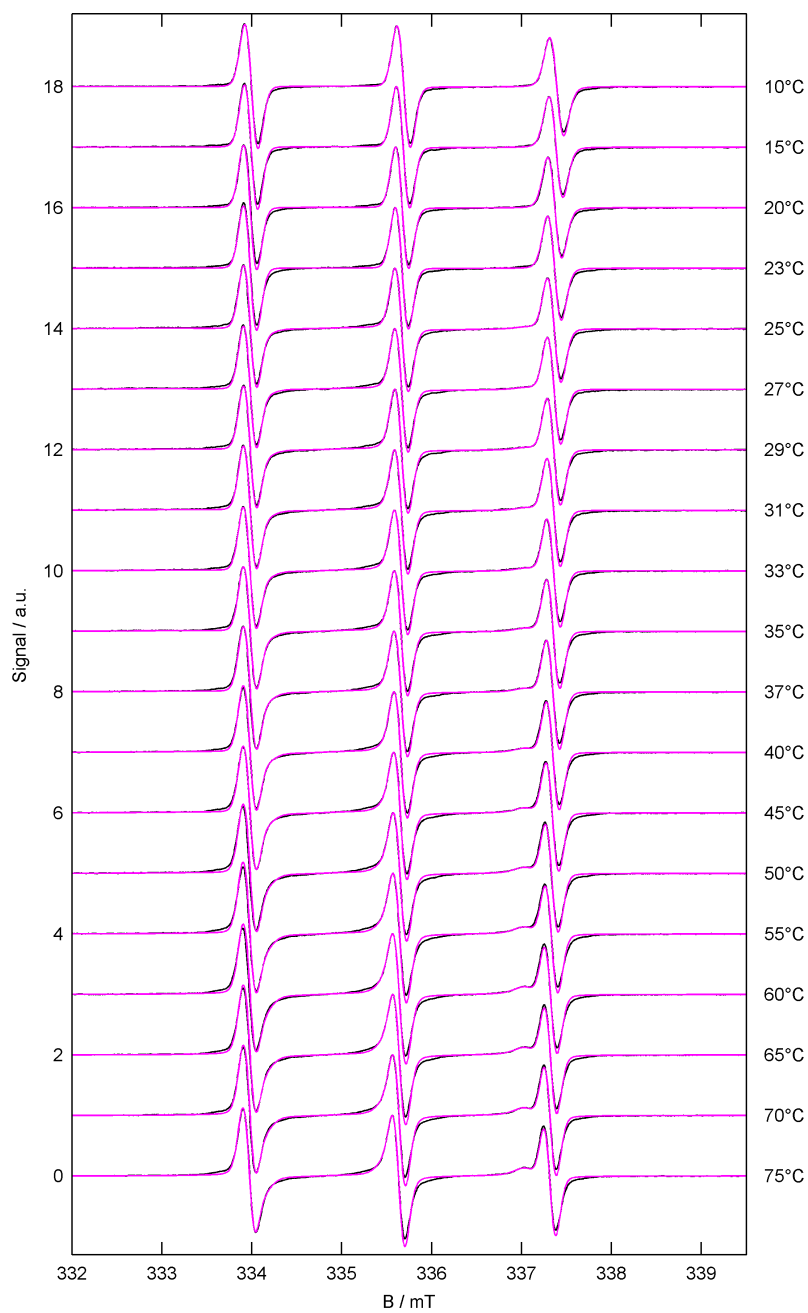


Figure A.37: All EPR spectral simulations of (TPVAVG)₈₀ (300 μM) with TB (1 mM) at temperatures between 10 and 75 °C during heating. Experimental data is shown in black, simulated data in magenta.

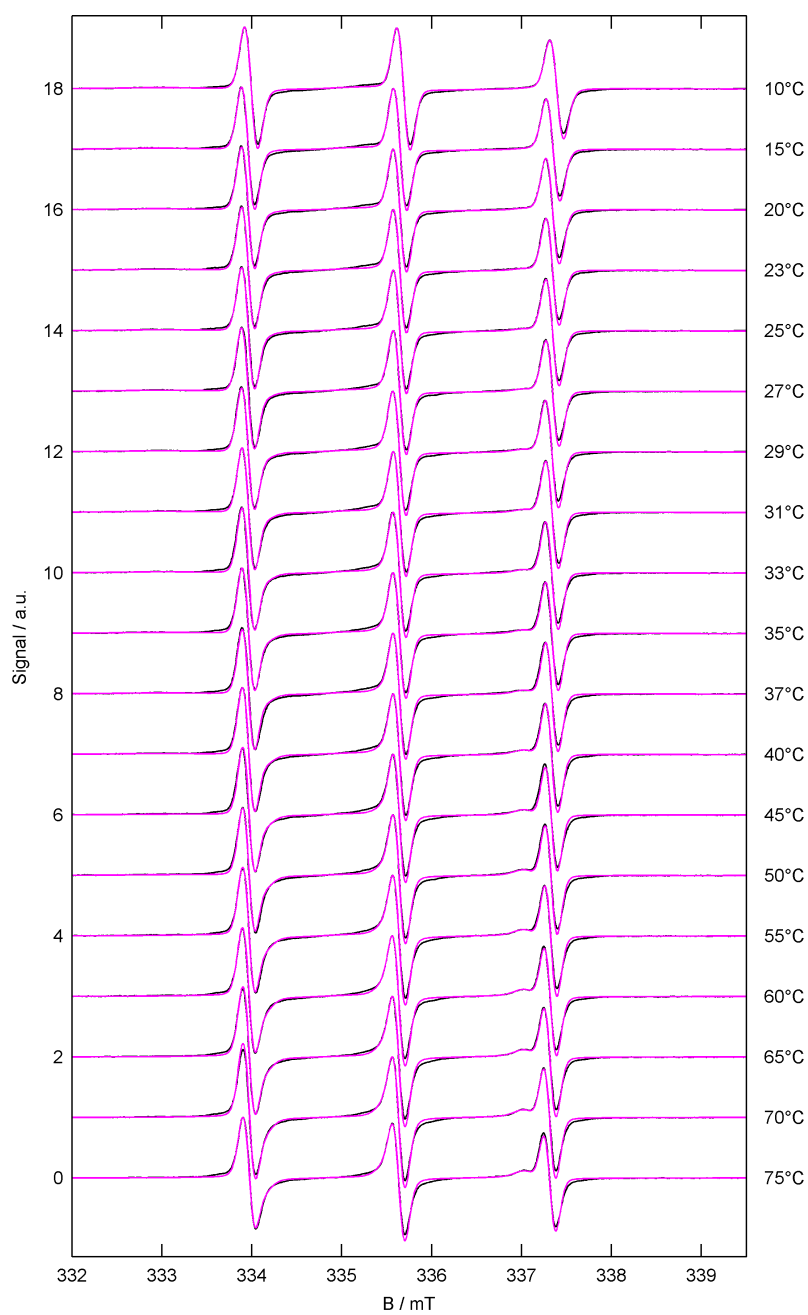


Figure A.38: All EPR spectral simulations of $(\text{TPVAVG})_{80}$ ($300 \mu\text{M}$) with TB (1 mM) at temperatures between 10 and 75°C during cooling. Experimental data is shown in black, simulated data in magenta.

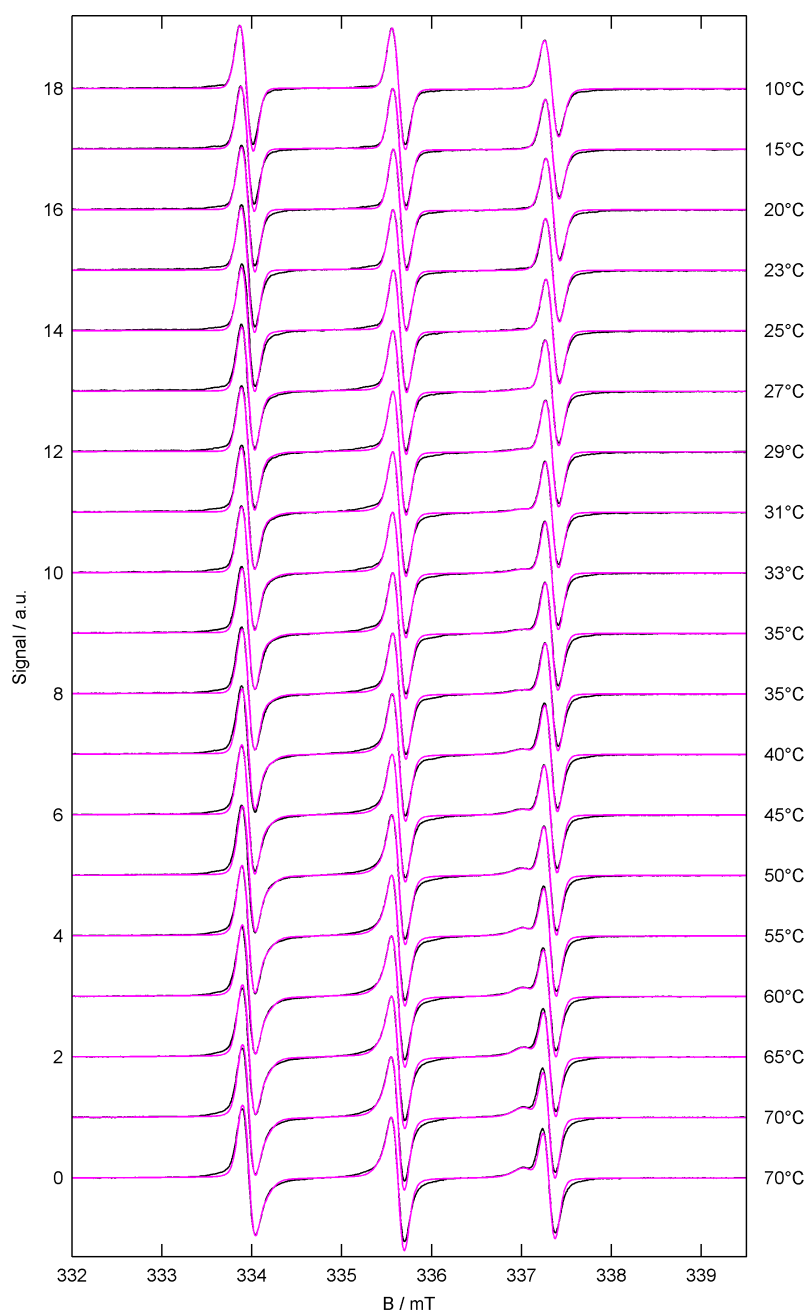


Figure A.39: All EPR spectral simulations of (TPVAVG)₄₀ (300 μM) with TB (1 mM) at temperatures between 10 and 75 °C during heating. Experimental data is shown in black, simulated data in magenta.

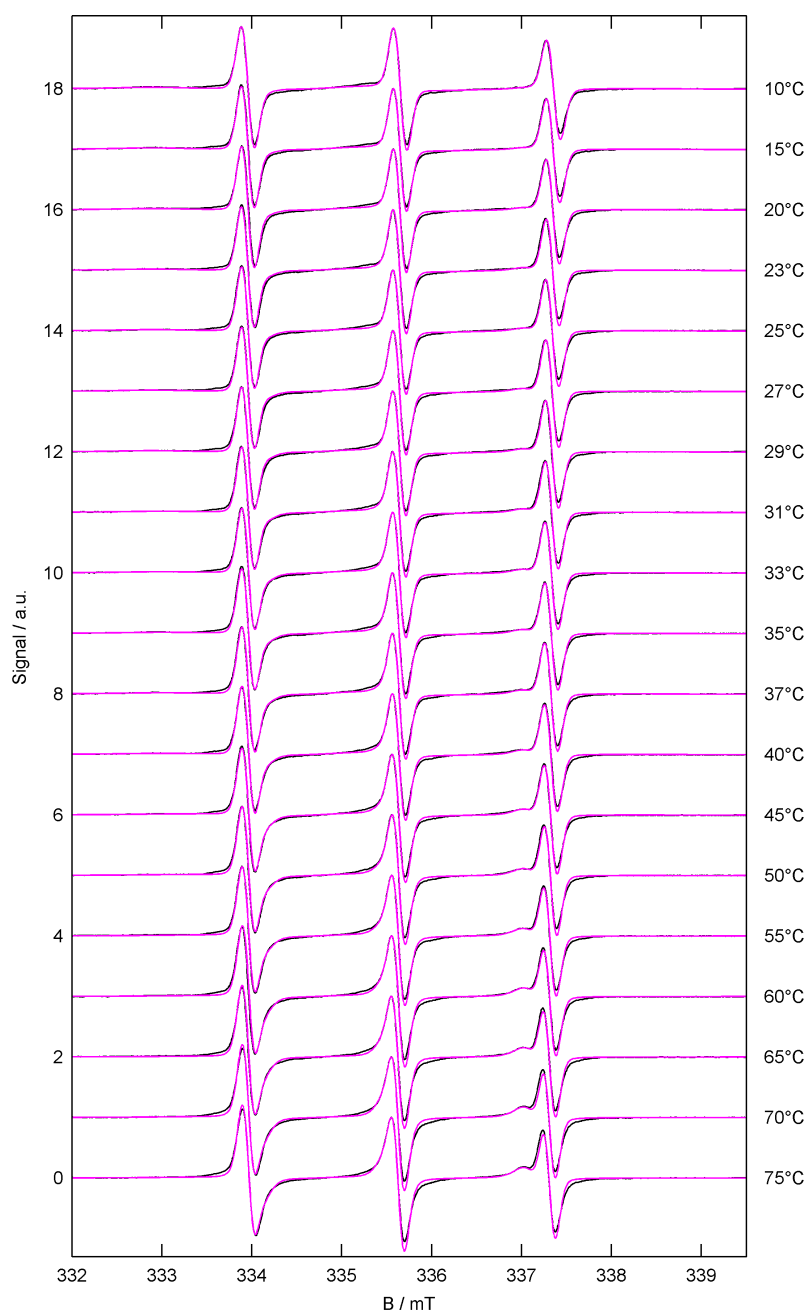


Figure A.40: All EPR spectral simulations of (TPVAVG)₄₀ (300 μM) with TB (1 mM) at temperatures between 10 and 75 °C during cooling. Experimental data is shown in black, simulated data in magenta.

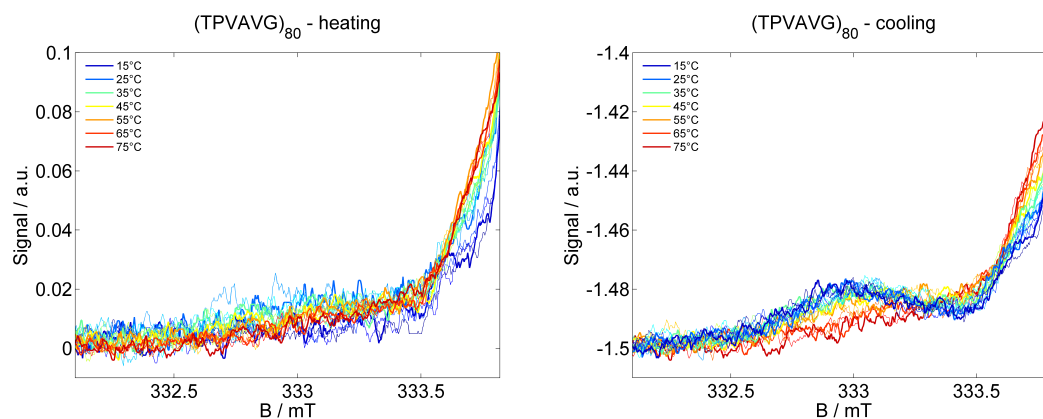


Figure A.41: Low field lines of the immobile component visible in the CW EPR spectra of $(\text{TPVAVG})_{80}$ during heating (left) and cooling (right).

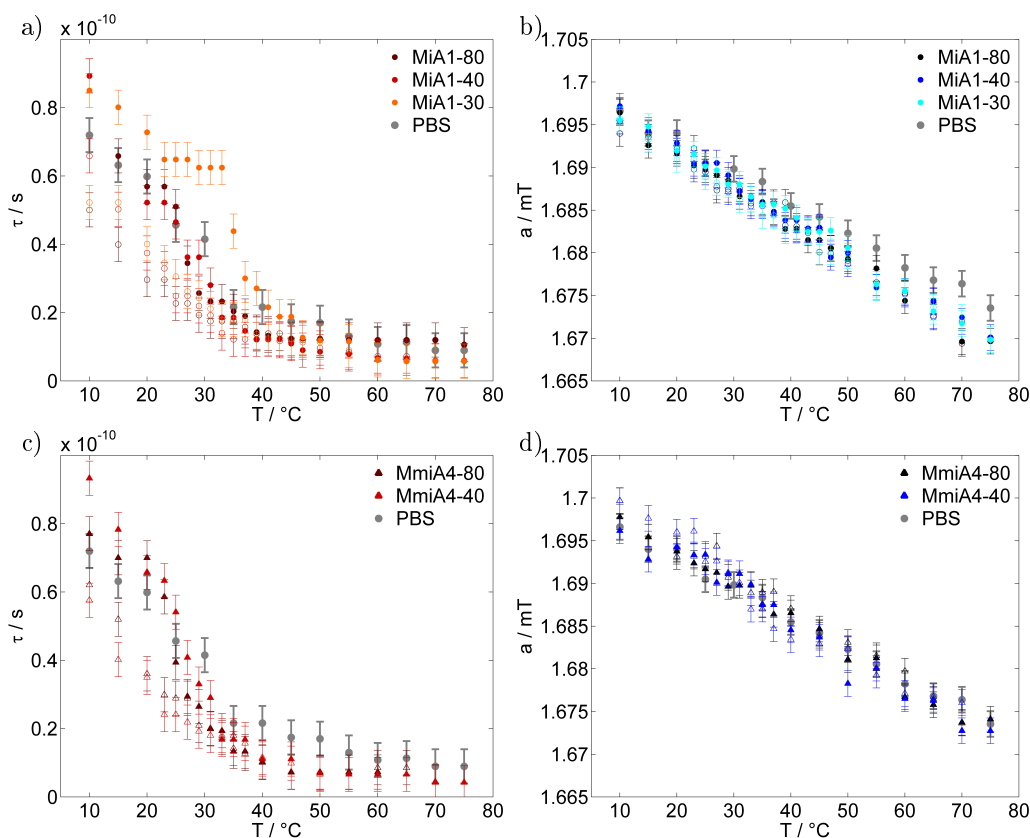


Figure A.42: Results of simulation of TB in buffer solution of hysteretic polymers: rotational correlation times (a) and c)) and hyperfine splitting constant (b) and d)) of the hydrophilic spectral component for different hydrophobic block lengths (a) and b)) and different hydrophilic blocks (c) and d)). Hyperfine splitting constants give half of the difference in B field of the high-field and of the low-field peak of the simulated EPR spectra of the respective component.

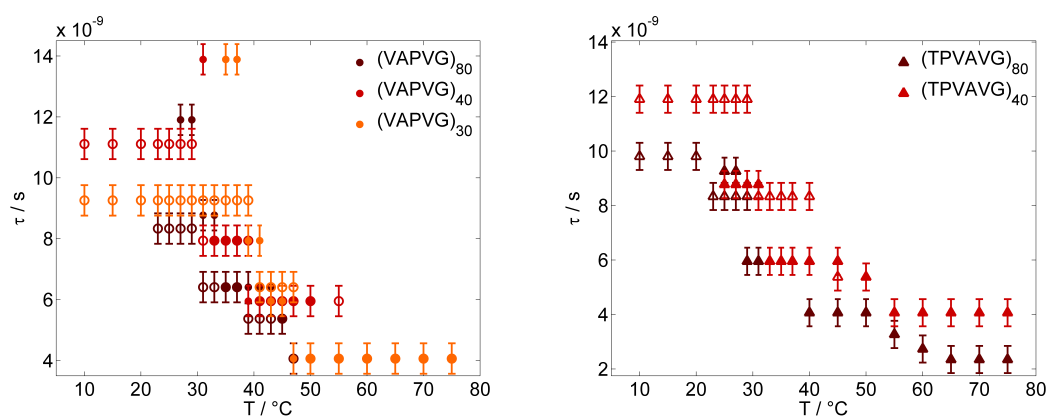


Figure A.43: Rotational correlation times of the simulated immobile component compared for same motif (left: (VAPVG) and right: (TPVAVG)).

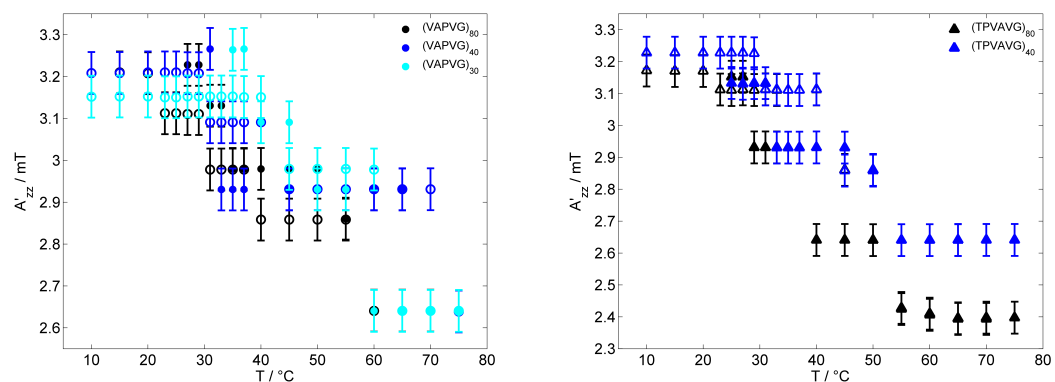


Figure A.44: Hyperfine splitting constants of the simulated immobile component compared for same motif (left: (VAPVG) and right: (TPVAVG)). Hyperfine splitting constants give half of the difference in B field of the high-field and of the low-field peak of the simulated EPR spectra of the respective component.

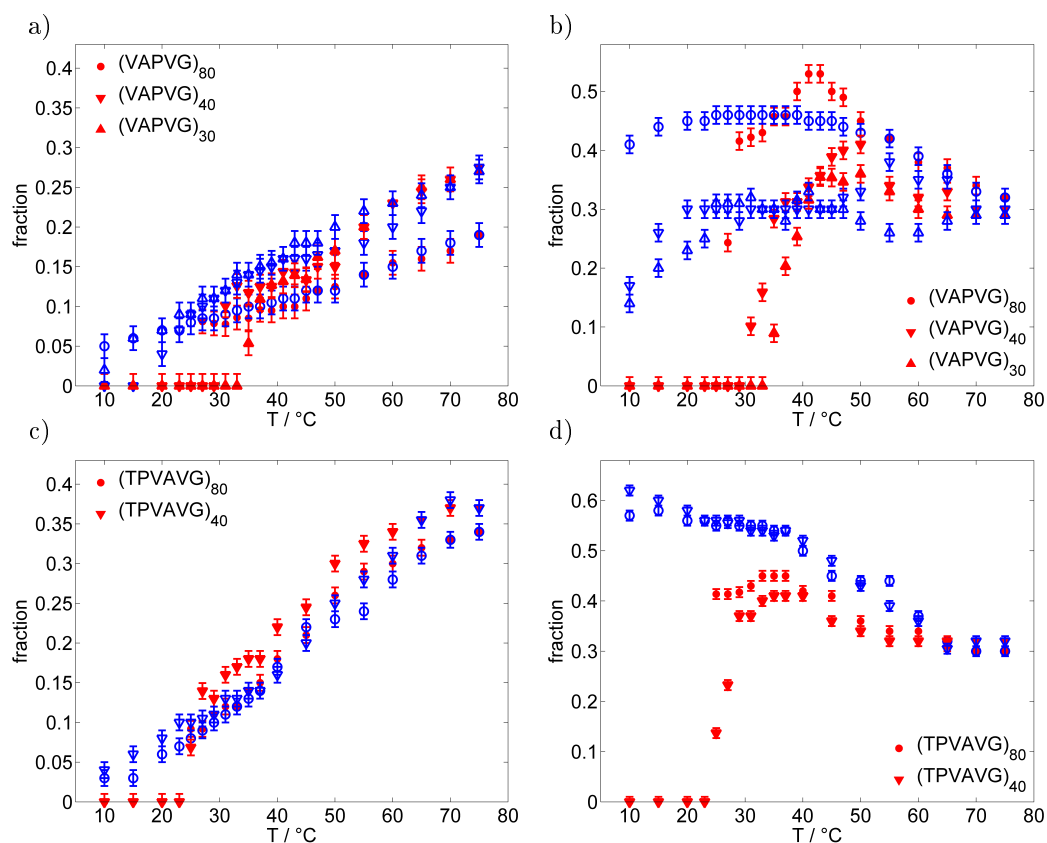
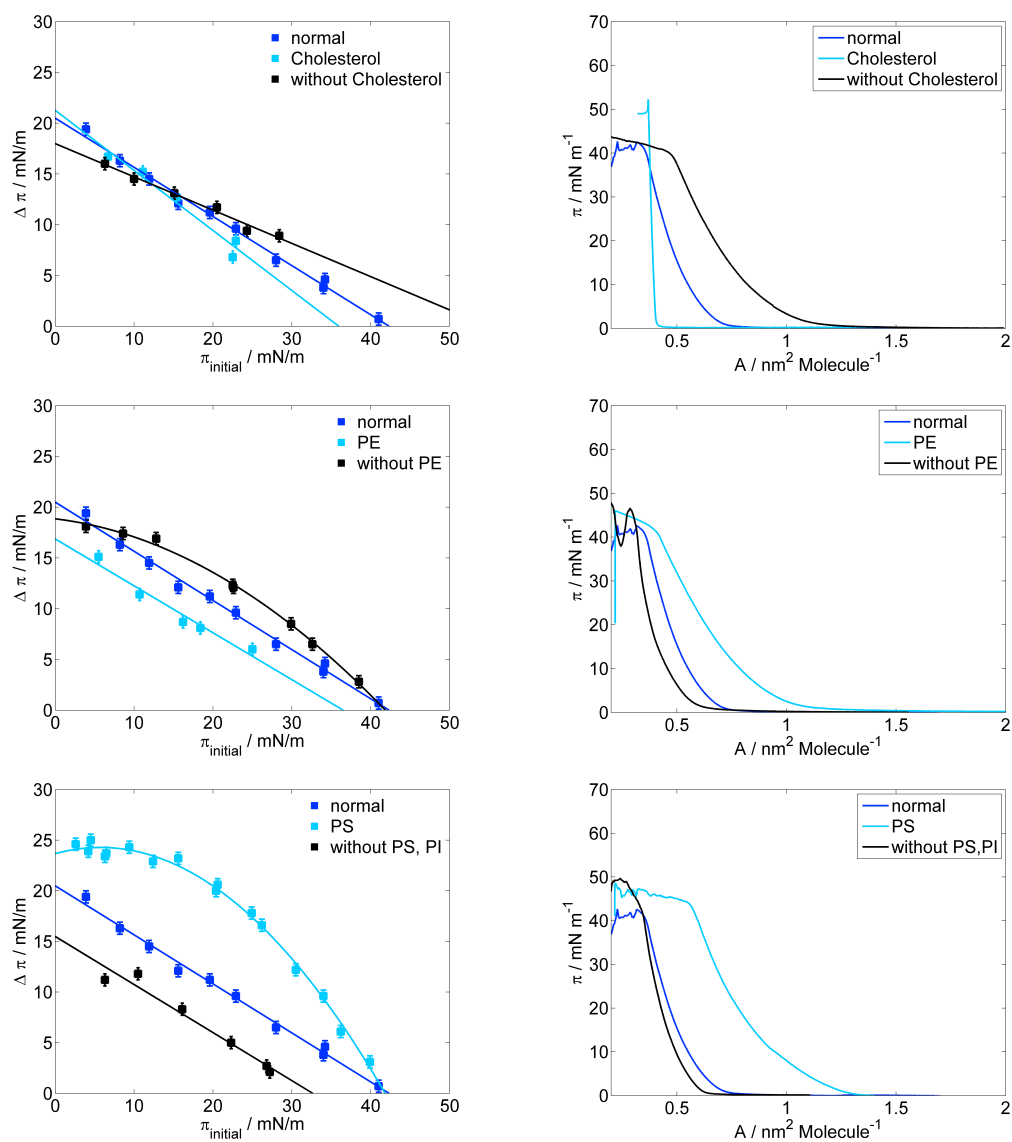


Figure A.45: Fractions of the components of the EPR spectra of the hysteretic polymers arising with the transition of the polymer from rigorous spectral simulation compared for different n . a) Fractions of the hydrophobic component of (VAPVG) _{n} , b) fractions of the immobile component of (VAPVG) _{n} , c) fractions of the hydrophobic component of (TPVAVG) _{n} , d) fractions of the immobile component of (TPVAVG) _{n} , ● heating and ○ cooling.

APPENDIX B

Myelin basic protein

B.1 Bovine myelin basic protein



(Figure is continued on the next page.)

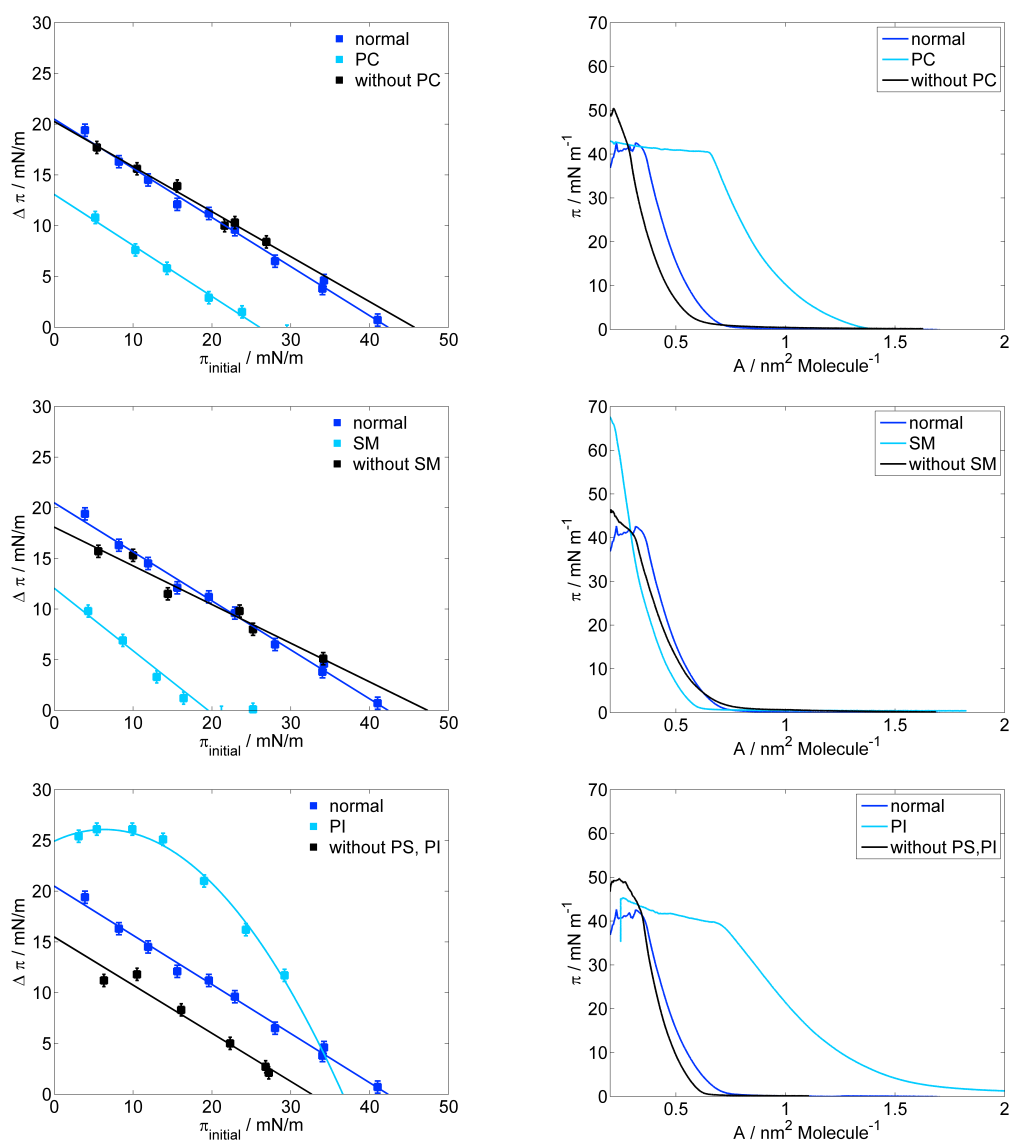
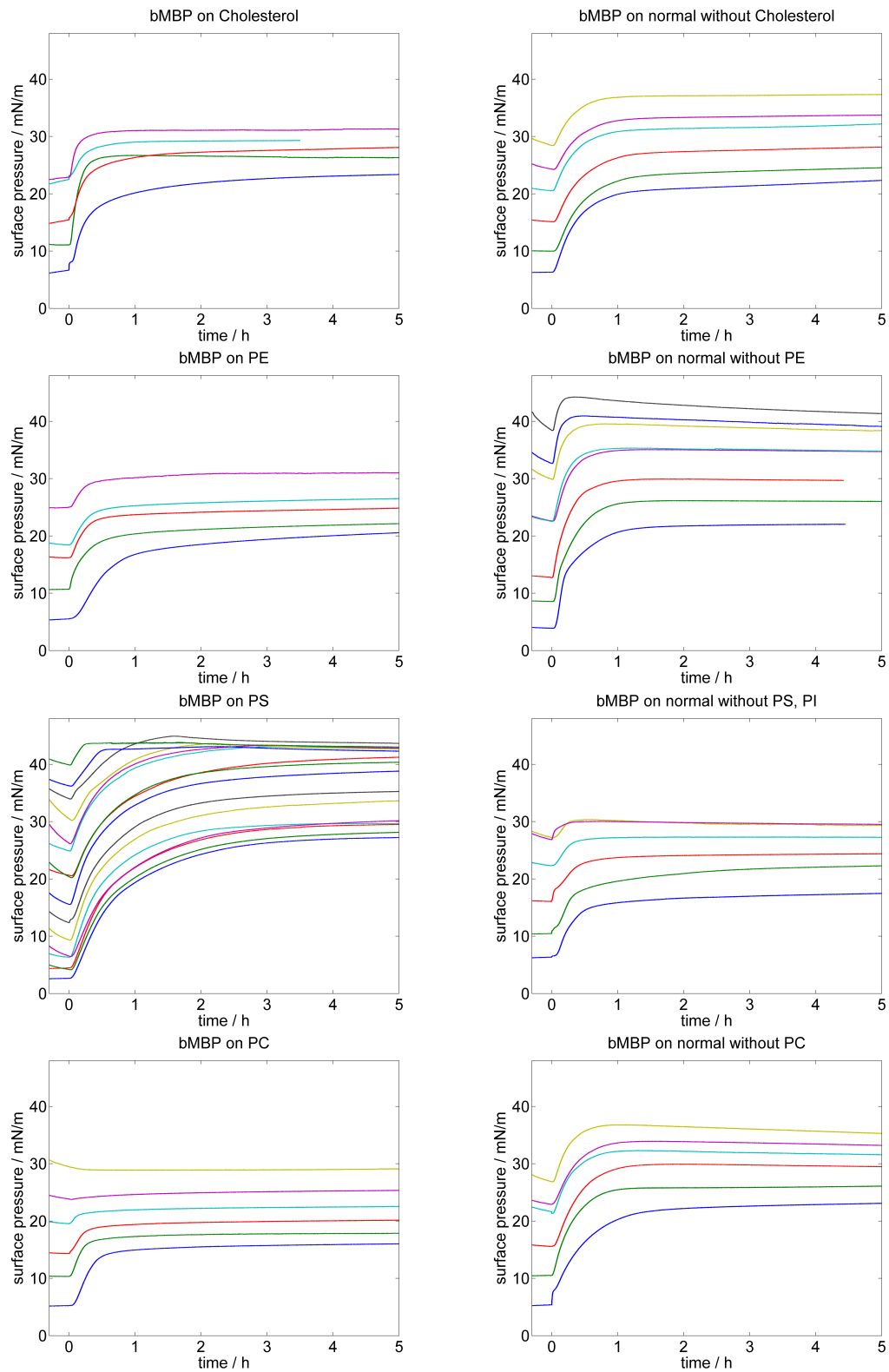


Figure B.1: Comparison of the several lipids with the normal myelin lipid composition and the normal composition without the respective lipid. Left: Difference of surface pressure $\Delta\pi(\pi_{ini})$ after maximal 5 h of adsorption of bMBP ($c = 100$ nM) to brain lipid monolayers as a function of the initial surface pressure π_{ini} . Regression curves are included. Right: Surface pressure-area isotherms of the lipid monolayers.



(Figure is continued on the next page.)

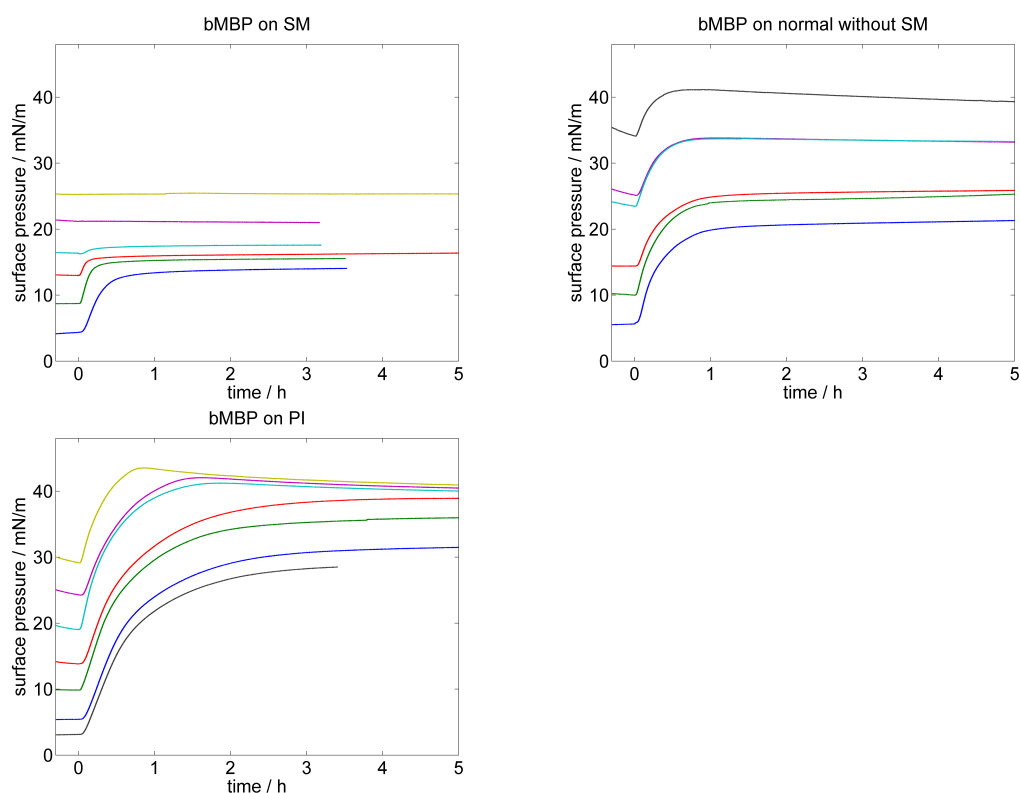


Figure B.2: Time-dependent surface pressure of bMBP injected at $t = 0$ h below monolayers of constant surface area.

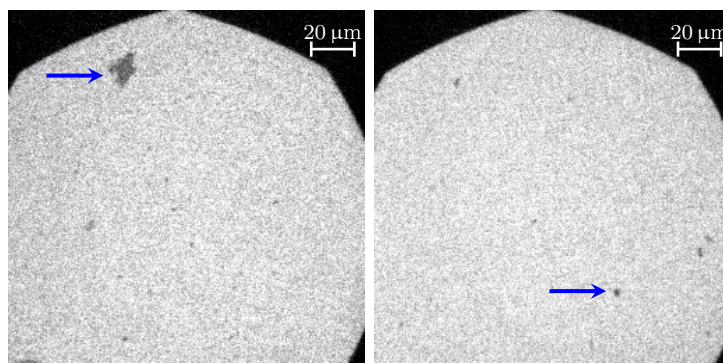


Figure B.3: Fluorescence microscopy images of a PS monolayer with bMBP at a pressure of 8.4 mN/m (left) 9 mN/m (right). Blue arrows highlight regions of higher order than the LE phase of PS representing lipid condensed parts. Lipid dye: 0.05 mol% Rh-DHPE.

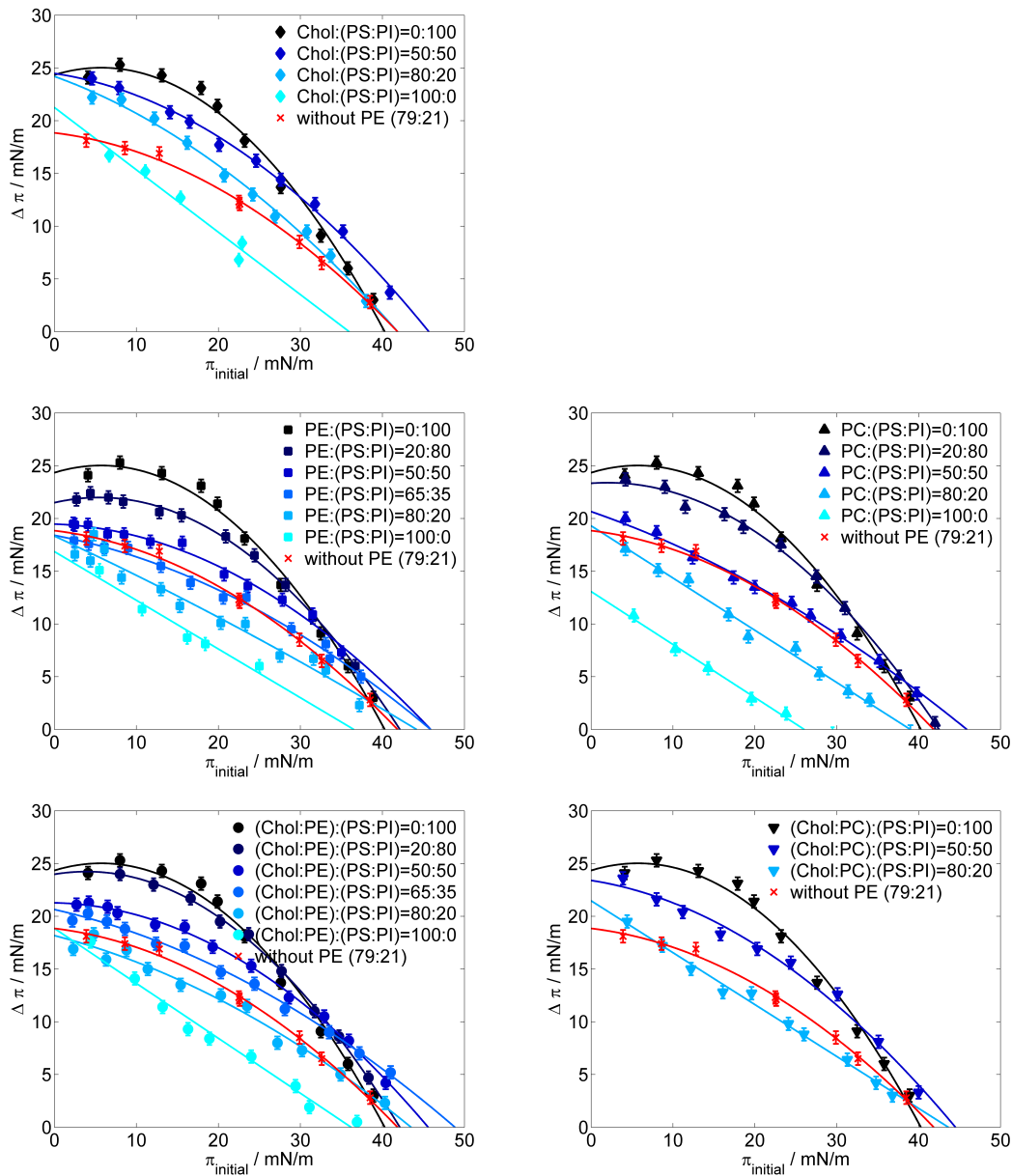
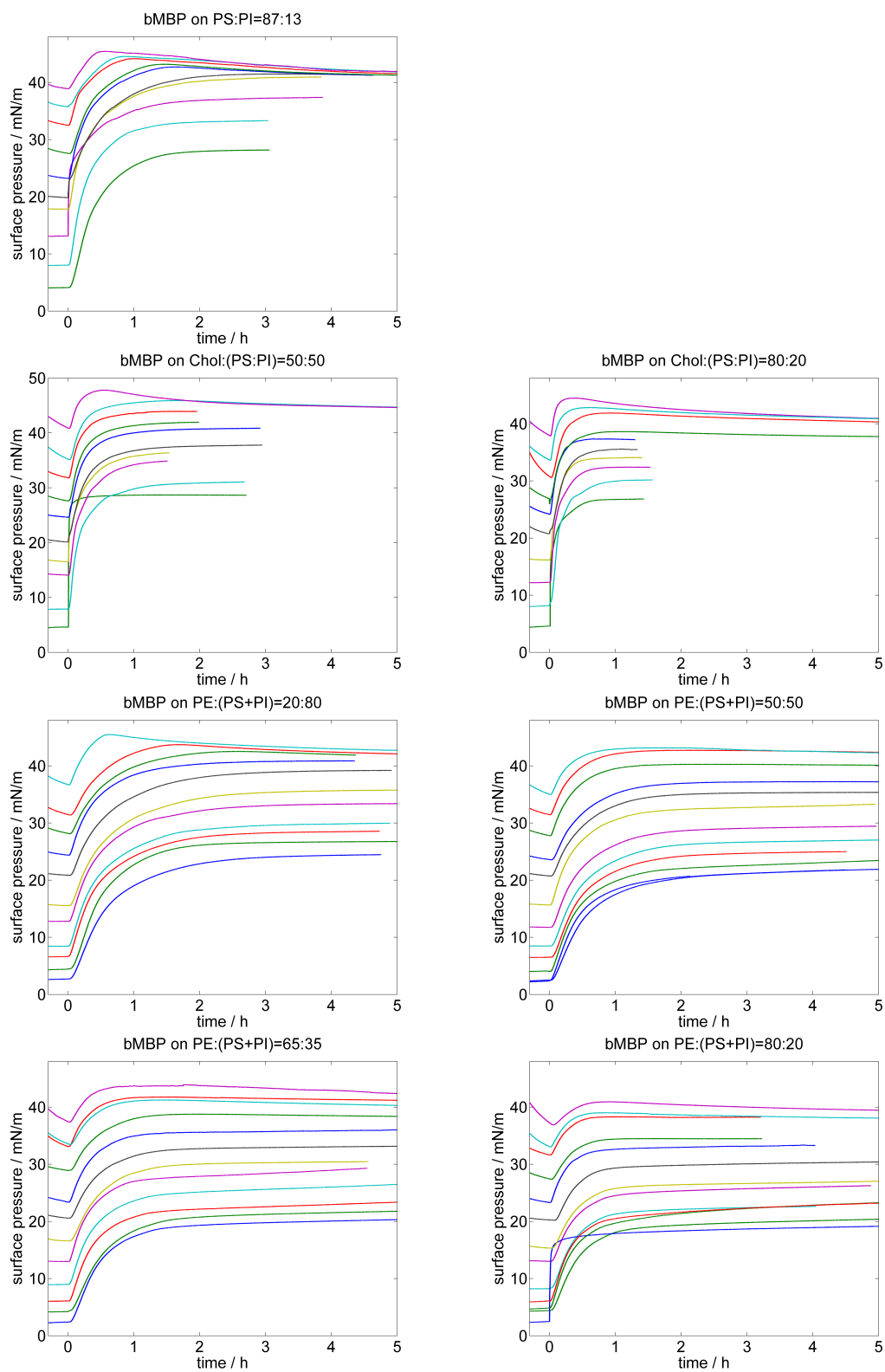
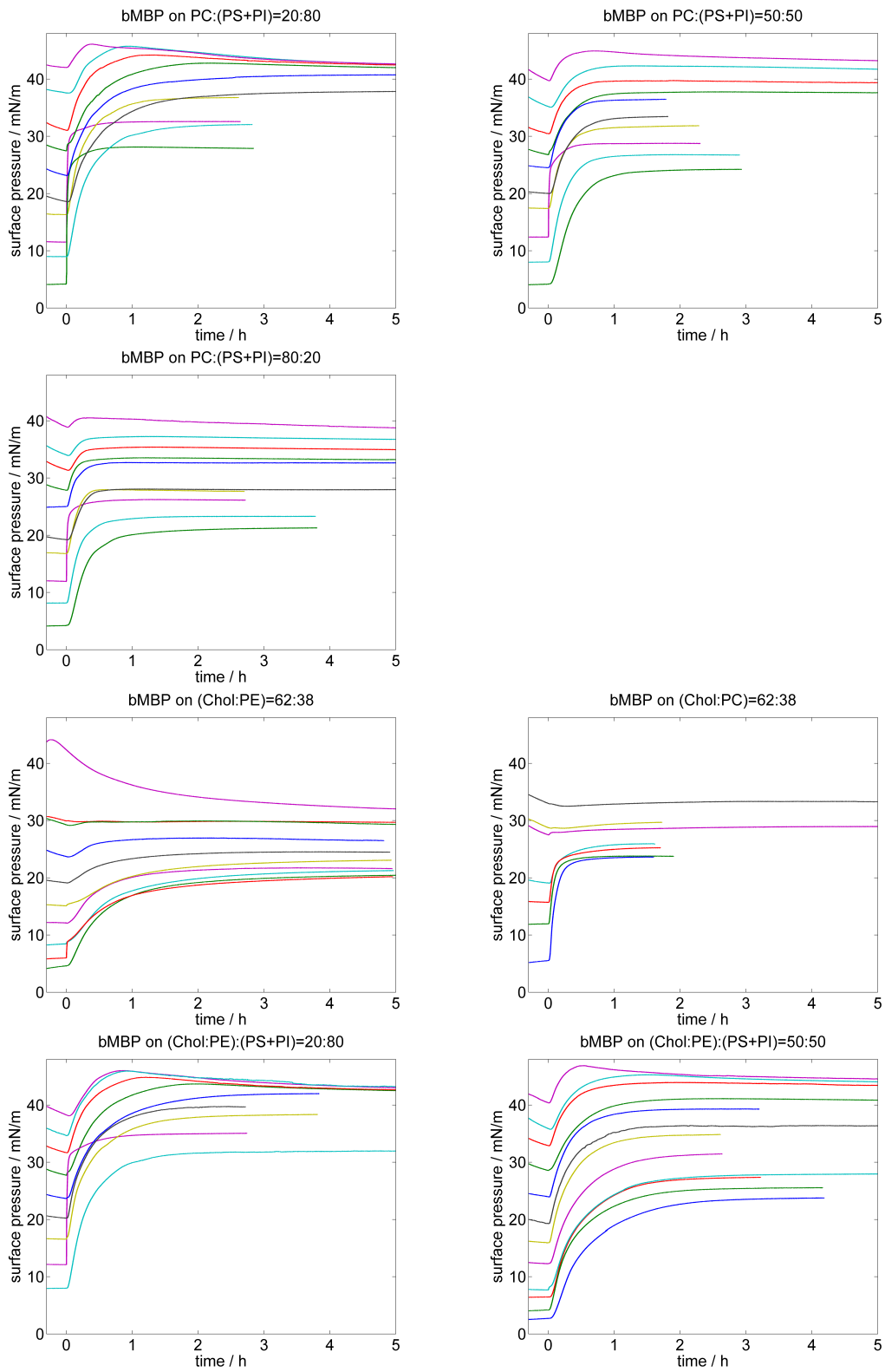


Figure B.4: Difference of surface pressure $\Delta\pi(\pi_{\text{ini}})$ after maximal 5 h of adsorption of bMBP ($c = 100 \text{ nM}$) to lipid monolayers as a function of the initial surface pressure π_{ini} . Different ratios of cholesterol, PE and PC to PS and PI were tested to investigate the influence of electrostatic interactions on the behaviour of $\Delta\pi(\pi_{\text{ini}})$. The red curves called ‘without PE’ correspond to the normal composition of the myelin without PE. The displayed ratios represent the mole ratio of uncharged to charged lipids. Regression curves are included.



(Figure is continued on the next page.)



(Figure is continued on the next page.)

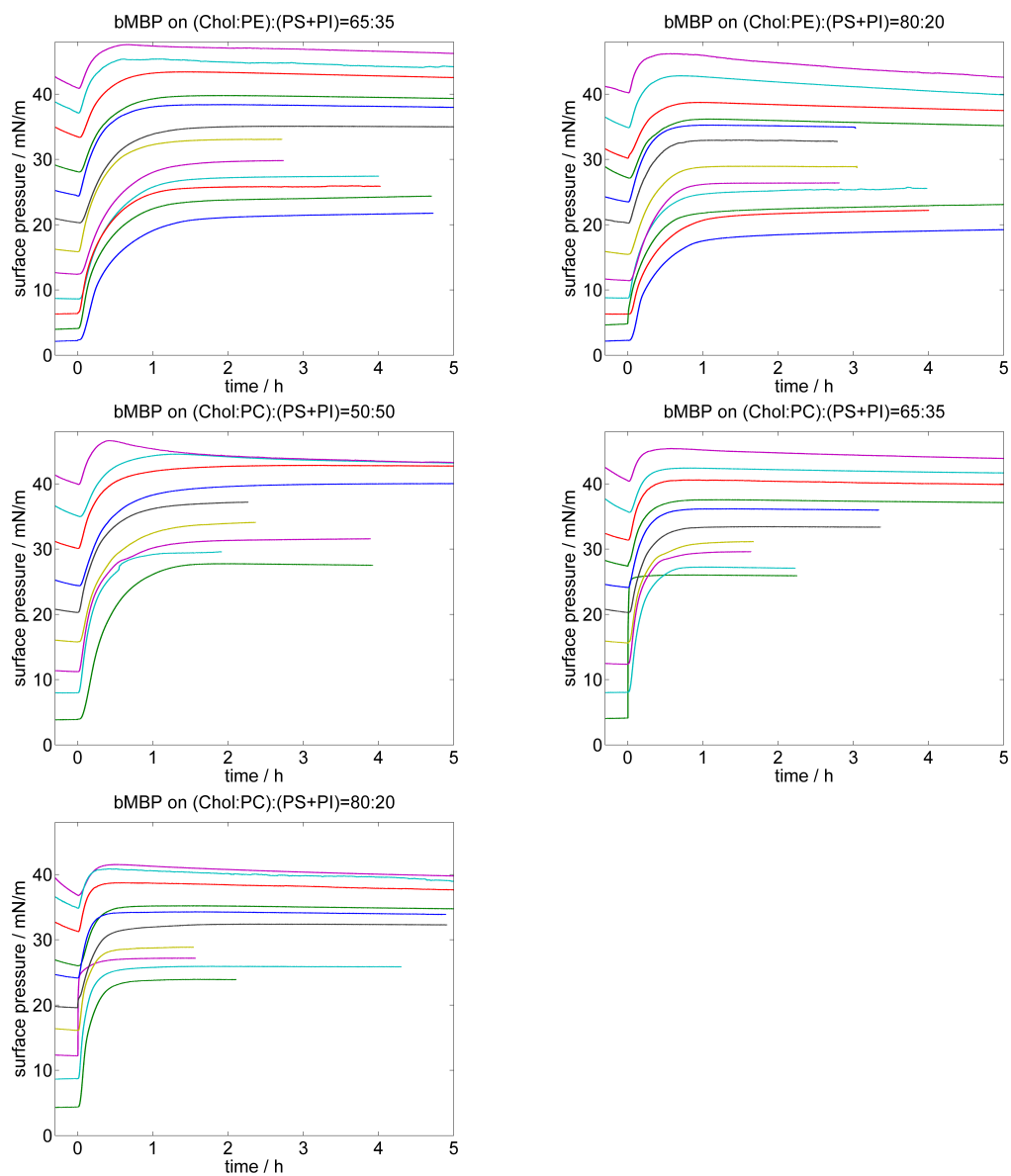


Figure B.5: Time-dependent surface pressure of bMBP injected at $t = 0$ h below monolayers of constant surface area.

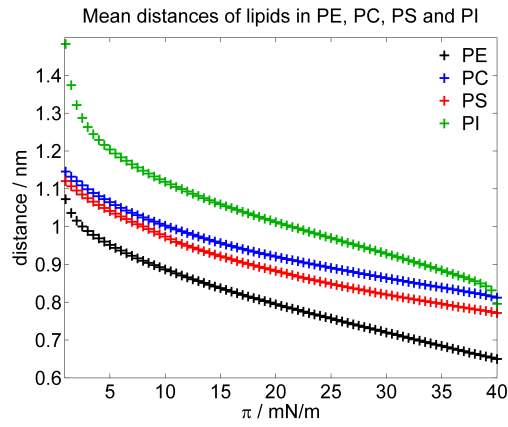


Figure B.6: Distances between two lipid molecules in PS, PI, PE and PC monolayers.

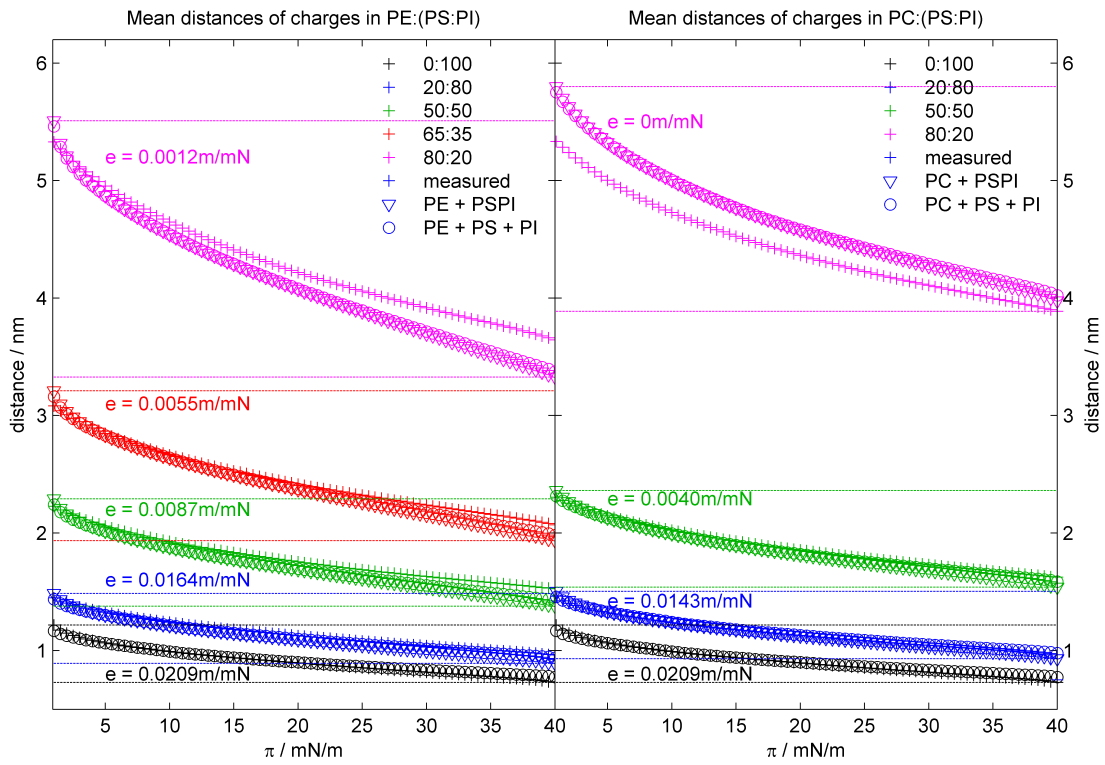


Figure B.7: Distances between two charged lipids in all compositions of PE:(PS:PI) (left) and PC:(PS:PI) (right).

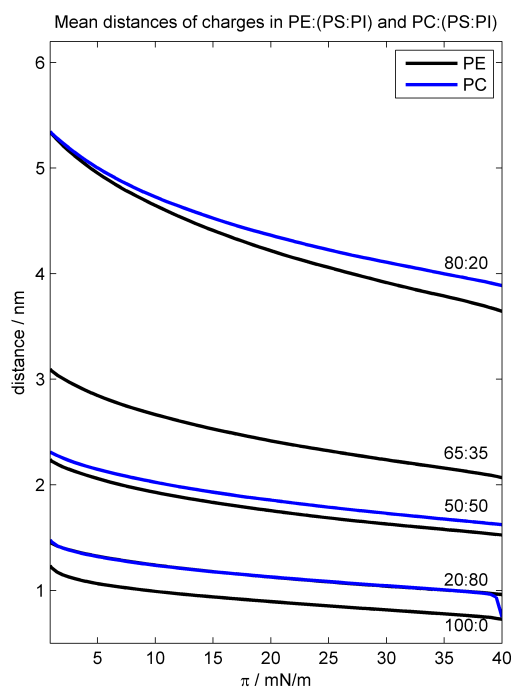


Figure B.8: Distances between two charged lipids calculated by Equation 1 in all compositions of PE:(PS:PI) compared to PC:(PS:PI).

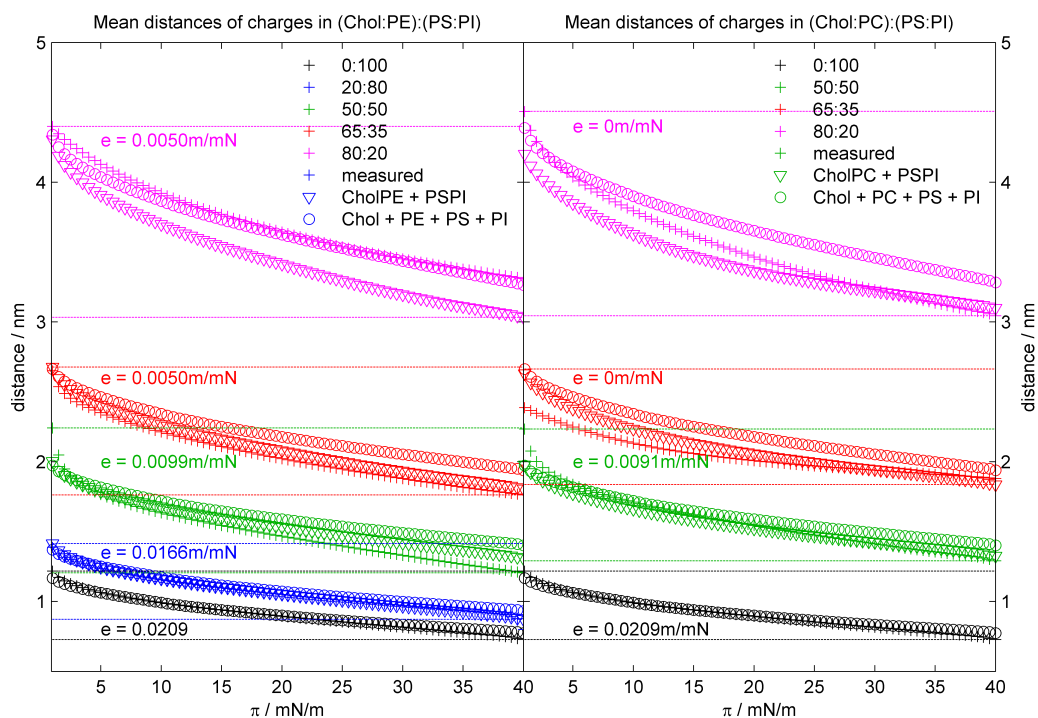


Figure B.9: Distances between two charged lipids in all compositions of (Chol:PE):(PS:PI) (left) and (Chol:PC):(PS:PI) (right).

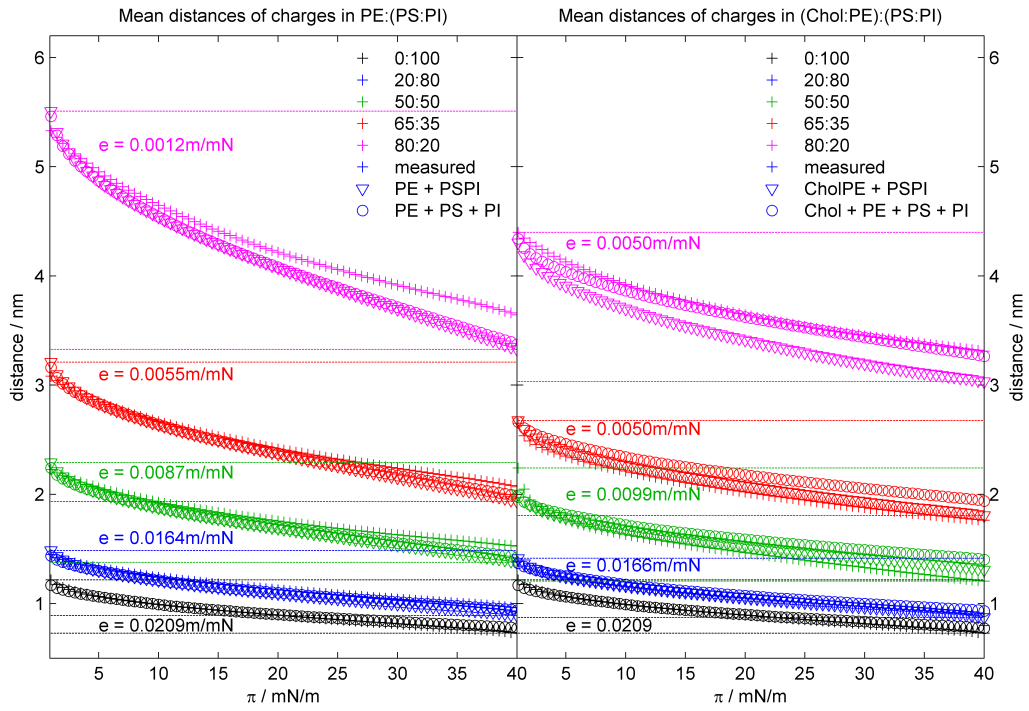


Figure B.10: Distances between two charged lipids in all compositions of PE:(PS:PI) (left) and (Chol:PE):(PS:PI) (right).

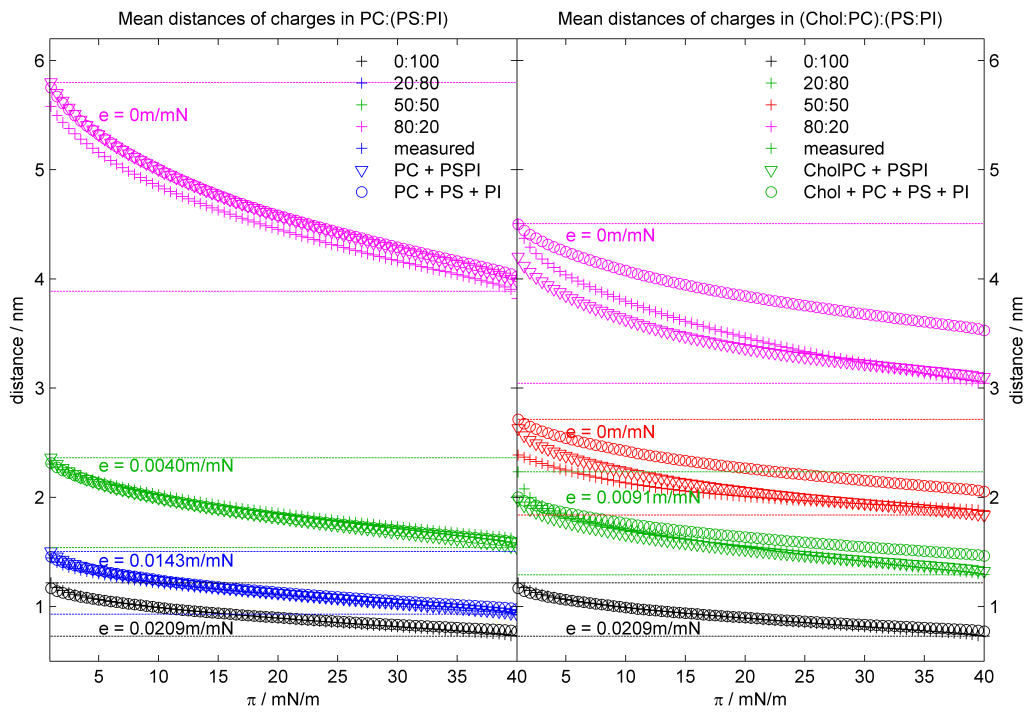


Figure B.11: Distances between two charged lipids in all compositions of PC:(PS:PI) (left) and (Chol:PC):(PS:PI) (right).

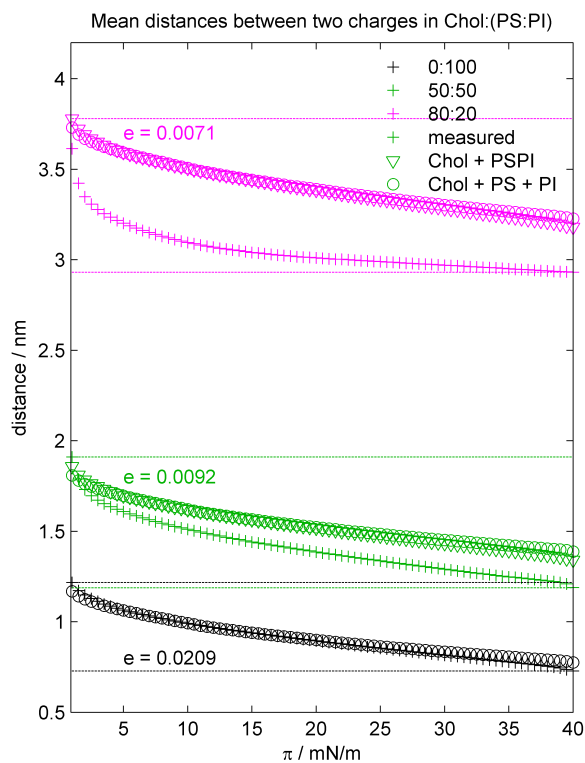


Figure B.12: Distances between two charged lipids in all compositions Chol:(PS:PI).

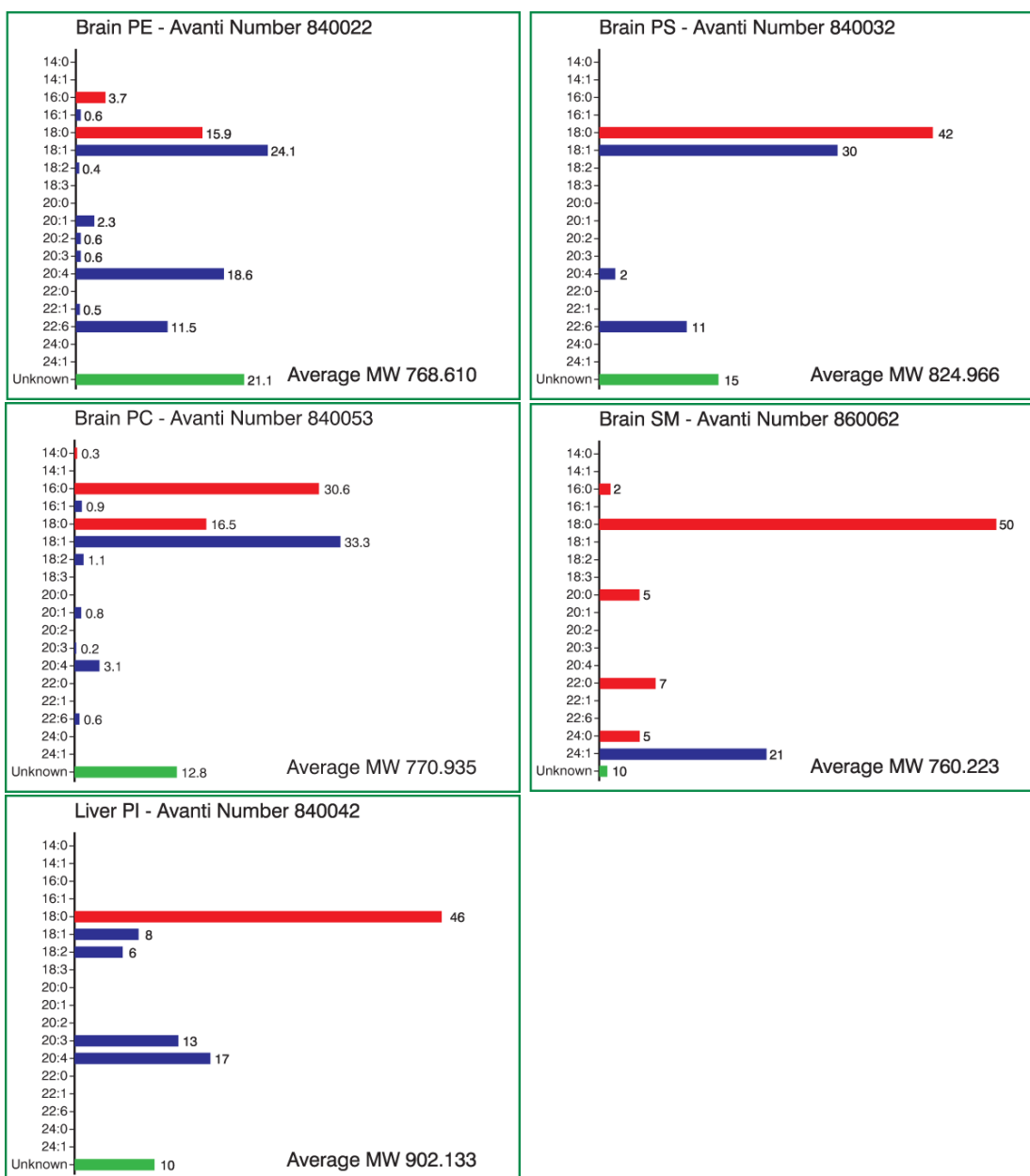


Figure B.13: Fatty acid distribution in the brain lipid solutions.

B.2 Recombinant murine myelin basic protein C1 and C8 charge variants

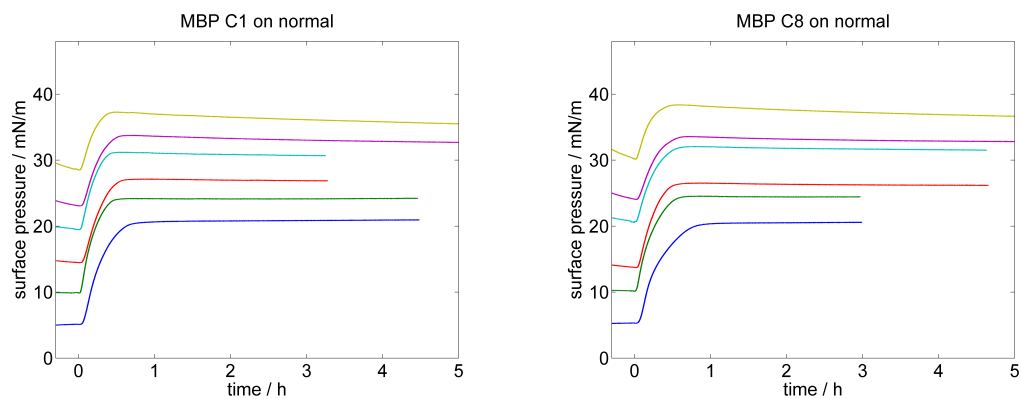


Figure B.14: Time-dependent surface pressure of MBP C1 and C8 injected at $t = 0$ h below a monolayer of the normal composition of constant surface area.

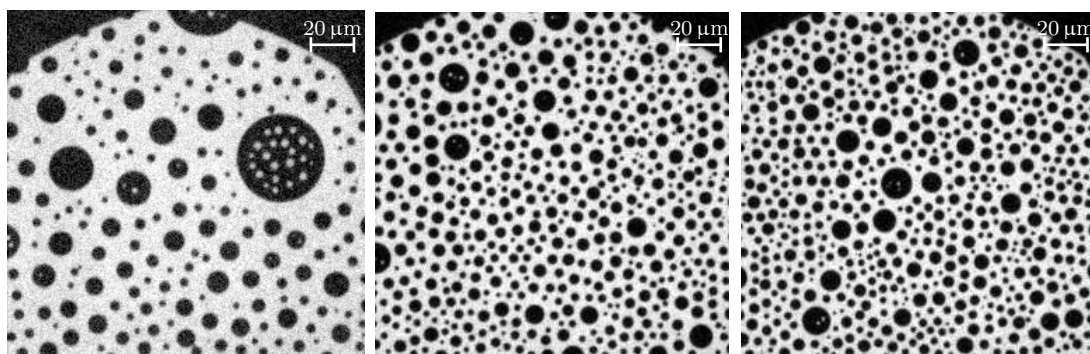


Figure B.15: Fluorescence microscopy images monolayer composed of the normal composition at a pressure between 5 mN/m and 10 mN/m. Lipid dye: 0.05 mol-% Rh-DHPE.

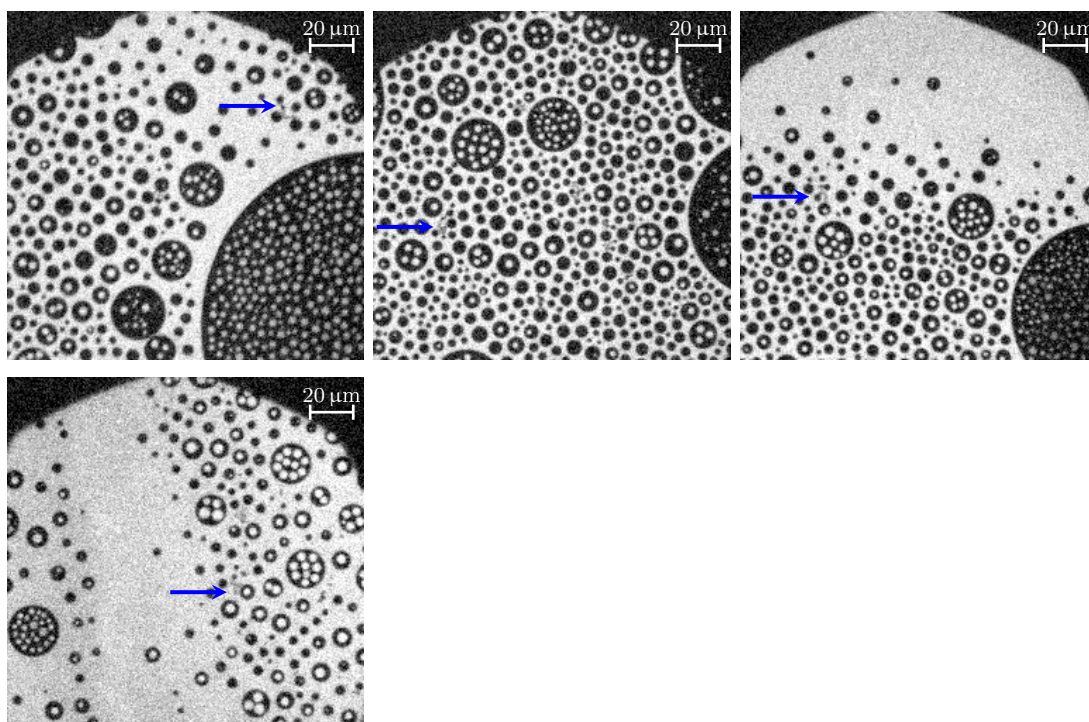


Figure B.16: Fluorescence microscopy images of MBP C1 adsorbed to a monolayer composed of the normal composition at a pressure between 5 mN/m and 10 mN/m. Lipid dye: 0.05 mol-% Rh-DHPE. The blue arrows highlight exemplary small regions arising from the adsorption of MBP to the myelin-like monolayer.

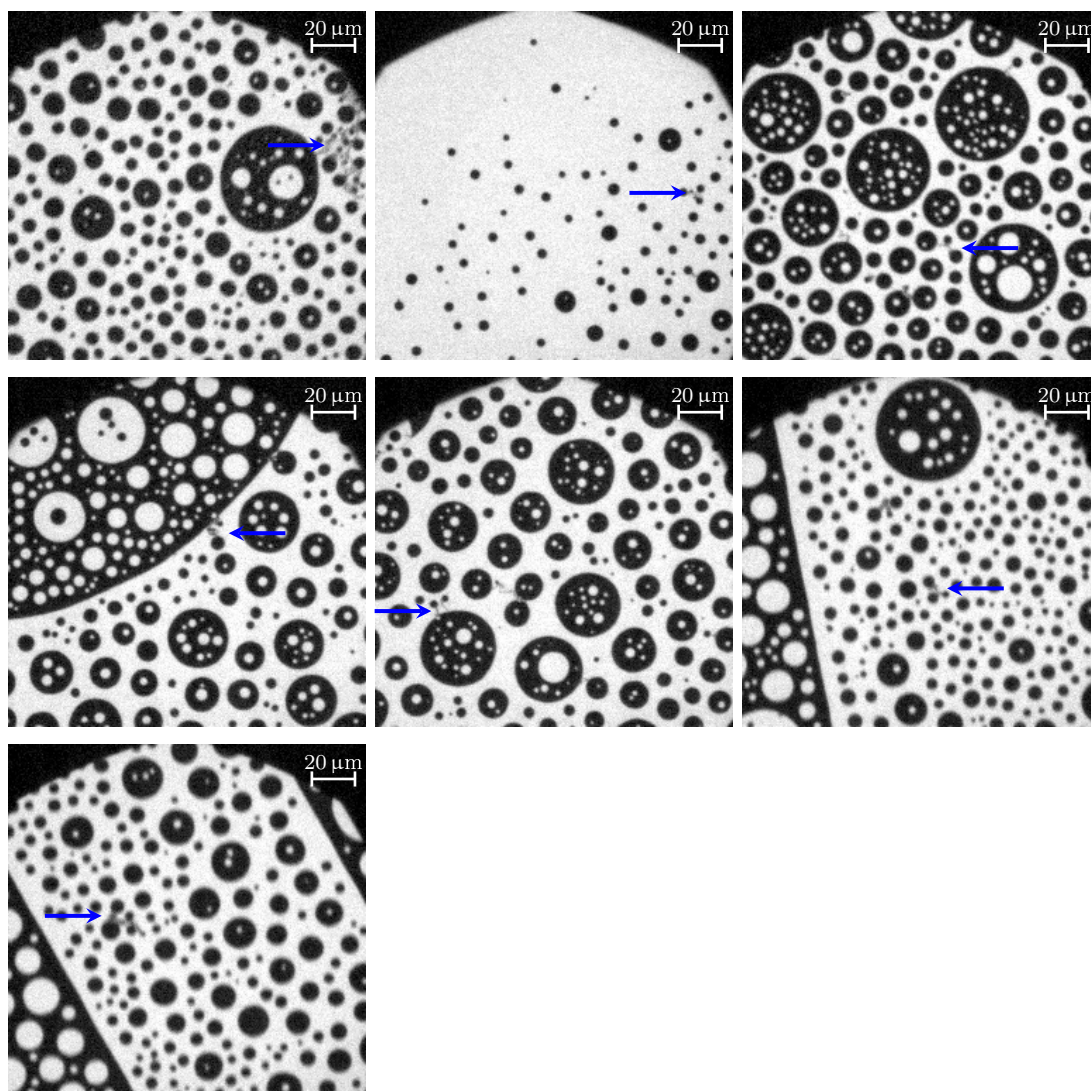


Figure B.17: Fluorescence microscopy images of MBP C8 adsorbed to a monolayer composed of the normal composition at a pressure between 5 mN/m and 10 mN/m. Lipid dye: 0.05 mol-% Rh-DHPE. The blue arrows highlight exemplary small regions arising from the adsorption of MBP to the myelin-like monolayer.

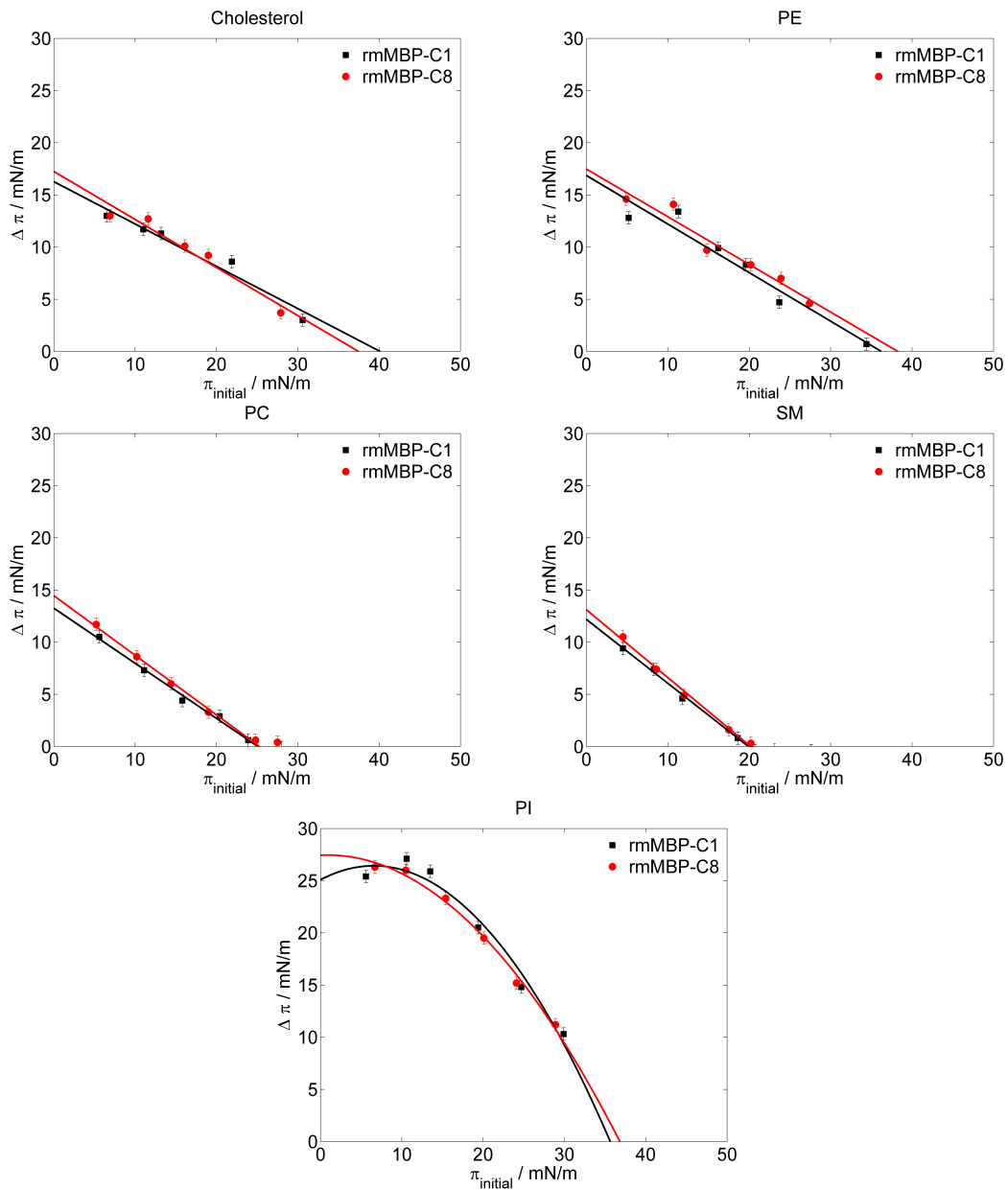
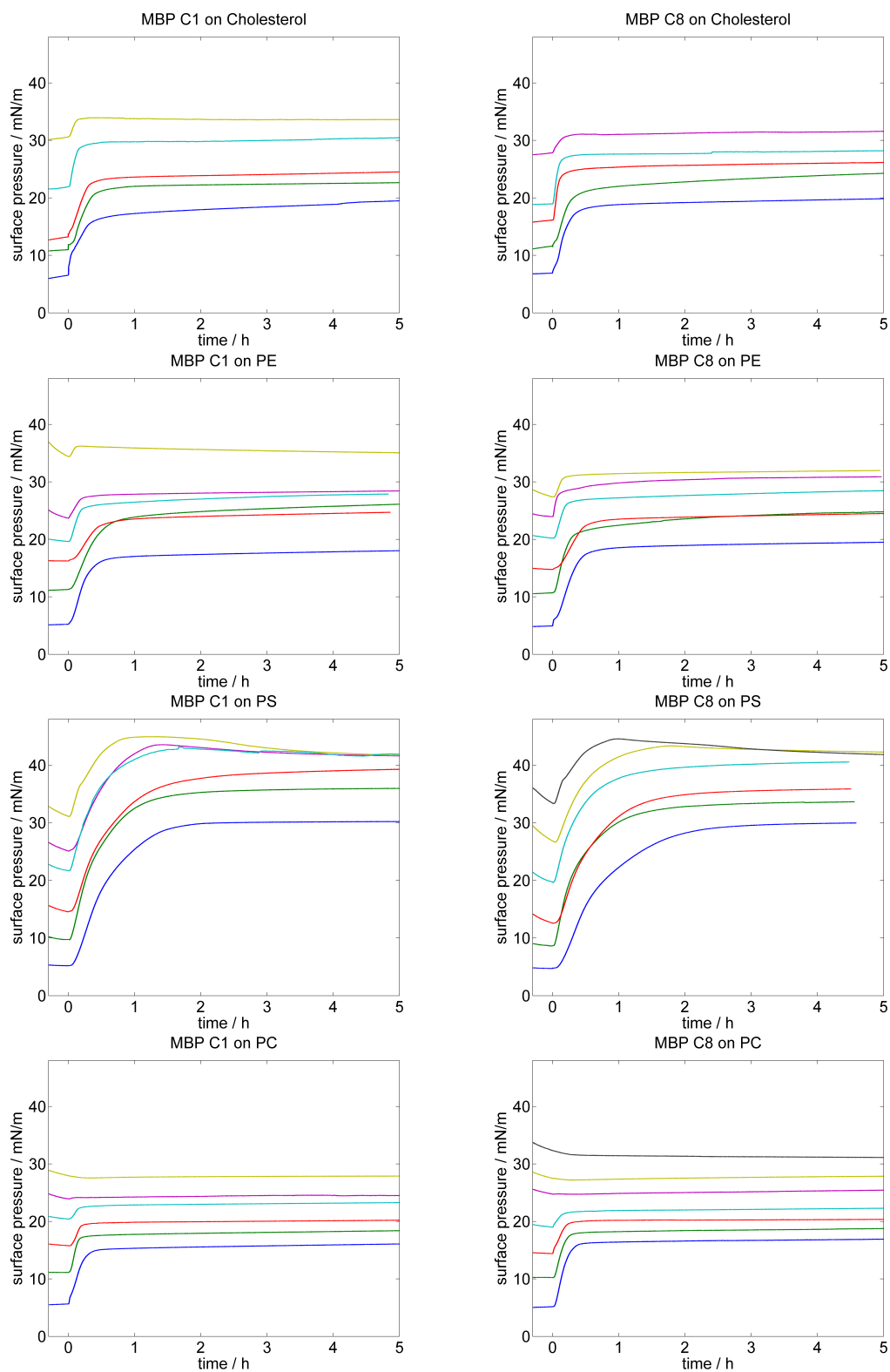


Figure B.18: Difference of surface pressure $\Delta \pi(\pi_{\text{ini}})$ after maximal 5 h of adsorption of myelin basic protein charge variants C1 and C8 ($c = 100$ nM) to lipid monolayers of the major single brain lipids of the cytoplasmic side of the oligodendrocyte membrane as a function of the initial surface pressure π_{ini} . Regression curves are included.



(Figure is continued on the next page.)

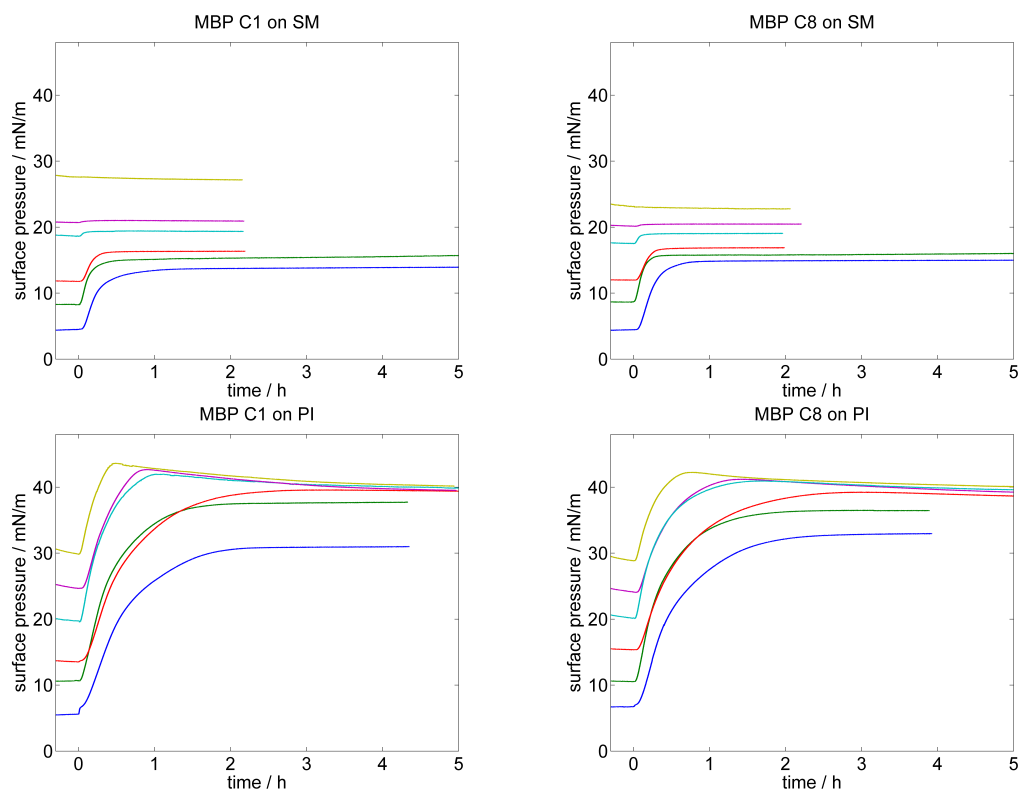


Figure B.19: Time-dependent surface pressure of MBP C1 and C8 injected at $t = 0$ h below monolayers of constant surface area.

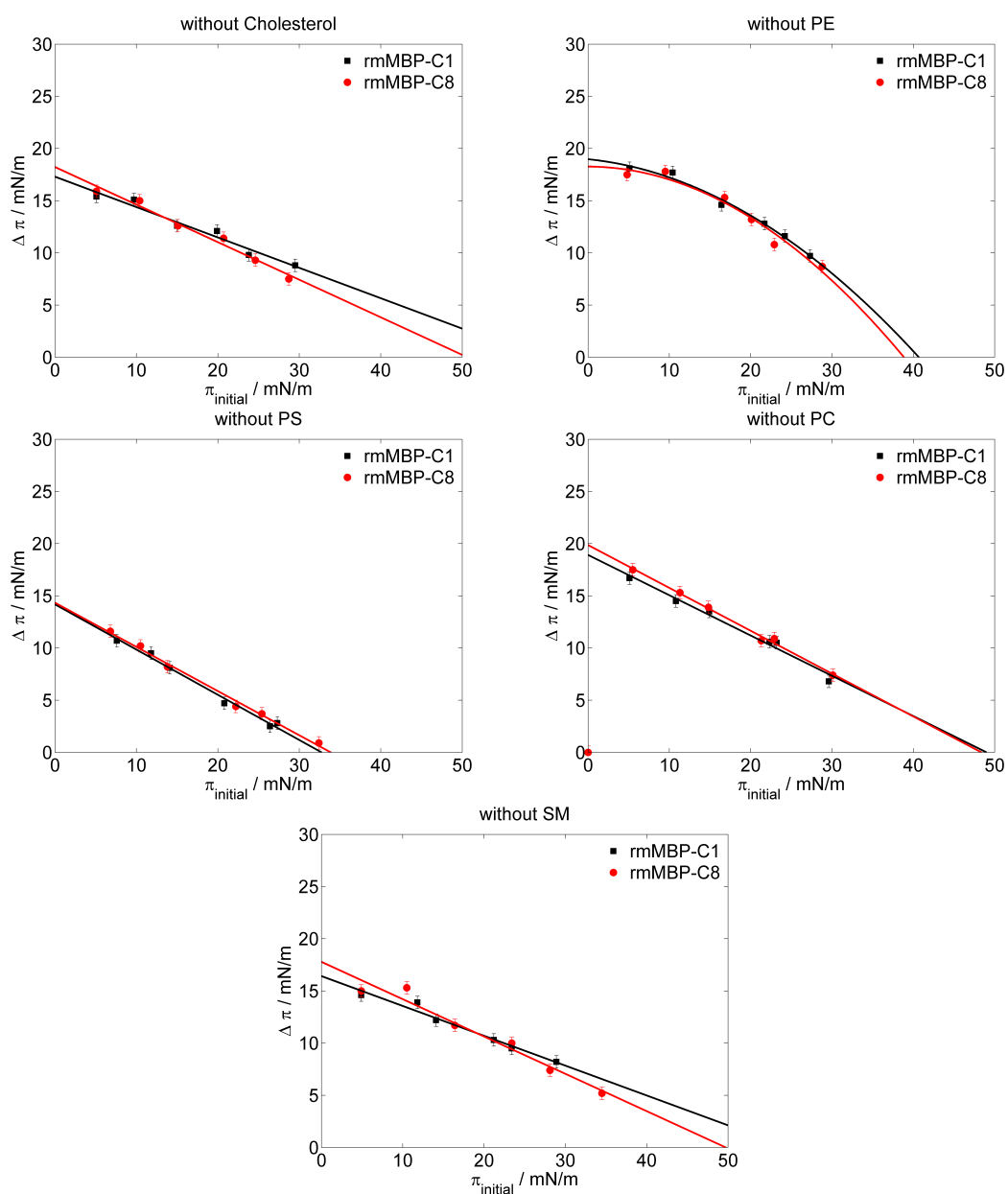
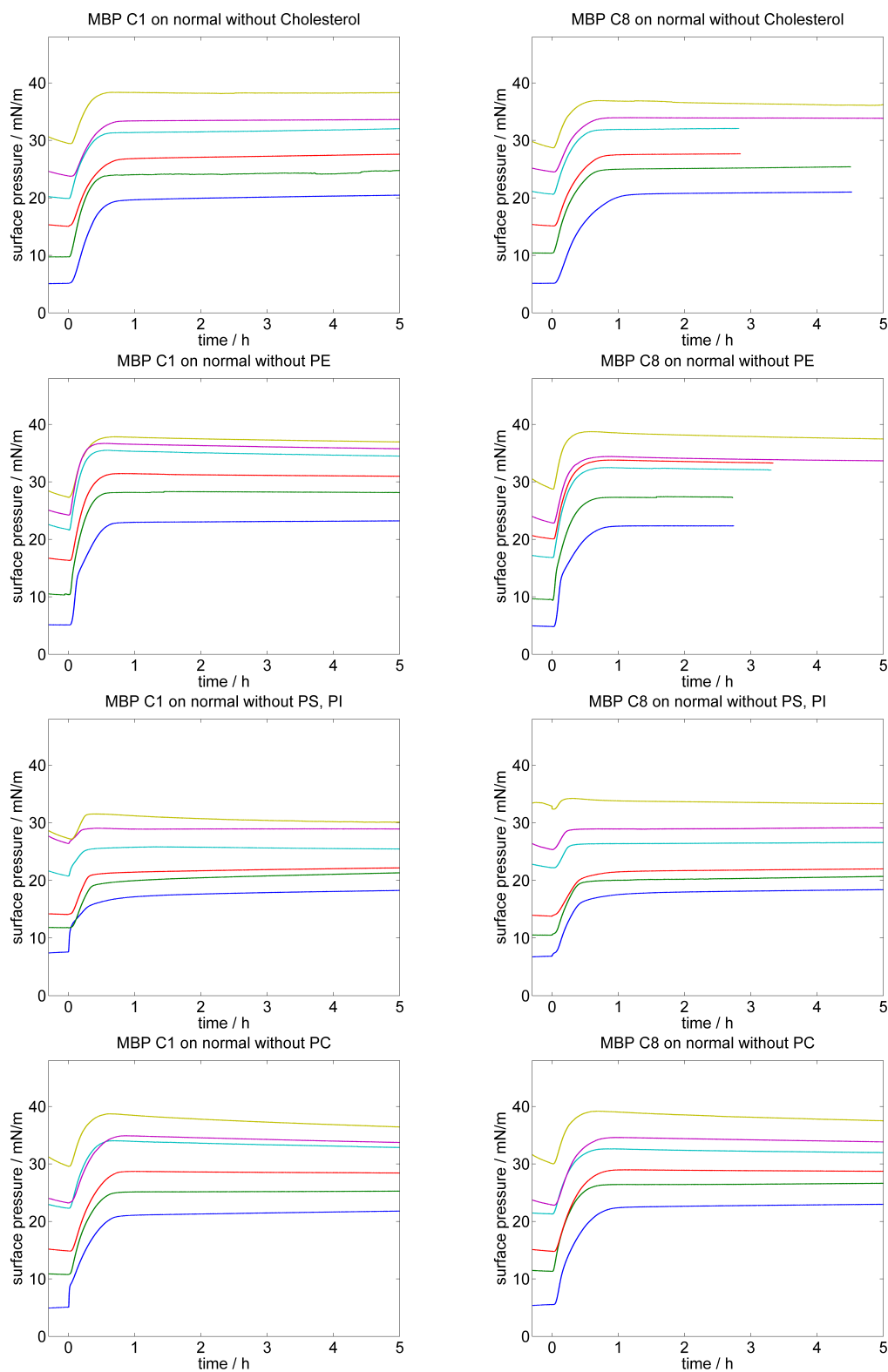


Figure B.20: Difference of surface pressure $\Delta\pi(\pi_{\text{ini}})$ after maximal 5 h of adsorption of myelin basic protein charge variants C1 and C8 ($c = 100$ nM) to lipid monolayers of the normal myelin-like composition without the respective lipid as a function of the initial surface pressure π_{ini} . Regression curves are included.

B.2 Recombinant murine myelin basic protein C1 and C8 charge variants



(Figure is continued on the next page.)

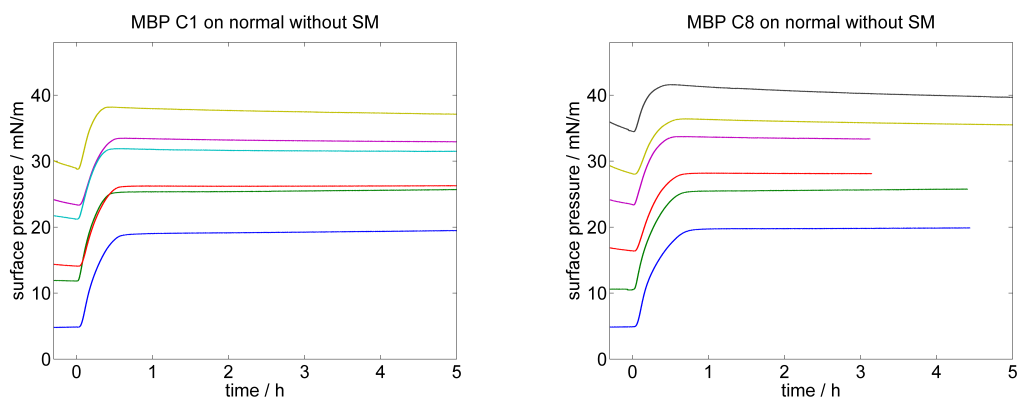


Figure B.21: Time-dependent surface pressure of MBP C1 and C8 injected at $t = 0$ h below monolayers of constant surface area.

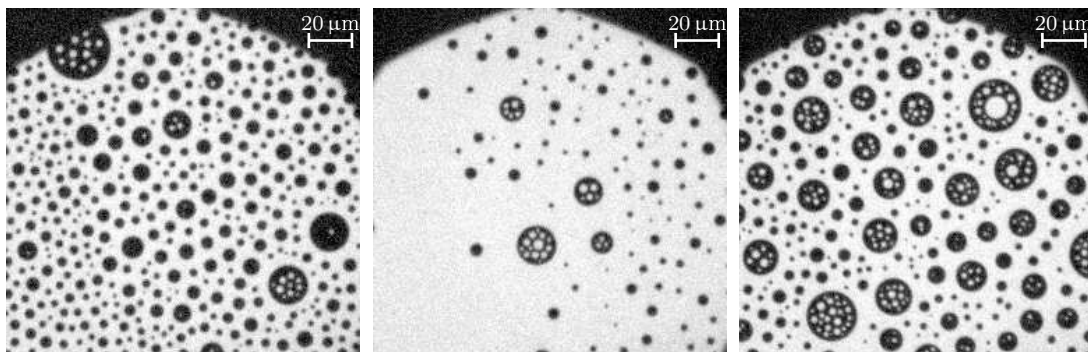


Figure B.22: Fluorescence microscopy images monolayer composed of the normal composition without SM at a pressure between 5 mN/m and 10 mN/m. Lipid dye: 0.05 mol-% Rh-DHPE.

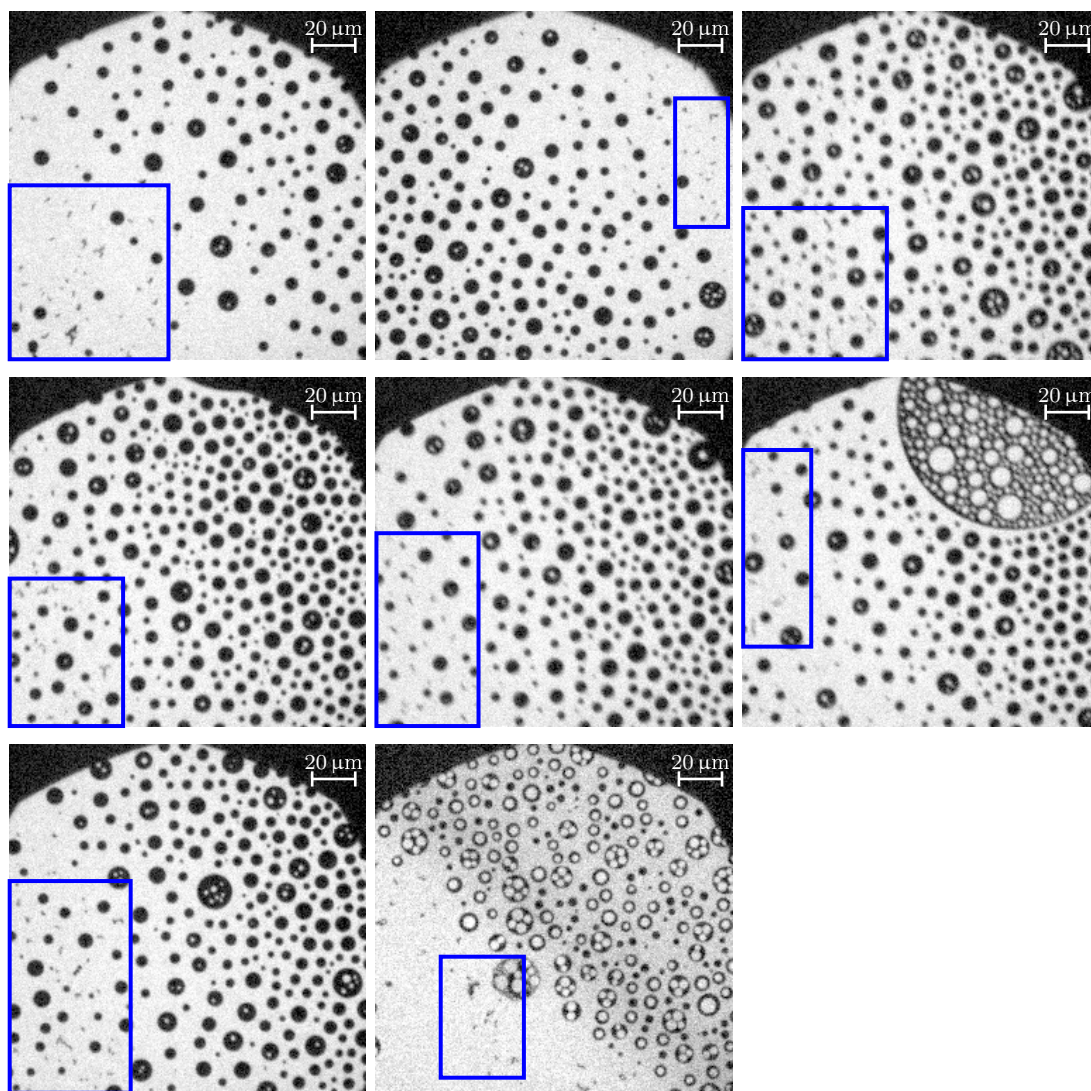


Figure B.23: Fluorescence microscopy images of MBP C1 adsorbed to a monolayer composed of the normal composition without SM at a pressure between 5 mN/m and 10 mN/m. Lipid dye: 0.05 mol-% Rh-DHPE. The blue rectangles highlight exemplary small regions arising from the adsorption of MBP to the myelin-like monolayer.

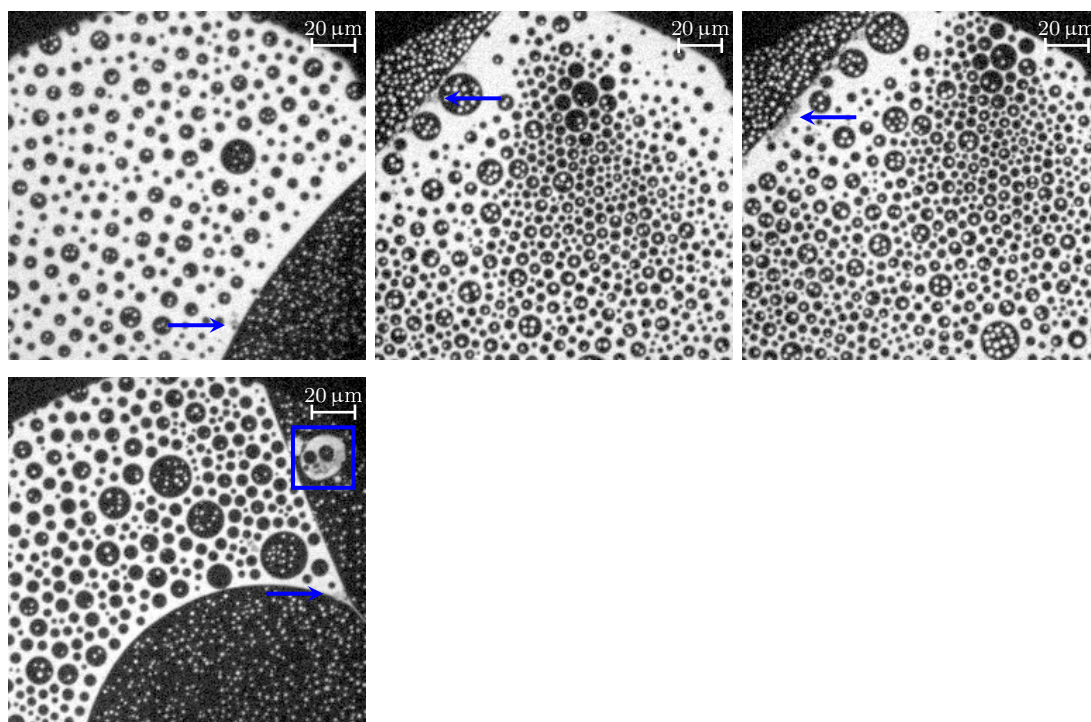


Figure B.24: Fluorescence microscopy images of MBP C8 adsorbed to a monolayer composed of the normal composition without SM at a pressure between 5 mN/m and 10 mN/m. Lipid dye: 0.05 mol-% Rh-DHPE. The blue arrows and the blue rectangle highlight exemplary small regions arising from the adsorption of MBP to the myelin-like monolayer.

B.3 Outlook

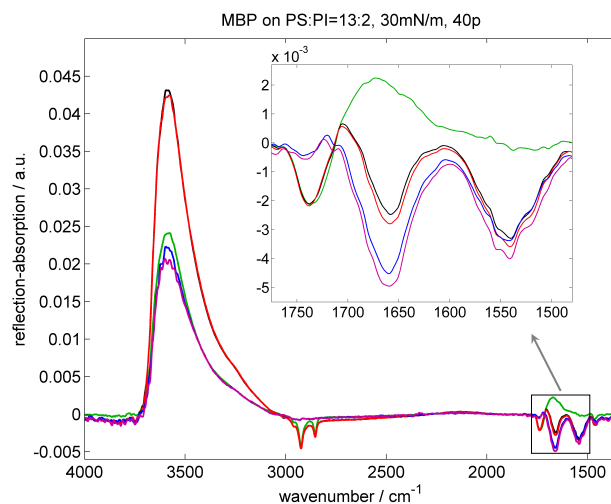


Figure B.25: IRRAS spectrum of (A) a monolayer of PS:PI=13:2 at 30 mN/m (green curve), (B) MBP C1 adsorbed to a monolayer of PS:PI=13:2 at 30 mN/m (black curve), (C) MBP C8 adsorbed to a monolayer of PS:PI=13:2 at 30 mN/m (red curve), (D) differential spectrum of (B) and (A) (blue curve) and (E) differential spectrum of (C) and (A) (purple curve). Spectra were recorded with p-polarised IR radiation at an angle of incidence of 40° .

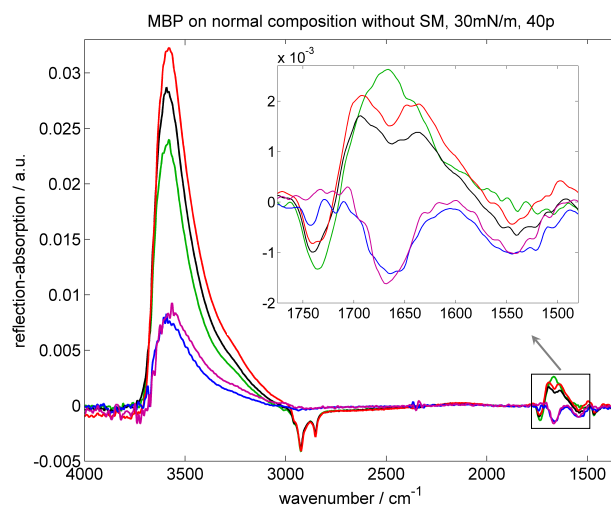


Figure B.26: IRRAS spectrum of (A) a monolayer of normal composition without SM at 30 mN/m (green curve), (B) MBP C1 adsorbed to a monolayer of normal composition without SM at 30 mN/m (black curve), (C) MBP C8 adsorbed to a monolayer of normal composition without SM at 30 mN/m (red curve), (D) differential spectrum of (B) and (A) (blue curve) and (E) differential spectrum of (C) and (A) (purple curve). Spectra were recorded with p-polarised IR radiation at an angle of incidence of 40° .

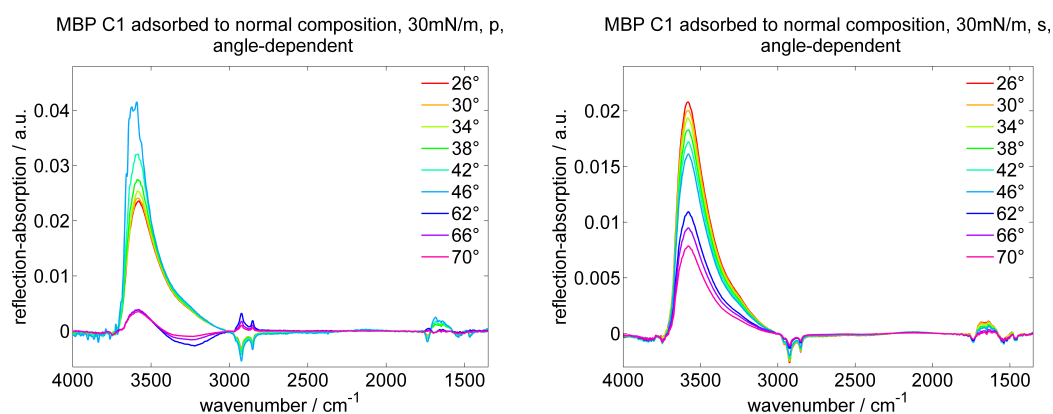


Figure B.27: Experimental spectra of MBP C1 adsorbed to a monolayer of the normal composition, recorded at various angles of incidence and polarisations (left: p-polarisation, right: s-polarisation).

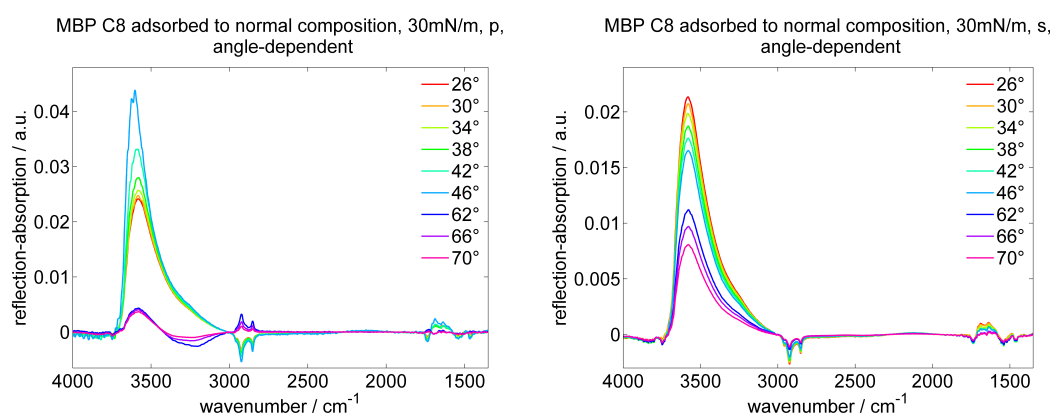


Figure B.28: Experimental spectra of MBP C8 adsorbed to a monolayer of the normal composition, recorded at various angles of incidence and polarisations (left: p-polarisation, right: s-polarisation).

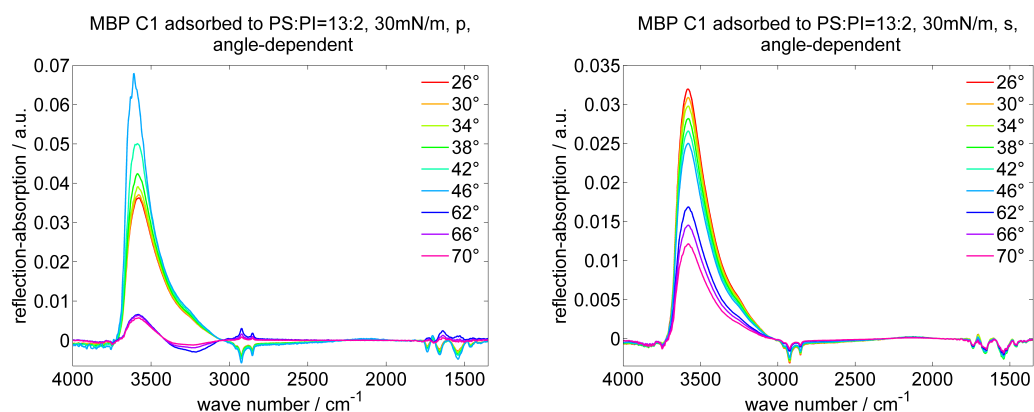


Figure B.29: Experimental spectra of MBP C1 adsorbed to a monolayer of PS:PI = 13:2, recorded at various angles of incidence and polarisations (left: p-polarisation, right: s-polarisation).

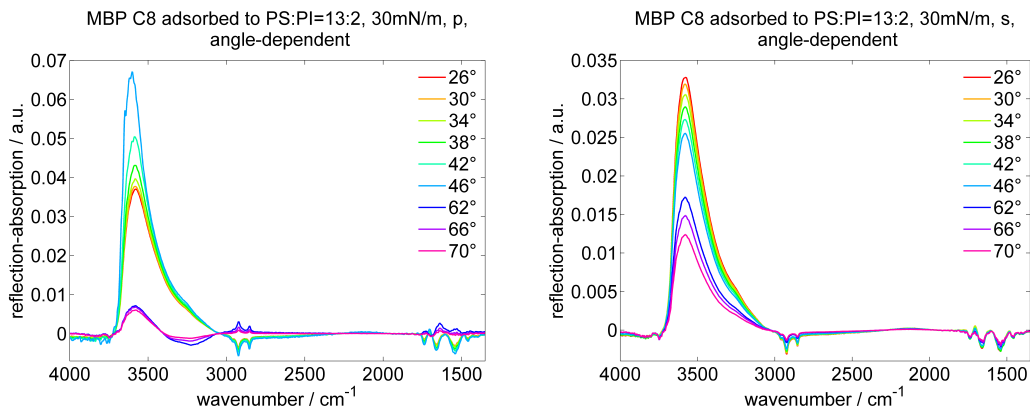


Figure B.30: Experimental spectra of MBP C8 adsorbed to a monolayer of PS:PI = 13:2, recorded at various angles of incidence and polarisations (left: p-polarisation, right: s-polarisation).

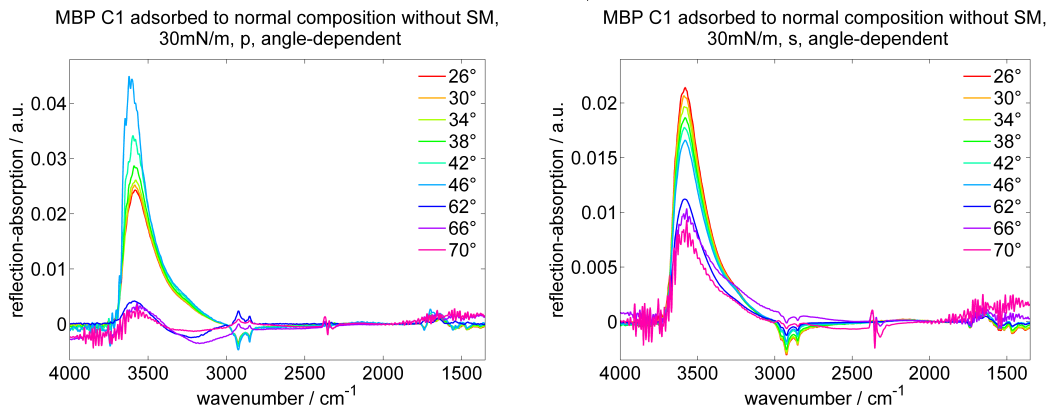


Figure B.31: Experimental spectra of MBP C1 adsorbed to a monolayer of the normal composition without SM, recorded at various angles of incidence and polarisations (left: p-polarisation, right: s-polarisation).

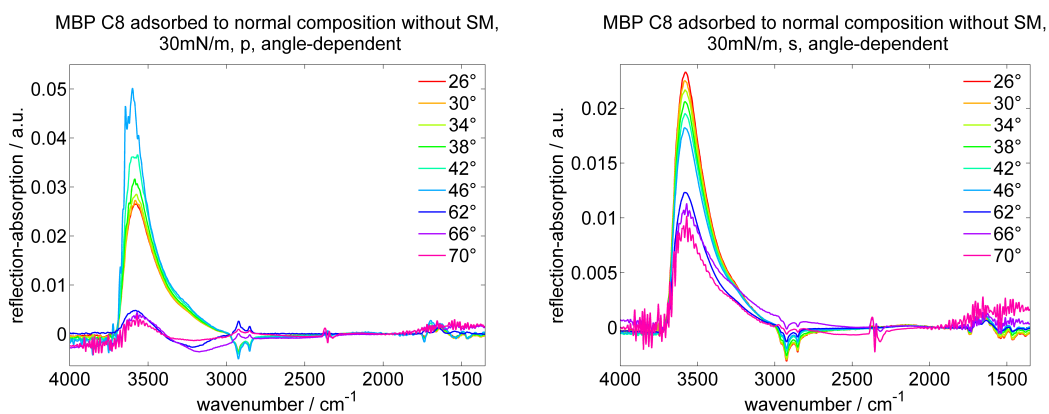


Figure B.32: Experimental spectra of MBP C8 adsorbed to a monolayer of the normal composition without SM, recorded at various angles of incidence and polarisations (left: p-polarisation, right: s-polarisation).

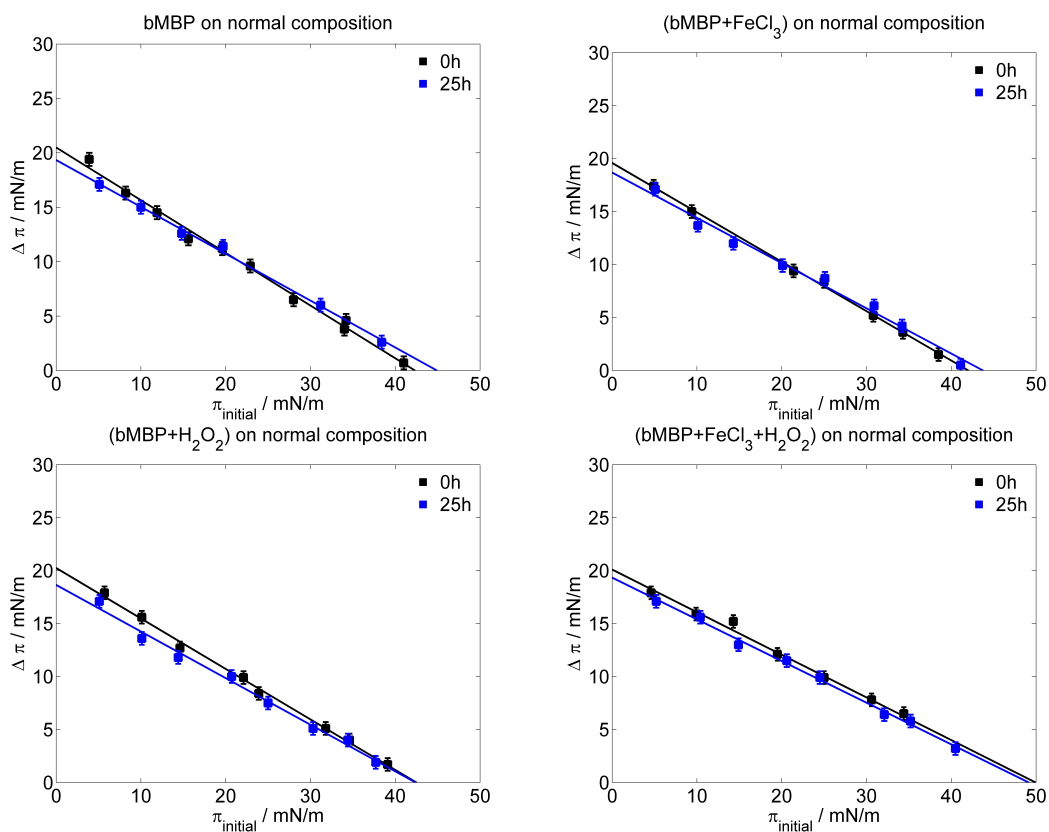


Figure B.33: Difference of surface pressure $\Delta\pi(\pi_{\text{ini}})$ after maximal 5 h of adsorption of bMBP ($c = 100$ nM), bMBP ($c = 100$ nM) with FeCl₃ ($c = 74$ nM), bMBP ($c = 100$ nM) with H₂O₂ ($c = 18.5$ nM) and bMBP ($c = 100$ nM) with FeCl₃ (74 nM) and H₂O₂ ($c = 18.5$ nM) to brain lipid monolayers as a function of the initial surface pressure π_{ini} . Regression curves are included.

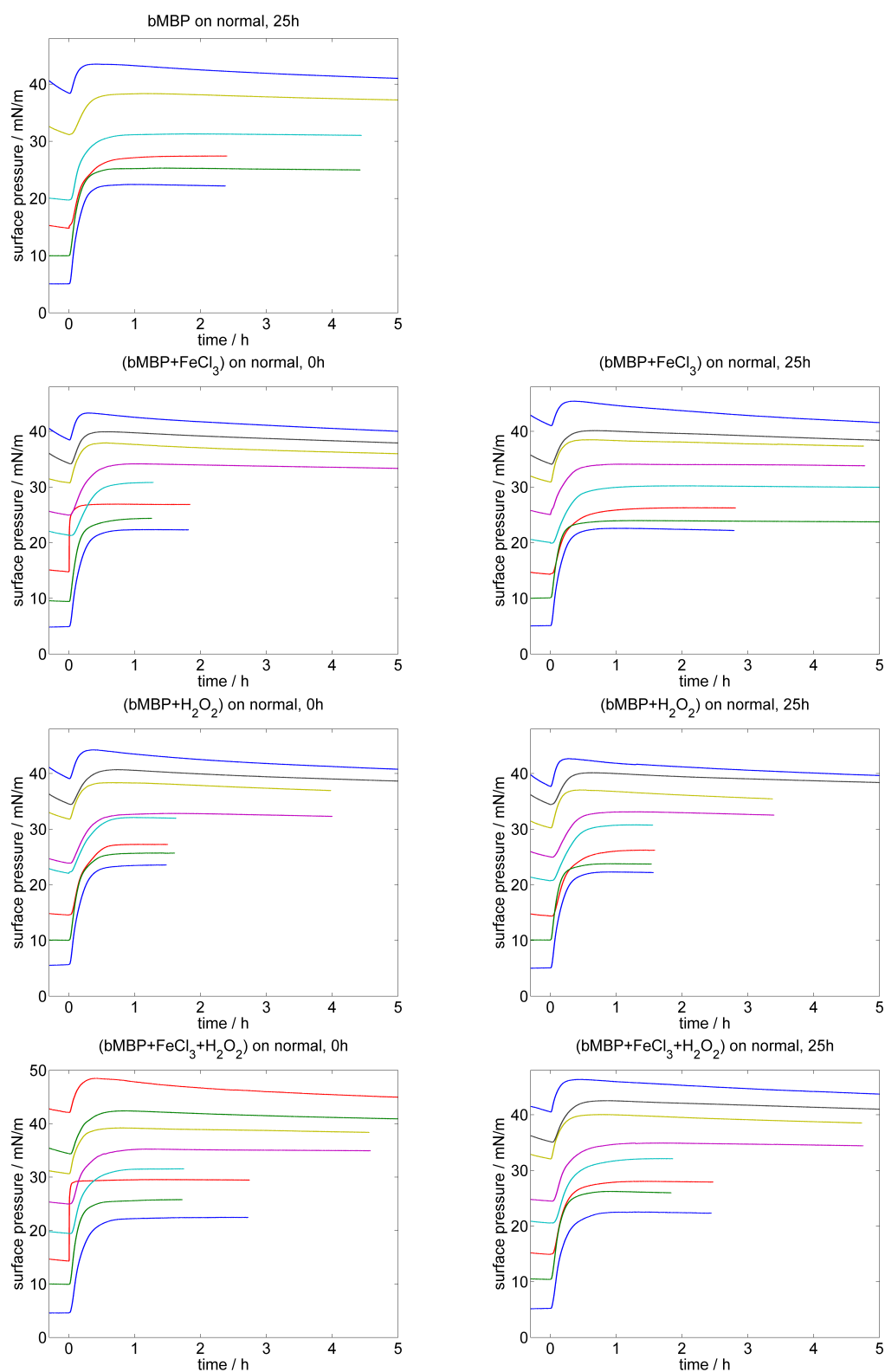


Figure B.34: Time-dependent surface pressure of bMBP incubated with FeCl_3 , H_2O_2 or both for 0h or 25h, respectively, injected at $t = 0$ h below monolayers of constant surface area.

Publications

- (1) D. Kurzbach, A. Vanas, A. G. Flamm, N. Tarnoczi, G. Kontaxis, N. Maltar-Strmečki, K. Widder, D. Hinderberger, and R. Konrat. Detection of correlated conformational fluctuations in intrinsically disordered proteins through paramagnetic relaxation interference. *Physical Chemistry Chemical Physics*, 18:5753-5758, 2016.
- (2) K. Widder, S. R. MacEwan, E. Garanger, V. Núñez, S. Lecommandoux, A. Chilkoti, and D. Hinderberger. Characterisation of hydration and nanophase separation during the temperature response in hydrophobic/hydrophilic elastin-like polypeptide (ELP) diblock copolymers. *Soft Matter*, 13:1816-1822, 2017.
- (3) K. Widder, J. Träger, A. Kerth, G. Harauz, and D. Hinderberger. Interaction of myelin basic protein with myelin-like lipid monolayers at air–water interface. *Langmuir*, 34:6095-6108, 2018.
- (4) K. Widder, G. Harauz, and D. Hinderberger. Myelin basic protein (MBP) charge variants show different sphingomyelin-mediated interactions with myelin-like lipid monolayers. *submitted*
- (5) K. Widder, F. G. Quiroz, A. Chilkoti, and D. Hinderberger. Nanoscopic characterisation of temperature hysteresis, hydration and dehydration processes of temperature-responsive peptide polymers. *in preparation*

Poster Contributions

- (1) K. Widder and D. Hinderberger. Characterisation of the hysteretic behaviour of thermoresponsive polymers by spin probing EPR. *12th Greta Pifat Mrzljak International School of Biophysics*, Primošten, Croatia, 2014.
- (2) K. Widder, E. Garanger, S. Lecommandoux, A. Chilkoti, and D. Hinderberger. Characterisation of the thermoresponsive behaviour of elastin-like polypeptides by spin probing EPR. *10th European Biophysics Congress*, Dresden, Germany, 2015.
- (3) K. Widder, F. G. Quiroz, A. Chilkoti, and D. Hinderberger. Characterisation of the hysteretic behaviour of thermoresponsive peptide polymers by spin probing EPR. *Biennial Meeting of the GDCh-Division Macromolecular Chemistry*, Halle (Saale), Germany, 2016.
- (4) K. Widder, A. Kerth, C. Schwieger, G. Harauz, and D. Hinderberger. Interaction of myelin basic protein with myelin lipid monolayers at the air–water interface. *19th IUPAB congress and 11th EBSA congress*, Edinburgh, United Kingdom, 2017.
- (5) K. Widder, G. Harauz, D. Hinderberger. Interaction of MBP C1 and C8 with myelin-like lipid monolayers at the air–water interface. *59th International Conference on the Bioscience of Lipids*, Helsinki, Finland, 2018.

Curriculum Vitae

PERSONAL DATA

Katharina Widder
* 30.12.1989, Bad Frankenhausen, Germany

EDUCATION

- 08.2000 – 06.2008 *Staatliches Gymnasium „Klosterschule“ Roßleben*
Abitur
- 10.2008 – 09.2011 *Martin-Luther-Universität Halle-Wittenberg*
Study of Medical Physics (Bachelor of Science)
Bachelor thesis on ‘*Laserablation einer Al₂O₃-Schicht von Schwarzem Silizium*’
- 10.2011 – 02.2014 *Martin-Luther-Universität Halle-Wittenberg*
Study of Medical Physics (Master of Science)
Master thesis on ‘EPR spectroscopy and imaging of controlled drug delivery systems’
- 04.2014 – 12.2018 *Martin-Luther-Universität Halle-Wittenberg*
PhD student in the group of Prof. D. Hinderberger, Institute of Chemistry, ‘Physical Chemistry - Complex Self-Organizing Systems’

Danksagung

An dieser Stelle möchte ich mich bei allen bedanken, die mich während meiner Promotion unterstützt haben.

Meinem Betreuer Prof. Dariush Hinderberger danke ich für die Aufnahme in seine Arbeitsgruppe und die Überlassung der bearbeiteten Themen. Ich bedanke mich für das Gewähren wissenschaftlicher Freiheiten und die ständige Bereitschaft zur Diskussion sowie für die Möglichkeit, meine Forschung auf Tagungen und Konferenzen zu präsentieren.

Prof. George Harauz danke ich für die gute Zusammenarbeit, zahlreiche Diskussionen und hilfreiche Ratschläge zum MBP-Projekt.

Bei Elisabeth Garanger und Felipe Garcia Quiroz bedanke ich mich für die Diskussionen über die thermoresponsiven Polymere.

Andreas Kerth und Christian Schwieger danke ich, für die Einarbeitung in die Filmwaagen- und IRRAS-Methodik.

Prof. Milton Stubbs und seiner Gruppe danke ich für die Bereitstellung der Labore und Geräte zum Exprimieren und Aufreinigen des rmMBP. Besonderer Dank gilt hierbei Anja Greschuchna und Arne Börgel für ihre tatkräftige Unterstützung.

Meinen Kollegen Peter, Jörg und Till, in denen ich gute Freunde gefunden habe, danke ich für ihr offenes Ohr bei wissenschaftlichen und menschlichen Problemen. Vor allem meinem Lieblingsbanknachbarn Peter habe ich zu danken, für all die Aufheiterungen und das gegenseitige Vertrauen.

Den technischen Assistentinnen Heike Schimm und Stefanie Weber sowie allen anderen Mitgliedern der Arbeitsgruppe danke ich für die angenehme Arbeitsatmosphäre, für ausgefallene Ideen beim Labor-Minigolf und für viele leckere Beiträge zur Kuchenrunde.

Meinen Freunden und meiner Familie danke ich für ihre uneingeschränkte Unterstützung und Akzeptanz in allen Lebenslagen.

Der größte Dank gilt meiner Freundin Anja, für ihren Beistand während all der Hochs und Tiefs, für ihre Geduld und ihre Liebe, ohne die ich so manche Hürde nicht gemeistert hätte.

Eidesstattliche Erklärung

Ich erkläre an Eides statt, dass ich die vorliegende Arbeit selbstständig und ohne fremde Hilfe verfasst, keine anderen als die von mir angegebenen Quellen und Hilfsmittel benutzt und die den benutzten Werken wörtlich oder inhaltlich entnommenen Stellen als solche kenntlich gemacht habe.

Halle (Saale),

Katharina Widder